Field measurements and finite element simulations of the interaction between dynamic strain ageing and ductile damage in metallic alloys

Sicong Ren

▶ **To cite this version:**

Sicong Ren. Field measurements and finite element simulations of the interaction between dynamic strain ageing and ductile damage in metallic alloys. Materials. Université Paris sciences et lettres, 2018. English. NNT : 2018PSLEM001 . tel-01843228

HAL Id: tel-01843228

https://pastel.hal.science/tel-01843228

Submitted on 18 Jul 2018

HAL is a multi-disciplinary open access archive for the deposit and dissemination of scientific research documents, whether they are published or not. The documents may come from teaching and research institutions in France or abroad, or from public or private research centers.

L'archive ouverte pluridisciplinaire **HAL**, est destinée au dépôt et à la diffusion de documents scientifiques de niveau recherche, publiés ou non, émanant des établissements d'enseignement et de recherche français ou étrangers, des laboratoires publics ou privés.

THÈSE DE DOCTORAT

de l'Université de recherche Paris Sciences et Lettres
PSL Research University

Préparée à MINES ParisTech

Mesures de champs et simulations par élément finis de l'interaction entre vieillissement dynamique et endommagement dans les alliages métalliques

Field measurements and finite element simulations of the interaction between dynamic strain ageing and ductile damage in metallic alloys

Ecole doctorale n°432

SCIENCES ET MÉTIERS DE L'INGÉNIEUR

Spécialité SCIENCE ET GÉNIE DES MATÉRIAUX

JURY :

Véronique FAVIER, Présidente/Examinatrice
Ecole Nationale Supérieure d'Arts et Métiers

Thomas BÖHLKE, Rapporteur
Karlsruhe Institute of Technology

Odd Sture HOPPERSTAD, Rapporteur
Norwegian University of Science and Technology

Ahmed BENALLAL, Examinateur
ENS de Cachan

Thilo F. MORGENEYER, Examinateur
Mines ParisTech

Gilles ROUSSELIER, Examinateur
Mines ParisTech

Samuel FOREST, Invité
Mines ParisTech, CNRS

Matthieu MAZIERE, Invité
Mines ParisTech

Soutenue par **Sicong REN**
le 18 janvier 2018

Dirigée par **Thilo F. MORGENEYER**
Matthieu MAZIERE
Samuel FOREST

MINES ParisTech | PSL RESEARCH UNIVERSITY PARIS

This thesis is dedicated to my beloved family.

Acknowledgement

First of all, I wish to express my deepest gratitude to my atypical and exceptional advisor team, Matthieu Mazière, Thilo F. Morgeneyer, Gilles Rousselier and Samuel Forest for their patient guidance and constant support. Matthieu has been very pedagogic and supportive who explained the strain ageing phenomenon and numerical aspects to me in great detail. I also hope to someday I could be able to command an audience as well as he can. Thilo is a friend-like mentor to me. He allowed me to discover the fascinating synchrotron facility in Grenoble where we met each other for the first time on the second day of my thesis. I got two turns to find the beamline ID19 located outside the main building. It is an honour for me to work directly with Gilles on the ductile fracture. Besides science, I am also grateful to Gilles for his kindness and generosity. I enjoyed very much the 'spectacle de feu'. I have been extremely lucky to be able to work with Samuel. His deep knowledge and insightful advices are the primary resource for pushing my thesis forward. His enthusiasm and energy for guiding students are contagious. Although he can not count how many students he has, he cares about everyone. They are my role model in my future career.

I also would like to extend my sincere gratefulness to the members of my PhD thesis committee. I have special thanks for Professor Thomas Böhlke from Karlsruhe Institute of Technology and Professor Odd Sture Hopperstad from Norwegian University of Science and Technology for taking time to review my work as rapporteurs. I am sorry for this extra burden on your Christmas holiday to do list. I am grateful to Professor Véronique Favier for being the president of the committee and Professor Ahmed Benallal for helpful comments during my thesis defence.

I am thankful for all the colleagues at Centre des Matériaux (CDM). Thanks to Jacque Besson, director of CDM at the beginning of my thesis, and Jérôme Crépin, current director of CDM for giving me the opportunity to carry out my PhD thesis in this centre; Henry Proudhon for helping me process laminography images using Pymicro package; The team VAL and DSI for solving technical problems related to Zebulon and cluster Rama. Experimental studies are conducted with the assistance of my colleagues at 'bocal'. Thanks to 'mon pote' Abdennour Meddour for his exceptional technical support during my mechanical tests; Stéphanie Tang for her advices about DIC measurement; Régis Clement for his smile and kindness; Maria Betbeder and Antoine Debray for SEM fractography; I also have to thank all the administrative staffs for their helps, especially Konaly Sar for her warm welcome and good sense of humour making my journey to France much easier; Véronique Matos, Catherine Rouil and Ziradjoudine Akber, Odile Elimort for solving the most practical problems during my stay: titre de séjour, canteen, travelling...

Next, I want to thank all the members of B109: Chao Ling (my Zebulon coach at the beginning), Juan-manuel Garcia (who proves CrossFit is helpful for belly growth), Quentin Roirand (thanks for your brilliant jokes), Nicolas Gueninchault (I dare not say anything, because he has too much muscle), Clément Soret and Guillaume Marion. Without you, the office life would be too quiet. I would like to thank my Chinese friends at CDM: Lv Fang, Qi Huang, Youbin Chen, Yang Zhang, Tang Gu. I cherish every enjoyable moment we shared together. I will miss two Czech visitors, Martin Horak and Luděk Stratil and one German visitor Anne Dennstedt. Especially thanks to Luděk Stratil for the nice beer, Becherovka and exposing me to the ice hockey game. I also want to thank Sakimoto-San, Ichikawa-San and Shibata-San for the interesting exchanges about Japanese culture during lunch time; all the PhD students at CDM, Joseph Marae-Djouda, Clément Defaisse, Hayat Abdesselam, Quentin Tonizzo, Frank Tioguem-Teagho, Tom Petit, Ante Buljac, Har-

ris Farooq, Nicolas Cliche, Hélène Godin, Mariem Trabelsi, Erembert Nizery, Pierre-alexis Poulet, François Rasselet...for your help during these years. Furthermore, special thanks are given to my Half-Marathon team Xiao Wei, Yifan Xia and Yi Zhang. You helped me maintain my physical health.

Finally, I would like to thank my parents for their love and support throughout my life. Thank you both for encouraging and supporting my study far away from home. Last but not least, I want to thank Ruiwei Chen (or Dr. Chen soon), my wife since 2015, for her support over the last 10 years. She has been a constant source of strength and inspiration. I hope we could continue to make progress together.

Sicong Ren
Paris, 19 February 2018

Contents

Chapter 1

Introduction

Résumé

Le lien entre la localisation de la déformation et l'endommagement pour les matériaux ductiles est encore un sujet à explorer. Le développement récent de la technique de laminographie aux rayons X (au synchrotron) permet d'observer en 3D des objets qui sont fins (~1 mm d'épaisseur) mais étendus dans un plan. Cela permet des observations in-situ de la rupture ductile dans des tôles gardant des conditions aux limites similaires aux applications en service ce qui est un grand avantage par rapport à la tomographie. L'évolution de l'endommagement d'un alliage d'aluminium pour une application sur fuselage a ainsi pu être observée récemment à une résolution micrométrique. Par ailleurs l'influence des phénomènes de vieillissement par la déformation (type bande de Lüders ou Portevin-Le Chatelier) sur la rupture est encore mal compris. Ces effets sont pourtant observés dans de nombreux alliages industriels comme les aluminiums séries-2000 ou 5000, ou par exemple, dans le cas des aciers C-Mn pour lesquels un creux de ductilité est observé dans la gamme de température ou ces effets sont les plus marqués. Cette thèse a pour objectif d'étudier l'interaction entre les phénomènes de localisation de la déformation et notamment ceux dus au vieillissement par la déformation, et le développement de l'endommagement ductile. La thèse se décompose en 6 chapitres. Dans ce premier chapitre, on montre tout d'abord le contexte de cette étude. Le deuxième chapitre présente une recherche bibliographique sur l'effet de vieillissement par la déformation, les matériaux et le lien possible entre le mode de rupture et le vieillissement par la déformation. Dans le troisième chapitre, on propose un nouveau modèle de vieillissement par la déformation basé sur la densité de dislocations. Dans le quatrième chapitre, l'observation directe de l'effet Portevin-Le Chatelier est effectuée avec corrélation d'images pour les alliages d'aluminium. Les résultats expérimentaux sont comparés à ceux de simulation. Dans le cinquième chapitre, on étudie l'influence de vieillissement dynamique sur la rupture par des éprouvettes entaillées du type SENT. Dans le dernier chapitre, un modèle couplé (polycristallin) est appliqué à la simulation de l'effet de vieillissement dynamique et la rupture en biseau dans une éprouvette CT.

1.1 Context

A better understanding of the deformation behaviour of materials, particularly the mechanism of ductile damage is necessary for a better prediction of fracture in industrial structures and for the optimization of material micro-structure.

Strain ageing effects (Lüders or Portevin-Le Chatelier (PLC)) are observed in many industrial alloys such as certain C-Mn steels and 5000-series aluminium alloys. This effect is known to induce serrations on the stress-strain curves and strain localization bands. However, the influence of strain ageing on the ductile fracture is still poorly understood.

For example, in a PWR (Pressurized Water Reactors) nuclear power plant, C-Mn steels are widely used as pipeline materials in the secondary circuit where steam is generated and flows to turbines. The service temperature of these pipelines ranges from 20 °C to 300 °C. These materials are very sensitive to strain ageing effect. A loss of ductility was reported within the temperature range (around 200 °C) where strain ageing effects are most pronounced [Belotteau, 2009; Wang, 2011]. Slant fracture was found in the PLC sensitive domain characterized by temperature and strain rate. In contrast, cup-cone fracture mode was found for the other test conditions as shown in Fig. 1.1. The simulation and prediction of these different fracture modes are still challenging due to lack of knowledge about the underlying failure mechanisms.

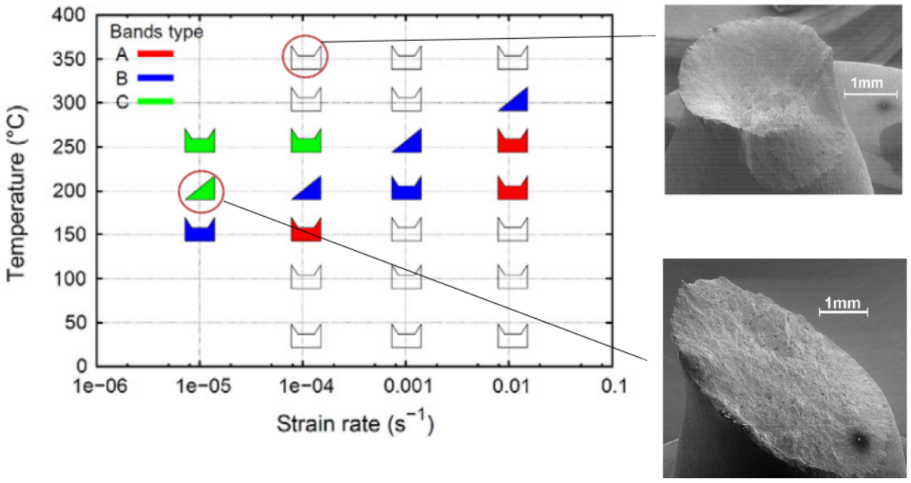

Figure 1.1 – Fracture modes of C-Mn steel round bar specimens tested at different strain rates and temperatures. The three colours represent three different types of PLC serrations. The blank symbol means PLC bands have not been observed [Wang et al., 2011]. Slant fracture is denoted by triangle.

The recent progress in synchrotron X-ray laminography technology provides a new tool for observing ductile fracture inside thin sheet specimens. The use of this technique is a significant advantage compared with tomography that can only be used for observing axi-symmetric or stick-shape-like specimens. The damage evolution in the latest generation Al-Cu-Li aluminium alloys applied for aircraft fuselage has been observed with micrometer scale resolution [Morgeneyer et al., 2014]. The early stage localization bands seem to be the precursor of ductile fracture in the CT-like specimen of this newly developed material. As shown in Fig. 1.2, the rapid void damage occurred in an slanted localization band at a very late stage which leads to a slanted crack. The origin of these

localization bands needs to be clarified. In contrast to C-Mn steels, PLC effect occurs around room temperature in aluminium alloys. Detailed characterisations of PLC effect in these Al-Cu or Al-Cu-Li alloys are still lacking.

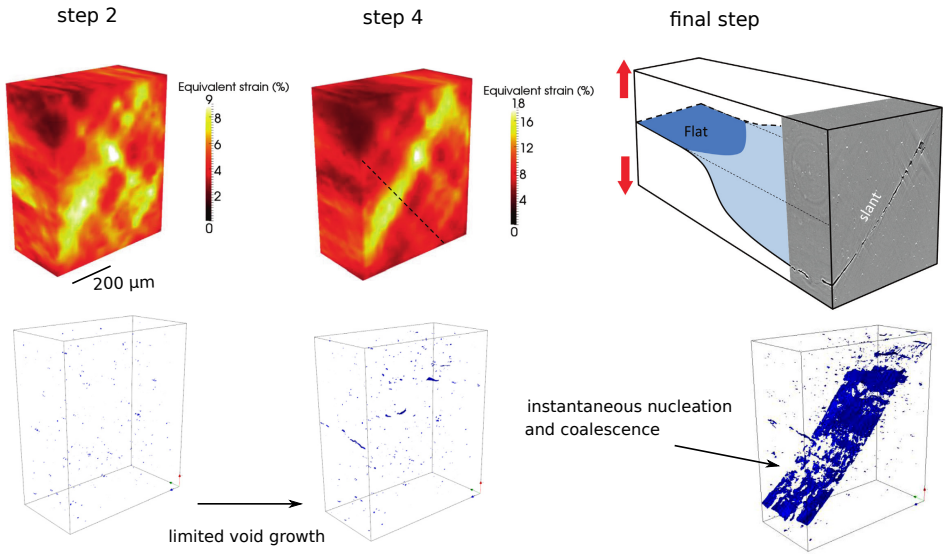

Figure 1.2 – Laminography-DVC results: cumulated equivalent strain field and void evolution during stepwise loading in front of the notch of a AA2198-T8R CT specimen. Steps 2 and 4 correspond to different loading steps [Morgeneyer et al., 2014]. Step 4 is the last loading step before failure.

1.2 Research objectives

The objective of the current work is to study the interaction between strain localisation due to strain ageing, and the evolution of ductile damage.

- For this purpose, different industrial alloys will be studied through mechanical tests and non contact field measurements such as digital image correlation (DIC). Some of these candidates might be found sensitive to strain ageing under certain test conditions, while others not. Thus it will be possible to evaluate the influence of strain ageing on the development of damage and the final fracture. The existing experimental results on a C-Mn steel will also be used and enriched.

- Numerical studies will also be considered. Firstly, based on previous experimental observations, a dislocation density based strain ageing model will be introduced and tested in order to better describe the influence of strain ageing on the hardening rate.

  Secondly, due to the fact that rapid void damage occurs at very late stage, a macroscopic constitutive model coupling strain ageing (type Kubin-Estrin-McCormick) and a modified damage term will be developed to simulate the localization guided ductile damage. This model will be applied for various specimen geometries, such as plate tensile, round bar and single edge notched tension (SENT), in order to evaluate its ability for predicting the spatio-temporal characteristics of PLC bands and the different fracture modes (flat or slant).

  Thirdly, a polycrystal model proposed by Rousselier and Quilici [2015] involving strain ageing and Coulomb criterion in the slip system will be applied to CT tests.

With this model, the influence of polycrystal framework and material anisotropy on the localization behaviour can be assessed.

1.3 Organization of the thesis

The current work is organised as bellow:

- Chapter 2: A literature review is given for experimental observations and existing modelling tools on strain ageing effects. A review about dynamic strain ageing effect in a new generation of Al-Cu(Li) alloy is made specifically. Finally, the possible link between slant fracture and strain ageing is discussed.

- Chapter 3: A strain ageing model based on dislocation density is presented. The additional strain hardening rate due to the impediment effect of dynamic strain ageing on the annihilation process is taken into account. Numerical validations are performed based on an existing experimental database of a C-Mn steel.

- Chapter 4: Experimental studies combined with digital image correlation are carried out for AA2139-T3 (Al-Cu) and AA2198 (Al-Cu-Li) alloys. The influence of loading path change involved by relaxation, unloading and strain rate jump is investigated. Based on these experimental results, the parameters of the strain ageing model are identified. Simulations of constant strain rate and relaxation tests are compared with DIC measurements. In order to investigate the influence of anisotropy on the localization, the strain rate patterns around notch area using the macroscopic strain ageing model are compared with those using a polycrystal model.

- Chapter 5: To study the influence of PLC effect on the fracture, we performed SENT test with a C-Mn steel which is known to be insensitive to PLC effect at room temperature while sensitive at around 200 °C. 20 °C and 175 °C are chosen for the experiments. The spatio-temporal characteristics of localization around notch tip at these two temperatures are compared using DIC measurement. Simulations with the macroscopic strain ageing model with and without damage are performed. The influence of PLC effect on flat to slant fracture will be studied.

- Chapter 6: Based on previous experimental observations, a modified nucleation term is introduced into Rousselier's damage model in order to simulate damage development inside localization bands. Simulation results of tensile tests and SENT tests using this model are presented. Another attempt for simulating slant fracture is made using a coupled damage model based on the polycrystalline framework which involves strain ageing term and Coulomb criteria in the slip system. Tearing test of CT specimens are simulated using parameters identified for AA2198-T8R alloy. The simulated localization bands around notch area as well as flat-to-slant fracture are compared with laminography-DVC.

Chapter 2

Literature review

Summary

Plastic instabilities related to the Portevin-Le Chatelier (PLC) and Lüders effects have received much attention from the scientific community. Firstly, a literature review of experimental aspects is given in this chapter to present the definition, characteristics, physical origins and consequence of the PLC effect in particular. The recent development of modelling these phenomena based on the strain ageing theory will be outlined. As the target material is the 2000 series aluminium in this thesis, a detailed review about theses alloys and the corresponding PLC effects are summarized and discussed. In addition, the relation between the slant fracture and the PLC effect is discussed. A review of slant fracture in different specimen geometries is given.

Résumé

Les instabilités plastiques liées à l'effet Portevin-Le Chatelier (PLC) et à l'effet Lüders ont reçu une grande attention de la communauté scientifique. Tout d'abord, une étude bibliographique de l'aspect expérimental est donnée dans ce chapitre pour présenter la définition, les caractéristiques, les origines physiques et les conséquences de l'effet PLC particulièrement. Étant donné que le matériau visé est l'aluminium de la série 2000 dans cette thèse, une étude détaillée de ces alliages et de la présence de l'effet PLC dans ces matériaux est présentée et discutée. En outre, la relation entre la rupture en biseau et l'effet PLC est un sujet à explorer. Une étude bibliographique de la rupture en biseau dans des éprouvettes de différentes géométries est donnée.

Contents

2.1 Experimental study of the strain ageing phenomenon

2.1.1 Static and dynamic strain ageing

The strain ageing phenomenon occurs in a large range of industrial materials such as steels and aluminium alloys. It is usually classified into two categories: the static strain ageing (SSA) and the dynamic strain ageing (DSA). Microscopically, both of these two mechanisms are considered to be related to the interaction between dislocations and solute atoms. The DSA represents the dynamic interaction of mobile dislocations and diffusing solute atoms which means the ageing happens during deformation. The SSA denotes the unpinning of initially locked dislocations (ageing before deformation). More details about these two mechanisms will be presented associated with the macroscopic features.

A sharp yield point on the stress-strain curve and a drop of flow stress into a plateau after yielding are the macroscopic manifestations of the SSA mechanism (see Fig.2.1). The unpinning of initially locked dislocations at yield stress causes a sharp yield point. The abrupt production of mobile dislocations locally induce a negative strain hardening. The stress plateau followed the yield point is related to the propagation of deformation bands as the deformation is concentrated in the band front during propagation. The progressive band propagation corresponds to the successive unpinning of the initially blocked dislocations located on the path of bands. Once initiated, they cross over the whole sample just one time. No further repinning can take place because the needed diffusing time is too large for solutes to recapture the dislocations. The first observations of such kind of plastic instabilities are reported by Piobert [1842] and then by Lüders [1860]. Thus, the macroscopic features of SSA is referred to as the Lüders or Piobert-Lüders effect.

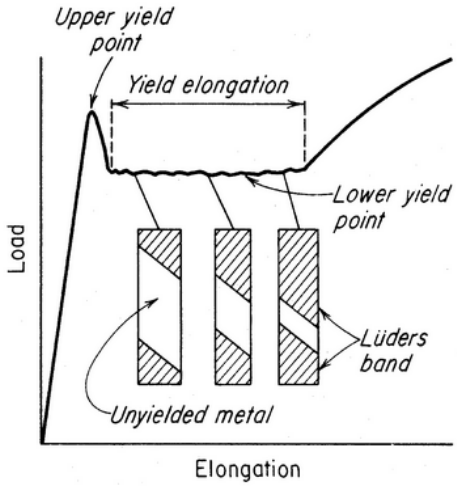

Figure 2.1 – Schematic of the Lüders behaviour [Subramanian and Duncan, 2000].

Macroscopically, the DSA is detected by the occurrence of serrations (or jerky flow) on the stress-strain curve during plastic deformation. The serrations could appear right after the elastic-plastic transition point and sustain until the final failure. It could also appear after a certain deformation (critical strain). The form of serrations and the critical strain are observed to depend significantly on the testing conditions such as strain rate and temperature (see Fig. 2.2). Simultaneously, a number of dynamic localization bands of few millimetres of width could be observed on the specimen surface, for example, by Digital Image Correlation (DIC). They result from the repeated pinning and unpinning of

dislocations temporarily arrested at forest dislocations by diffusing solute atoms. The observations of these macroscopic features could be traced back to the early 20th century such as [Le Chatelier, 1909; Portevin and Le Chatelier, 1923]. This phenomenon, therefore, is usually mentioned as the Portevin-Le Chatelier effect (PLC).

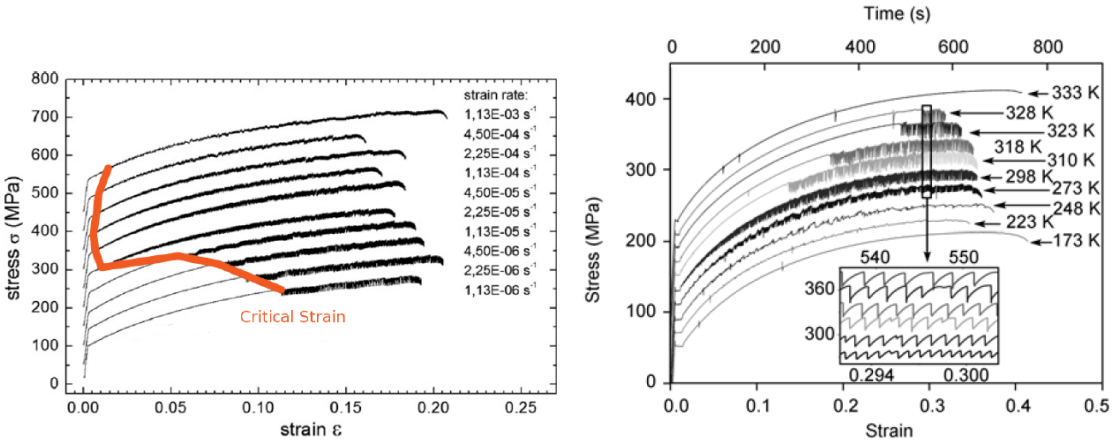

(a) Different strain rates

(b) Different temperatures

Figure 2.2 – (a) PLC serrations observed through tensile tests of AA5754 Al-Mg alloy specimens at room temperature for different strain rates [Mazière and Dierke, 2012]. (b)The shifted stress-strain curves of AA5456 Al-Mg alloy tested at different temperatures taking the same strain rate $5.4 \times 10^{-4} s^{-1}$ [Fu et al., 2011].

The differences between these two phenomena could be summarised below.

- The Lüders bands generally only cross the whole sample once, but the PLC bands propagate repeatedly [Wijler and Van Westrum, 1971]. The dislocations behind PLC bands become aged during the propagation of the bands. As the band will preferably start at the area where the pinning is weakest, the PLC band will usually come back to the original point when reaching the other grip. The Lüders bands do not show significant preference of initiation point. Once the band reaches the grip no reflection could happen because the dislocations behind the band are not aged.
- Lüders bands propagate along with a constant stress plateau. The PLC bands propagate along with a positive slope of stress-strain curves that can be explained by the strain gradient along the specimen length. The deformation wave, in which the deformation rate exceeds that for homogeneous deformation, propagates along the specimen length and creates a strain gradient. Due to the strain gradient, there will be an internal stress gradient along the gauge length which has to be overcome by the deformation band. Hence a gradual increase of stress is required for continuous propagation of the band [Wijler and Van Westrum, 1971].
- In addition, the PLC instability is considered as strain-rate softening phenomenon (negative strain rate sensitivity), but the Lüders bands are regarded as strain softening [Kubin, 1994]. The PLC effect is thermally activated while the Lüders effect is not.

2.1.2 Serrations and localization bands of PLC effect

The current thesis will focus on the PLC effect. The serrations of the PLC effect can be classified into several different types as suggested by Strudel [1979], Karimi [1981], Lacombe [1985] (See Fig. 2.3). On a stiff machine, serrations of type A, B and C are the most dis-

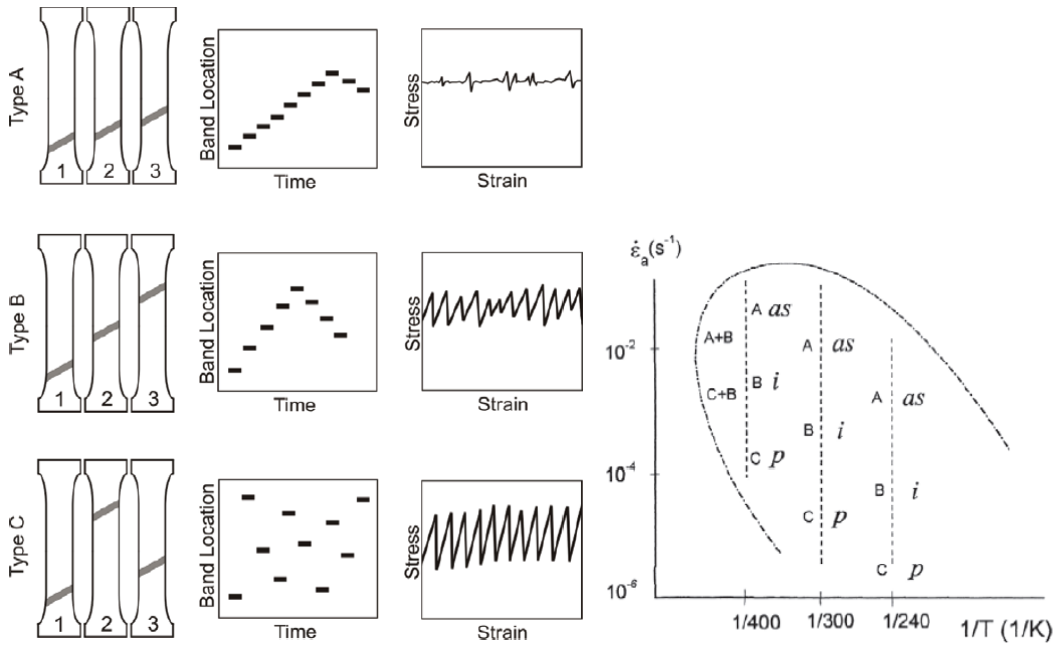

(a) (b)

Figure 2.3 – (a) Schematics of motion, orientation, spatio-temporal appearances and strain-controlled tensile curve characteristics of the PLC bands [Yilmaz, 2016]. (b) Classification of the types of serrations and stress drop statistics in an strain rate-temperature map. Typical band types (A, B, C, A+B, C+B) in the serrated flow range of an Al–Mg alloy; 'i', 'p' and 'as' refer to the different distributions of stress drop number-magnitude histogram [Lebyodkin et al., 2000].

cussed in literature. A schematic view of the spatio-temporal evolution of different types of band is given in Fig. 2.3(a). The serration types are highly related to the strain rate and temperature. Some authors gave a classification schema of serrations as a function of strain rate and temperature as shown in Fig. 2.3(b).

Type A serration is usually seen at high strain rate or low temperature. It is characterized by a sudden increase of stress followed by a drop before recovering to an average value. The serration is increasing slowly and serrated with a low frequency. The corresponding bands always initiate near the same grip section and disappear on the other side after propagating continuously through the whole specimen. The stress increases again until the formation of a new band.

Type B serration appears at intermediate temperature and strain rate. The stress exceeds the average level then drops sharply before increasing again. Several "hopping"bands travelling simultaneously through the specimen can be observed.

Type C serration is observed at low strain rate or high temperature. The load drop after the threshold point is brutal while the reload process is progressive. The localization bands appear and disappear in the specimen almost at random without propagating (stochastic nucleation).

2.1.3 Negative strain rate sensitivity

The PLC effect is also accompanied by a negative strain rate sensitivity which is regarded as an evidence of this effect. Fig. 2.4 shows an example of the strong negative strain rate sensitivity in a C-Mn steel at 200 °C. The negative strain rate sensitivity is the result of the

superposition of DSA and thermally activated flow stress.

It is also important to note that the instabilities of Portevin-Le Chatelier are not systematic in the presence of dynamic strain ageing [Kubin and Estrin, 1991]. The PLC domain is a subset of DSA domain as shown in Fig. 2.5 though this figure can be further discussed since the PLC domain at low temperature and strain rate is not a closed circle [Lebyodkin et al., 2000]. In addition, using negative sensitivity (S=0) as a criterion for predicting the onset of PLC effect is not in agreement with experimental observations Mazière and Dierke [2012].

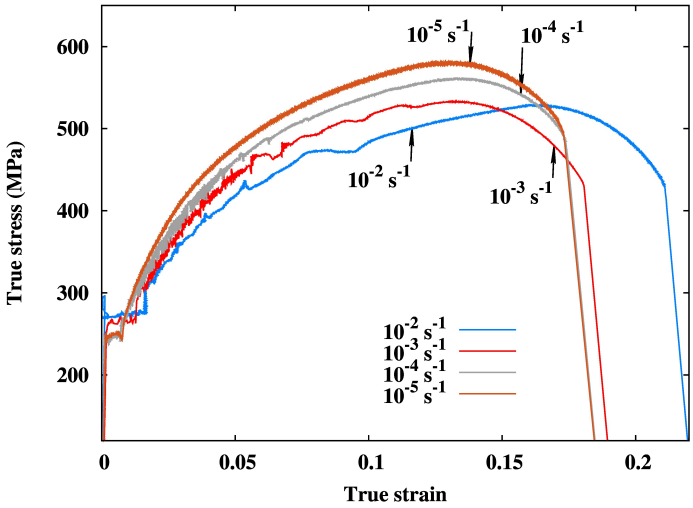

Figure 2.4 – Negative strain rate sensitivity shown on the tensile stress-strain curves of a C-Mn steel at 200°C (results reproduced from [Wang, 2011]).

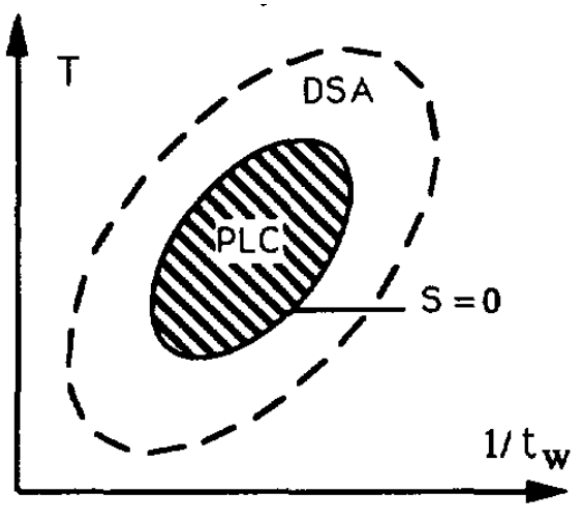

Figure 2.5 – DSA-PLC domain as a function of strain rate and temperature [Kubin and Estrin, 1991].

2.1.4 Influence of strain ageing on the mechanical properties

Besides the abnormal stress flow and localized deformation, significant drop of toughness and ductility have been reported within the DSA active domain. Generally, the experimental study of the fracture toughness is obtained by tearing test $J - \Delta a$ curve. The

unloading compliance technique is recommended by ASTM E1820 for determining the instantaneous crack length through measuring CMOD-based elastic unloading compliance in a single specimen test. When the material is sensitive to the strain ageing effect, the reloading peak and serrations could be seen on the curves as shown in Fig. 2.6.

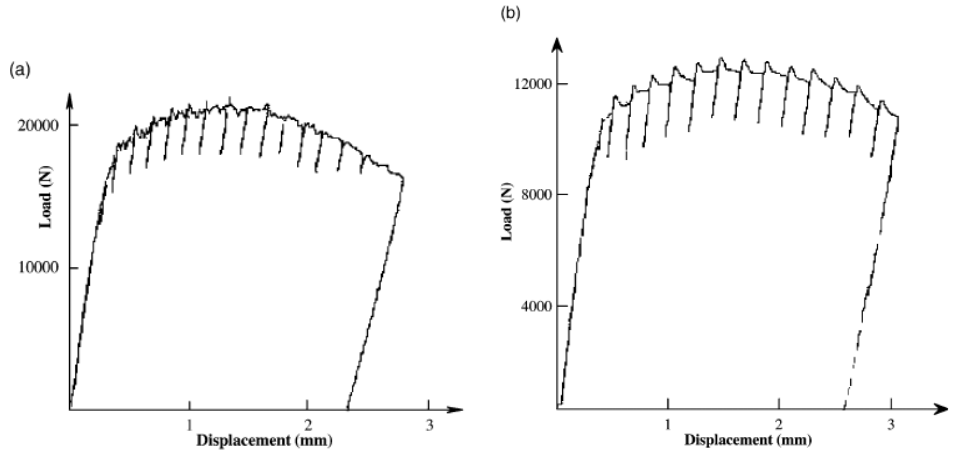

(a) (b)

Figure 2.6 – Load–displacement curves of tearing test at 200°C (a) and 100°C (b) for a C-Mn steel (A48) [Wagner et al., 2002].

Chakravartty et al. [1983] observed the PLC effect in A203D steel tensile specimens around 200 °C and reported a loss of ductility. Miglin et al. [1985] observed the reduced ductility and toughness in a carbon steel SA515-70 around 200 °C through unloading compliance J test on CT specimens. Amar and Pineau [1985] reported the reduction of toughness (CT specimen) and ductility (notched specimen) of A508 steel around 300 °C. The material shows DSA features like negative strain rate sensitivity at 300 °C without serrations of PLC effect. Wagner et al. [1998] reported ductility loss and increase of ultimate tensile strength in a C-Mn steel around 200 °C through tensile tests. Yoon et al. [1999] reported (see Fig. 2.7) that the minimum toughness line is located on the serration disappearing line (SA516-70 steel). Kim et al. [2004] confirmed the loss of toughness within DSA regime of the SA516-70 steel. Belotteau [2009] and Wang [2011] reported the loss of toughness of TU48C (C-Mn) steel around 200 °C.

Some researchers tried to relate such deterioration in fracture toughness with DSA related localization. Calonne et al. [2004] carried out an experimental study about the CF8M duplex stainless steels at room temperature (no PLC effect) and 320 °C (with PLC effect) with smooth cylindrical specimens. At room temperature the fracture occurred in three steps: ferrite cleavage initiation, cleavage crack extension and growth in austenite. At 320 °C, damage mechanism consisted of cleavage, shearing and ductile fracture in ferrite. Necking and bulk damage are very limited. The author explained this with the DSA related localization: as soon as cleavage cracks occur in ferrite, localization will appear and force damage to develop inside the bands.

Gupta et al. [2006] studied a 12% Cr martensitic stainless steel (AISI 403). Within the DSA temperature regime the material showed reduced fracture toughness. SEM fractography showed that traditional dimples of ductile fracture occur in all cases. However, the author noticed the crack growth instabilities and the presence of underdeveloped dimples (flat area A) interspersed between well developed dimpled areas within DSA domain as presented in Fig. 2.8. The author related theses flat areas to the DSA related strain localization at crack tip. He thinks the plastic deformation at crack tip will localize in the

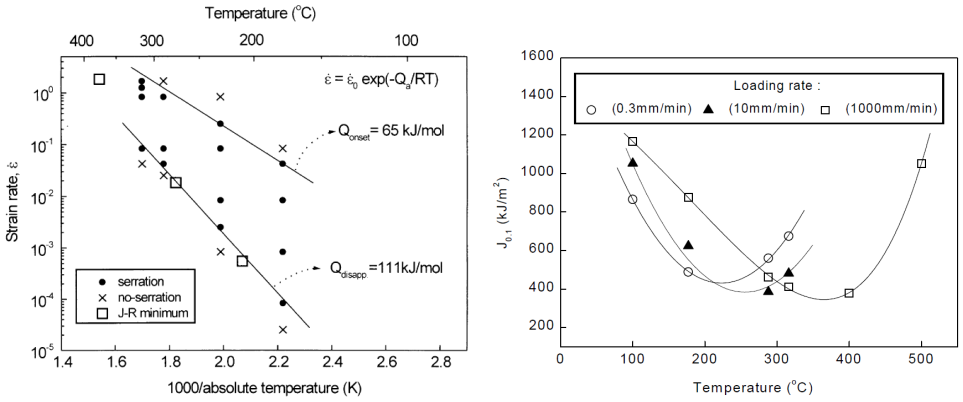

(a) (b)

Figure 2.7 – (a) Serration map and positions of minimum toughness position (b) Variations of J values, corresponding to crack growth of 2.54 mm on J–δa plots, as a function of temperature at different loading rates [Yoon et al., 1999]

PLC band which promotes the propagation of crack. The flat area containing few ductile dimples are signatures of the occurrence of the crack jumps. Because rapid separation of the crack faces leaves less time for a large number of voids to nucleate during ductile crack growth.

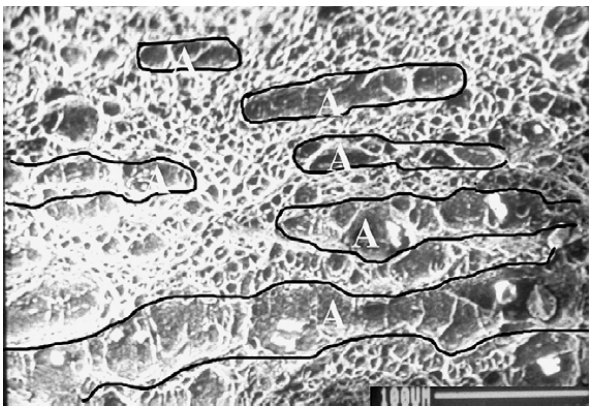

Figure 2.8 – SEM fractograph showing the presence of flat surfaces (area A) within the classical dimpled areas. Test of CT specimen carried out at 300 °C and loading rate 3.33 µm/s [Gupta et al., 2006].

Belotteau [2009] studied the fractography of three types of specimens: axi-symmetric smooth tensile, axi-symmetric notched and compact tension in order to reveal the mechanism of fracture with the presence of DSA. The material showed PLC effect around 200 °C. The smooth tensile specimens showed cup-cone fracture surface at room temperature and slant surface at 200 °C. At 20 °C, sectional view showed the region around fracture surface have more voids with bigger size compared with 200 °C. SEM fractography observation showed spherical dimples in both temperatures without significant difference as shown in Fig. 2.9. The author suggested that striction appears inside a oriented PLC band at 200 °C. As the deformation inside the band is higher than the outside parts, void growth and coalescence will develop along this band as shown in Fig. 2.10. This hypothesis explained the small amount of voids in the area away from the crack surface at 200 °C. In an earlier work, Moreno [1998] also reported that the size of dimples do not

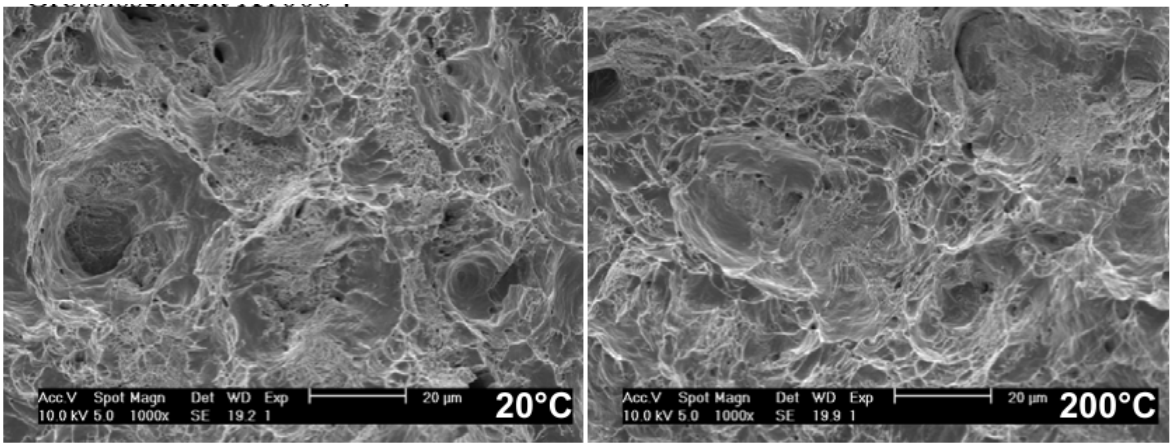

Figure 2.9 – Fractography by SEM of the axi-symmetric tensile specimens at 20 °C and 200 °C [Belotteau, 2009]

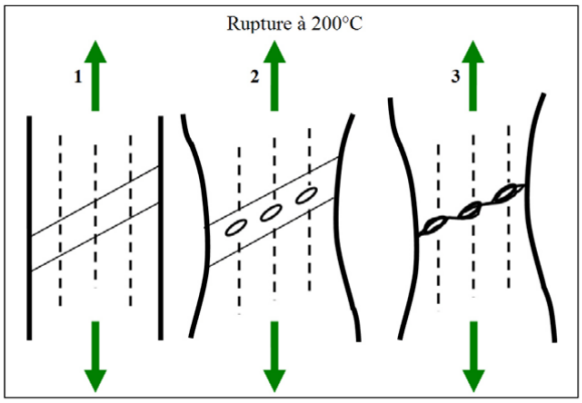

Figure 2.10 – Schematic of the ductile fracture process with the presence of PLC effect [Belotteau, 2009]

vary with temperature thus the early ductile fracture is not affected by DSA. The author suggested that the DSA might act on the final coalescence stage of fracture.

2.1.5 PLC bands, necking and shear bands

Kang et al. [2006] discussed the relation between PLC bands, diffuse necking and shear bands through DIC measurement on AA5754 tensile specimens. The author suggested that PLC bands can provide local plastic deformation which makes the Considère criterion to be reached locally before it is reached globally in the whole area of specimen. This could explain the drop of ductility in the smooth tensile specimens. The interaction of PLC bands and shear bands begins to occur after the onset of diffuse necking (see Fig. 2.11). The PLC bands propagate in the gauge area randomly until one of these superposes the position of a macroscopic shear band. A conjugated set of shear bands were observed at the beginning. However, only one single band results, which is due to the interaction with PLC bands.

Halim et al. [2007] confirmed that PLC effect causes a reduction in ductility by triggering an early onset of necking in uniaxial tension of AA5754 flat tensile specimens. However, the shear band formation is independent of the occurrence of PLC banding. The author concluded that the development of a macroscopic shear band originates from the formation of grain-scale shear bands taking place in an early stage of the deformation

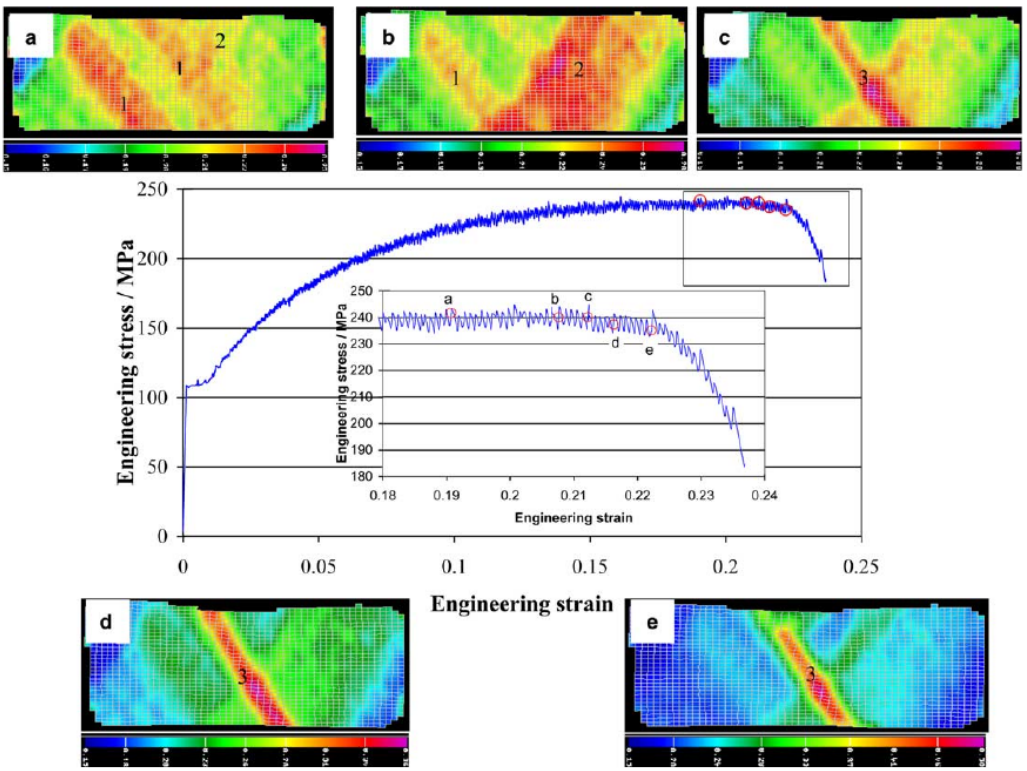

Figure 2.11 – Strain field in a uniaxial tensile specimen (AA5754 alloy) at strain rate $6 \times 10^{-4}\,s^{-1}$ measured by DIC: (a) onset of diffuse necking; (b) final part of diffuse necking; (c) onset of localized necking; (d) and (e) post localized necking. Numbers 1, 2 and 3 represent PLC band, diffuse necking band and localized band, respectively [Kang et al., 2006].

process.

In a recent paper, Yuzbekova et al. [2017] investigated PLC effect in a Al-3%Mg alloy through tensile tests combined with DIC measurement. The authors observed that the onset of necking corresponds to the Considère strain that reflects the condition of the loss of stability of a homogeneous plastic flow. The PLC bands did not produce premature necking. Meantime, the development of the neck is related to the slowing down PLC bands. The PLC bands lose their mobility and considerably slow down close to the Considère strain. A slowing down PLC band eventually serves to form the ultimate localized shear band. The author also noticed the alternating behaviour of localization of plastic deformation within the pair of conjugate deformation bands as demonstrated in Fig. 2.12. The alternating behaviour is associated with serrations appeared on the descending part of stress-strain curve.

From numerical aspects, Hopperstad et al. [2007] studied the influence of PLC effect on necking with a strain ageing model with parameters identified based on AA5083 alloy. Their simulations predicted a significant reduction in the strain to necking with the presence of PLC bands. The authors concluded that the increased surface roughness due to PLC bands may initiate a neck. Wang et al. [2011] simulated the tensile tests of a C-Mn steel with the KEMC model. It has been showed that the necking initiated in a PLC band in round smooth specimens. The onset of necking is accelerated by the strain localization bands associated with PLC effect.

In contrast to the previous works, Zhang et al. [2012] demonstrated that there is no significant relation between serrated flow (or related localization) and strain to necking in a uniaxial tension test by numerical simulations. The authors suggested that the main

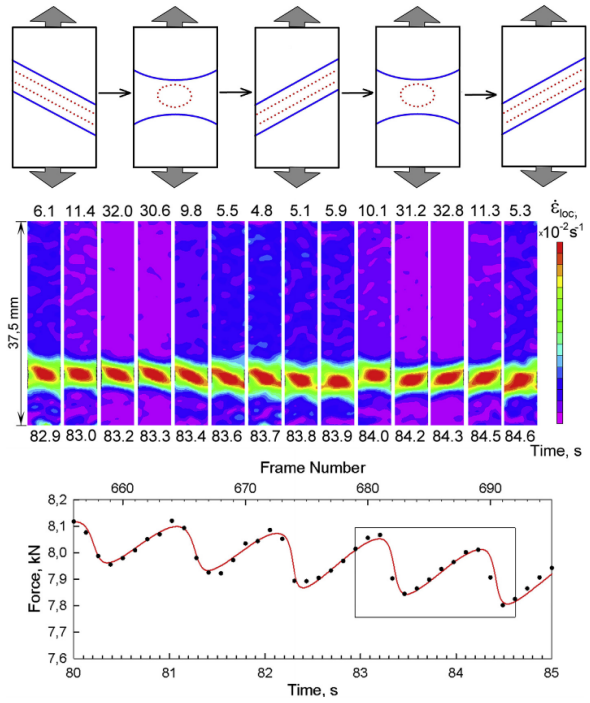

Figure 2.12 – Schematic representation of the alternating behaviour of localization bands in the necking region and the DIC measurement on a Al-3%Mg alloy tensile specimen [Yuzbekova et al., 2017].

parameter controlling the occurrence of necking and the subsequent final failure is the hardening rate (negative strain rate sensitivity).

2.1.6 Loading path dependency

In addition to the characterizations of the PLC effect in terms of the nSRS and serrations, the critical strain for the occurrence of PLC instabilities is another important feature. As diffusion of solutes is involved, there is a limited active zone of PLC effect within a certain range of temperature and strain rate. Many experimental observations about the onset of PLC instability are based on constant strain rate tensile tests. It seems that only a few emphases have been laid on the influence of interruptions on the triggering of PLC effect.

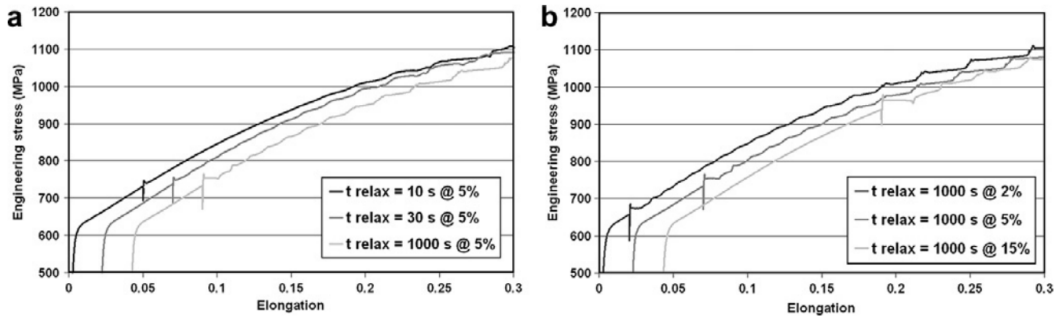

Figure 2.13 – Tensile tests involving relaxations of a FeMnC steel at room temperature: (a) relaxation applied at $\varepsilon = 0.05$ and the influence of different durations (b) relaxation applied at different strain levels. [Allain et al., 2011].

Balík et al. [2000] showed the influence of prestrain on the critical strain for the onset of PLC effect through tensile tests on Al-Mg alloys by involving strain rate change, relaxation and unloading under different temperatures and strain rates. Allain et al. [2011] carried out relaxation tests on a FeMnC alloy. The authors reported the premature triggering of serrations induced by the relaxation. As shown in Fig. 2.13(a), the longer the duration of the relaxation, the more prominent the serrations in this material. Two possible explanations based on the strain ageing mechanism have been mentioned: 1. modification of local carbon distribution by diffusion and ageing during relaxation; 2. First local strain and strain rate heterogeneity due to Lüders effect after reloading trigger serrations. Considering that type A serrations are also observed for very low applied strain rates, the authors attributed the triggering of serrations to the triggering of twinning promoted due to dislocation pinning during relaxation. The triggering effect of the PLC effect by relaxation has also been reported for the AA2024 alloy in [Leacock et al., 2007]. Gupta et al. [2017] recently reported the occurrence of Lüders effect after strain rate change on the 2024 aluminium alloy which does not show highly serrated flow for monotonic tests according to the authors.

It should be pointed out that the materials like Al-3Mg, FeMnC and AA2024 all showed PLC instabilities or serrations (FeMnC may have different mechanism) in monotonic tensile tests.

2.2 Physical mechanisms and modelling

2.2.1 Discussion on the physical mechanisms at microscopic scale

Cottrell and Bilby [1949] set the basis of the strain ageing phenomenon detailing the mechanical interactions between dislocations and solute atoms. The concept of Cottrell atmosphere, which denotes a cloud of foreign atoms gathered around the dislocations, was introduced by Cottrell and Bilby [1949] to explain the role of solute atoms in the plastic deformation of alloys.

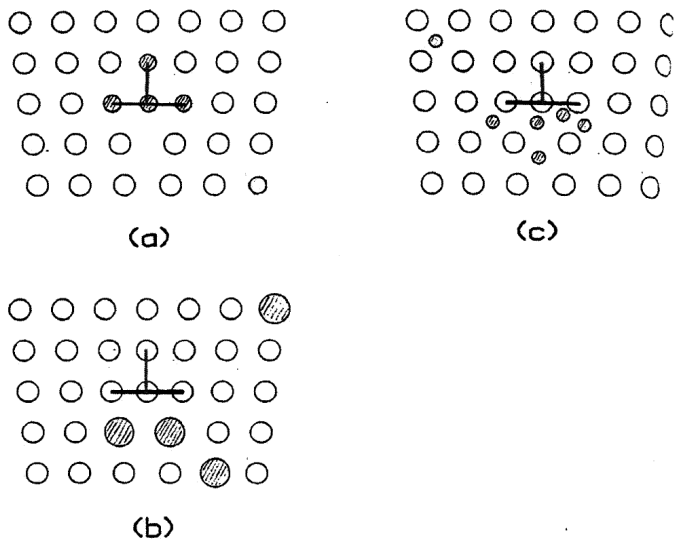

Figure 2.14 – Cottrell atmosphere made of different solute atoms around a dislocation: substitutional atoms having a size inferior (a) and superior (b) to those of the lattice atoms; (c) Interstitial atoms [Graff, 2006].

According to Cottrell and Bilby [1949], interstitial and substitutional atoms can diffuse in volume (bulk diffusion) around the dislocations. The substitutional atoms having a size inferior to those of the lattice atoms can diffuse to the compressive part of the stress field of dislocations (see Fig. 2.14 (a)). The substitutional atoms with larger diameter to the lattice atoms and interstitial atoms can diffuse to the tensile zone of the stress field of dislocations (see Fig. 2.14 (b)(c)). Once the atom has diffused into the dislocation core the atom will stay. According to Cottrell, strain ageing results from the continuous movement

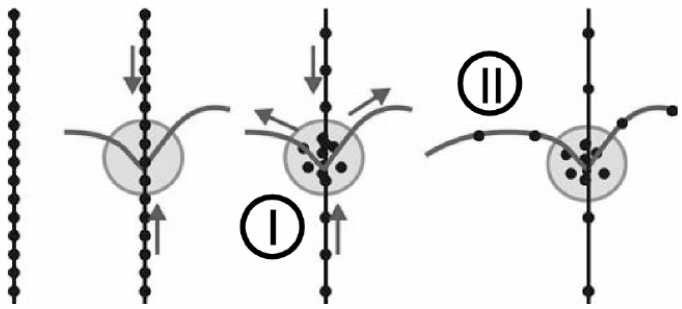

Figure 2.15 – Scheme of the pipe diffusion processes within the scope of strain ageing illustrating the intersection strengthening. The straight lines represent immobile dislocations (for instance forest dislocations) intersected by a bowed mobile dislocation [Graff, 2006].

of dislocations dragging solute atoms with them. If the applied force is small, the dislocations cannot escape from their atmospheres and the solute atoms must migrate with the dislocations. By applying a sufficiently large force, however, the dislocations can be torn from their atmospheres producing an observed upper yield point on a stress–strain curve. After unpinning, dislocations are free to move in the crystal, which results in a subsequent lower yield point. These two modes explain the yield peak that is observed during tensile tests on some mild steel gives rise to the Lüders effect. Similarly, the PLC effect is explained by the recapture of the dislocations by clouds of impurities with a sufficiently high diffusion capacity at proper temperature. This explains the serrations observed on the tensile curve.

Contrary to Cottrell's view, Van den Beukel [1975] later recognised that the motion of mobile dislocations is an intermittent process, and the solute atoms diffuse to mobile dislocations temporarily arrested by obstacles such as by forest dislocations. Tabata et al. [1980] observed this discontinuous motion of dislocations by Transmission Electron Microscopy (TEM) during in-situ deformation of Al-Mg single crystals. Consequently the local solute concentration is controlled by the waiting time of arrest t_w and the solute diffusion coefficient. During the waiting time, with solute atoms diffusing towards arrested dislocations, an over stress is required to continue dislocation motion. Louat [1981] then suggested the solute diffusion towards arrested dislocations should have a saturation value. Otherwise, the ageing rate will be too high at long ageing time.

Following a proposal of Sleeswyk [1958], the model created by Mulford and Kocks [1979] not only postulates the arresting of the stopped dislocation by volume diffusion, but additionally by a simultaneously running pipe diffusion, which denotes the enhanced diffusion of foreign atoms along the distorted lattice around the dislocation lines and cores. This theory suggests that solute atmospheres form on forest dislocations and then drain by pipe diffusion from the forest dislocations to the mobile dislocations during the time spent by the mobile dislocations while they are waiting at the forest dislocations. Fig.2.15 shows the two different diffusion mechanism: (I) an intersection strengthening mechanism proposed by Mulford and Kocks [1979] happens at lower temperatures and higher stresses, (II) a line strengthening mechanism becomes dominant at higher temperatures [Van den Beukel, 1975].

Despite the complicated atom-scale mechanism, the strain ageing effect shows some general characteristics related to strain rate and temperature in the macroscopic scale.

Temperature acts on the diffusion of solute atoms: at low temperature mobile dislocations interact with fixed solute atoms which has been observed through in-situ straining test in a TEM by Caillard [2013]. At intermediate temperatures, solute atoms become sufficiently mobile to move to the nearest dislocations and pin them, the DSA effect occurs. At high temperatures solute atoms are mobile enough to follow gliding dislocations. The yield stress decreases with increasing temperature, the strain hardening decreases and the ductility increases.

Strain rate acts on the dislocation movement: at low strain rate, the dislocation moves together with its Cottrell atmosphere, which is the so called dragging mode. For this circumstance the flow stress maintains on a high level, because of the dislocation movement in a pinning state which corresponds to the saturated state in the KEMC model. At high strain rate, the flow stress is much lower which corresponds to a totally unpinning movement of dislocation. In this case, the motion of dislocations is fast enough to avoid pinning by solute atoms. At intermediate strain rate, the competition between solute diffusion and dislocation movement is maximum. This competition leads to a heterogeneous deformation of the specimen, since in some places of the specimen, according to

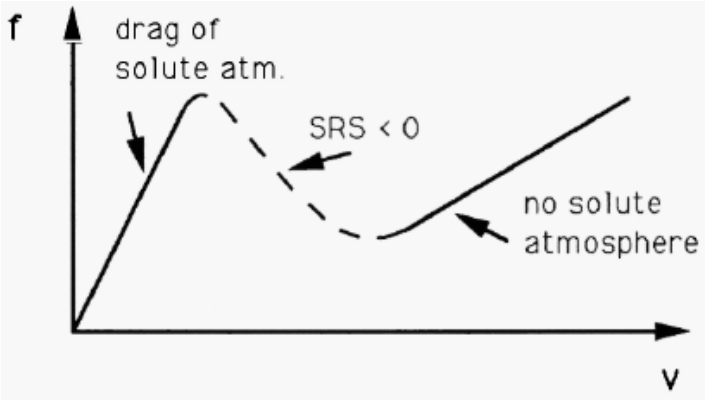

Figure 2.16 – Friction stress f as a function of dislocation velocity v. The dotted portion of the curve gives rise to a negative strain rate sensitivity [Estrin and Kubin, 1989].

the strain rate locally reached, dislocations are arrested, while in other places dislocations escaped from their atmosphere, causing a local softening and strain localization.

2.2.2 Modelling of strain ageing

Models have been proposed to represent the physical mechanisms of strain ageing and are able to capture the anomalies such as serrated yielding and negative strain rate sensitivity. This requires correct description of the interaction between solutes and dislocations. The generally accepted models could be classified into two groups.

One is the phenomenological model based on jump rule. This model is initially proposed by Penning [1972] and improved by Kubin and Estrin [1985]. Finite element simulations were later performed by Benallal et al. [2006]; Kok et al. [2002].

The other one is the phenomenological model based on dislocation-solute interaction by introducing an internal variable t_a called the ageing time controlling the local solute concentration at temporarily arrested dislocations. This model is initially proposed by McCormick [1988] then applied for finite element simulations [Zhang et al., 2001; Graff et al., 2005].

Jump rule based model

Penning [1972] was the first to link the PLC effect with a negative strain rate sensitivity in intermediate range of strain rate and temperature. Later, Kubin and Estrin [1985]; Estrin and Kubin [1989] proposed a constitutive model involving two groups of dislocations namely the mobile and forest dislocations. The authors suggested that the stress σ required to move a dislocation can be decomposed in three main contributions as follow:

$$\sigma = \sigma_d^a + \sigma_d^{th} + F \tag{2.1}$$

where σ_d^a and σ_d^{th} denote the athermal and the thermal contributions for stress originating from interactions of mobile dislocations with forest dislocations in the absence of solute atoms. F is the friction stress due to interactions between mobile dislocations and solute atoms. The evolution of F is not monotonic with respect to dislocation velocity v as shown in Fig. 2.16. At small velocities, solute atoms have enough time to diffuse to temporarily arrested dislocations. At high velocities, such pinning is suppressed as the waiting time is too short for diffusion process to take place. The velocity between these

two states allow the negative dependence of F on v to occur. The Orowan relation between the plastic strain rate and the dislocation velocity is established:

$$\dot{\varepsilon} = \phi \rho_m b v \tag{2.2}$$

where ϕ is a geometric factor, ρ_m is the mobile dislocation density, and b the magnitude of the Burgers vector. The equation of waiting time t_w is introduced by assuming the average spacing between localized obstacles, l, is proportional to the average spacing between forest dislocations, $\rho_f^{-1/2}$, and negligible flying time of unpinned dislocations:

$$v = l / t_w \sim \left(\rho_f^{1/2} t_w\right)^{-1} \tag{2.3}$$

Combining eq. 2.3 and 2.2, one can get

$$t_w = \frac{w}{\dot{\varepsilon}}, \quad w = \phi b \rho_m \rho_f^{1/2} \tag{2.4}$$

where w is defined as the deformation increment when an elementary activation step is accomplished by all mobile dislocations. In many following studies, the parameter w is usually kept constant. The definition of t_w has also been adopted in the McCormick [1988] model.

The serrated flow is explained with the negative strain rate sensitivity by the jump rule. The assumption is that when the plastic strain rate reaches $\dot{\varepsilon}_2$ it must jump to a higher value $\dot{\varepsilon}_H$ as shown in Fig. 2.17. Similarly, there is a jump from to $\dot{\varepsilon}_1$ to a lower value $\dot{\varepsilon}_L$. The region between $\dot{\varepsilon}_2$ and $\dot{\varepsilon}_1$ can never be reached. This concept is the key for explaining the instabilities in this kind of model.

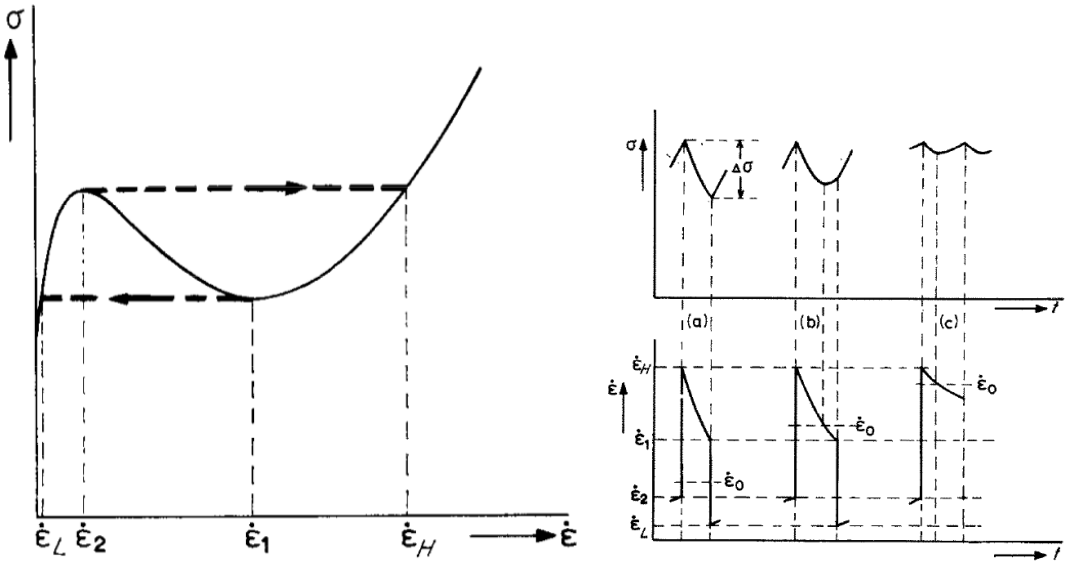

(a) (b)

Figure 2.17 – (a) Strain rate jump from $\dot{\varepsilon}_2$ to $\dot{\varepsilon}_1$ with actual stress-strain evolution; (b) Influence of the loading rate $\dot{\varepsilon}_0$ on the stress evolution [Penning, 1972].

Inspired by Estrin and Kubin [1989], Benallal et al. [2006] proposed the following equations:

$$\sigma = \sigma_y + R(p) + \sigma_v(\dot{p}) \tag{2.5}$$

where σ_y is yield stress, R is strain hardening and σ_v is viscous stress. The viscous stress is assumed to include a bounded region of negative strain rate sensitivity. This model

has been implemented in the finite element code. The author showed that this model is able to describe the serrated stress–strain curves, propagating deformation bands and the overall steady-state behaviour as function of the applied strain rate.

Ageing time based model

The McCormick model includes a time–varying state variable, representing the mean local over concentration of solute atoms at dislocations, C_s, which depends on the internal variable t_a. This idea is based on several previous works like [Van den Beukel, 1975] who introduced the concept of ageing time denoting the effective time that arrested mobile dislocations have spent at obstacles. The corresponding simplified equation of C_s could be written as:

$$C_s(t_a) = C_0(KDt_a)^{2/3} \tag{2.6}$$

where C_0 is the alloy solute composition, D is the solute diffusion coefficient and K is a constant which includes the solute dislocation binding energy [Graff, 2006]. This model predicts negative strain rate sensitivity, however it does not include the saturation of solute atoms at dislocations which results in a large negative strain rate sensitivity at low strain rates inconsistent with experimental observations.

Based on eq. 2.6, Louat [1981] gives the solute concentration equation including saturation at long ageing time:

$$C_s(t_a) = C_m\left[1 - \exp\left(\frac{-C_0(KDt_a)^{2/3}}{C_m}\right)\right] \tag{2.7}$$

where C_m is the saturation value of C_s.

Later, McCormick [1988] introduced another important feature namely the transient response of strain ageing to the model. According to experimental observations, McCormick [1988] proposed that the local composition of solute atoms cannot respond instantaneously to a sudden strain rate change. Two different strain rate sensitivities states are observed: (1) the instantaneous positive strain rate sensitivity which can be observed after the transient moment of strain rate jump ($\Delta\sigma_i$ in Fig.2.18); (2) the steady-state strain rate sensitivity can be positive or negative due to the contribution of strain ageing ($\Delta\sigma_{SS}$ observed after a period in Fig.2.18). The steady state strain rate sensitivity decreases with increasing strain, becoming negative at a strain ε_0. In order to take into account the transient behaviour, McCormick [1988] introduced the "effective time that the arrested mobile dislocation have aged" t_a to be differentiated from the notion of waiting time of dislocations at obstacles t_w. The ageing time obeys a Boltzmann type relaxation equation:

$$\frac{dt_a}{dt} = \frac{t_w - t_a}{\tau} \tag{2.8}$$

where τ is the relaxation time which will be taken equal to t_w in the following studies using this model. Based on this, a concentration equation based on eq. 2.7 could be build using the new t_a.

The total flow stress equation is given as:

$$\sigma = \sigma_f(\varepsilon) + M_i \ln\left(\frac{\dot{\varepsilon}}{\dot{\varepsilon}_0}\right) + M_i H_c C_s(t_a) \tag{2.9}$$

where M_i is the transient strain rate sensitivity, which is always positive. The third term is related to strain ageing. The author also performed stability analysis using the linear

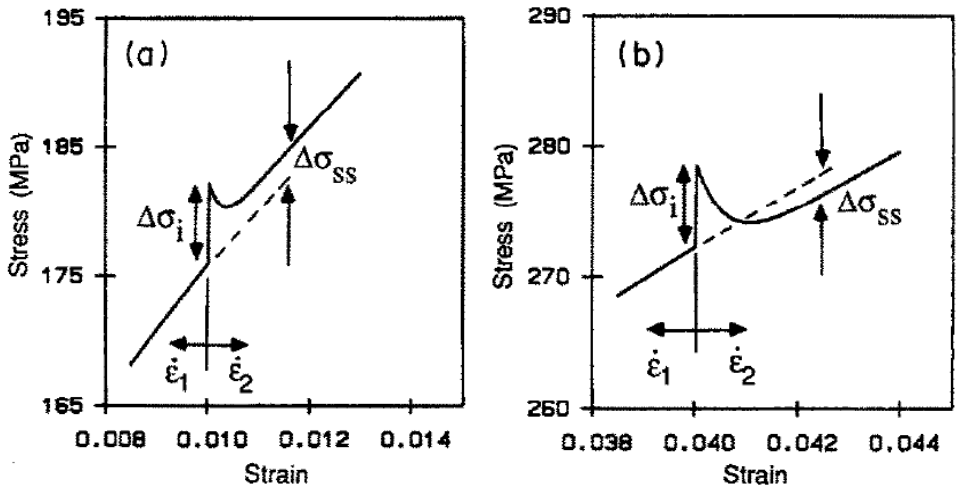

(a) $\dot{\varepsilon}_2/\dot{\varepsilon}_1 = 10; \varepsilon = 0.01$ (b) $\dot{\varepsilon}_2/\dot{\varepsilon}_1 = 10; \varepsilon = 0.04$

Figure 2.18 – Calculated flow stress transient associated with a sudden strain rate increase for two different strain levels [McCormick, 1988].

perturbation method. Three criteria were discussed: (1) the negativeness of steady state strain rate sensitivity; (2) oscillating growth of the perturbation; (3) exponential growth of the perturbation.

The McCormick type model has been reformulated and applied for finite element simulations by many authors [Zhang et al., 2001; Graff, 2006; Mazière et al., 2010; Wang, 2011].

McCormick and Ling [1995] performed simulations with a model combined curtains ingredients developed by Estrin and McCormick [1991] and Kubin and Estrin [1985] together with the DSA model presented in McCormick [1988]. These simulations were performed on a tensile specimen discretized with 250 blocks. The different types of PLC serrations (A and B), critical strain and propagation bands have been reproduced successfully. This kind of model is usually referred to as Kubin-Estrin-McCormick (KEMC) model. Zhang et al. [2001] later implemented the KEMC model into the ABAQUS code. The elasto-visoplastic model successfully simulated the PLC effect on a 3D axisymmetric tensile bar. The conical shape band was reported for the first time.

Based on the formulations in [Zhang et al., 2001], Graff [2006] proposed elasto-viscoplastic constitutive equations including the thermally activated processes. Our development is also based on this model that has been implemented in Z-set software. The constitutive equations are written using general expressions as presented by Graff [2006]

The second and fourth order tensors are defined by a single tilde $\underset{\sim}{\boldsymbol{Z}}$ and a double tilde $\underset{\approx}{\boldsymbol{Z}}$ respectively. The strain rate is decomposed into elastic and plastic parts:

$$\dot{\underset{\sim}{\boldsymbol{\varepsilon}}} = \dot{\underset{\sim}{\boldsymbol{\varepsilon}}}^e + \dot{\underset{\sim}{\boldsymbol{\varepsilon}}}^p, \quad \underset{\sim}{\boldsymbol{\sigma}} = \underset{\approx}{\boldsymbol{C}} : \underset{\sim}{\boldsymbol{\varepsilon}}^e \tag{2.10}$$

where $\underset{\approx}{\boldsymbol{C}}$ is the Hooke tensor of elasticity. The plastic flow is described by the normality rule

$$\dot{\underset{\sim}{\boldsymbol{\varepsilon}}}^p = \dot{p}\,\underset{\sim}{\boldsymbol{n}}, \quad \underset{\sim}{\boldsymbol{n}} = \frac{\partial F}{\partial \underset{\sim}{\boldsymbol{\sigma}}}, \tag{2.11}$$

where $\dot{p}$ is the plastic strain rate which is computed from the flow rule (e.g., viscoplastic

hyperbolic)

$$\dot{p} = \dot{p}_0 \sinh\left(\frac{\langle F\rangle}{K}\right), \quad \langle F\rangle = \max(0, F) \tag{2.12}$$

$$\dot{p}_0 = \dot{\varepsilon}_0 \exp\left(-\frac{E_a}{k_B T}\right), \quad K = \frac{k_B T}{V_a} \tag{2.13}$$

where F is the yield function; $\dot{\varepsilon}_0$ is a constant denoting the strain rate limit for triggering thermal activation; k_B is the Boltzmann constant; V_a is the activation volume; E_a is the activation energy. The yield function F is written in the form

$$F(\underset{\sim}{\sigma}, p, t_a) = \sigma_{eq}(\underset{\sim}{\sigma}) - R(p) - R_a(t_a), \tag{2.14}$$

where R is the conventional hardening function

$$R(p) = R_0 + Q[1 - e^{-bp}] \tag{2.15}$$

where Q and b are parameters describing the non-linear hardening [Lemaitre and Chaboche, 1994]. R_0 is the elastic limit. The strain ageing hardening term takes the following form

$$R_a(t_a) = P_1 C_m \left[1 - \exp\left(-(t_a/t_0)^n\right)\right] \tag{2.16}$$

P_1 translates the influence of strain ageing on the flow stress. The characteristic time t_0 controls the saturation rate. The exponent n= 2/3 was used for many authors as presented in this section, while Springer and Schwink [1991] indicated that 1/3 should be used in the strain ageing models when the pipe diffusion is the main diffusion mechanism of solute atoms towards arrested dislocations.

The ageing time t_a is defined by the following evolution law:

$$\dot{t}_a = 1 - \frac{t_a}{t_w}, \quad t_w = \frac{w}{\dot{p}}, \quad t_a(t=0) = t_{a0}, \tag{2.17}$$

where w is the increment of the plastic strain produced when all arrested dislocations overcome their obstacles. The t_{a0} controls the Lüders effect at yield point. More details can be found in [Marais, 2012].

The influence of the controlling parameters in the steady state ($t_a = t_w$) can be found in Fig. 2.19. The parameter n controls the slope of the transition between the pinned state and the unpinned one. $P_1 C_m$ controls the maximum force in the fully pinned state as well as the transition slope.

2.2.3 Dislocation density based models

According to Bergström [1970]; Kocks [1976], the flow stress could be linked with forest dislocation densities, such as

$$\sigma = \gamma \mu b \sqrt{\rho} \tag{2.18}$$

where γ is a scaling parameter, b is the magnitude of the Burgers vector. Some dislocation dynamics based DSA models have been recently proposed.

Inspired by Estrin and Kubin [1989] model, Fressengeas et al. [2005] proposed a dislocation density based strain ageing model. The evolution of forest and mobile dislocation

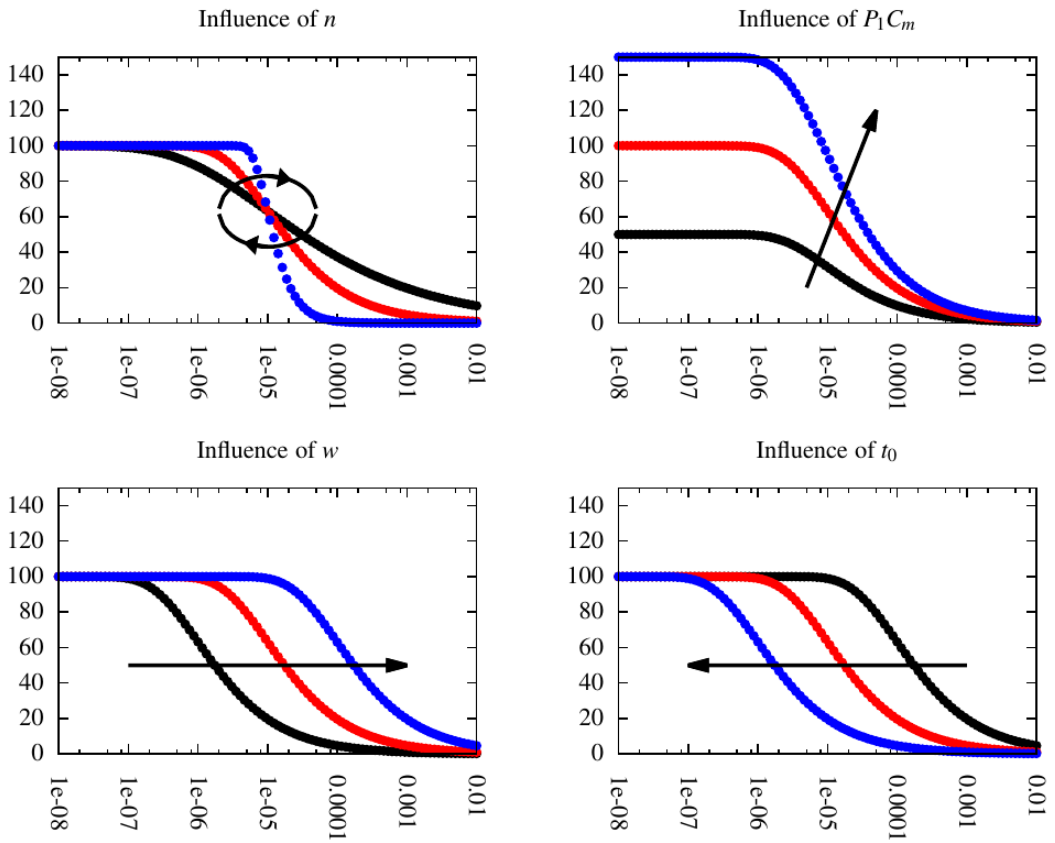

Figure 2.19 – Influence of the ageing parameters on the steady state evolution of the overhardening R_a with respect to the plastic strain rate $\dot{p}$ [Mazière, 2017].

densities are coupled with ageing time t_a which results in a contribution to the ageing hardening. The stress consist of four parts:

$$\sigma = \sigma_a + \sigma_h + \sigma_s + \sigma_v \tag{2.19}$$

$$\sigma_h = \gamma \mu b \sqrt{\rho_f} \tag{2.20}$$

$$\sigma_s = C\left(1 - \exp\left(-\left(\frac{t_a}{\tau}\right)^{2/3}\right)\right), \quad \dot{t}_a = 1 - \frac{\rho_m b v}{\Omega} t_a \tag{2.21}$$

$$\dot{\rho}_m = \left(C_1/b^2 - C_2\rho_m - (C_3/b)\rho_f^{1/2}\right)\rho_m b v - A_1 p(\rho_m b v)\rho_m/t_1 \tag{2.22}$$

$$\dot{\rho}_f = (C_2\rho_m + (C_3/b)\rho_f^{1/2} - C_4\rho_f)\rho_m b v + A_1 p(\rho_m b v)\rho_m/t_1 \tag{2.23}$$

where σ_a is the constant thermal stress, σ_h is the forest hardening stress, σ_s is the solute pinning stress, σ_v is the viscous stress. C_1 stands for the multiplication of mobile dislocations by loop generation, C_2 for their mutual annihilation, C3 for their immobilization through interaction with forest dislocations, and C4 for dynamic recovery. ρ_m and ρ_f are the densities of mobile and forest dislocations respectively. The dislocation velocity v ($\sim \dot{p}$) is thermally activated. This model proposed an indirect coupling between strain ageing and strain hardening based on two different dislocation populations (mobile and forest dislocations). However, it is rather complex to be applied for full field finite element simulations due to a large number of parameters to be identified.

Recently, a modified McCormick type model based on the dislocation density is used in finite element simulations [Colas et al., 2014; Marais et al., 2012; Mazière et al., 2017]. These models account for a single population of dislocations. The conventional harden-

ing term is governed by dislocation density ρ

$$\sigma = R(\rho) + R_v(\dot{p}) + R_a(t_a) \tag{2.24}$$

$$R(\rho) = \sigma_0 + \gamma\mu b\sqrt{\rho} \tag{2.25}$$

where μ is the shear modulus; γ is a material scale parameter; b is the magnitude of the Burgers vector. The evolution of dislocation density is controlled by the plastic strain rate as proposed by Fressengeas et al. [2005].

$$\dot{\rho} = A\left(1 - \frac{\rho}{B}\right)\dot{p} \tag{2.26}$$

In theses models, DSA has almost no influence on the hardening. A modified McCormick type model including the influence of strain ageing on the hardening will be presented in Chapter 3.

2.3 PLC effects in Al-Cu Alloys

Since the 1930s, aluminium alloys have been the primary structural material for aircraft due to their physical and mechanical properties. Although composite materials are increasingly being used in fuselage recently, aluminium alloys remain attractive in the airframe construction (Aluminium alloys >20%, composite >50% in B787 and A350). Comparing with composite materials, aluminium alloys still have some advantages due to their lower certification and production costs, relatively high resistance to impact and stable mechanical behaviour due to change in environmental conditions (moisture/temperature), mature assembly techniques, repair and maintenance procedures and ease of recycling at the end of the aircraft's life [Dursun and Soutis, 2014].

2.3.1 Alloy designations and tempers

According to the Wrought Alloy Designation System, aluminium alloys can be categorized into a number of groups based on a 4 digit designation. The first digit indicates the principal alloying element and is often used to describe the aluminium alloy series. The second single digit indicates a modification of the specific alloy, and the third and fourth digits are arbitrary numbers given to identify a specific alloy in the series. The 1xxx, 3xxx, and 5xxx series wrought aluminum alloys are non-heat treatable and are strain hardenable only. The 2xxx, 6xxx, and 7xxx series wrought aluminum alloys are heat treatable and the 4xxx series consist of both heat treatable and non-heat treatable alloys. The heat treatment conditions can be presented by a series of letters and numbers following the 4 digits. Table 2.1 shows some common treatment conditions according to the International Alloy Designation System [Polmear, 2005].

In the current work, all the studied aluminium alloys are heat treatable. Fig. 2.20 gives a typical manufacturing process for aluminium alloy. The increase of strength and hardness is based on precipitation hardening. The treatments about these alloys are listed in the category "T" in Table. 2.1. A brief introduction about these process are presented below.

Solutionizing (or solution treatment) is made by heating the material above solvus temperature (typically from 450 to 575°C) for a few hours followed by rapid quenching. The purpose of the solutionizing procedure is to take the alloying elements into solution to form a Supersaturated Solid Solution (SSSS) like making a saturated solution of salt and water. During this treatment atoms will diffuse within a solid material, so that the material progresses towards its equilibrium state. The annealing process is similar to solutionizing except for lower cooling rate.

Quenching is to rapidly cool the material to some lower temperature using water, water-polymer (glycol) solution or forced air. A quick quench can preserve as nearly intact as possible the solid solution formed at the solutionizing temperature. A slow quench can make solute to precipitate which can no longer contribute to solid solution strengthening of the material.

In some 2000 series alloys, cold working of freshly quenched materials could significantly increase its response to later precipitation treatment thus an additional step could be added as indicated by T_51, _52, _53 and _54.

After solution treatment and quenching, the SSSS is highly unstable. The extra solute atoms diffuse to numerous nucleation sites. Precipitates grow either at room temperature by natural ageing or at higher temperature by artificial ageing. The fine precipitates in the alloy impede dislocation movement by forcing the dislocations to either cut through the

Table 2.1 – Temper designation systems for wrought aluminium alloys [Benedyk, 2009].

Letter	Condition	Digit	Process
F	As fabricated		
O	Annealed		Lowest strength, highest ductility temper
H	Strain hardened	1	Cold working only
		2	Cold working and partially annealing
		3	Cold working and stabilizing
W	Solution heat treated		
T	Thermally treated	1	Annealing and natural ageing
		2	Annealing, cold working and natural ageing
		3	Solutionizing, cold working and natural ageing
		4	Solutionizing and natural ageing
		5	Annealing and artificial ageing
		6	Solutionizing and artificial ageing
		7	Solutionizing and artificial over-ageing
		8	Solutionizing, cold working and artificial ageing
		9	Solutionizing, artificial ageing and cold working
		10	Annealing, artificial ageing and cold working
	Additional specifications	T_51	Stress relieved by stretching
		T_52	Stress relieved by compression
		T_53	Stress relieved by thermal treatment
		T_54	Stress relieved by combined stretching and compressing (cold forge)

precipitated particles or go around them, thus the alloy is strengthened. The differences of precipitated particles in type, volume fraction, size, and distribution due to the ageing condition govern material properties (see e.g., Chen [2011]).

The naturally aged material presents high fracture toughness and resistance to fatigue. This treatment in 2000 series alloys may take several days until reaching stable state. The mechanical properties of some other material, such as the 6000 and 7000 series alloys can still be unstable after several years ageing at room temperature.

Artificial ageing at higher temperature not only accelerates the precipitation process but also changes the microstructure in fundamental ways different from those occurring at room temperature. This process induce the formation of dispersed precipitate in the alloy. It is usually accompanied by an increase in strength and a decrease in ductility.

2.3.2 Al-Cu alloys

Precipitations in Al-Cu alloys

The 2000 series aluminium alloys involving Cu as principal alloying element are particularly used in airframe structural applications due to their superior damage tolerance. The addition of Cu gives higher strength resulting from the precipitation of Al_2Cu and

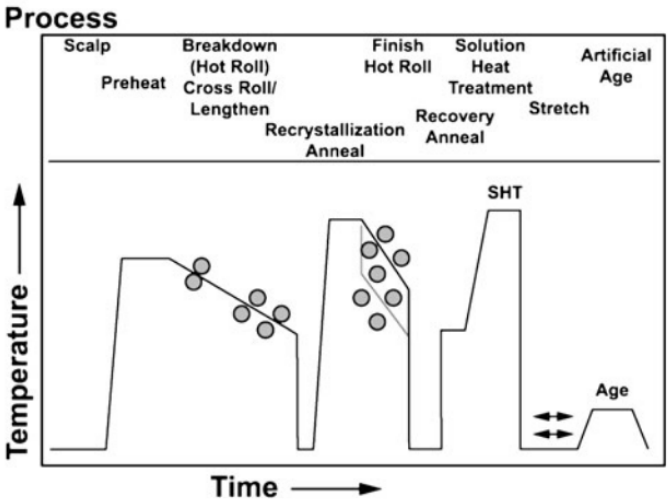

Figure 2.20 – A typical fabrication process for Al plate products [Rioja and Liu, 2012].

Al_2CuMg phases. According to Cu/Mg ratio (wt.%) in the Al-Cu-Mg system, the main precipitation reactions are summarised below [Wang and Starink, 2005]:

- Cu/Mg=4-8, SSSS → GP zones → θ"(Al_3Cu)→ θ'(Al_4Cu) → θ(Al_2Cu)
- Cu/Mg=1.5-4, SSSS → GPB zones → S"→ S' → S(Al_2CuMg)

AA2024 is a well known example of Al-Cu-Mg alloy which has a Cu/Mg ratio around 3.16. S phase is the main precipitation in the AA2024-T3 [Lin et al., 2013] material. The AA2139 alloy has a much higher Cu/Mg ratio ranging from 5.62 to 27. Ω (Al_2Cu), which is also formed by Al and Cu, is the main precipitation due to the addition of some amounts of Mg and Ag [Cho and Bes, 2006].

PLC effect in Al-Cu alloys

The PLC effect has been investigated in the Al-Cu alloys with different tempers including annealing, solution-treatment and ageing.

Rosen and Bodner [1969] reported PLC effects in 2024 alloy in the fully annealed and solution-treated condition except for the over aged condition. The tensile curves of fully aged and fully annealed specimens are shown in Fig. 2.21. The fully aged specimens were subjected to solution-treatment at 490°C for 1 h, quenched in water and naturally aged for three days at room temperature. The fully annealed specimens were heated for 1 h at 490°C and slowly cooled in furnace at a rate of approximately 2°C per minute. Serrated flow is more pronounced in the fully annealed specimens which contain more solute atoms and less precipitates. Jiang et al. [2006] observed that the onset of the PLC effect is earlier in solution-treated 2017 alloy than in annealed temper. In addition, serrations are significantly reduced with increased natural ageing time due to the formation of precipitates as shown in Fig. 2.22. With longer natural ageing time and formation of precipitates, less solute could diffuse in the bulk. Xiong et al. [2009] confirmed that precipitations are not the main reason for serrations by comparing the results at different tempers of a 2024 alloy(one temper with more precipitations than the other). The diffusing solute atoms are necessary for the appearance of PLC effect while the cutting of the precipitate particles alone can not lead to this phenomenon. The shearing of precipitates can influence the amplitude of serrations only at intermediate strain rates.

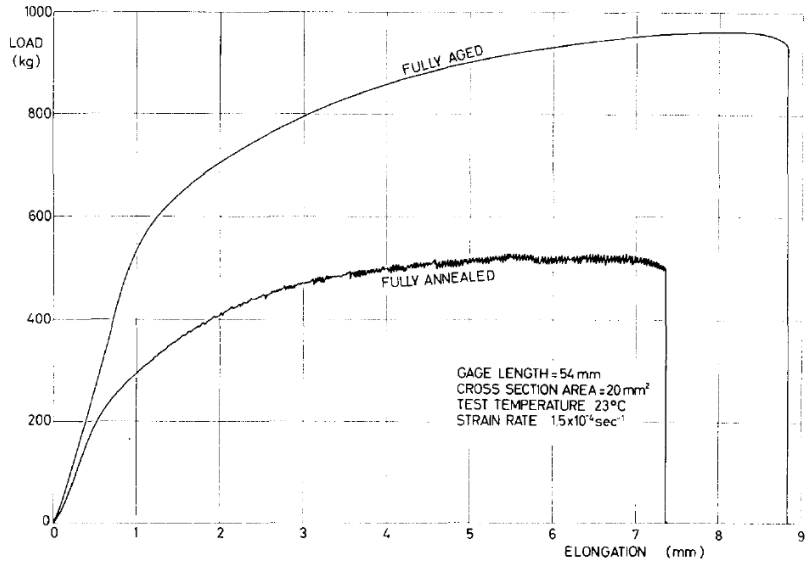

Figure 2.21 – Load-elongation curves for fully aged and fully annealed AA2024-T3 specimens [Rosen and Bodner, 1969].

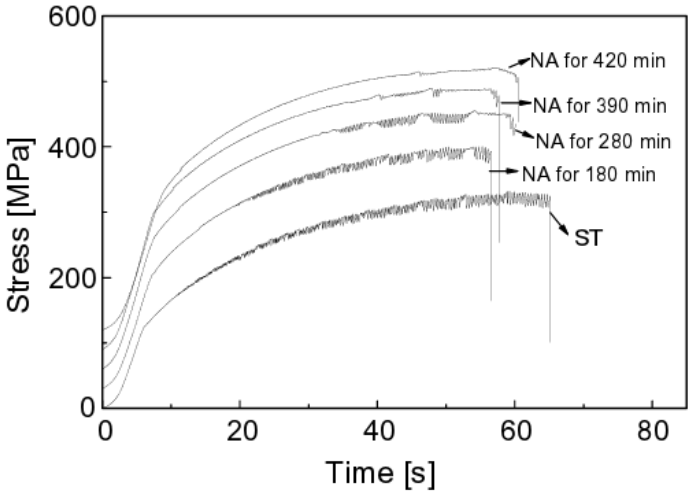

Figure 2.22 – Effect of natural ageing on the serrated yielding in the AA2017 Al-Cu alloy [Jiang et al., 2006].

PLC effect has also been reported by other authors like Böhlke et al. [2009] in 2024 specimens that are annealed at 493 °C for 40 min and quenched or in other unspecified Al-Cu alloys with specific heat treatment favouring higher solute density such as in [Ranc and Wagner, 2005, 2008].

In summary, the precipitates are considered as an influencing (or preventing) rather than initiating factor for serrations in Al-Cu alloys. DSA remains the main mechanism for the onset of PLC effect. This conclusion can be extended to some other alloys as reported by [Pink and Król, 1995; Dablij and Zeghloul, 1997; Thevenet et al., 1999] in other materials.

An additional comment could be made by comparing the PLC effect in 2024 and 2139 alloys. PLC effects have been widely reported in the 2024 alloys for the T3 temper, while the 2139 alloy seems not sensitive to this phenomenon. Combining the fact that the 5000 Al-Mg alloys are very sensitive to the PLC effect, we can suggest that the less pronounced PLC effect in 2139 alloy is due to the smaller amount of Mg which is the main solute atom

initiating PLC effect in these materials.

2.3.3 Al-Cu-Li alloys

Currently, the Al-Cu-Li alloys are considered to replace the role of Al-Cu alloys in aeronautic industry. As the lightest metal, lithium additions result in significant weight reduction (3% for each 1%Li added), which was considered as the most effective way of lowering the structural weight of aircraft in order to increase fuel efficiency.

However, binary Al-Li alloys suffer from low ductility and toughness due to severe strain localization that arises because coherent δ' precipitates are readily sheared by moving dislocations. This can lead to cracking along grain boundaries [Polmear, 2005]. The addition of Copper can reduce the solid solubility of lithium so that precipitation of δ' is enhanced and leads to coprecipitation of phases such as GP zones and θ' that form in binary Al-Cu alloys.

The first generation of Al-Cu-Li alloy was developed in the 1950s with a relatively low Li content (i.e., AA2020 with Li 1.2%wt). However, the production of alloy AA2020 is abandoned due to its low toughness. The second generation Al-Cu-Li alloys (AA2091, AA2090) developed in the 1980s increased the content of Li >2%wt which results in a lower density, higher modulus and fatigue resistance. However, its low toughness and significant anisotropy limited its application in aircraft industry.

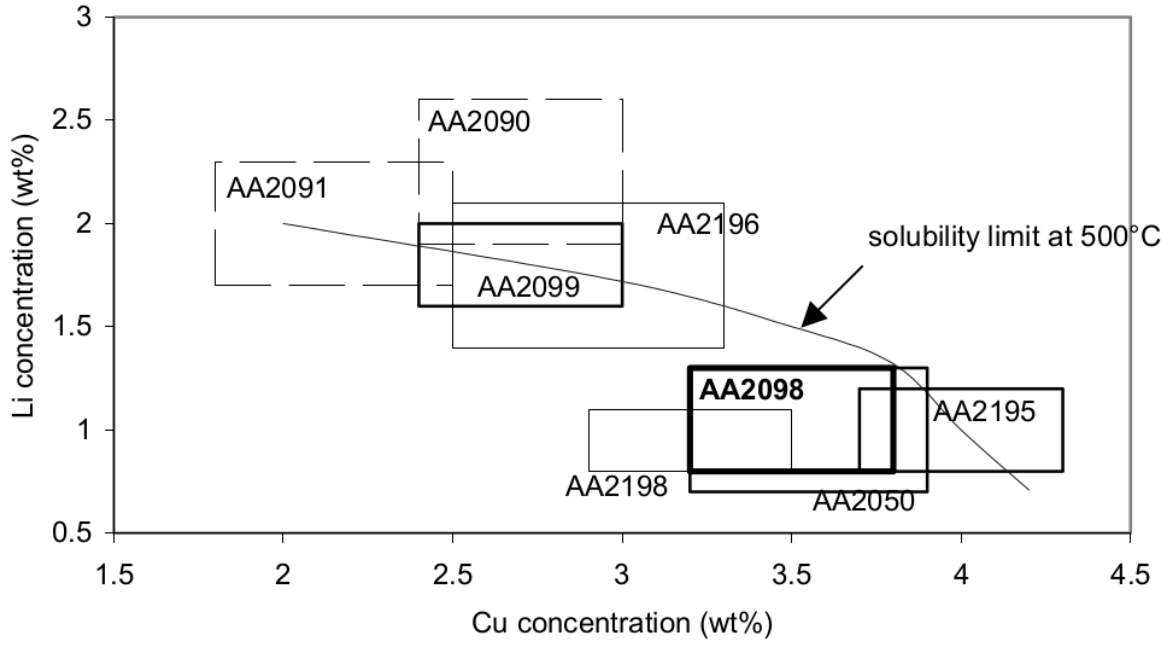

Figure 2.23 – Evolution of Cu and Li content in the Al-Cu-Li alloys from the second generation (2090 and 2091) to the new generation (3rd) (2099, 2196, 2098, 2050, 2195, 2198)[Warner, 2006].

To overcome the disadvantages of the 2nd generation Al-Cu-Li alloys, the new generation of Al-Cu-Li alloy has been optimised through chemical composition, thermal mechanical processing and precipitate microstructure control [Prasad et al., 2013] . As shown in Fig. 2.23, the new generation alloys have higher Cu/Li ratio compared to the previous ones. The new generation Al-Cu-Li alloys achieved a good strength/toughness balance, corrosion resistance and formability.

Precipitations in Al-Cu-Li alloys

It has been shown that for the Al–Cu–Li system a small difference in Li content translates into a very different precipitation sequence [Decreus et al., 2013]. The improvement of these mechanical properties are related to the formation of the strengthening precipitates like T_1 (Al_2CuLi), δ' (Al_3Li), θ (Al_2Cu), δ' (AlLi), T_2 (Al_5CuLi_3) and T_B (Al_7Cu_4Li). The schematic microstructure and corresponding functions of these precipitates are illustrated in Fig. 2.24. Other precipitates like GP zones, Ω (Al_2Cu), S' (Al_2CuMg), and β'(Al_3Zr) can also been found [Rioja and Liu, 2012].

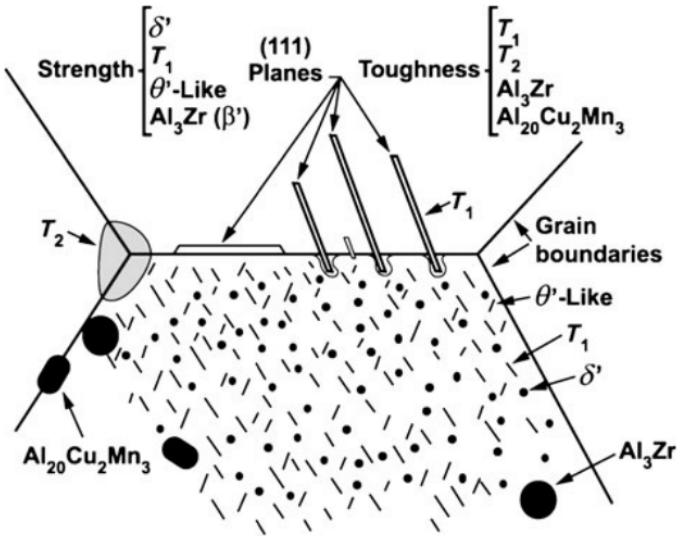

Figure 2.24 – Schematic precipitate microstructure in Al-Li 2099 and 2199 alloys [Rioja and Liu, 2012].

Jo and Hirano [1987]; Prasad et al. [2013] have summarized the precipitation reactions in the Al-Li-Cu ternary system as a function of Cu/Li ratio (wt.%):

- Cu/Li>4, SSSS → GP zones → θ" (Al_3Cu)→ θ'(Al_4Cu)
- Cu/Li=2.5-4, SSSS → GP zones → GP zones+δ'(Al_3Li) → θ"+θ'+δ'→ δ'+T_1→ T_1
- Cu/Li=1-2.5, SSSS → GP zones + δ' → θ'+δ'→ δ'+T_1 → T_1
- Cu/Li<1, SSSS→ δ'+T_1→ T_1 (Al_2CuLi)

The current AA2198 alloys has a Cu/Li ratio ranging from 2.6 to 4.3. Two tempers namely T3 (natural ageing) and T8 (artificial ageing) in the recrystallized state are taken into consideration. A former TEM study by Chen [2011] showed, for T8 state, inter-granular precipitations can be found along almost all grain boundary or subgrain boundary areas. T_1 and θ' can be seen distributed homogeneously. For naturally aged T3 material, precipitates T_1 and θ' are absent. There is no precipitate decoration at grain boundaries or subgrain boundaries. Dispersoids like $Al_{20}Cu_2Mn_3$ or Al_3Zr can be seen (see Fig. 2.25).

PLC effects in Al-Cu-Li alloys (AA2198)

The debate on the PLC effect in Al-Cu-Li alloys is focused on the role of Li atoms and precipitates. Two explanations of serrated flow in Al-Li can be found in the literature. Gregson et al. [1988]; Kubin et al. [1992]; Kumar et al. [1996]; Chmelík et al. [1998] suggested that Li based DSA is responsible for serrated flow. In contrast to the classical DSA theory, the effect is also believed to be caused directly by the shearing of precipitates like δ'

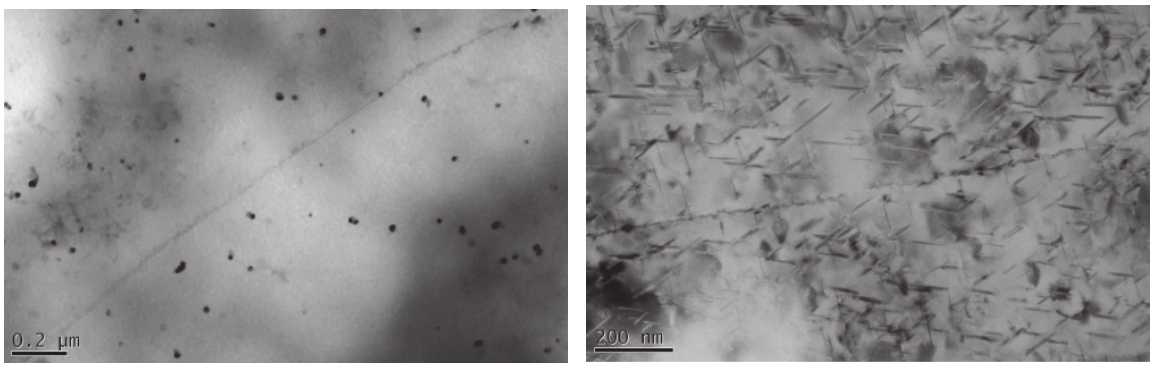

(a) T3 (b) T8

Figure 2.25 – TEM investigation of naturally aged 2198-T3F and artificially aged fibrous material T8F: (a)Precipitates T_1 and θ' are absent in T3 material; (b) Presence of T_1 and θ' in T8 material [Chen, 2011].

[Kumar and Pink, 1995; Brechet and Estrin, 1995; Behnood and Evans, 1989; Zambo and Wert, 1993; Pink et al., 2000].

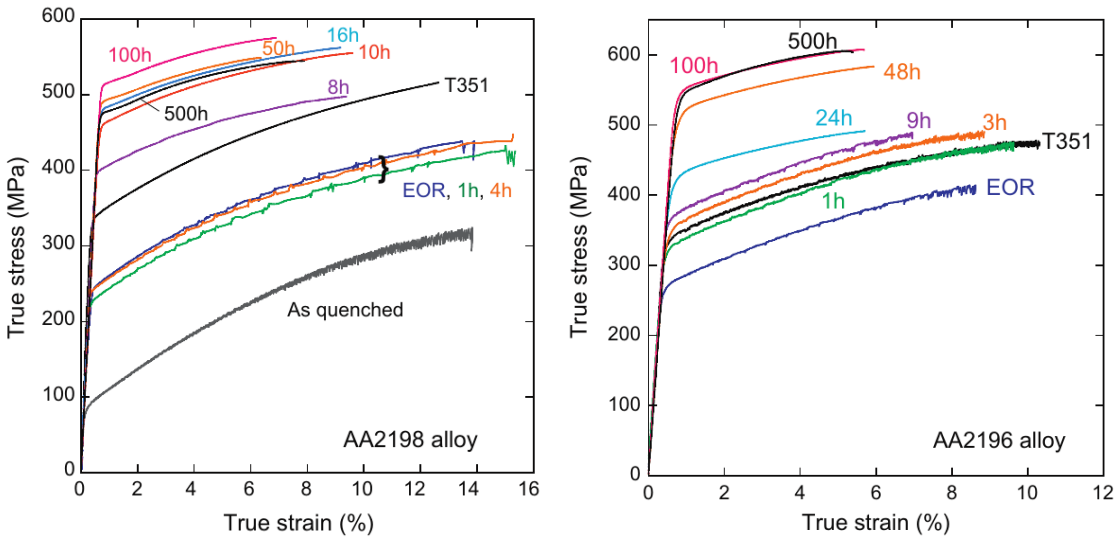

(a) AA2198 (b) AA2196

Figure 2.26 – Tensile curves in different ageing conditions along a heat treatment at 155°C [Deschamps et al., 2013].

Decreus et al. [2013]; Deschamps et al. [2013]; Ovri et al. [2015]; Ovri and Lilleodden [2015] published a series of papers about the influence of precipitates on PLC effects in AA2198 alloy. The concerned temper conditions and associated precipitates are summarised below:

- Natural ageing (NA): stretched to 2% elongation followed by natural ageing (T351).
  - no precipitate except δ' (Al_3Li); solute content much higher than other tempers [Ovri and Lilleodden, 2015; Ovri et al., 2015]
  - Cu-rich clusters; does not present δ' phase at any time [Deschamps et al., 2013]
  - No PLC

- End of heating ramp (EOR) for artificial ageing at 155°C (<2h after heating) based on T351 material.
  - dissolution of the clusters [Deschamps et al., 2013]
  - with PLC
- Peak ageing (PA): artificial ageing at 155°C for 16 h [Deschamps et al., 2013] (14 h in [Ovri et al., 2015]) based on T351 material.
  - high density T_1 (Al_2CuLi) (agree)
  - No PLC
- Over ageing (OA) at 155°C (>16h) based on T351 material [Deschamps et al., 2013]
  - majority of T_1 (Al_2CuLi) and some θ' [Deschamps et al., 2013]
  - No PLC
- Over ageing (OA) at 370°C for 10 h based on T351 material [Ovri and Lilleodden, 2015].
  - more δ' compared with NA + high density T_2 (Al_5CuLi_3) and T_B (Al_7Cu_4Li)
  - with PLC

Although there are some disagreements on the identification of precipitates at each temper, the overall tendency is consistent. In the NA temper, Li solute content is much higher than that in the artificial ageing tempers.

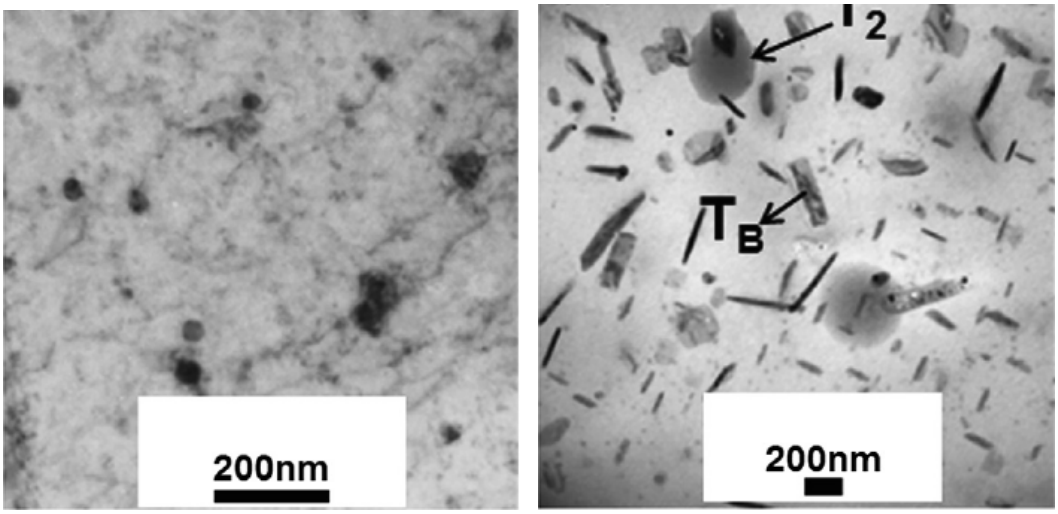

(a) Naturally aged (NA) (b) Over aged (OV)

Figure 2.27 – (a)δ'/β' is the only matrix precipitate present in the NA temper. (b)Several precipitates including T_2, T_B and δ'/β' are present in the matrix of OV temper [Ovri et al., 2015].

Deschamps et al. [2013] did not find PLC effect in AA2198 for T351 temper (see Fig. 2.26(a)). After heating at 155°C for less than 2h, serrations are observed on the tensile curves due to the dissolution of atom clusters. For longer ageing time (>8h), serrations disappear. It is worth noting that serrated flow is observed in another very similar alloy 2196 in T351 temper which contains more δ' phase and higher Li content (1.4-2.1) compared to AA2198 (0.8-1.1) (see Fig. 2.26(b)). In addition, it can be observed that the plastic instabilities are still active until 9h artificial ageing. After 24h onwards, serrations are suppressed with the nucleation of T_1 phase. By comparing these two cases, we can infer that

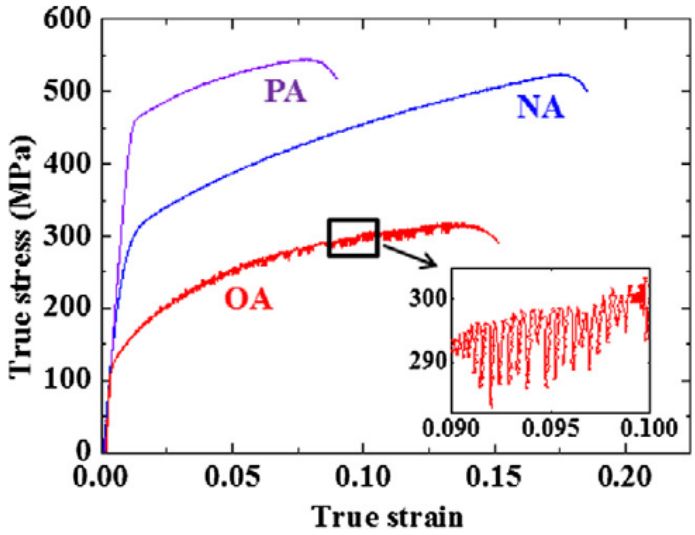

Figure 2.28 – Tensile curves of AA2198 at different tempers. PA: peak aged; NA: naturally aged; OA: over aged [Ovri and Lilleodden, 2015].

the additional Li content in 2196 makes the 2196 alloy still sensitive to PLC effects after 9h heating. The serrations are suppressed earlier in the AA2198 alloy due to lower Li content. The behaviour can still be explained by the DSA theory.

However, Ovri and Lilleodden [2015] later observed PLC phenomenon in AA2198 alloy for an over aged temper at a higher temperature (370°C) different from Deschamps et al. [2013]. Though TEM study showed that the OA AA2198 material contains less Li solute in the matrix due to high density T_2 and T_B precipitates (see Fig. 2.27), it showed serrations. Meanwhile, plastic instability has not been observed in the NA temper in which higher concentration of solute atoms is found. The authors made the conclusion that the DSA cannot sufficiently account for the occurrence of plastic instability in AA2198 alloy. A diffusion-controlled mechanism which involves the operation of a pseudo-locking mechanism that accompanies order hardening is proposed.

The observation of PLC effect in naturally aged AA2198 alloy is still questionable as we can clearly see the serrations on the tensile curves for the naturally aged state as shown in Alexopoulos et al. [2013]. However, the author did not mention it. A detailed investigation combined with DIC measurement is needed.

Table 2.2 gives a list of publications about the PLC effect in 2000 aluminium alloys.

Table 2.2 – 2000 series aluminium alloys showed PLC effect.

Desig.	Type	Temper	References
AA2017	Al-Cu	T1/T4	Jiang et al. [2006]
		T1	Jiang et al. [2007]
		T1	Van Den Brink et al. [1977]
AA2024	Al-Cu	T4	Böhlke et al. [2009]
		T4	Wu et al. [2014]
		T4	Delaunois et al. [2017]
		Anneal (0)/Solutionizing (W)	Rosen and Bodner [1969]
		T3	Lipski and Mroziński [2012]
AA2139	Al-Cu	T8 base material after FSW	Hornbuckle et al. [2017]
other	Al-Cu	Solutionizing (quench)	Ranc and Wagner [2005, 2008]
AA2091	Al-Cu-Li	underaged T351 at 150 °C	Delafosse et al. [1993]
	Al-Cu-Li	underaged T351 at 150 °C	Gomiero et al. [1992]
AA2196	Al-Cu-Li	underaged T351 at 155 °C/T351	Deschamps et al. [2013]
AA2198	Al-Cu-Li	underaged T351 at 155 °C/as quenched	Deschamps et al. [2013]
		overaged T351 at 370 °C	Ovri and Lilleodden [2015]

2.4 Slant fracture in ductile materials

2.4.1 Experimental observations of slant fracture

If the fracture surface is inclined with respect to the loading direction, it is referred to as slant fracture. Slant fracture is widely observed during crack propagation in ductile materials for various types of specimens, such as flat, round tensile specimens, compact tension (CT), Kahn specimen and double-edge notched specimens etc.

As shown in Fig. 2.29(a), slant fracture surfaces are observed in the sheet plane or in the thickness plane of a flat tensile specimen. Experimental observations suggest that, slant fracture occurs in the sheet plane for a high width/thickness ratio specimen. For an intermediate width/thickness ratio specimen, the slant fracture tend to happen in the thickness plane. For a thick specimen (e.g., cubic section), a cup-cone style fracture surface with shear lips can be observed. The angle of fracture surface can vary a lot according to the thickness as shown in Fig. 2.30. The section geometry plays a very important role in determining the fracture mode and fracture plane in flat tensile specimens.

For axisymmetric specimens, the fracture mode is easier to describe compared to flat specimens. The most common fracture mode is cup-cone, which is composed of a central flat area with significant void damage and surrounding shear lips. The slant fracture surface is also observed in certain materials under certain test conditions as shown in Fig. 2.29(b). It is also noted that axisymmetric stress states are more resistant against localization than those under plane strain conditions [Needleman and Rice, 1978].

In a thin sheet tearing tests using CT or Kahn specimens, a flat to slant crack is usually observed as shown in Fig. 2.29(c). In the triangular flat transition zone, coarse surface with dimples could be seen which indicates that void growth is important [Chen, 2011]. In the slant region, the surface is rather smooth. Void growth is very limited. Very small secondary dimples can be observed at higher magnification [Chen, 2011]. This flat to slant crack is not due to out-of-plane displacement since it can be observed in pure Mode

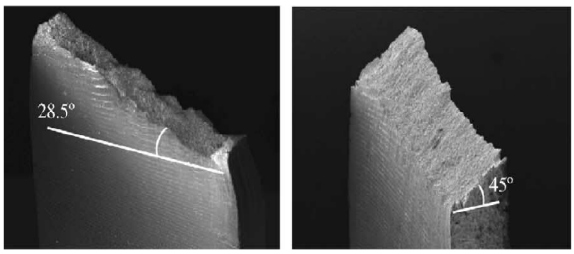

(a) Flat tensile specimen

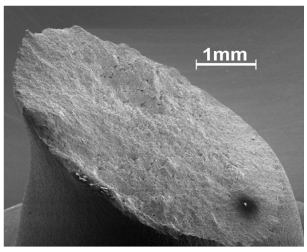

(b) Round tensile specimen

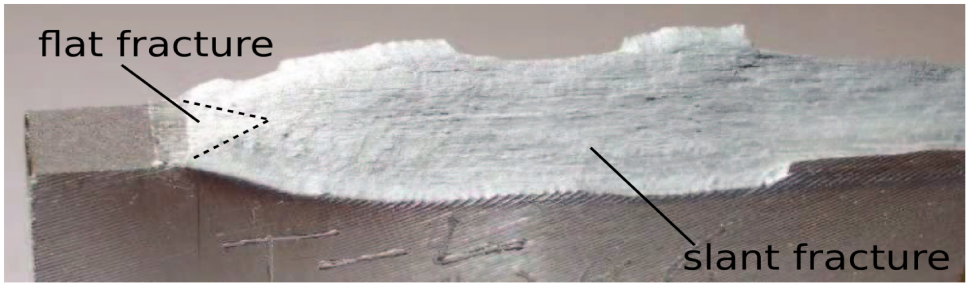

(c) Thin sheet tearing

Figure 2.29 – (a) Slant fracture in the transverse plane and thickness plane of flat tensile specimen [Asserin–Lebert et al., 2005]. (b) Slant fracture surface in a round tensile specimen [Wang et al., 2011]. (c) Flat to slant fracture in thin sheet tearing test [Chen, 2011].

I loading as confirmed by many authors like Mahmoud and Lease [2003]; Chen [2011]; Asserin–Lebert et al. [2005].

2.4.2 Strain localization and damage

The localization of damage in narrow bands has been recognised as the precursor of fracture [Needleman and Tvergaard, 1992; Besson et al., 2003]. Slant fracture, which tends to lower the fracture resistance of material [Lan et al., 2006; Kumar and Hirth, 1991], corresponds to the case where the localization plane is inclined to the main loading direction. The long-standing problem is whether macroscopic localization occurs prior to void damage or whether the two occur simultaneously [Tekoğlu et al., 2015; Morgeneyer et al., 2014].

Tekoğlu et al. [2015] summarised the possible damage mechanisms related to localization and suggested classifying them into two categories including 5 mechanisms as presented in Fig. 2.31:

- Macroscopic localization prior to failure (1, 2, 3 in Fig. 2.31)
- Void coalescence dominated failure (4, 5 in Fig. 2.31): coalescence induced internal necking and plastic localization.

The five mechanisms are (see schematic in Fig. 2.31):

1. Failure without void damage in a diffuse neck or shear band owing to the absence of void nucleation sites. This mechanism only appears for very pure metals.

2. Localization of plasticity into shear bands within a non-porous material owing to various possible softening mechanisms followed by void damage due to the accumulation of large plastic strains inside the band.

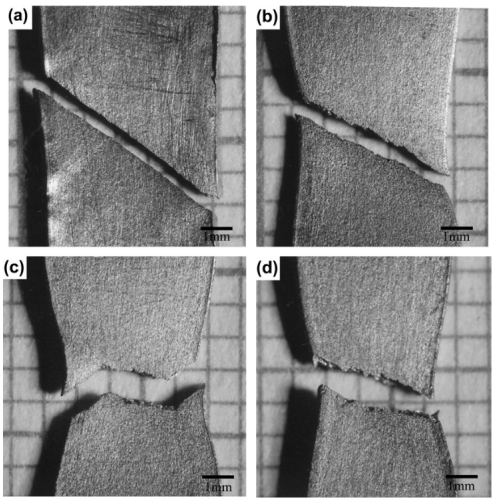

(a) 0.25 (a), 0.5 (b), 0.75 (c) and 1 mm (d)-thick specimen.

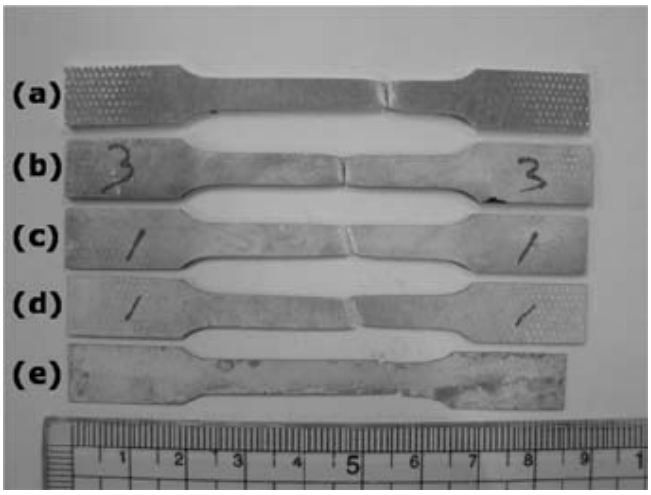

(b) 1.58 (a), 1.40 (b), 1.04 (c), 0.72 (d), and 0.40 (e) mm-thick specimen.

Figure 2.30 – (a)The stereo tensile fracture surfaces of a commercially pure titanium specimens with different thicknesses [Nasiri-Abarbekoh et al., 2013] (b) An aluminum alloy (6K21-T4) [Suh et al., 2010]

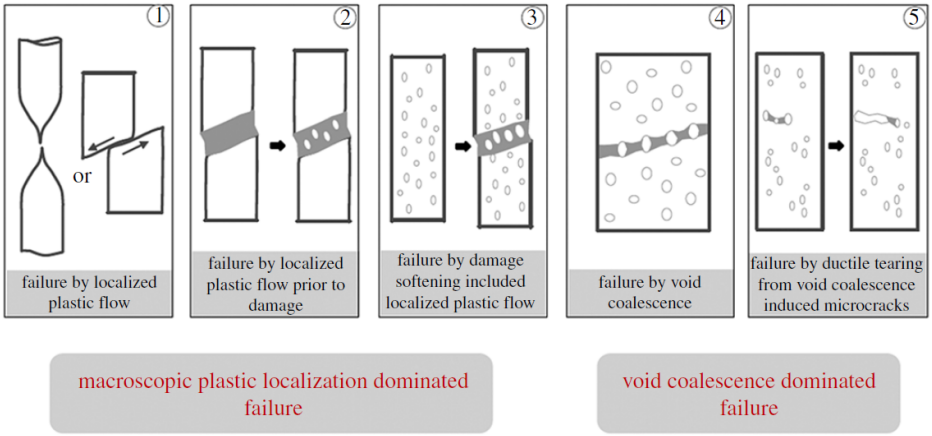

Figure 2.31 – The five scenarios of ductile fracture. Figure reproduced from [Tekoğlu et al., 2015].

3. Damage nucleation in the material prior to macroscopic localization. The cumulated porosity will induce localization.

4. Macroscopic localization and coalescence occurring simultaneously without requiring prior localization owing to the growth mechanism.

5. Different from mechanism 4, this mechanism only involves few voids. The crack growth occurs by the void-by-void mechanism.

As reported by Morgeneyer et al. [2014]; Hickey and Ravi-Chandar [2016], the localization bands set prior to damage softening (mechanism 2 in Fig. 2.31) is the dominant failure mechanism in certain newly developed aluminium alloys. A better understanding of the origin of these localization bands is important for the prediction of failure event. In the following section, a literature review about the slant fracture in different specimens and the possible presence of PLC effect will be given.

2.4.3 Slant fracture in ductile materials and the link with DSA

Axisymmetric specimens

In axisymmetric tensile bar, the fracture path is usually a mix of flat and slant fracture leading to the cup-cone surface. Void damage is formed first at the center of the necking zone where the highest triaxiality is located. As the the crack approaches the lateral surface, the crack turned into a slanted plane. The specimen is finally sheared to form the cone part. However, pure slant fracture of round tensile specimen in the PLC active domain has also been reported in several works.

Belotteau [2009] compared the fracture surfaces of a C-Mn steel (TU48C) axisymmetric tensile specimens tested at 200 °C (with PLC) with those tested at 20 °C in the absence of PLC effect ($\dot{\varepsilon}$ =10^{-4} s^{-1}). There was usual cup-cone fracture in the specimens tested at 20 °C in contrast to slantwise fracture observed in those tested at 200 °C (see Fig. 2.32). In addition, the microscopic observation showed that there were more cavities distributed far away from the fracture surface at 20 °C. At 200 °C, the cavities are more localized and smaller than that at 20 °C. To some extent, these observations confirmed the results of CF8M steel presented by Calonne et al. [2004]. As mentioned in section 2.1.4, the author suggested that with the presence of dynamic strain ageing at 200 °C, necking is oriented by a PLC band in which the deformation is larger and localized. As a consequence, the damage was localized within this area which explained why there were less cavities been observed at 200 °C.

Following the work of Belotteau [2009], Wang et al. [2011] studied the behaviour of the same C-Mn steel (TU48C) at various strain rates (10^{-2} s^{-1} and 10^{-4} s^{-1}) and temperatures (from 20 °C to 350 °C). The fracture mode of all the tested round bar specimens are summarized in Fig. 1.1 in terms of temperatures and strain rates. Some of the smooth round bars tested in the PLC domain exhibit typical cup-cone fracture surfaces (Fig. 2.32 (a)), whereas others showed slant fracture surfaces as shown in Fig. 2.32(b). From Fig. 1.1, they suggested that the topology of fracture surface could be related to PLC band types. Their FEM simulations also showed two kinds of localization bands: inclined bands and conical bands, that might finally lead to slantwise and cup-cone fracture surfaces respectively. According to SEM observation, the dimples on the slant fracture surface are rather spherical (but the dimple is more flat compared to that at 20 °C). Simulations with PLC model showed that the stress triaxiality ratio reaches its maximal value right after the PLC localization band. They confirmed the idea of Belotteau [2009] and concluded that a slant fracture surface is caused by the growth and coalescence of voids within an inclined PLC band.

Slant fracture has also been observed in aluminium round tensile specimens at room temperature. Sometimes authors ignored the PLC effect in their material. Xue [2007] performed tensile tests on round bar specimens of AA2024-T351 Al-Cu alloy with different diameters. The heat treatment of this material consists of solution heat treatment, stress-relieved stretch and then cold working. According to Fig. 2.33, slant fracture appears to be the dominant type of crack in 9 mm diameter tensile specimens. For the 6 mm diameter specimen, there is a flat area in the centre of the crack and the shear lips are found on the two separated sides. The author stated that the fracture in 15 mm diameter specimens is a mixed slant and cup-cone mode. However, the author did not specify their testing conditions such as strain rates and temperatures. In fact, the PLC effect has been found in this material at room temperature as shown in Table 2.2.

Clausen et al. [2004] performed series tensile tests on the AA5083-H116 alloy. From Fig. 2.34, we can notice that slant fracture only occurred at 20 °C and 100 °C where PLC

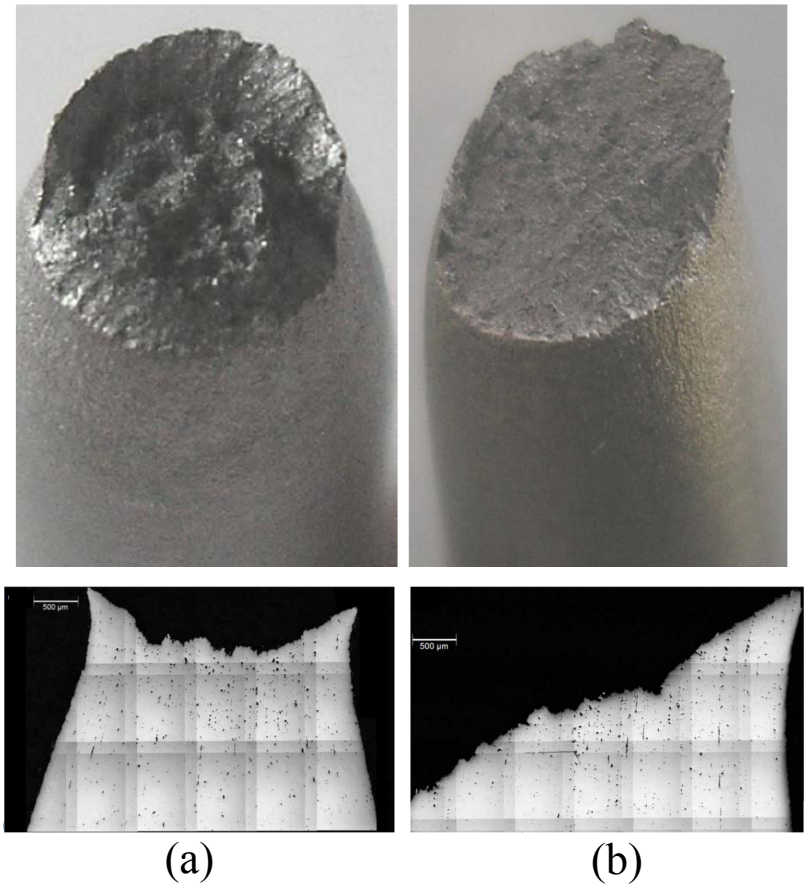

Figure 2.32 – Fracture surfaces of TU48C steel axisymmetric tensile specimens tested at (a) 20 °C and (b) 200 °C [Belotteau, 2009].

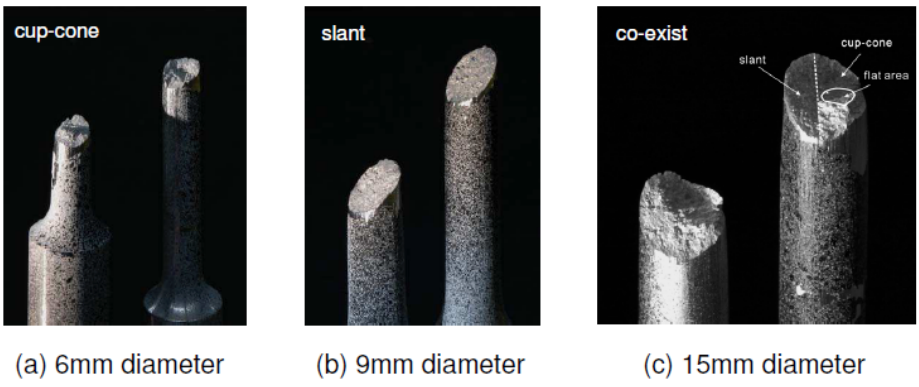

Figure 2.33 – Different fracture modes were observed for round tensile bars of 2024-T351 with different geometries [Xue, 2007]

serrations are shown on the tensile curves. At other temperatures without PLC effect, the fracture mode is typical cup-cone one.

Sometimes the fracture remains cup-cone in the DSA domain, but shows special features. Verma et al. [2015] performed tensile tests on a modified 9Cr-1Mo steel at three strain rates $10^{-5}\,s^{-1}$, $10^{-4}\,s^{-1}$ and $10^{-3}\,s^{-1}$ over a large range of temperatures. DSA phenomenon is observed at strain rate $10^{-4}\,s^{-1}$ between 250 °C and 400 °C. As shown in Fig.

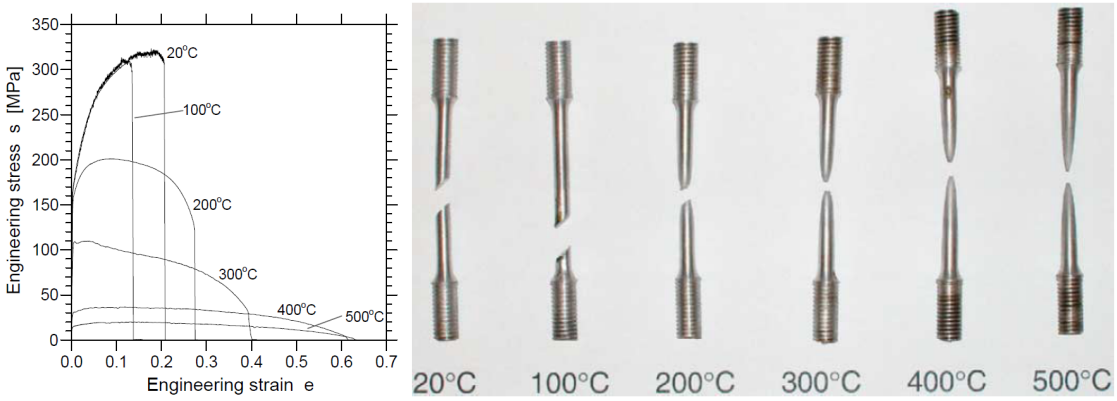

Figure 2.34 – Stress-strain curves and corresponding photos of specimens of AA5083H116 at different temperatures and strain rate 1.7×10^{-3} s^{-1} [Clausen et al., 2004].

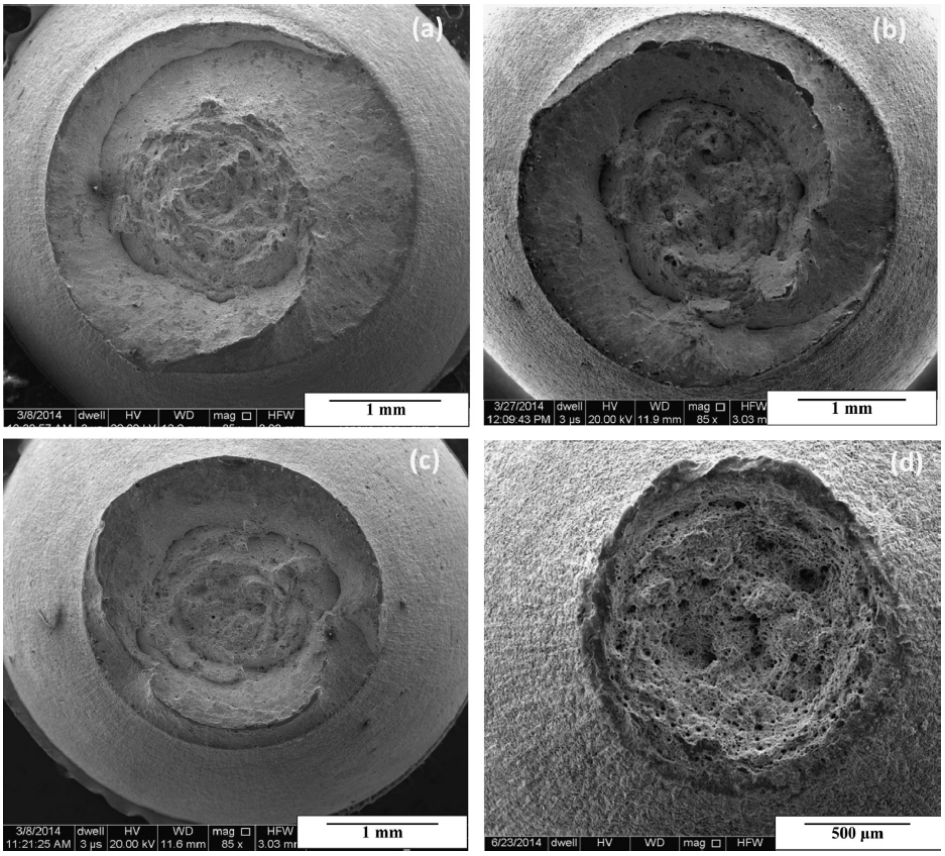

Figure 2.35 – Fracture surfaces of the samples tested: (a) 200 °C, (b) 350 °C, (c) 450 °C, (d) 600 °C at strain rate 10^{-4} s^{-1} [Verma et al., 2015].

2.35, spiral (double) shear lip zones were observed around the central dimple zone in the DSA active temperature range. At the temperatures outside DSA domain (600 °C), the spiral shear lip zone vanished and was replaced by the usual cup and cone fracture surface.

Similarly, Brindley [1970] showed that a loss of ductility is strongly associated with dynamic strain ageing. However, the fracture mode remains unchanged under DSA conditions, although ductile crack propagation occurs more easily. It seems that PLC effect (or DSA) is not a sufficient condition for slant fracture in round bar, while it might be a necessary condition.

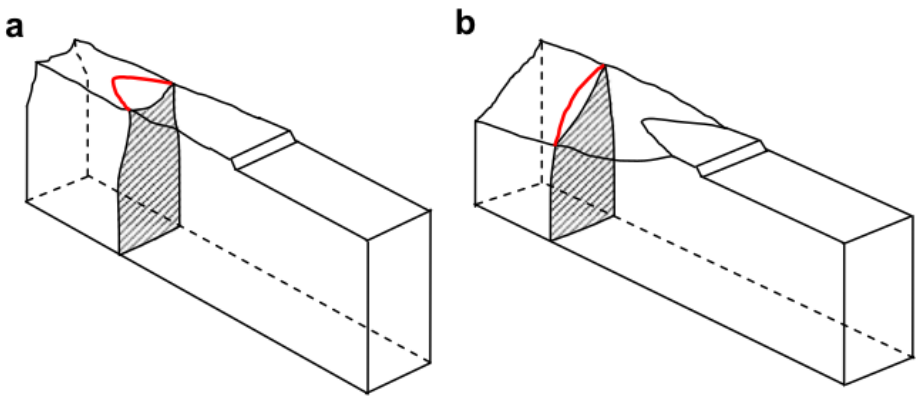

Figure 2.36 – Schematics of flat and slant fracture in tearing specimen. Red line indicates the crack front [Xue and Wierzbicki, 2009].

Tearing test

Notched or pre-cracked specimens like CT, SENT, Kahn and Arcan are usually used in experimental fracture mechanics to evaluate fracture toughness. The flat and the flat to slant fracture modes are usually observed. Significant necking through thickness direction often precedes the appearance of a ductile flat crack. Only very little necking can be observed ahead of a slant crack tip. A flat crack front also shows significant tunnelling in the mid plane. A flat crack propagates much faster in the centre, while a slant crack propagates nearly with the same speed through the thickness (see schematic in Fig. 2.36). The crack mode in those specimens depends on sheet thickness, material strain hardening capacity, anisotropy and strain rate [Pineau et al., 2016]. There is a competition between flat and slant fracture during crack propagation. The underlying physical mechanism for triggering slant fracture is still unclear. As the role of DSA in those notched specimens have not been discussed before, a review about the slant fracture in notched specimen is given here.

Generally, a flat to slant fracture is more common in thin sheet tearing test [Pardoen et al., 2004]. Within notched thin sheet specimen under load, different stress states could be found in different areas. Stress triaxiality η is usually used to quantify the stress state, which is defined as

$$\eta = \frac{\sigma_h}{\sigma_{eq}} \tag{2.27}$$

where σ_h is the hydrostatic stress and σ_{eq} is the equivalent stress. Mahgoub et al. [2003] investigated the crack propagation of a meshed flat and a slant crack. The stress fields ahead of the cracks under mode I loading have been compared. For a slant crack, the triaxiality ahead of the crack is reduced, whereas the equivalent stress is augmented compared to flat crack. Slant fracture has been found to promote shearing type. The evolution of stress triaxiality in Kahn tear test specimen during crack initiation and crack propagation has been investigated via a FE analysis in Bron and Besson [2006]. The stress triaxiality is higher at crack initiation (0mm) than at slant crack propagation area (10mm from the notch) for this 1.6 mm thick material (see 2.37(a)). Fig. 2.37(b) shows the logarithmic deformation in 3 directions as a function of the COD. It can be seen that in the slant region (10 mm) the deformation in crack growth direction E_{prop} is close to 0. In other words a situation very close to a plane strain state can be found in a plane that is perpendicular to the propagation direction [Morgeneyer, 2008]. This situation promotes easy strain lo-

calization as mentioned by Needleman and Rice [1978] and justifies the observed slant fracture mode and the limited void growth. The observed localization angle (45°) is that corresponding to plane strain conditions. At notch root, E_S (deformation along thickness direction) and E_{prop} are close which delays band localization.

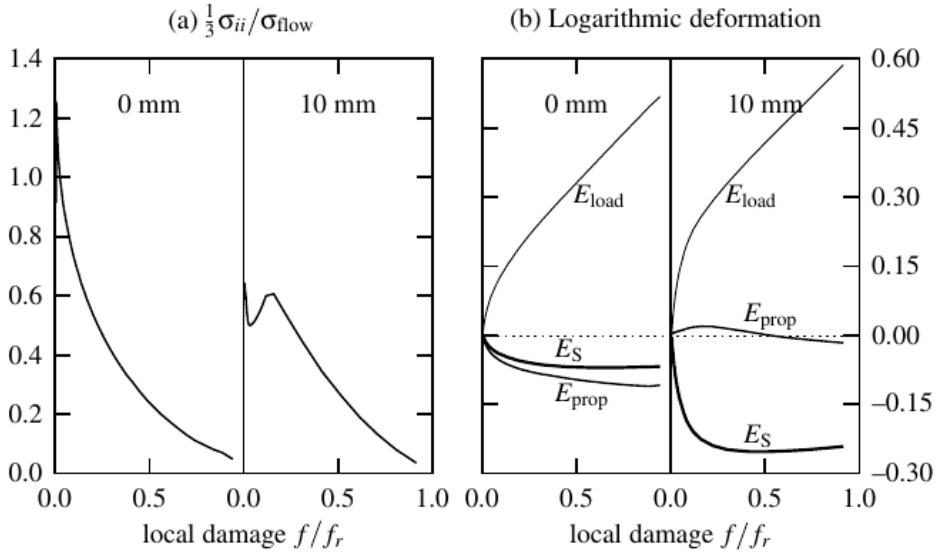

Figure 2.37 – Evolution of local variables in the flat zone (0 mm) and the slant zone (10 mm) in 3D Kahn simulation: (a) stress ratio controlling damage growth in constitutive model and (b) strain rate. E_{load}, E_{prop} and E_S stand for the logarithmic deformations in the loading direction, in the propagation direction and in the thickness direction [Bron and Besson, 2006].

An increase of the thickness changes the stress state at the crack tip by increasing the stress triaxiality, leading to a decrease of the preference for slant fracture [Asserin–Lebert et al., 2005; Mahmoud and Lease, 2003; Pineau et al., 2016].

The influence of strain hardening has been found by Asserin–Lebert et al. [2005]. The author reported slant fracture in the age hardened heat treated condition and a flat fracture in the annealed state of AA6056 aluminium alloy. The author concluded a slant crack is easier to happen for low strain hardenable materials. This result has also been kept by Hickey and Ravi-Chandar [2016] who tested AA6061-T6 and AA6061-O SENT specimens with DIC measurement. The T6 alloy has higher yield strength and lower strain hardening. Slant fracture was observed for T6 state while flat fracture for O state (see Fig. 2.38). DIC measurement showed significant differences in the development of plastic strain fields. The deformation in AA6061-T6 localizes along planes that are oriented at 45° to the crack front. The authors attributed this localization phenomenon to the low strain hardening of T6 alloy which inhibits development of an extensive plastic zone.

The influence of plasticity anisotropy has also been reported. Sutton et al. [1995] found that the fracture of AA2024-T3 middle crack tension specimen was slant when loaded in the L-T configuration but flat when loaded in the T-L configuration.

Recently, new insight has been provided. Morgeneyer et al. [2014] investigated an area in front of the notch tip (~ 970 µm) of a CT specimen (Al-Cu-Li AA2198 alloy) by 3D in-situ laminography-DVC measurement. Multiple strain localization bands were observed at very early stage of loading steps. However, almost no void growth could be observed until very late stages as shown in Fig. 1.2 from loading step 2 to 4 (steps are characterised by notch opening displacement). The equivalent strain magnitude within the area of the final single localization band increased continuously. The final fracture occurred instanta-

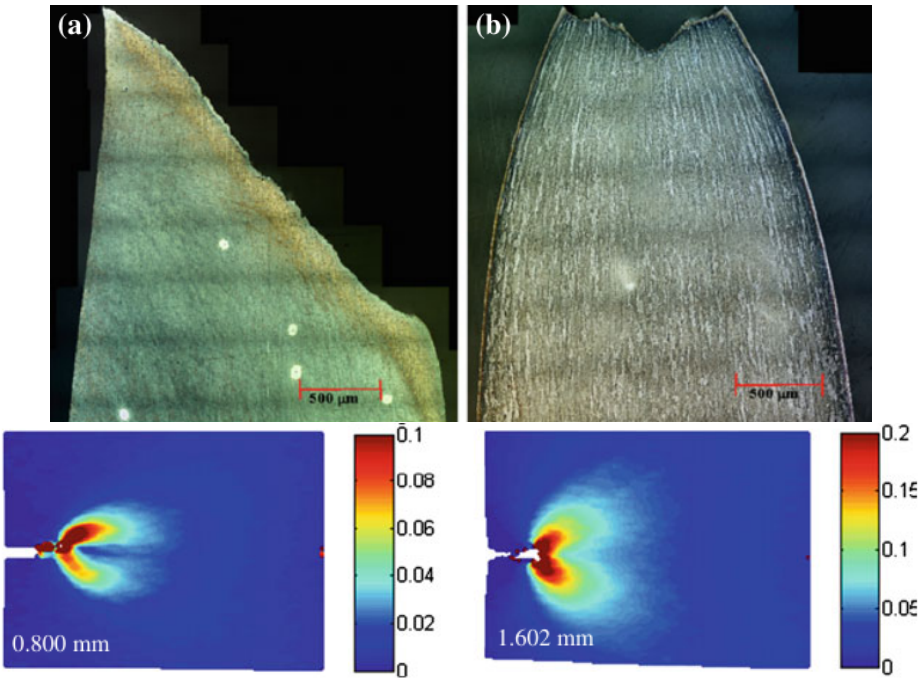

Figure 2.38 – Thickness section of the fractured SENT specimens with slant fracture surface in AA6061-T6 (a) and flat fracture surface in 6061-O. Strain field around notch of 6061-T6 (left) and 6061-O (right) at different CMOD levels by DIC [Hickey and Ravi-Chandar, 2016].

neously within the inclined localization band. Numerical studies using von Mises, Tresca plasticity model or GTN damage model can not reproduce these localization bands. Similar multiple bands have also been reported in the T3R state of AA2198 alloy as shown in Fig. 2.39, in the AA2139-T8 (Fig. 2.40) and the AA2139-T3 (Fig. 2.41) CT specimens through 3D in-situ laminography-DVC measurement. The origin of these localization bands is still a subject to be discussed. The PLC effect or texture, as presented by Kuroda and Tvergaard [2007], seem to be candidates to reproduce the observations.

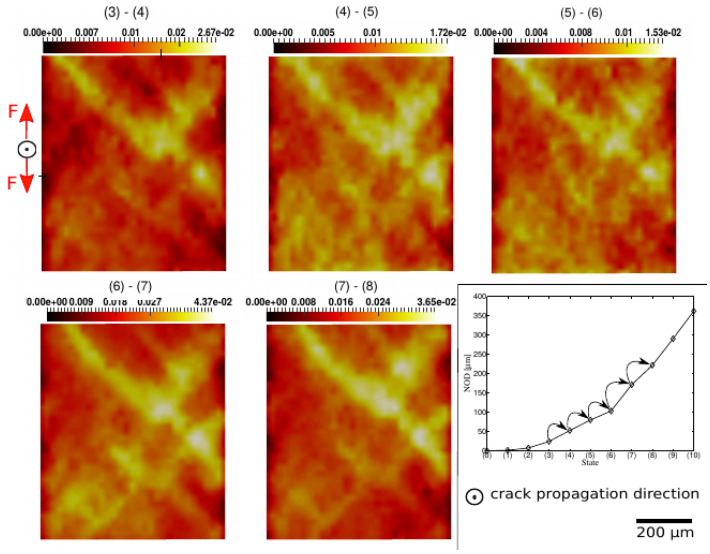

Figure 2.39 – Laminography-DVC results: incremental equivalent strain fields ahead of the notch of a AA2198-T3R CT specimen [Buljac, 2017].

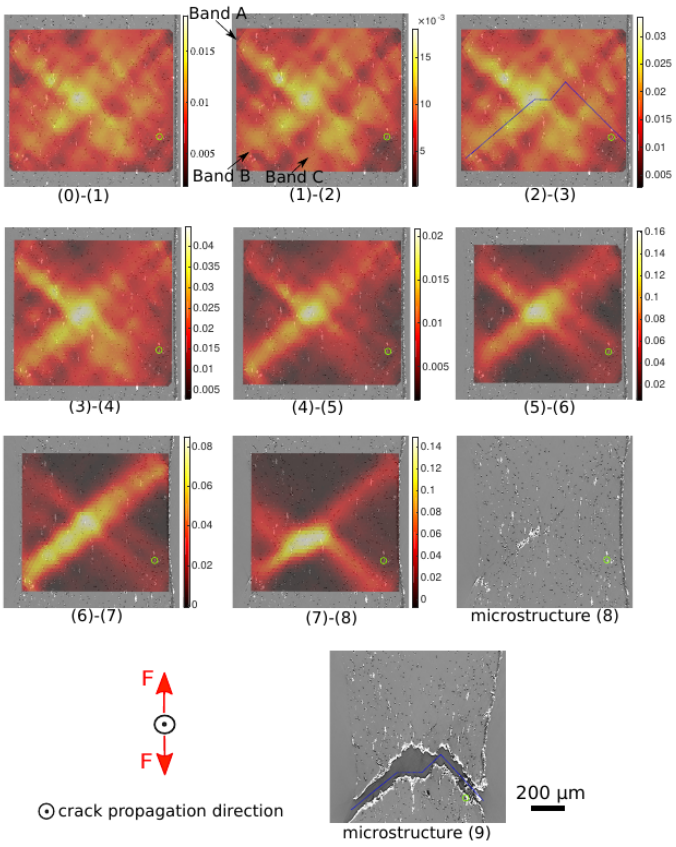

Figure 2.40 – Laminography-DVC results: incremental equivalent strain fields ahead of the notch of a AA2139-T8 CT specimen [Buljac, 2017].

Some other fracture modes similar to slant fracture, such as “flip-flop" in tearing test, have been discussed in the literature. Gruben et al. [2013] observed an occasional shear lip switch under Mode I tearing of a dual-phase steel. Rivalin et al. [2001] observed cup-cone crack during quasi-static tearing and flipping slant crack during dynamic tearing in a X70 ferritic-pearlitic steel. Simonsen and Törnqvist [2004] reported slanted crack which systematically “flips” back and forth in a roughly 45 ° orientation in rolled normal strength steel as well as in high tensile strength aluminium alloy AA5083-H116 by mode I tearing tests. Fig.2.43 left shows the “flip-flop”fracture mode observed in the 10 mm AA5083-H116 aluminium alloy edge crack specimen. In the appendix of their paper, tensile stress-strain curves are given (see Fig. 2.43). It’s worth noting that the repeated serrations on the stress-strain curves showed an evidence of PLC effect in this material. It’s naturally to think about the relation between the PLC instability and the flip-flop cracking behaviour. In fact, the PLC effect in AA5083-H116 has been reported in many works [Benallal et al., 2006]. El-Naaman and Nielsen [2013a] performed SEM analysis of the fracture surface of such kind of flipping crack. They suggest that the “flipping” action is strongly related to the slanting shear bands form in front of the leading crack tip. The driving force for “flipping” action was not fully understood. Recently, Felter and Nielsen [2017]; Nielsen and Hutchinson [2017] attributed the flipping behaviour to a slight out-of-plane deflection that develops due to loss of symmetry when slanting of the crack occurs.

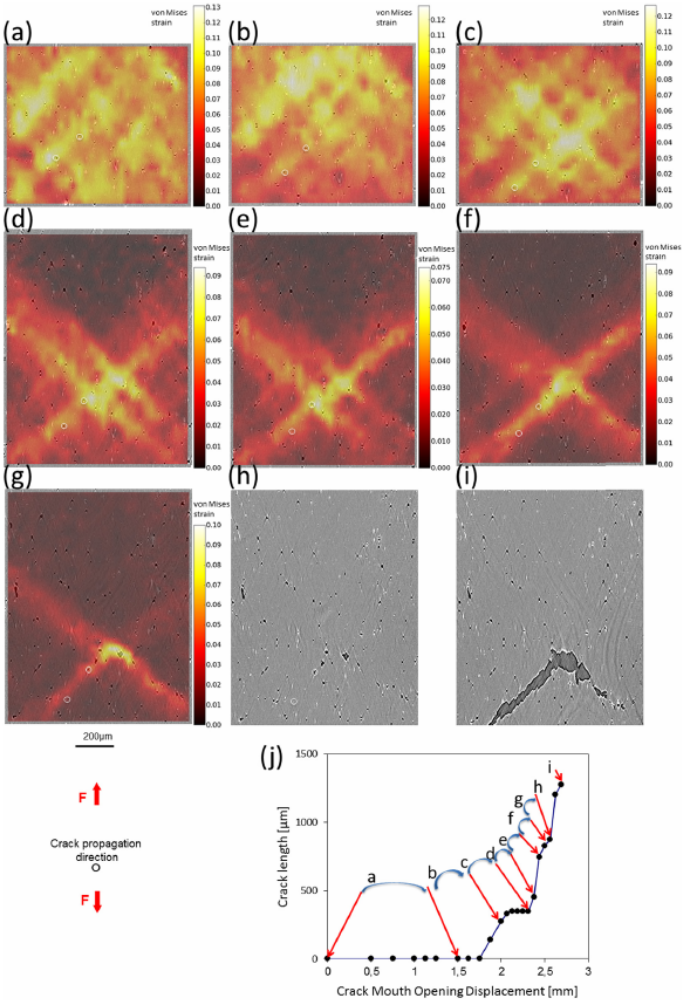

Figure 2.41 – Laminography-DVC results: incremental equivalent strain fields ahead of the notch of a AA2139-T3 CT specimen [Buljac, 2017].

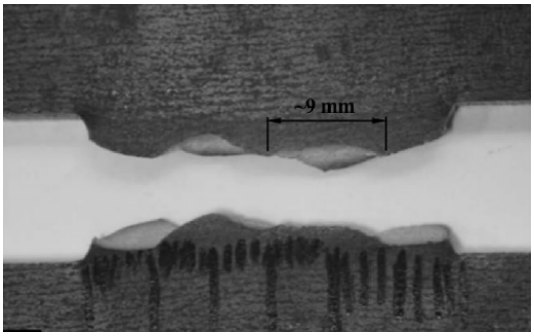

Figure 2.42 – 4 mm NS (normal strength) steel double edge notched tension (DENT) specimen exhibiting slant fracture in a “flip-flop" pattern [El-Naaman and Nielsen, 2013a].

Flat tensile specimens

The case of flat tensile specimen is put in the end of this chapter, because the fracture mode is strongly influenced by the section geometry. Slant fracture can usually be observed in the transverse or in the thickness planes. It is difficult to assess the possible influence of localizations due to PLC. In thin sheets with high width/thickness ratio, plane

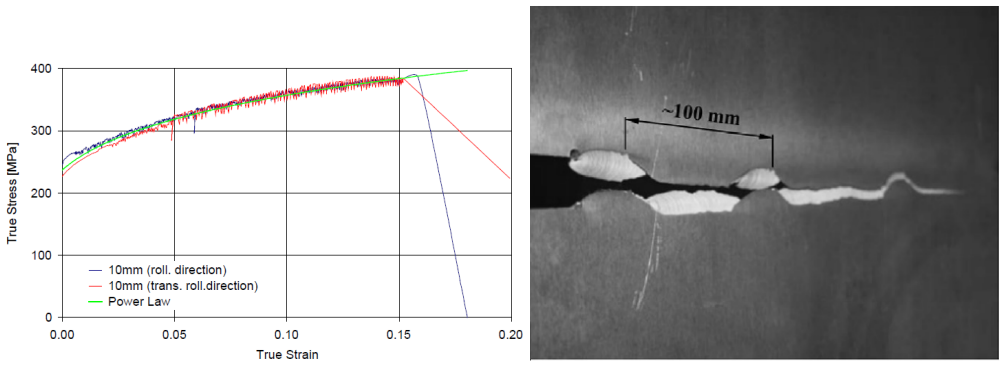

Figure 2.43 – Left: “flip-flop" fracture in a 10 mm high tensile strength aluminium alloy (AA5083-H116) edge crack specimen. Right: tensile curves of this aluminium sheet [Simonsen and Törnqvist, 2004].

stress condition prevails, slant fracture may occur in the transverse plane of the specimen [Asserin–Lebert et al., 2005]. The theoretical localization angle is given as a function of the Lankford coefficient l as:

$$\theta = \arctan\left(\sqrt{\frac{l}{1+l}}\right) \tag{2.28}$$

With increasing specimen thickness (slightly lower width/thickness ratio), necking occurs preferentially along the thickness direction, so that deformation along the transverse direction is inhibited. This leads to a plane strain condition in the centre of the neck and slant fracture with an angle equal to 45° which is characteristic of plane strain state.

The influence of PLC effect still can be observed in certain works though neglected by the author (see Fig. 2.44). At first, a commonly observed phenomenon in this kind of specimen is that the propagating PLC band will slow down in a position before the on set of necking. The fracture will later develop in this area.

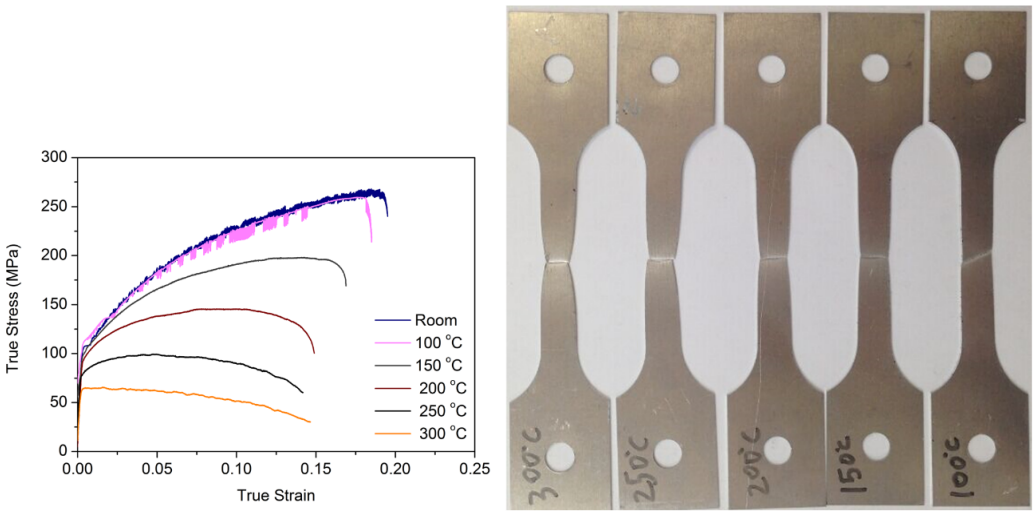

Figure 2.44 – Tensile curves and corresponding fracture modes of a AA5754 aluminium alloy subject to continuous electric currents presented by Zhao and Fan [2016]

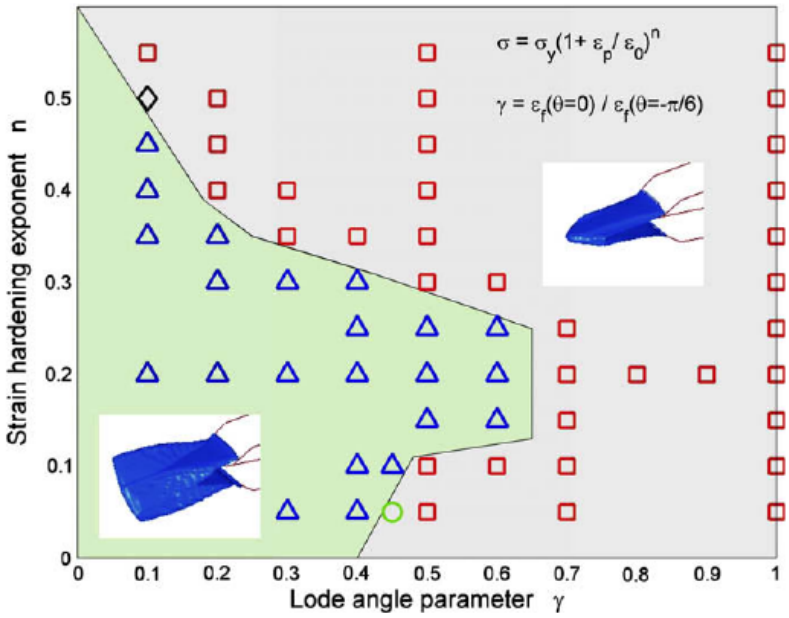

Figure 2.45 – A flat to slant fracture mode transition determined from a series of numerical simulation results where the strain hardening exponent n and the Lode angle dependence parameter γ are two varying material constants. Triangles denote slant cracks; squares denote flat cracks. [Xue and Wierzbicki, 2009].

Numerical simulations

The prediction of slant fracture by numerical method remains to be a challenge [Besson, 2010]. Most of the existent works for simulating slant fracture are based on the damage induced localization mechanism.

Tvergaard and Needleman [1984] simulated the cup–cone fracture pattern through plane strain 2D mesh with a modified Gurson model (known as the GTN model later).

Besson et al. [2001b, 2003] used Rousselier and Gurson models to study cup-cone fracture in round bar (2D axisymetric) and the shear lip formation in 2D plane strain specimen. From comparative numerical studies, they give some important points for modelling slant fracture. At first, a minimum number of elements must be used to discretize the cross section. Increasing viscosity will lead to flat fracture. It is also found that the shear lip is formed more easily when employing the Rousselier model due to the shape of the yield function. The deformation rate tensor of Rousselier's model always keeps a shear component Reducing hardening will lead to earlier failure and an easier formation of slant fracture. Strain controlled nucleation favours shear lip formation. quadratic elements will more easily produce slant fracture. The cup-cone fracture has also been reproduced by cohesive zone model [Scheider and Brocks, 2003]. Besson et al. [2001a] modelled the flat to slant transition in 3D notched specimens with Rousselier model.

Xue and Wierzbicki [2009] simulated the flat to slant fracture mode with 3D CT specimen using a modified Gurson model integrated the Lode angle dependence. Many features about the flat to slant transition have been captured such as the influence of material hardening capacity (see Fig. 2.45), the tunnelling effect and the thickness dependence. A similar idea is taken by Morgeneyer and Besson [2011]. A shear void nucleation term based on the Lode parameter is introduced into the Gurson model. The authors obtained a slant crack on a 3-D tilted mesh of the Kahn tear test sample.

With GTN model combined with “computational cell" methodology, Besson et al. [2013] simulated the flat to slant fracture in a 3D double cantilever beam with tilted mesh. It has been shown that the dissipated energy reaches a minimum when the crack is slanted.

Rousselier and Luo [2014] combined Mohr–Coulomb model with Rousselier damage model and crystal plasticity. The slant fracture in notched tensile specimens was captured. Inspired by the idea that PLC effect could be the physical mechanism of early localization observed in Morgeneyer et al. [2014], Rousselier and Quilici [2015] integrated the DSA model in it. The application of this model will be presented in Chapter 6.3.

Concerning the flip-flop crack, Felter and Nielsen [2017] applied combined tension and torsional loading for simulations on a double edge notched tensile test (DENT) specimen using Gurson model. The flipping crack was reproduced. However, the physical meaning for applying an out of plane movement is questionable.

Table 2.3 gives a list of papers trying to deal with the problem of simulating slant fracture.

Table 2.3 – Previous papers about cup-cone and slant fracture prediction.

Authors/years	specimen/fracture type	model description
Besson et al. [2001b, 2003]	2D round bar and plane strain (cup-cone shear lip)	Gurson and Rousselier models
Besson et al. [2001a]	3D V-notched and Kahn specimens (flat to slant transition)	Rousselier model with plastic anisotropy
Teng [2008]	2D plane strain (cup-cone shear lip)	Lemaitre's continuum damage
Xue and Wierzbicki [2008, 2009]	3D CT	Lode parameter dependant damage model
Morgeneyer and Besson [2011]	3D Kahn	Lode parameter dependant Gurson model
Besson et al. [2013]	3D modified double cantilever beam with tiled mesh	GTN model with computational cells
Rousselier and Luo [2014]	3D notched tensile specimen	Rousselier model + Coulomb + Polycrystalline
Rousselier and Quilici [2015]	3D notched tensile specimen	Rousselier model + Coulomb + Polycrystalline + PLC
Rousselier et al. [2017]	3D CT	Rousselier model + Coulomb + Polycrystalline + PLC
Felter and Nielsen [2017]	3D DENT (slant flip-flop)	Gurson model with torsion loading

2.5 Conclusion

In this chapter, the bibliographical background for the present study is introduced in four principle parts.

In the first section, we summarised the experimental observations about the key features of the Portevin-Le Chatelier effect. The underlying physical mechanisms of these features are interpreted with the dynamic strain ageing (DSA) theory. The influence of DSA on the fracture especially the reduction of ductility and toughness is found to be a common phenomenon in steels tested in the DSA active domain. In addition, the premature triggering effect after loading path change (relaxation, strain rate change) on the PLC effect is found in several materials. These materials are also sensitive to PLC effect under constant strain rate loading condition.

In the second section, a summary was made on the phenomenological models describing the strain ageing phenomenon. The KEMC model has been proven to be capable of simulating both static and dynamic strain ageing in various specimen geometries. However the experimental observation of the influence of dynamic strain ageing on the hardening rate is lacking. A modification based on the KEMC model involving dislocation density is needed (see Chapter 3).

Previous studies about the PLC effect in aluminium alloy were mainly focused on the 5000 series Al-Mg alloys which show intensive serrations at room temperature. In the third section, a thorough review about the PLC effect in 2000 series aluminium alloys (Al-Cu and Al-Cu-Li) is given. Most of the works suggest DSA is still the main mechanism for causing PLC effect in the 2000 series alloy. The manifestation of PLC effect strongly depends on the heat treatment under the same test conditions as the formation of precipitates would strongly influence the solute concentration. In contrast, some other mechanisms have also been proposed. One of the objectives of the current work is to characterise the possible PLC effect in the AA2198 and AA2139 alloys under different heat treatment conditions (see Chapter 4). As mentioned in the first section, the effect of loading path change on the triggering of PLC effect is investigated in Chapter 4 by tensile tests combined with digital image correlation measurement. These results could provide a possible explanation for the origin of multiple localizations bands found in the CT specimens made of these aluminium alloys through laminography-DVC [Morgeneyer et al., 2014].

In the fourth section, a review about the slant fracture in the flat tensile, round bar and notched tearing specimens is presented. For flat tensile specimens, the fracture mode is strongly influenced by the width/thickness ratio. Slant fracture is always found in the thickness plane or in the transverse plane which is dominated by the plane stress and plane strain conditions. For round bar specimens, the cup-cone fracture is found in most cases. However, for certain materials (e.g., TU48C C-Mn steel), the slant fracture is observed within the DSA active domain, while the cup-cone fracture is found outside the domain. The SEM fractography analysis showed little difference between these two cases. This phenomenon could be explained by the void damage localized in the slanted PLC band. For tearing tests, the flat to slant transition usually occurs for thin sheet specimens. The thickness and strain hardening dependence has been simulated by several researchers using damage model combined with shear sensitive Lode parameter. However, the actual material such as the C-Mn steel does not show big difference in strain hardening, whereas the slant fracture is found in the DSA active domain and the flat fracture is found outside the domain. This observation suggests that the PLC effect induced localization bands might be the precursor of slant fracture. The tearing test on this material

is still absent. An experimental investigation combined with DIC measurements at high temperature (DSA active domain) could provide insight into the development of fracture (see Chapter 5).

Chapter 3

A dislocation density based strain ageing model

Summary

One of the most successful models for describing the Portevin-Le Chatelier effect in engineering applications is the Kubin-Estrin-McCormick model (KEMC). In this chapter, a DSA model involving the influence of dynamic strain ageing on dynamic recovery due to dislocation annihilation is introduced in order to improve the original KEMC model. This modification accounts for additional strain hardening rate due to limited dislocation annihilation by the diffusion of solute atoms and dislocation pinning at low strain rate and/or high temperature. The parameters associated with this novel formulation are identified based on tensile tests for a C-Mn steel at 7 temperatures ranging from 20°C to 350°C. The validity of the model and the improvement compared to existing models are tested using 2D and 3D finite element simulations of the Portevin - Le Chatelier effect in tension.

Résumé

L'un des modèles les plus efficaces pour décrire correctement l'effet de Portevin-Le Chatelier dans les applications industrielles est le modèle de Kubin-Estrin-McCormick (KEMC). Dans ce chapitre, un terme tenant compte de l'influence du vieillissement dynamique sur la restauration dynamique due à l'annihilation des dislocations est introduit afin d'améliorer le modèle KEMC original. Cette modification tient compte du taux d'écrouissage supplémentaire dû à l'annihilation empêchée par la diffusion des atomes de soluté et l'ancrage des dislocations à faible vitesse de déformation et/ou à haute température. Les paramètres associés à cette nouvelle formulation sont identifiés sur les essais de traction d'un acier C-Mn à 7 températures allant de 20°C à 350°C. La validité du modèle et l'amélioration par rapport aux modèles existants sont testées avec les simulations de l'effet Portevin-Le Chatelier en traction par éléments finis en 2D et 3D.

This chapter is reproduced from (except section 3.5): Ren, S., Mazière, M., Forest, S., Morgeneyer, T. F., & Rousselier, G. (2017). A constitutive model accounting for strain ageing effects on work-hardening. Application to a C–Mn steel. *Comptes Rendus Mécanique*, 345(12), 908-921.

Contents

3.1 Introduction

Serrated flow and propagating plastic strain localization bands are salient features of the Portevin-Le Chatelier (PLC) effect that is observed during tensile tests in many industrial metallic alloys within a given range of strain rates and temperatures. It has been reported in alloys containing substitutional atoms, such as Al-Cu alloys [Jiang et al., 2005; Ranc and Wagner, 2005; Böhlke et al., 2009], Al-Mg alloys Dierke et al. [2007]; Louche et al. [2005]; Picu et al. [2005]; Halim et al. [2007], or involving interstitial elements like carbon in steels [Wang et al., 2012; Belotteau, 2009]. It has also been observed in nickel Fournier et al. [2001]; Rao et al. [1995] and titanium [Prasad and Kamat, 2008] based alloys. The PLC effect is usually associated with a negative strain rate sensitivity (nSRS) of the flow stress which means that the latter decreases when the prescribed strain rate increases. Besides the abnormal flow stress, the localization of strain into Lüders or PLC bands and the negative strain rate sensitivity, some other severe changes in mechanical properties have been reported within the PLC active domain, such as loss of toughness and ductility [Chakravartty et al., 1983; Miglin et al., 1985; Gomiero et al., 1992; Wang et al., 2012; Kim et al., 2004; Wagner et al., 1998; Amar and Pineau, 1985]. Some authors have shown that the strain localization associated with the PLC effect promotes the initiation of cracks and consequently results in a reduced material toughness in fracture mechanics CT specimens [Belotteau, 2009]. In contrast, the authors in [Zhang et al., 2012] noticed a reduction of the strain for initiation of necking in smooth tensile specimens but they did not report any decrease of the strain to failure. The main parameter controlling the occurrence of necking and the subsequent final failure is the hardening rate. A proper description of the coupling between strain ageing and hardening is therefore necessary to explain the deterioration in mechanical properties within the PLC domain.

At the microscopic scale, it is widely accepted that the PLC effect in alloys is caused by dynamic strain ageing (DSA) which refers to the interaction between mobile dislocations and the diffusion of solute atoms. Cottrell and Bilby [1949] were the first to interpret PLC effects based on the DSA mechanism. The interaction was assumed to take place between continuously moving dislocations and a solute atmosphere. Later, Penning [1972] investigated several important aspects of the PLC effect from a mathematical point of view, including the propagative localised plastic deformation band, the influence of machine stiffness and most importantly the necessity of negative strain rate sensitivity. These two pioneering works set the basis for the development of DSA models accounting for the PLC effect. Van den Beukel [1975] took into account the discontinuous motion of dislocations in the DSA model by introducing the waiting time t_w of arrested dislocations at obstacles. During the waiting time, solute atoms diffuse towards arrested dislocations and an over-stress is required to trigger further dislocation motion. The movement of an unpinned dislocation to the next obstacle is assumed to be almost instantaneous: this flying time is negligible compared with the waiting time. Kubin and Estrin [1985, 1990] proposed a relation between the waiting time and strain rate which has been widely used in the following works [Graff et al., 2004; Mazière et al., 2010]. The critical conditions for the onset of PLC effect were discussed in detail by these authors. McCormick [1988] further developed a complete mechanical model accounting for the transient behaviour observed during strain rate jump tests by underlying the difference between the effective ageing time t_a and waiting time t_w.

The KEMC model as proposed by McCormick [1988] and Kubin and Estrin [1985] is based on the introduction in the total flow stress of an over-stress due to dynamic strain ageing and depending on the ageing time t_a. This over-stress is maximal for low strain

rates, high temperatures, or large values of the initial ageing time. Since the ageing time evolution depends on the waiting time t_w, which depends itself on the plastic strain rate, the ageing over-stress is an implicit function of the latter, allowing the modelling of the negative strain rate sensitivity. The KEMC model predicts both Lüders and Portevin - le Chatelier instabilities as it can be noticed in numerous works using this model for finite element simulations [Zhang et al., 2001; Graff et al., 2004; Benallal et al., 2008; Böhlke et al., 2009; Mazière et al., 2010; Wang et al., 2012; Klusemann et al., 2015]. In the original version of the KEMC model [McCormick, 1988] and in many of the following studies [Zhang et al., 2001; Graff et al., 2004], the waiting time t_w is also assumed to be a function of the plastic strain. Since the number of obstacles increases with plastic strain, the waiting time should grow as well. On the contrary, the maximum over-stress level due to strain ageing is assumed to be independent of the plastic deformation. Finally, in the KEMC model, dynamic strain ageing only has a limited influence on the hardening rate with evolving prescribed strain rate. In some alloys, however, such as C-Mn steels, the influence of DSA on strain hardening rate is rather strong [Wang et al., 2012]. This interaction has also been observed in Magnesium alloy [Li et al., 2010], Cobalt based super alloys [Chaboche et al., 2013], or in Nickel based super alloys [Mazière, 2007].

In addition to the original KEMC model, dislocation dynamics based models for DSA and PLC have been recently proposed [Fressengeas et al., 2005; Marais et al., 2012; Gupta et al., 2017]. The strain hardening is then controlled by the dislocation density evolution, divided into a production and an annihilation term. In [Marais et al., 2012] the model accounts for a single population of dislocations. It is rather similar to the original KEMC model since the over-stress is added to the total flow stress and increases consequently but DSA has almost no influence on the hardening rate. On the contrary, in [Fressengeas et al., 2005] and [Gupta et al., 2017], an indirect coupling between strain ageing and strain hardening is proposed in a model based on two different dislocation populations (mobile and forest dislocations). The coupling between strain ageing and strain hardening is introduced by an increase of the forest dislocation density in order to represent the “probability of dislocation pinning by solute atoms at some obstacles such as forest dislocations". The model proposed in [Fressengeas et al., 2005] and [Gupta et al., 2017] is however rather complex with a large number of parameters to identify. On the other hand, the original KEMC model was modified by Böhlke in [Böhlke et al., 2009] to account for the influence of DSA on the hardening rate by introducing a strain dependent maximal value of the over-stress due to strain ageing (σ_{B0} in [Böhlke et al., 2009]). This modification of the original KEMC model is purely phenomenological and mainly motivated by a better description of the critical plastic strain for PLC in aluminium alloys. The same approach has been used in some following articles to account for the interaction between strain ageing and strain hardening [Chaboche et al., 2013; Klusemann et al., 2015].

To achieve the goal of a better description of the experimental hardening rate within a simple and physically sound model, the idea of the present work is to propose a modification of the hardening rate by the impediment of the annihilation of dislocation segments by solute atoms. This dislocation mechanism has actually been observed in TEM observations as shown in [Caillard, 2016; Hong and Lee, 2005]. The objective of the present work is therefore to formulate a modified Kocks-Mecking model into which DSA effects are introduced in the yield function like in [Marais et al., 2012] but also in the dynamic recovery term of the dislocation density evolution. The advantages of this constitutive model will be highlighted.

The work is organised as follows. The theoretical considerations about the new model are presented in section 3.2. The dislocation evolution law is separated into the multipli-

cation and annihilation parts. The influence of strain ageing is introduced in the dislocation annihilation term. A systematic identification procedure is provided in section 3.3 to calibrate the material parameters for a C-Mn steel tested at several strain rates from room temperature to 350°C. However a model accounting for DSA is valid only if serrations are predicted within the accurate strain rate domain. For that purpose, finite element simulations must be performed for the whole specimens and not only at the material volume element level. In section 3.4, validation tests are then carried out and presented using the identified material model for 2D and 3D finite element meshes.

3.2 Formulation of the constitutive model

The proposed constitutive model is presented within the finite strain framework using the concept of local objective frames following [Besson et al., 2009]. The second and fourth order tensors are defined by a single tilde $\underset{\sim}{\square}$ and a double tilde $\underset{\approx}{\square}$ respectively. Observer invariant stress and strain rate measures $\underset{\sim}{\boldsymbol{\sigma}}$ and $\underset{\sim}{\dot{\boldsymbol{\varepsilon}}}$ are defined by the transformation of the Cauchy stress tensor $\underset{\sim}{\boldsymbol{T}}$ and the Eulerian strain rate tensor $\underset{\sim}{\boldsymbol{D}}$ into the corotational frame characterized by the rotation $\underset{\sim}{\boldsymbol{Q}}$ ($\underline{\boldsymbol{x}}$,t) at each material point:

$$\begin{cases} \underset{\sim}{\boldsymbol{\sigma}} = \underset{\sim}{\boldsymbol{Q}}.\underset{\sim}{\boldsymbol{T}}.\underset{\sim}{\boldsymbol{Q}}^T \\ \underset{\sim}{\dot{\boldsymbol{\varepsilon}}} = \underset{\sim}{\boldsymbol{Q}}.\underset{\sim}{\boldsymbol{D}}.\underset{\sim}{\boldsymbol{Q}}^T \\ \underset{\sim}{\boldsymbol{Q}} \quad \text{such as} \quad \underset{\sim}{\dot{\boldsymbol{Q}}}^T.\underset{\sim}{\boldsymbol{Q}} = \underset{\sim}{\boldsymbol{\Omega}} \quad \text{(corotational)} \end{cases}$$

where $\underset{\sim}{\boldsymbol{D}}$ and $\underset{\sim}{\boldsymbol{\Omega}}$ respectively are the symmetric and skew-symmetric parts of the velocity gradient.

3.2.1 Constitutive equations

The strain rate is then decomposed into elastic and plastic parts:

$$\underset{\sim}{\dot{\boldsymbol{\varepsilon}}} = \underset{\sim}{\dot{\boldsymbol{\varepsilon}}}^e + \underset{\sim}{\dot{\boldsymbol{\varepsilon}}}^p, \quad \underset{\sim}{\boldsymbol{\sigma}} = \underset{\approx}{\boldsymbol{C}} : \underset{\sim}{\boldsymbol{\varepsilon}}^e \tag{3.1}$$

where $\underset{\approx}{\boldsymbol{C}}$ is the Hooke tensor of elasticity. The plastic flow is described by the normality rule

$$\underset{\sim}{\dot{\boldsymbol{\varepsilon}}}^p = \dot{p}\,\underset{\sim}{\boldsymbol{n}}, \quad \underset{\sim}{\boldsymbol{n}} = \frac{\partial F}{\partial \underset{\sim}{\boldsymbol{\sigma}}}, \tag{3.2}$$

where p is the cumulative plastic strain and the yield function, f, is taken in the form

$$F(\underset{\sim}{\boldsymbol{\sigma}}, \rho, t_a) = \sigma_{eq}(\underset{\sim}{\boldsymbol{\sigma}}) - R(\rho) - R_a(t_a), \tag{3.3}$$

In the previous equation, σ_{eq} is the equivalent stress measure. The threshold for yielding is the sum $R(\rho) + R_a(t_a)$ where $R(\rho)$ is the usual yield stress depending on the total dislocation density ρ and $R_a(t_a)$ is yield stress enhancement (over–stress) due to ageing.

In addition, an hyperbolic flow rule is introduced in the current model that accounts for the thermal activation phenomenon:

$$\dot{p} = \dot{\varepsilon}_0 \exp\left(-\frac{E_a}{k_B T}\right) \sinh\left(\frac{V_a \langle F \rangle}{k_B T}\right), \tag{3.4}$$

where $\langle F \rangle = \max(F, 0)$. The threshold strain rate at which the thermal activation takes place is $\dot{\varepsilon}_0$ and k_B and T are respectively the Boltzmann constant and the temperature in Kelvin. V_a and E_a are respectively the activation volume and the activation energy.

The last term $R_a(t_a)$ on the right side of equation (5.3) is the yield over-stress due to strain ageing:

$$R_a = P_1 \phi(t_a), \tag{3.5}$$

with

$$\phi(t_a) = 1 - \exp(-(t_a/t_0)^n), \tag{3.6}$$

where $\phi(t_a)$ is the relative concentration of solute atoms pinning the dislocations. It varies between 0 and 1. $\phi = 1$ means that dislocations are totally pinned while $\phi = 0$ corresponds to the unpinned case. P_1 is the maximal stress drop magnitude from the pinned state $\phi = 1$ to the unpinned state $\phi = 0$. The parameter t_0 is related to the diffusivity of solute atoms, see Marais et al. [2012].

The ageing time t_a is defined by the following evolution law:

$$\dot{t_a} = 1 - \frac{t_a}{t_w}, \quad t_w = \frac{w}{\dot{p}}, \quad t_a(t=0) = t_{a0}, \tag{3.7}$$

where t_w denotes the average waiting time of dislocations at obstacles. It is worth noting that t_a is equal to the waiting time t_w only for steady state [McCormick, 1988]. The initial time t_{a0} is related to the presence of static ageing. A proper initial time value allows a good description of Lüders peak and plateau. The parameter ω represents the strain increment produced when all arrested dislocations overcome local obstacles and move forward to the next pinned configuration.

The second term $R(\rho)$ on the right side of equation (5.3) represents the isotropic hardening which is expressed in terms of the total dislocation density ρ:

$$R(\rho) = \sigma_0 + \gamma \mu b \sqrt{\rho}, \quad R_0 = \sigma_0 + \gamma \mu b \sqrt{\rho_0} \tag{3.8}$$

where μ is the shear modulus; γ is a material scale parameter [Kocks, 1976]; b is the magnitude of the Burgers vector. For the sake of simplicity, we do not distinguish between forest and mobile dislocation densities.

The evolution of dislocation density is based on a modified Kocks-Mecking equation [Kocks, 1976]:

$$\dot{\rho} = \left(a_0 \sqrt{\rho} - b_0 (1 - \zeta \phi) \rho\right) \dot{p}. \tag{3.9}$$

where the first term $a_0 \sqrt{\rho}$ on the right-hand side of equation (3.9) describes the multiplication of dislocations. The second term $b_0(1 - \zeta\phi)\rho\dot{p}$ is related to the annihilation (dynamic recovery) process for dislocation dipoles which is considered to be affected by strain ageing. This coupling with strain ageing is absent in earlier formulations of the KEMC model. Physically, the short range motion of dislocations required for annihilation or dynamic recovery is impeded by the trapping of solute atoms at dislocations (especially at low strain rates or high temperatures). Consequently, strain ageing reduces the ability of the material to exhibit dynamic recovery. In Eq. (3.9), the strain ageing influence on dynamic recovery depends on the current value of the function $\phi(t_a)$. When $\phi(t_a)$ is maximal, i.e. for low strain rates or high temperatures, the dynamic recovery process is significantly reduced by strain ageing, which results in larger dislocation density production rate $\dot{\rho}$, and, accordingly, in a larger hardening rate. On the contrary when $\phi(t_a)$ is minimal, i.e. for high strain rates or low temperatures, the strain ageing has no influence on dislocation annihilation allowing for standard dynamic recovery and a reduced dislocation density growth rate $\dot{\rho}$ and associated hardening rate. Finally the hardening rate will then be larger for low strain rates than for large strain rates as experimentally observed [Wang et al., 2012]. The parameter ζ, $0 \leq \zeta \leq 1$, has to be identified in order to control the level of influence of strain ageing on strain hardening ($\zeta = 0$ means no influence, while $\zeta = 1$ the maximal influence).

3.2.2 New features in the macroscopic response of the new model

After introducing the ageing effect on dislocation annihilation and consequently in the isotropic hardening term $R(\rho)$, R_a is no longer the only term in the model responsible for dynamic strain ageing effects. This new feature of the model is now illustrated in the case of the C-Mn steel for which the KEMC material parameters were previously identified, see [Wang, 2011].

The modified model has been identified anew based on the same experimental curves as in [Wang, 2011]. This identification procedure is presented in section 3.3. In the present subsection, the main features of the model are illustrated by setting ζ to $\zeta = 1$ to enhance the effect. Actually, the optimal value $\zeta = 0.2$ was found for the current identification as shown in Table 3.2. The details about the identification will be presented in the next section.

The strain rate sensitivity of the models is investigated in Fig. 3.1 that shows the evolution of the 1D steady state stress as a function of the plastic strain rate at three different plastic strain levels (0.05, 0.10 and 0.15) for the C-Mn steel using the original KEMC model and the novel formulation. The original version of the model is retrieved for $\zeta = 0$. The curves of Fig. 3.1(a) display the usual S-shape for strain ageing materials. The role of the parameter P_1, see Eq. (3.5), is investigated. Four situations are considered in Fig. 3.1: $P_1 \neq 0, \zeta = 0$ (original KEMC model), $P_1 = 0, \zeta = 0$ (truncated KEMC model), $P_1 \neq 0, \zeta = 1$ (new model), $P_1 = 0, \zeta = 1$ (truncated new model). Setting $P_1 = 0$ amounts to killing the over–stress $R_a(t_a)$.

A negative strain rate sensitivity (nSRS) domain can be observed for the original as well as for the new model for the cases $P_1 \neq 0$ as shown in Fig. 3.1 (a) and (b).

For $P_1 = 0$, see Fig 3.1 (c), a slight positive sensitivity can be observed, which indicates that the dynamic strain ageing effect is completely eliminated for $P_1 = 0$ in the original KEMC model. On the contrary the new model can still produce a negative strain rate sensitivity even for $P_1 = 0$ as shown in Fig. 3.1 (d). Such a feature of the modified model can be particularly useful since in the original KEMC model the parameter $P_1 = 0$ controls simultaneously the amplitude of the serrations and the amplitude of the negative strain rate sensitivity domain. These two amplitudes being for some materials (especially steels) different by one order of magnitude, a compromise has to be made in the parameter identification of the KEMC model. In the new model, the negative strain rate sensitivity is not only controlled by the R_a term but also induced by the coupling between strain ageing and strain hardening in Eq. (3.9). The material parameter P_1 can then be devoted to an accurate description of serrations only.

In Fig. 3.2, tensile stress-strain curves under various global prescribed strain rates predicted by the two models are compared. The red arrow indicates the direction of increasing applied strain rate. Both figures show the strain rate sensitive behaviour in the nSRS zone (i.e. between 10^{-5} and 10^{-1} s^{-1}). It can be noticed that the curves obtained by the original model at different strain rates are almost parallel to each other. This indicates that the evolution of hardening rate is the same at each strain rate during straining (see Fig.3.2 (a)). In contrast, some experimental observations on C-Mn steels show that the distance between curves increases with strain Wang et al. [2012]. A better modelling of this effect was proposed by Böhlke et al. [2009] prescribing a linear increasing evolution for P_1 with respect to the cumulative plastic strain p. From a physical point of view, it is expected that the apparent hardening rate should also be influenced by strain ageing due to the interaction between dislocations perturbed by the pinning of segments. The proposed new model includes such an influence of strain ageing on strain hardening rate, via the function $\zeta\phi$ in Eq. (3.9). The stress strain curves produced by the modified

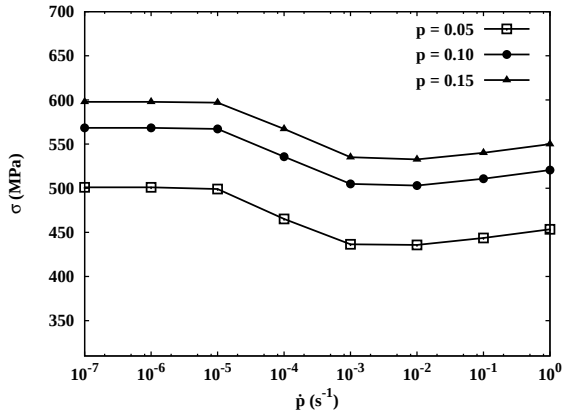

(a) $P_1 \neq 0$ using the original model Wang [2011]

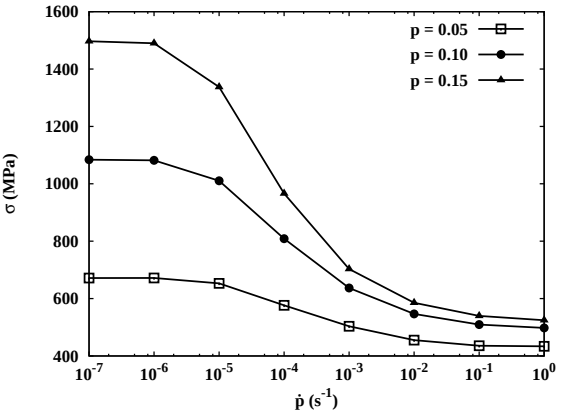

(b) $P_1 \neq 0$ using the new model with $\zeta = 1.0$

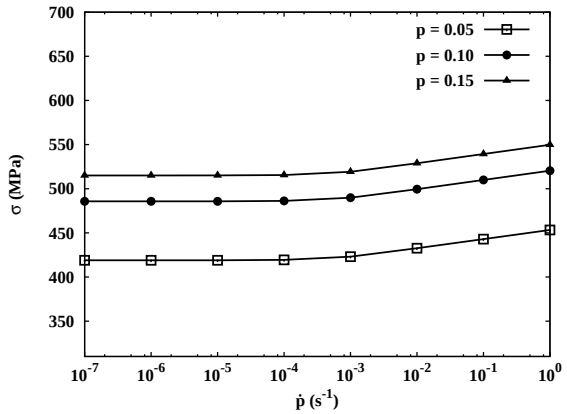

(c) $P_1 = 0$ using the original model Wang [2011]

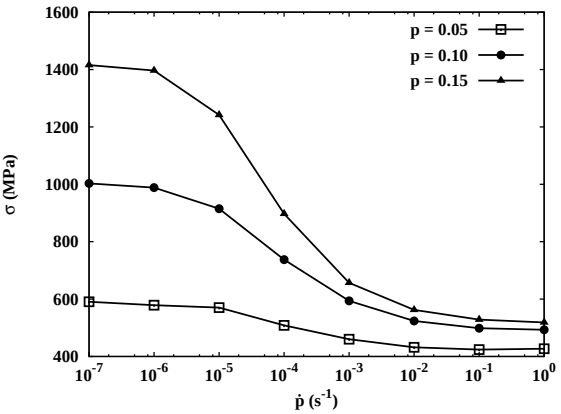

(d) $P_1 = 0$ using the new model with $\zeta = 1.0$

Figure 3.1 – Strain rate sensitivity according to the original KEMC and new models for uniaxial tension under prescribed plastic strain rate. The corresponding stress is given at three distinct plastic strain levels.

model are close to each other at low strain and spread at higher strain level which shows a strong similarity to the experimental results (see Fig.3.4 (a)) that are presented in the next section.

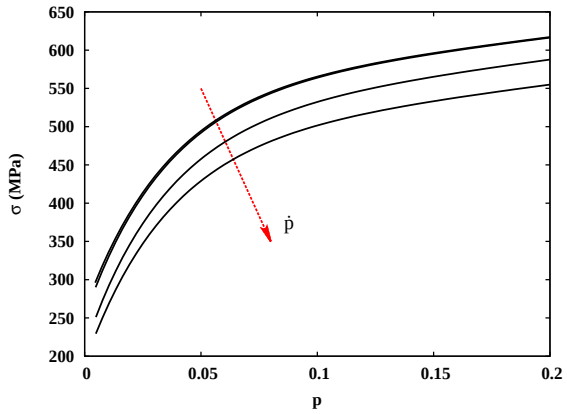

(a) KEMC model Wang [2011]

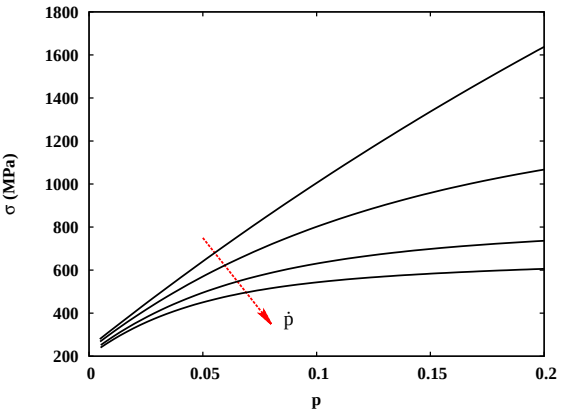

(b) the new model

Figure 3.2 – Comparison of the stress-strain curves for different applied strain rates $\dot{E}$.

3.3 Identification of the new model for a C-Mn steel

3.3.1 Experiments

The considered C-Mn steel is used for the secondary system pipelines of pressurized water reactor (PWR) in nuclear power plants [Belotteau et al., 2009]. The chemical composition of this material (TU48C) is given in Table 5.1. Its tensile mechanical behaviour was characterized in the temperature range between 20°C and 350°C [Wang et al., 2012]. The interstitial atoms like carbon and nitrogen act as solid solute atoms and make this material sensitive to strain ageing phenomena. The geometry of the round tensile specimens used for tensile testing are shown in Fig. 3.3.

Table 3.1 – Chemical composition (mass fraction in %) of the C-Mn steel considered in the current study.

C	S	P	Si	Mn	Ni	Mo	Nb	V	Cu	Sn	N	Al
0.19	0.0074	0.011	0.27	1.07	0.04	0.01	< 0.01	< 0.01	0.05	< 0.05	0.011	0.0085

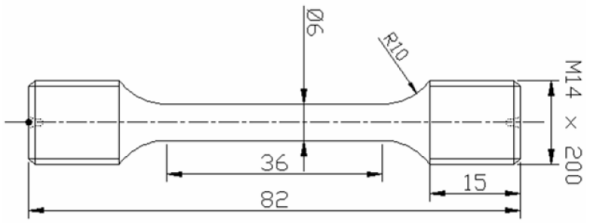

Figure 3.3 – Geometry of the round tensile specimens Belotteau [2009].

Tensile tests were performed at 7 temperatures from 20°C to 350°C. At each temperature, various strain rates from 10^{-2} to 10^{-4} s^{-1} (or 10^{-5} s^{-1}) were considered. The PLC effect is observed in the temperature range from 150°C to 300°C for the considered strain rates. Fig. 3.4 shows the stress-strain curves tested at 200°C. A marked negative strain rate sensitivity and some serrated plastic flow (both Lüders and PLC effects) can be observed.

The first step of the identification strategy consists in smoothing the curves, thus eliminating the Lüders plateau and the PLC serrations, for the determination of the strain hardening parameters, see the dotted lines in Fig. 3.4(a). The hardening rates obtained from these smooth curves are presented in Fig. 3.4(b). The identification is based on the true stress strain curves.

3.3.2 Identification

Several model parameters can be taken from the literature dealing with similar steels. The activation energy E_a in equation (3.4) is chosen to be 0.6 eV, and the parameter $\dot{\varepsilon}_0$ is equal to 6.2 s^{-1} according to Marais et al. [2012]. The activation volume V_a is taken from [Wang, 2011].

The identification of the ageing term R_a (Eq. (3.5), (3.6) and (3.7)) is the essential part and involves 4 distinct parameters: P_1, t_0, n, w. The initial ageing time t_{a0} must also be chosen. The parameter w remains constant with the value $2. \times 10^{-4}$ for all temperatures, referring to [Wang et al., 2012]. The parameter n can be fixed at 0.66 or 0.33 corresponding to bulk or pipe diffusion according to [Springer and Schwink, 1991]. The latter value was

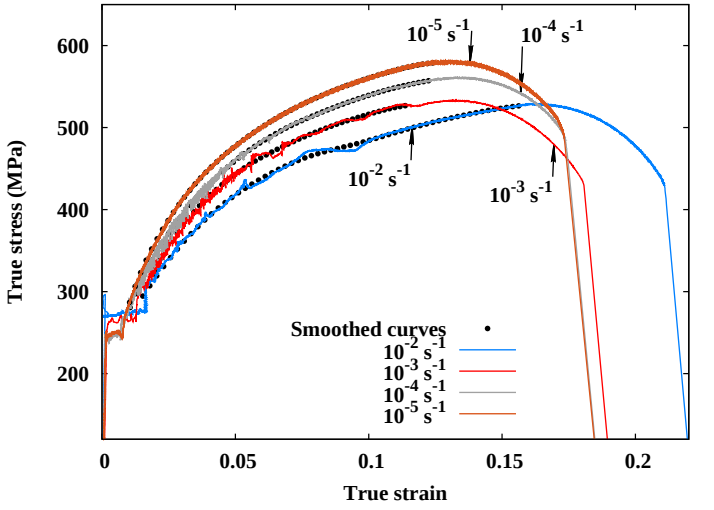

(a)

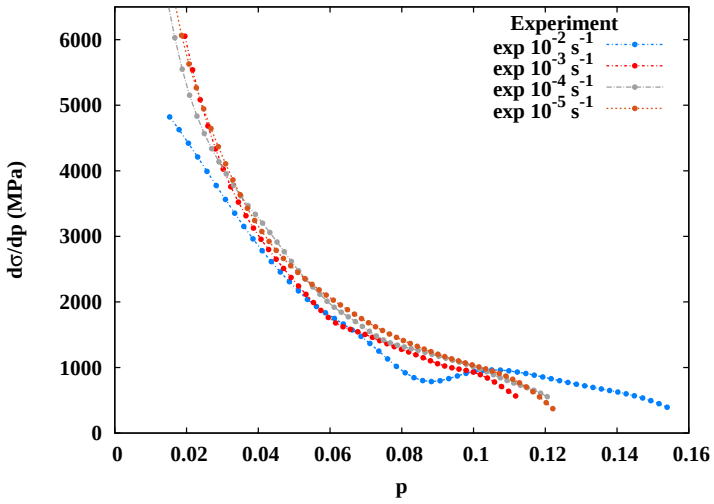

(b)

Figure 3.4 – (a) Experimental and smoothed tensile curves at 200°C (reproduced from [Wang, 2011]) serve as initial data for model calibration. (b) Hardening rate evolution as a function of plastic strain under different strain rates.

found to provide better results in the current model for this material. In the current study, t_{a0} is in a first step of the identification set to 0 to exclude the initial Lüders effect. The other two parameters P_1 and t_0 are those which remain to be identified. In the isotropic hardening term, the Burgers vector b takes the value 0.29 nm and the initial dislocation density is $\rho_0 = 1.0 \times 10^7$ mm^{-2} [Wang et al., 2012].

The next step consists in identifying the 7 remaining parameters accounting for strain hardening behaviour, including σ_0, a_0, b_0, ζ, P_1, t_0.

An optimisation procedure using the Levenberg-Marquardt algorithm is used to minimize the deviation between data from material point simulations and that of the smoothed experimental stress-strain curves. This strategy avoids time-consuming FEM simulations on full dimension specimens [Marais et al., 2012]. However, the localization pattern related to strain ageing require a field analysis and cannot be captured by volume element simulations. Simulations on full size specimens are therefore necessary in a third step to validate the model identification and possibly adjust the parameter w.

The Table 3.2 provides the optimized parameters for all temperatures.

Table 3.2 – Identified material parameters of the constitutive model.

T (°C)	20	100	150	200	250	300	350
E(GPa)	210	205	201	198	195	192	188
ν	0.3	0.3	0.3	0.3	0.3	0.3	0.3
σ_0(MPa)	166	160	139	116	94	74	72
γ	0.3	0.3	0.3	0.3	0.3	0.3	0.3
b(mm)	2.9e−7	2.9e−7	2.9e−7	2.9e−7	2.9e−7	2.9e−7	2.9e−7
a_0	1.44e6	1.52e6	1.75e6	2.46e6	2.92e6	2.96e6	3.00e6
b_0	32.0	37.0	44.1	57.1	59.0	62.3	64.2
ζ	0.2	0.2	0.2	0.2	0.2	0.2	0.2
P_1(MPa)	136	120	114	101	95.3	91.7	85.0
t_0(s)	1.78e5	6.72e2	1.30e1	1.05	7.68e−1	3.89e−2	5.11e−3
ω	2.0e−4	2.0e−4	2.0e−4	2.0e−4	2.0e−4	2.0e−4	2.0e−4
n	0.33	0.33	0.33	0.33	0.33	0.33	0.33
ρ_0(mm^{-2})	1.0e7	1.0e7	1.0e7	1.0e7	1.0e7	1.0e7	1.0e7
V_a(b^3)	43.29	48.60	53.46	58.82	64.19	69.01	73.87
$E_a(eV)$	0.6	0.6	0.6	0.6	0.6	0.6	0.6
$\dot{\varepsilon}_0$(s^{-1})	6.2	6.2	6.2	6.2	6.2	6.2	6.2

The results of the material parameter identification at 200°C and 300°C are plotted respectively in Fig. 3.5 and 3.6. The material point simulation responses are compared with the smoothed and truncated experimental curves for the original model as proposed by Wang et al. [2012] and the new one.

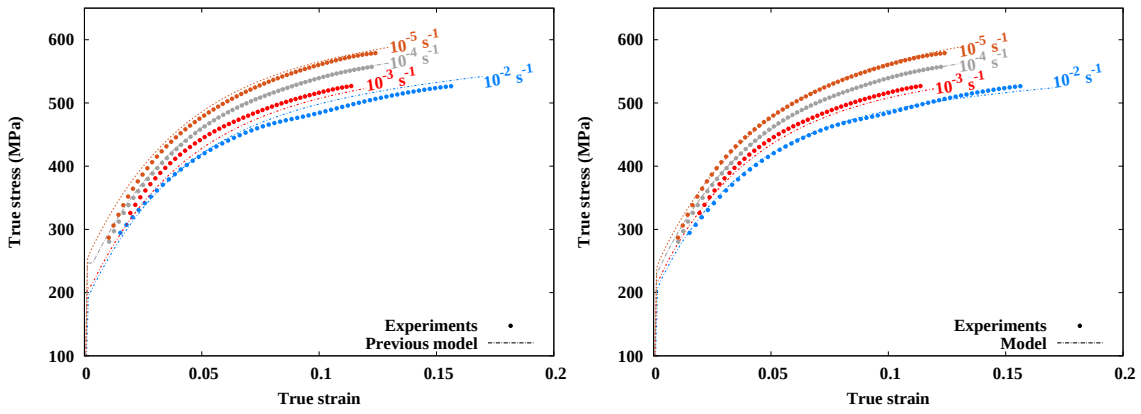

Figure 3.5 – (a) Identification results at 200°C proposed by Wang et al. Wang et al. [2012]. (b) Identification of the new model at 200°C.

As shown in Fig. 3.5 and Fig. 3.6, both models reproduce the effect of temperature and simulate the different levels of yield stress and hardening at different strain rates. However it can be noticed that the distance between the experimental curves at different strain rates increases with strain as mentioned in section 3.2.2. The original model does not capture this feature. In the original model the ageing over-stress influences the yield stress in such a way that a pair of stress/strain curves for two different prescribed strain rates are simply translated by a given constant stress value. The hardening rate for each prescribed strain rate remains constant as shown in Fig. 3.7 (a), which is not in agreement

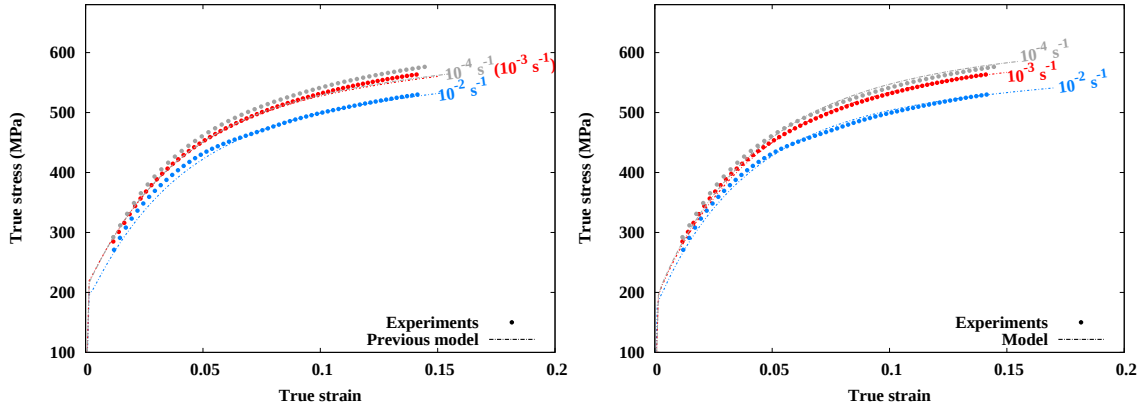

(a) (b)

Figure 3.6 – (a) Identification results at 300°C proposed by Wang et al. Wang et al. [2012]. (b) Identification of the current model.

with experimental results (see figure 3.4(b)).

In contrast, the dislocation density model proposed in this work that includes a strain ageing influence on the dislocation annihilation rate accurately account for this effect. As presented in Fig. 3.7 (b), the hardening rate is different for each prescribed strain rate using the current model. This result is close to the one plotted in Fig.3.4 (b) which gives the experimental hardening rate evolution curves as functions of plastic strain.

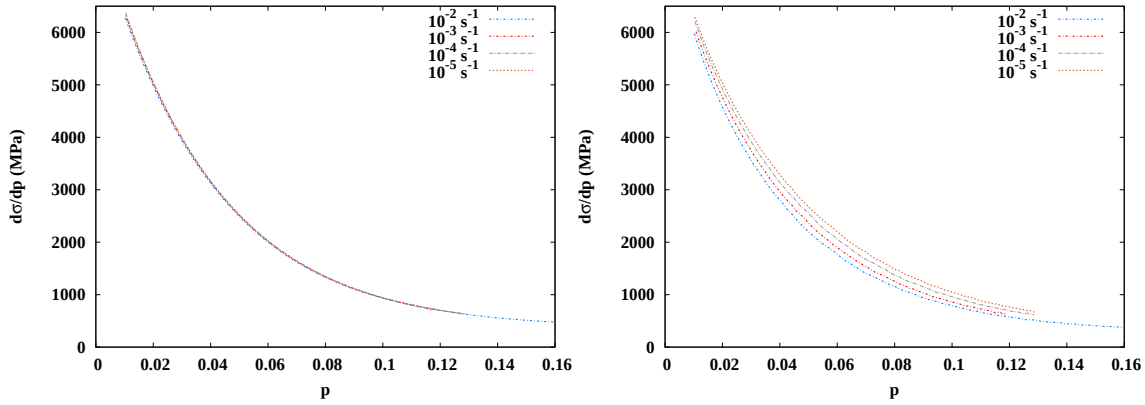

(a) Original KEMC model Wang [2011]. (b) Current model.

Figure 3.7 – Comparison of the hardening rate curves for the original KEMC model Wang et al. [2011] and the current model at 200°C.

3.3.3 Evolution of parameter t_0 with temperature

The material parameters have been identified independently for each temperature. It is however essential to check the evolution of parameters with temperature and possibly point out some possible Arrhenius dependence. This is checked here for the parameter t_0. Following the original work by Cottrell and Bilby [1949], this parameter should have the following temperature dependence:

$$t_0(T) \propto \frac{T}{D(T)} \propto T \exp\left[\frac{Q_m}{k_B T}\right] \tag{3.10}$$

where $D(T)$ is the diffusion coefficient of solute atoms, and Q_m the activation energy of the diffusion process. Such a function has been fitted on the results of table 3.2 as it can be seen from Fig. 3.8.

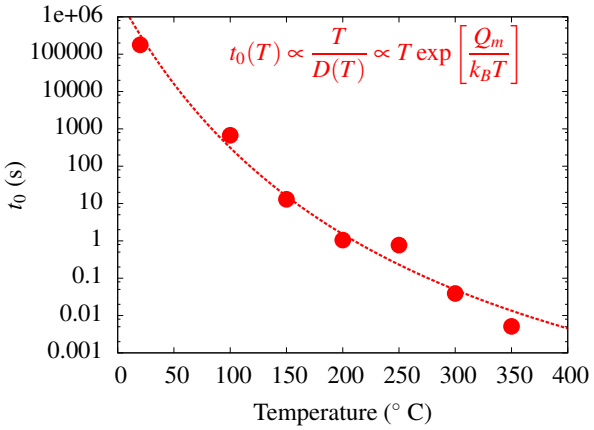

Figure 3.8 – Evolution of parameter t_0 with temperature and calibration of the associated activation energy.

The parameter Q_m/k_B is found to be equal to 9880K that leads to $Q_m = 19.5$ kcal/mole which is close to the value of $Q = 18.65$ kcal/mole estimated by Da Silva and McLellan [1976] for the diffusion of carbon in B.C.C. iron. The value estimated by the same author for the diffusion of nitrogen in B.C.C. iron is smaller and equal to 17.54 kcal/mole. This identification provides a clear physical basis to the proposed strain ageing equations.

3.4 Validation on 2D and 3D geometries

The previous identification was based on material point simulations and smoothed experimental curves. In order to verify the ability of the model to capture the localization patterns, it must be tested on the whole real specimen geometry. Considering that the simulation on a 3D finite element mesh is time-consuming, a 2D mesh is firstly used for testing strain rate effects. A 2D rectangular plate with dimensions 6 mm × 20 mm used for uni-axial tension simulation is presented in Fig. 3.9 (a). Axial displacement boundary conditions are prescribed to the upper and lower ends of the plate. Complementing displacement conditions are imposed to fix the rigid body motion. Plastic strain rate localization bands are predicted at strain rates 3×10^{-2} s^{-1} and 4×10^{-4} s^{-1}. They are shown in Fig. 3.9. The X-shaped strain rate localization band is observed at $\dot{E} = 3 \times 10^{-2}$ s^{-1}. The simulation at lower strain rate leads to inclined localization bands. Similar phenomenon has been reported in the literature [Mazière et al., 2010].

Fig. 3.9 (b) shows 9 stress-strain curves simulated at 200°C with different strain rates ranging from 1.0×10^{-5} s^{-1} to 3.0×10^{-2} s^{-1}. The shape of serrations can be seen to be strain rate dependent. The amplitude and frequency of serrations decrease with strain rate. This trend is in agreement with experimental observations (see Fig. 3.4). The strain rate dependence of the frequency and size of the stress serrations has been discussed in [Kubin et al., 1988].

Another important feature of PLC effect is the critical condition for the occurrence of instabilities. This condition is usually measured by the critical plastic strain. Experimental observations show that the critical plastic strain strongly depends on the applied strain

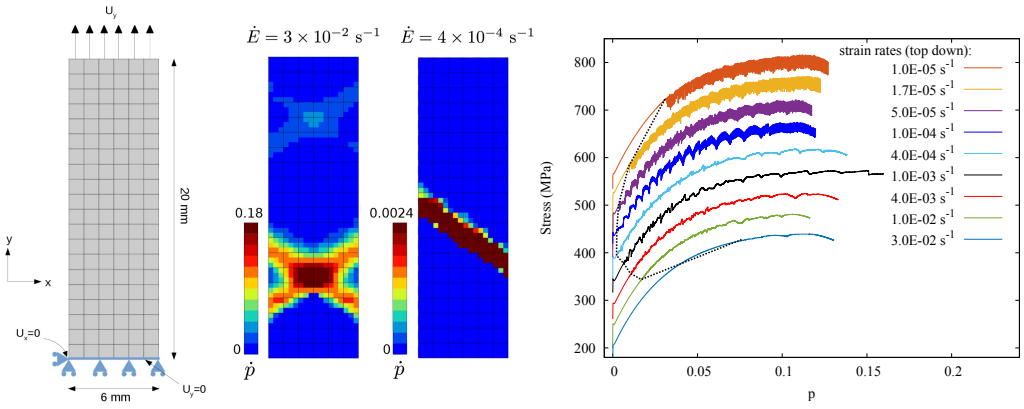

(a) (b)

Figure 3.9 – (a) Finite element mesh of a 2D plate; plastic strain rate bands for several prescribed strain rates. (b) Stress-strain curves over a large range of strain rates obtained by FEM simulations (plane stress) using the parameters identified at T= 200°C. The successive curves are shifted by 40 MPa for better illustration.

rate (see e.g. [Fu et al., 2012; Dierke et al., 2007]). A U-shape curve can be observed if the first significant stress drop is considered to estimate the critical strain (see dashed line in Fig. 3.9 (b)). The U-shape curve shows that the unstable zone only occurs within a certain range of strain rates at a given temperature. In fact, this phenomenon is well–known and has been already discussed in some experimental [Fu et al., 2012] or numerical [Mazière and Dierke, 2012] papers. In the following section, a numerical study on the critical strain of the current model will be presented following the method proposed in Mazière and Dierke [2012].

2D simulations are known to be prone to strain localization so that more realistic 3D simulations are necessary for the validation. Such 3D simulations are carried out on round tensile specimens at T= 200°C. The specimen is meshed with quadratic brick elements with reduced integration. The specimen geometry and boundary conditions are shown in Fig. 3.10 (a). Simulations are conducted under two different macroscopic strain rates $\dot{E} = 10^{-4}$ s^{-1} and $\dot{E} = 10^{-2}$ s^{-1}. For the simulation at strain rate $\dot{E} = 10^{-4}$ s^{-1}, inclined plastic strain rate $\dot{p}$ bands are observed while conical ones are found at a higher strain rate $\dot{E} = 10^{-2}$ s^{-1}. The rotation of slant bands travelling along the gauge length is a typical phenomenon (see Fig. 3.10 (b)) observed in cylindrical specimens in the simulations. This effect may explain the spiral (double) shear lips found on the fracture surface [Verma et al., 2015]. The FEM tensile curve at $\dot{E} = 10^{-2}$ s^{-1}, together with the experimental curve, is plotted in Fig. 3.10 (c). A good agreement with the experimental one is found.

According to [Marais et al., 2012], a small perturbation of the boundary conditions can lead to a symmetry-breaking mode. This has been tested in the present study. A small transverse displacement $U_x = 0.1$ mm along x-axis is applied to the upper surface of the cylindrical specimen. Fig. 3.11 displays both Lüders and PLC localization bands as shown by the plastic strain rate field $\dot{p}$ obtained at an overall strain rate $\dot{E} = 10^{-2}$ s^{-1}. The double Lüders bands formed at the plateau exhibit a conical shape in the absence of any perturbation (see Fig. 3.11 (a)). In contrast, the symmetry of Lüders bands is easily broken by the presence of a very small perturbation, as shown in Fig. 3.11 (b). The PLC bands, however, remain conical (Fig. 3.11 (c)). In addition, the mesh effect is apparent: The band width is approximately that of one layer of elements. A regularization procedure should be used in future work [Mazière and Forest, 2015; Mazière et al., 2017].

Fig. 3.12 shows the spatio-temporal graphs corresponding to the 3D simulations pre-

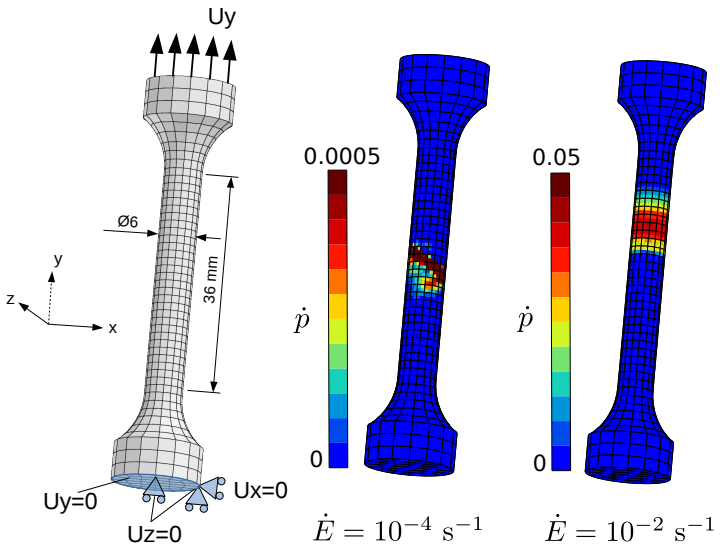

(a)

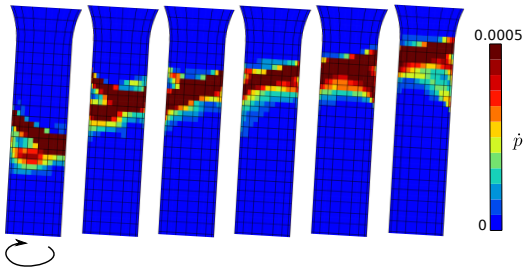

(b)

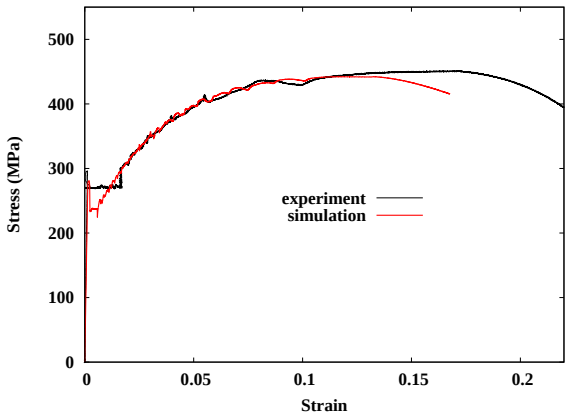

(c)

Figure 3.10 – (a) Mesh of a 3D round tensile specimen simulated at T= 200°C: strain rate $\dot{p}$ bands at two different applied macroscopic strain rates ($\dot{E} = 10^{-4}$ and $\dot{E} = 10^{-2}$ s^{-1}); (b) Band rotation at strain rate $\dot{E} = 10^{-4}$ s^{-1}; (c) Comparison of the tensile curves at $\dot{E} = 10^{-2}$ s^{-1}.

sented in Fig. 3.10. This method allows to describe the location of bands at different stages of the test. The idea is to put a line (Y-line) along the gage area to measure the strain rate over the whole deformation process (see Fig. 3.10(a)). The colour contour is a measure of the ratio between measured and applied strain rates. It can be noted that the bands at $\dot{E} = 10^{-2}$ s^{-1} are typical type A bands. At $\dot{E} = 10^{-2}$ s^{-1}, type B bands are obtained.

It can also be noticed that the critical strain obtained by 3D simulations is different from 2D ones. The 2D simulations are performed on a perfect rectangular plate. In contrast, 3D simulations are performed on a 3D round bar specimen with shoulders and

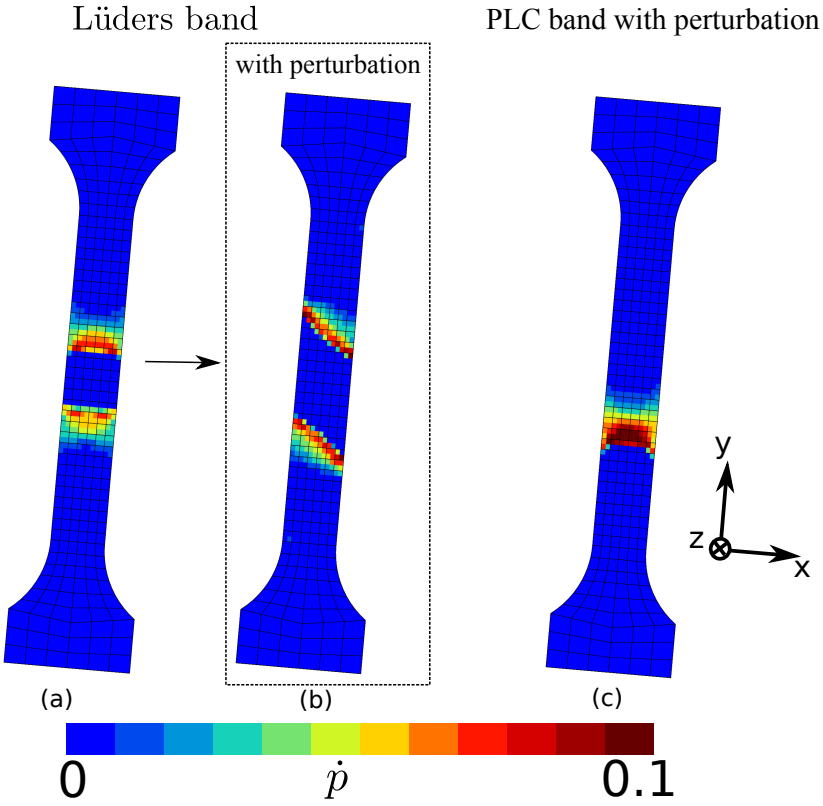

Figure 3.11 – Simulations of plastic strain rate bands at macroscopic strain rate $\dot{E} = 10^{-2}$ s^{-1} (view of the internal half plane cutting the round bar): (a) Conical Lüders band without perturbation of the boundary conditions; (b) Slant Lüders band when a small perturbation is applied in the x direction; (c) Conical PLC bands when a small perturbation is applied.

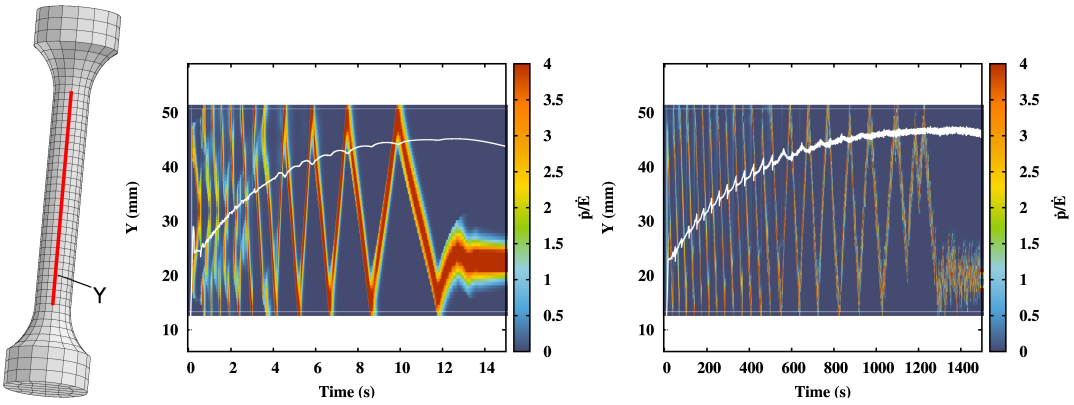

(a) Line Y (b) $\dot{E} = 10^{-2}$ s^{-1} (c) $\dot{E} = 10^{-4}$ s^{-1}

Figure 3.12 – The spatio-temporal graphs corresponding to the simulation at strain rate $\dot{E} = 10^{-2}$ s^{-1} and $\dot{E} = 10^{-4}$ s^{-1}.

heads. Simulations and experimental results show that the initiation of instabilities are usually located in the shoulders. This could explain the earlier triggering of PLC effect in 3D simulations. As shown in Fig. 3.13, the critical strain using an ideal cylindrical bar appears later than that obtained by a round bar specimen with shoulders.

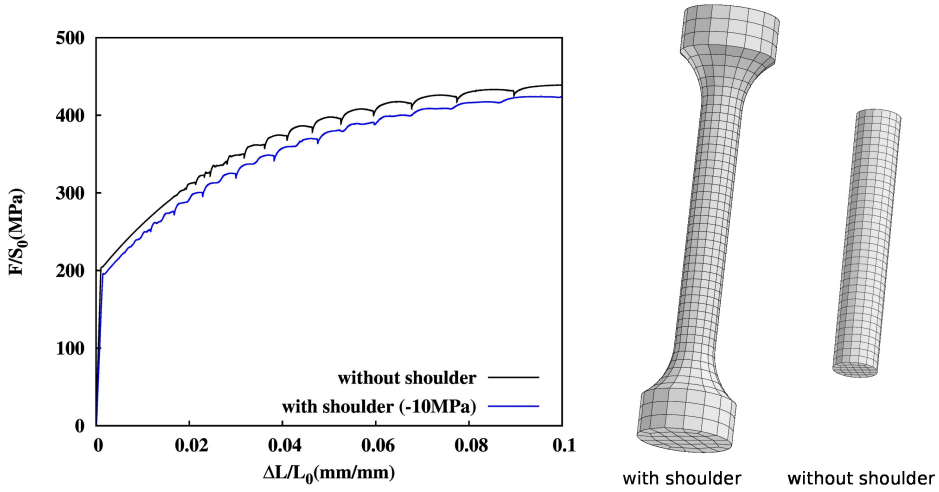

Figure 3.13 – 3D simulations using a cylindrical bar and a round bar specimen with shoulders at the same strain rate $\dot{E} = 10^{-2}$ s^{-1}.

3.5 Perturbation analysis for the prediction of the critical strain

The prediction of the occurrence of plastic instabilities is a complex task and a very important issue for better calibrating the constitutive model. In this section, a perturbation analysis is carried out for the stability analysis [Mazière and Dierke, 2012]. The basic idea of perturbation analysis is to introduce an infinitesimal perturbation $\{\delta p(t), \delta t_a(t), \delta\sigma(t), \delta\rho(t)\}$ to the initially homogeneous solution at a given state of the internal variables $\{p(t), t_a(t), \sigma(t), \rho(t)\}$. Here, the variables are evaluated at one material point. Only the temporal variation is taken into account. If the perturbation is found to increase at a given state, the instability could occur.

3.5.1 Theoretical analysis

Two assumptions are made here. Firstly, considering a uniaxial tensile state, the only non zero component of the stress tensor is then the tensile stress:

$$\sigma = R(\rho) + R_v(\dot{p}) + R_a(t_a). \tag{3.11}$$

The perturbation of stress can then be represented as:

$$\delta\sigma = \frac{dR}{d\rho}\delta\rho + \frac{dR_v}{d\dot{p}}\delta\dot{p} + \frac{dR_a}{dt_a}\delta t_a. \tag{3.12}$$

Considering equation (3.7), we have

$$\delta\dot{t}_a = -\frac{1}{w}t_a\delta\dot{p} - \frac{1}{w}\dot{p}\delta t_a. \tag{3.13}$$

For displacement-controlled tests, the elongation of specimens increases at a constant prescribed strain rate $\dot{E}_{tot}$. This strain rate will not be influenced by perturbation in the analysis. The nominal stress induced by the external axial force F_{ext} reads

$$\sigma_N = \frac{F_{ext}}{A}, \tag{3.14}$$

where the force F_{ext} is not influenced by the perturbation ($\delta F_{ext} = 0$; $\delta\sigma_N = 0$) [Zaiser and Hähner, 1997]. Assuming that material volume remains constant, the true stress is related to nominal stress by relation

$$\sigma = \sigma_N(1+\varepsilon_N), \tag{3.15}$$

where ε_N is the nominal strain and σ_N is the nominal stress. Neglecting elastic strain, the true strain (plastic) reads

$$p = \ln(1+\varepsilon_N), \quad \varepsilon_N = \exp(p) - 1 \tag{3.16}$$

Thus, considering plastic incompressibility and the uniformity of the axial load along the tensile specimen axis, we have the relation

$$\delta\sigma = \delta\sigma_N \exp(p) + \sigma\delta p = \sigma\delta p \tag{3.17}$$

It should be pointed out that, for small strain formulations (difference between Cauchy and nominal stresses is not accounted), we have $\delta\sigma = 0$ for Eq. 3.17. Eq. 3.17 can then be substituted into Eq.(3.12).

$$\delta\dot{p} = \frac{1}{dR_v/d\dot{p}}(\sigma\delta p - \frac{dR}{d\rho}\delta\rho - \frac{dR_a}{dt_a}\delta t_a). \tag{3.18}$$

By introducing Eq.(3.18) into Eq.(3.13), the perturbation of the rate of ageing time reads

$$\delta\dot{t}_a = -\frac{t_a}{w}\frac{1}{dR_v/d\dot{p}}\sigma\delta p + \frac{t_a}{w}\frac{1}{dR_v/d\dot{p}}\frac{dR}{d\rho}\delta\rho + (\frac{t_a}{w}\frac{1}{dR_v/d\dot{p}}\frac{dR_a}{dt_a} - \frac{\dot{p}}{w})\delta t_a \tag{3.19}$$

The perturbation of the dislocation density rate is

$$\delta\dot{\rho} = [a_0\sqrt{\rho} - b_0(1-\zeta\phi)\rho]\delta\dot{p} + \dot{p}(\frac{a_0}{2}\frac{1}{\sqrt{\rho}}\delta\rho - b_0\delta\rho + b_0\zeta\phi\delta\rho + b_0\zeta\rho\delta\phi) \tag{3.20}$$

$$= \frac{\partial\rho}{\partial p}\frac{1}{dR_v/d\dot{p}}\sigma\delta p + (\dot{p}\frac{a_0}{2}\frac{1}{\sqrt{\rho}} - \dot{p}b_0 + \dot{p}b_0\zeta\phi - \frac{\partial\rho}{\partial p}\frac{1}{dR_v/d\dot{p}}\frac{dR}{d\rho})\delta\rho \tag{3.21}$$

$$+[\frac{\dot{p}b_0\zeta\rho n}{t_0}(\frac{t_a}{t_0})^{n-1}e^{-(\frac{t_a}{t_0})^n} - \frac{\partial\rho}{\partial p}\frac{1}{dR_v/d\dot{p}}\frac{dR_a}{dt_a}]\delta t_a \tag{3.22}$$

We first put these relations in matrix form

$$\begin{bmatrix}\delta\dot{p}\\ \delta\dot{t}_a\\ \delta\dot{\rho}\end{bmatrix} = [\mathbf{M}]\begin{bmatrix}\delta p\\ \delta t_a\\ \delta\rho\end{bmatrix} \tag{3.23}$$

where

$$[\mathbf{M}] = \frac{1}{dR_v/d\dot{p}}\begin{bmatrix}\sigma & -\frac{dR_a}{dt_a} & -\frac{dR}{d\rho}\\ -\frac{t_a}{w}\sigma & \frac{t_a}{w}\frac{dR_a}{dt_a} - \frac{\dot{p}}{w}\frac{dR_v}{d\dot{p}} & \frac{t_a}{w}\frac{dR}{d\rho}\\ \frac{\partial\rho}{\partial p}\sigma & \frac{dR_v}{d\dot{p}}\frac{\dot{p}b_0\zeta\rho n}{t_0}(\frac{t_a}{t_0})^{n-1}e^{-(\frac{t_a}{t_0})^n} - \frac{\partial\rho}{\partial p}\frac{dR_a}{dt_a} & \dot{p}[\frac{a_0}{2\sqrt{\rho}} + b_0(\zeta\phi-1)]\frac{dR_v}{d\dot{p}} - \frac{\partial\rho}{\partial p}\frac{dR}{d\rho}\end{bmatrix} \tag{3.24}$$

is the matrix, linking the perturbation of internal variables and the perturbation of their rates, noted as the transfer matrix **M**. Following elements are necessary for numerical development

$$\frac{dR_v}{d\dot{p}} = \frac{k_BT}{V_a}\frac{\exp(E_a/k_BT)}{\sqrt{\dot{\varepsilon}_0^2 + (\exp(E_a/k_BT)\dot{p})^2}}. \tag{3.25}$$

$$\frac{dR_a}{dt_a} = P_1 \frac{d\phi}{dt_a}, \quad \frac{d\phi}{dt_a} = \frac{n}{t_0} \exp\left(-\left(\frac{t_a}{t_0}\right)^n\right)\left(\frac{t_a}{t_0}\right)^{n-1} \tag{3.26}$$

$$\frac{dR}{d\rho} = \frac{\gamma \mu b}{2\sqrt{\rho}}. \tag{3.27}$$

$$\frac{d\rho}{dp} = a_0\sqrt{\rho} - b_0(1-\zeta\phi)\rho. \tag{3.28}$$

For matrix (3.24), there exists at least one real eigenvalue (L_1) and a complex conjugate pair of eigenvalues (L_2 and L_3) or three real eigenvalues. Fig. 3.14 gives an example of the evolution of eigenvalues.

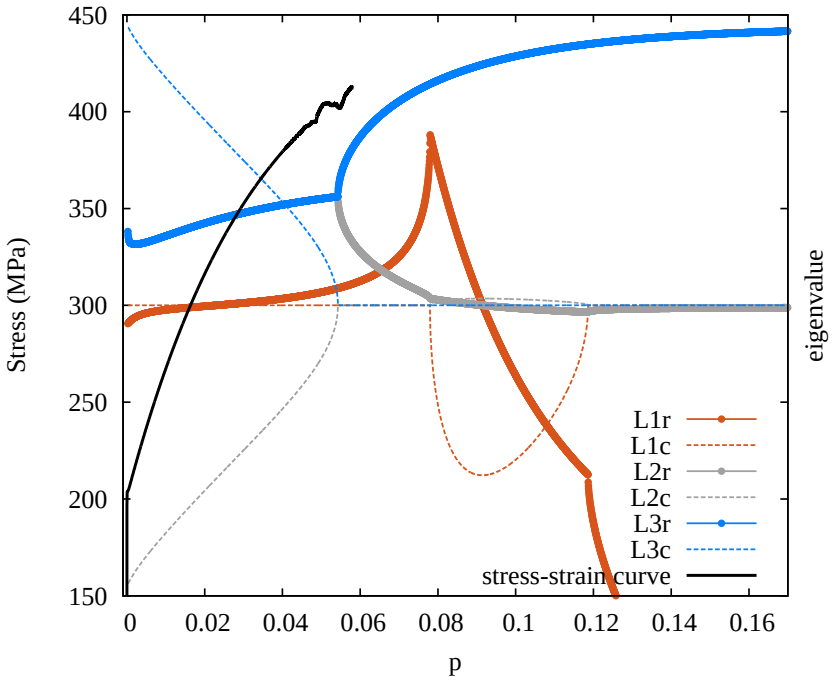

Figure 3.14 – Evolution of eigenvalues as a function of plastic strain. There are two conjugate complex eigenvalues: L1 is the non-conjugate eigenvalue; L2 and L3 are conjugate eigenvalues. “r”denotes the real part of an eigenvalue. “c”denotes the complex part of an eigenvalue. there are three real eigenvalues: they are sorted from least to greatest.

For a model with 2 internal variables, the 2×2 matrix analysis leads to 3 criteria that have been discussed in [Mazière and Dierke, 2012]. The first one is based on the negative strain rate sensitivity which is generally not sufficient to detect the occurrence of PLC effect. The second criterion corresponds to the case when the real part of one eigenvalue is positive. It means that the perturbation may follow a growing oscillating evolution. The third criterion assumes a real and positive eigenvalue which ensure an exponential growth of perturbation. This criterion is the most adequate one [Mazière and Dierke, 2012]. In the current case, the matrix becomes 3×3 since 3 internal variables (p, t_a, ρ) are accounted for. We test the validity of these criteria and compare with 2D finite element simulations in the next part.

3.5.2 Numerical study to validate the theoretical criterion

In the experiments of the current C-Mn steel, the PLC instability is usually triggered very early and has been hidden in the Lüders plateau. For numerical simulations, we killed artificially the Lüders plateau in order to better identify the critical strain for the onset of PLC effect and verify the theoretical criterion. A 2D rectangular plate with dimensions of 6 mm× 20 mm is used for uni-axial tension simulation. The prescribed displacement boundary condition is applied on the upper side of the plate (see Fig. 3.9(a)). The lower boundary is restricted. The following aspects for detecting the critical plastic strain is

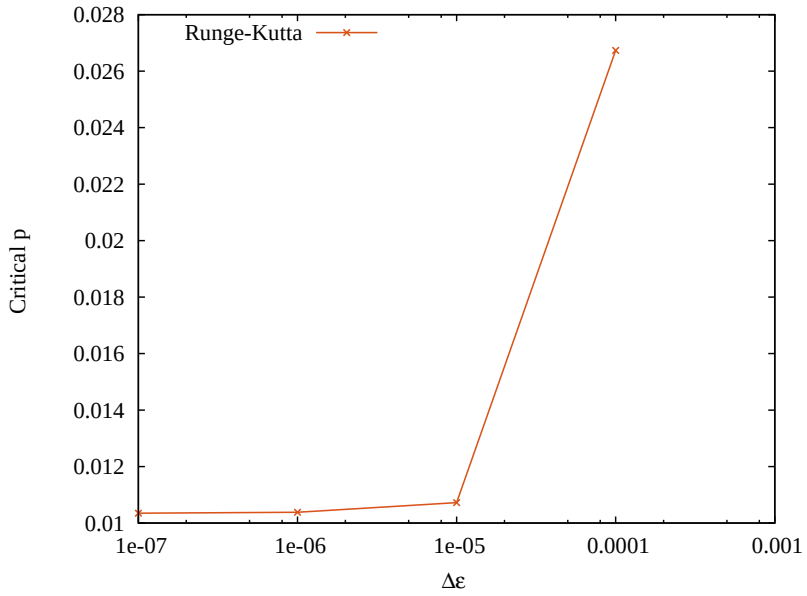

Figure 3.15 – Critical strain obtained by using different strain increments with Runge-Kutta method tested at the strain rate $10^{-3}\,s^{-1}$.

addressed here:

(1) The control of strain increment.

In the current numerical procedure, a maximal allowed strain increment $\Delta\varepsilon$ for each time stepping is applied. Fig. 3.15 shows the variation of critical strains by using different values of $\Delta\varepsilon$. The critical strain tends to stabilise along with the decrease of $\Delta\varepsilon$ value. Values below $\Delta\varepsilon = 10^{-5}$ are adopted for the following simulations for which the accuracy is sufficient.

(2) The criterion for determining the numerical critical strain of PLC effect.

For determining the numerical critical strain of PLC effect, a criterion should be set. The criterion could be built by taking the first stress drop on the stress strain curve. However, the detection could be delayed at high strain rate cases, where the magnitude of oscillations is smaller than that at lower strain rate and the stress keeps growing despite the appearance of oscillations. Here, we use a criterion based on the heterogeneity of strain rate fields. Fig. 3.16 gives the strain rate fields when the maximal strain rate value reach $2 \times \dot{E}$, $5 \times \dot{E}$ and $8 \times \dot{E}$. Indeed, the heterogeneity appears slightly earlier than stress drop (see the case criteria=$2 \times \dot{E}$). We choose the $5 \times \dot{E}$ as the local criterion which seems to be consistent with stress drop criterion but also applicable for high strain rate cases.

Fig. 3.9 shows 10 stress-strain curves simulated at 200 °C with different strain rates in the range between $1 \times 10^{-5}\,s^{-1}$ and $3 \times 10^{-2}\,s^{-1}$. The critical plastic strain extracted using

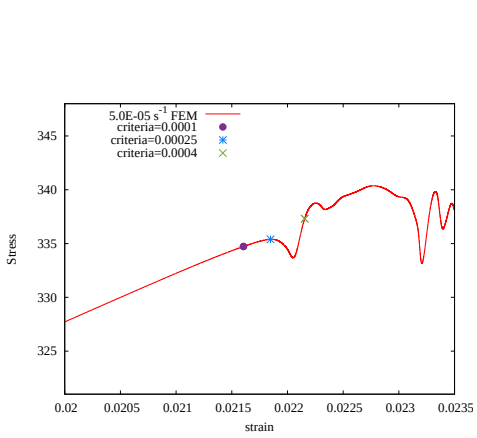

(a) Positions of 3 detected points according to different criteria.

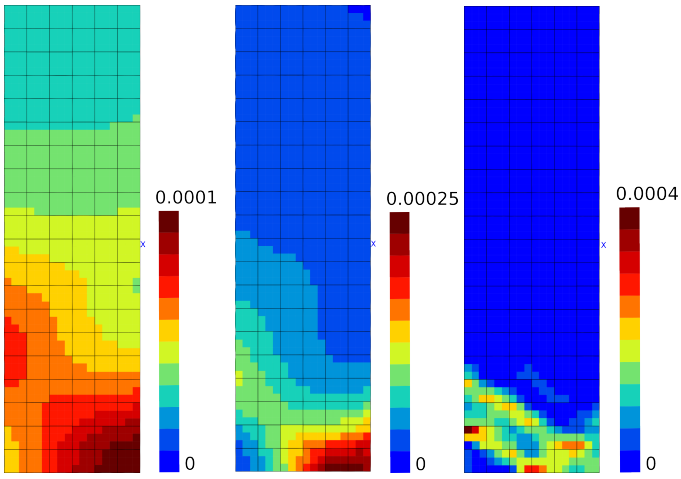

(b) criteria= $2 \times \dot{E}$ (c) criteria= $5 \times \dot{E}$ (d) criteria= $8 \times \dot{E}$

Figure 3.16 – Detection of heterogeneity as the critical sign for the onset of instabilities. Simulations performed at strain rate =5×10^{-5} s^{-1}.

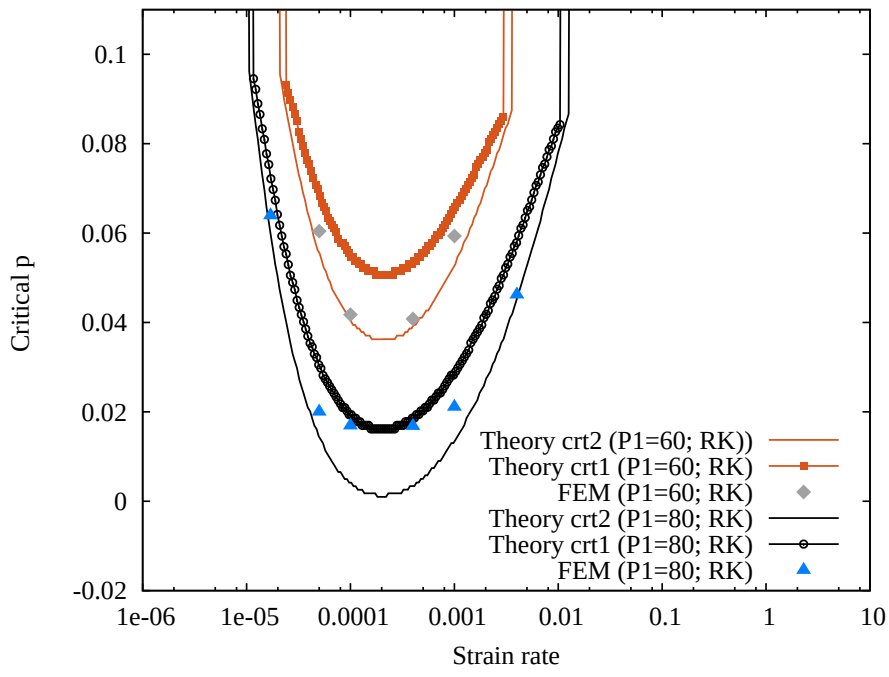

Figure 3.17 – Critical strain determined by FEM simulations and perturbation analysis for two different values of P_1.

local heterogeneity criterion applied on a 2D plate mesh and using theoretical criterion are plotted on Fig. 3.17. We found two possible criteria relevant for the prediction of critical strain (see Fig. 3.14).

- The first criterion (crt1) is activated when all the eigenvalues are real and positive (L1r > 0 and L1c = 0; L2r > 0 and L2c = 0; L3r > 0 and L3c = 0).

- The second criterion (crt2) corresponds to the case the matrix **M** has one real and positive eigenvalue and two complex conjugate eigenvalues with positive real parts.

In addition, the absolute value of the real part is larger than the absolute value of the complex part (L1r > 0 and L1c = 0; L2r = L3r > |L2c| = |L3c|).

As shown in Fig. 3.17, the critical strain obtained by FEM falls between these two criteria. This result is validated with two different values of P_1. The criterion 1 can be refereed to as the exponential growth criterion reported in [Mazière and Dierke, 2012] which gives a slightly higher prediction of critical strain than FEM for the current case. The oscillating criterion 2 with two complex eigenvalues gives a lower value than FEM. The gap between these two criteria seems to be an unstable zone for the growth of perturbation in which PLC effect can be triggered at any time.

Effect of parameters

The influence of parameters on the variation of critical strain is presented in Fig. 3.18. When P_1 decreases, the onset of instabilities is delayed (see Fig. 3.18(a)). At the same time, the U-shape curve decreases for large value of P_1. Fig. 3.18(b) shows the U-shape curves obtained with different values of n. A larger n value will lead to earlier onset of PLC effect and narrow the sensitive zone. Fig. 3.18(c) demonstrates that a larger w will shift the position of sensitive zone toward high strain rate and delay the onset of PLC effect. These parameters could be identified by fitting with experimental critical strains detected from digital image correlation pattern using heterogeneity criteria.

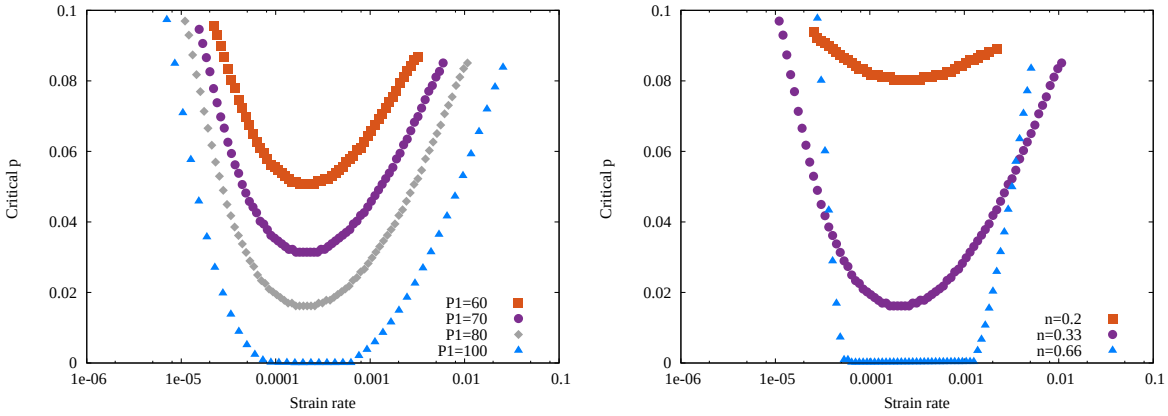

(a) P_1 (b) n

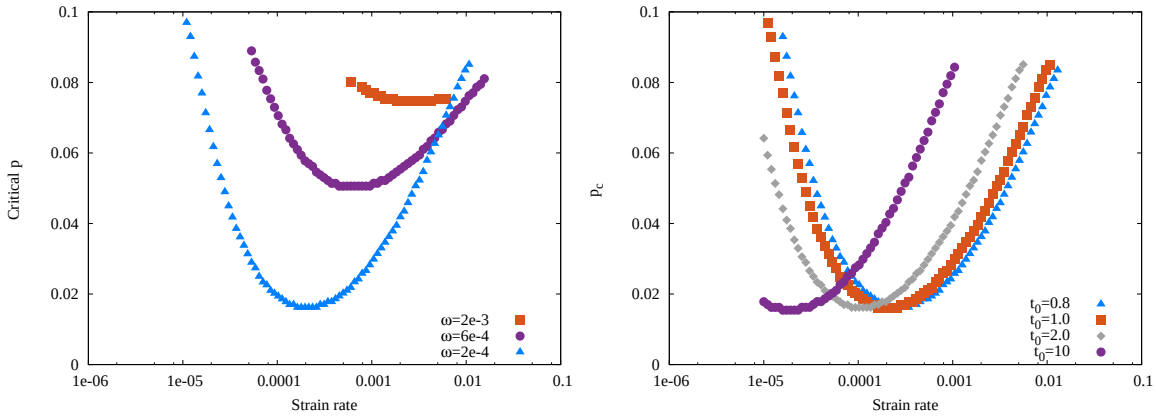

(c) ω (d) t_0

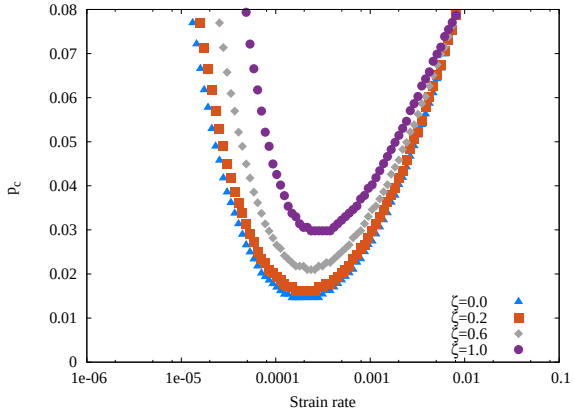

(e) ζ

Figure 3.18 – Parameter effect on the evolution of critical strains.

3.6 Conclusions

In this work, a dislocation density based modified Kubin-Estrin-McCormick (KEMC) model has been proposed in order to better describe the interaction between strain hardening and strain ageing phenomena. The coupling between dynamic strain ageing and strain hardening is accounted for by introducing a limitation of the dynamic recovery process due to DSA. This modification allows to increase the hardening rate in the temperature and strain rate domain where the pinning of dislocations by solute atoms is the most active i.e. for low strain rates or high temperatures. The cost for the introduction of this coupling is rather low since it requires no additional internal variable and only one additional material parameter ζ.

The new model formulation has been identified using material point simulations for a C-Mn steel over a large range of temperatures and strain rates. Results show a significant improvement on the description of hardening with respect to previous identifications. Serrations on the stress/strain curves as well as the associated plastic strain rate localization bands have been reproduced and illustrated using 2D and 3D finite element simulations. One major advantage of the proposed model compared to previous formulations including the evolution of various types of dislocation densities (e.g., [Fressengeas et al., 2005; Gupta et al., 2017]) is its relative simplicity allowing for structural engineering finite element computations to be performed, as demonstrated by the 3D simulations in the present work. Furthermore, the limitation of the current model might be its ability to simulate complex thermo-mechanical paths like combinations of heat treatment and tension/compression/relaxation/creep loadings. In those cases, the more sophisticated model [Fressengeas et al., 2005; Gupta et al., 2017] might give more realistic results.

The modified model has been tested on a C-Mn steel for which the proposed interaction between dynamic strain ageing and strain hardening is clearly visible. The perturbation analysis is performed and gives a prediction of the critical strain in uni-axial tension without strain rate change. The same work could be applied to some nickel based superalloys [Max et al., 2014] and some Al-Mg aluminium alloys [Halim et al., 2007] since the features of DSA and the Portevin - Le Chatelier effect are very similar. It would probably be more difficult for certain aluminium alloys, such as 2000 series Al-Cu and Al-Cu-Li alloys, for which the negative strain rate sensitivity is not very pronounced and some other phenomena than DSA can be responsible for serrated yielding [Brechet and Estrin, 1994].

Concerning C-Mn steels, the accuracy of the model could be tested using more advanced experimental devices like digital image correlation, or digital image thermography, combined with a statistical analysis of stress drops. Such experimental information could then be compared with the results of finite element simulations. Finally it would be relevant to use the modified model in order to investigate the failure of C-Mn steel in the DSA domain and particularly the loss of ductility that is observed in this domain [Belotteau et al., 2009; Wang et al., 2012].

Chapter 4

Study of the PLC effect in Al-Cu and Al-Cu-Li alloys

Summary

Serrated flow is observed during non monotonic tensile tests for Al-Cu (AA2139-T3) and Al-Cu-Li (AA2198-T3R) alloys in naturally aged state. The associated propagative localization bands are observed by digital image correlation (DIC). In particular, the triggering of Portevin-Le Chatelier (PLC) effect and also Lüders bands are observed for interrupted tests with holding time and also for tests with partial unloading and holding. Strain rate jumps also trigger localization bands. These observations indicate the existence of the PLC effect in these materials which were formerly considered insensitive to it at room temperature. Indeed, no evidence of PLC effect is found during constant strain rate tests for the tested AA2139-T3 alloy. The premature triggering of localization is observed in both AA2139-T3 and AA2198-T3R alloys compared to their counterparts under constant strain rate conditions. A strain ageing finite element model is used and it captures the experimentally found PLC triggering effects.

Résumé

Des oscillations ont été observées lors des essais de traction non monotones pour les alliages Al-Cu (AA2139-T3) et Al-Cu-Li (AA2198-T3R) dans l'état de vieillissement naturel. Les bandes de localisation propagatives associées sont observées par corrélation d'images (DIC). Le déclenchement des effets Portevin-Le Chatelier et Lüders est observé en particulier pendant les essais de relaxation avec un temps de maintien et aussi pour ceux avec un déchargement. Les sauts de vitesse déclenchent également les bandes de localisation. Ces observations indiquent l'existence de l'effet PLC auquel ces matériaux étaient auparavant considérés comme insensibles à température ambiante. En effet, l'effet PLC n'a pas été observé lors des essais de traction à vitesse de déformation constante pour l'alliage AA2139-T3. Le déclenchement prématuré de la localisation est observé dans les alliages AA2139-T3 et AA2198-T3R par rapport à leurs homologues dans des conditions de vitesse constante. Les simulations par éléments finis avec un modèle de vieillissement par déformation ont réussi à reproduire le déclenchement prématuré trouvé pendant les essais.

Contents

4.1 Digital Image Correlation (DIC) measurement

4.1.1 Experimental set-up

All the experimental results presented in this chapter are conducted on a MTS-10t servo-hydraulic tensile machine. The load cell measuring range is 0–100 kN. In the current experimental set up, the hydraulic grip has been used. The extensometer (MTS634.12F-21) with an initial gage length of 25 mm was used to record the displacement in the longitudinal direction only for the fist monotonic tensile test at each strain rate. It has then been removed for the other tests in order to obtain a large exposed area for DIC measurement. Those tensile specimens have been slightly polished before painting in order to achieve a better adhesion property of paint.

The set-up of the DIC system is illustrated in Fig. 4.1. The tensile machine output including force and displacement is synchronised on PC1 with camera signals which allows to precisely record the displacement state corresponding to each image. Several major features of the current DIC system are listed below:

- Dual camera system: 4.1 Mpixels each (Manta G419)
- Maximum frequency of acquisition: 27 images/second for high resolution images
- Correlation software Vic-3D

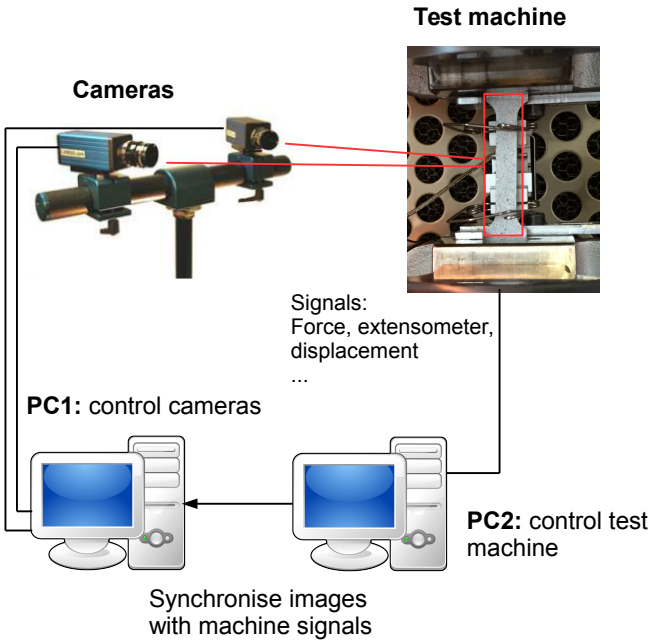

Figure 4.1 – Schematic diagram of DIC system.

4.1.2 Principle of Digital Image Correlation (DIC)

The digital image correlation method (DIC) is a non-contact optical technique to calculate surface displacement and surface strain field. Subset-based DIC (local DIC)[Sutton et al., 1991] and finite element-based DIC (global DIC)[Hild and Roux, 2006] are the two most commonly used DIC algorithms. Global DIC may lead to better displacement results due to the displacement continuity assumption [Hild and Roux, 2012]. In contrast,

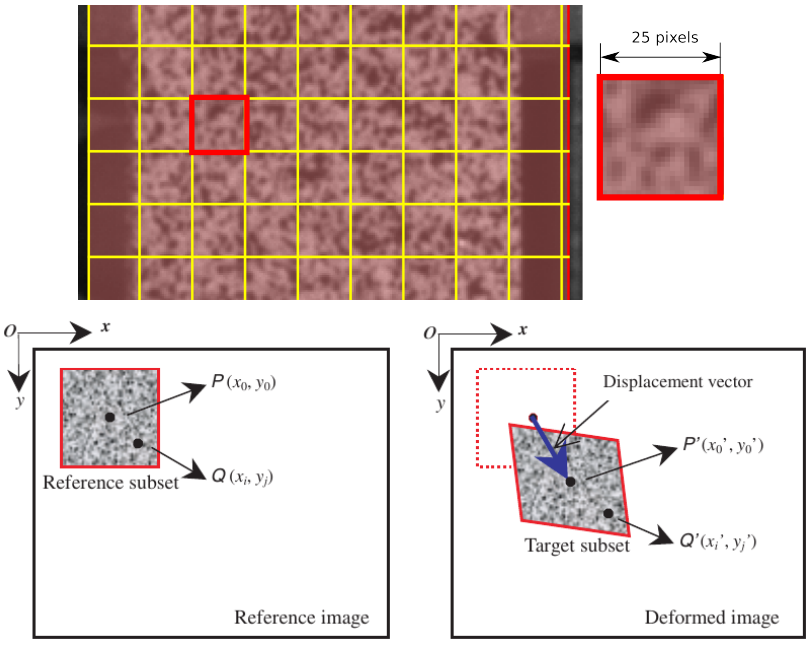

Figure 4.2 – A selected virtual subset with a size of 25×25 pixels in Vic-3D; Schematic figure of reference and deformed subsets in DIC [Pan et al., 2009].

Wang and Pan [2016] also claim that the local DIC offers better displacement precision and higher efficiency. In local DIC, adjacent subsets are analysed independently without imposed continuity conditions a priori, thus resulting in separate or overlapping of deformed subsets. Global DIC tracks the position of all the nodes (i.e., calculation points) simultaneously, thus being able to evaluate the entire displacement field at a time with the explicitly ensured displacement continuity among elements.

As the current Vic-3D software uses a subset-based local DIC algorithm, the basic principles of local DIC is recalled in this section. At first we need random patterns on the specimen surface to obtain the full-field surface displacements by matching the subsets of interest before and after deformation. A subset is a collection of pixel values containing a signature (grayscale pattern) to be tracked in the deformed image. An algorithm will search the subset which has a maximum similarity, which is usually evaluated by a predefined criterion, with the original subset in the reference image. To make a unique signature, a random speckle pattern has to be applied such as handily performed spray painting on the specimen surface. As shown in Fig. 4.2, the differences of the positions of the reference subset centre and the target subset centre yield the displacement vector (u and v) at centre point $P(x_0, y_0)$.

The sum of squared differences (SSD) correlation criteria used to evaluate the similarity degree takes the following form:

$$C_{SSD} = \sum_{i,j=-n/2}^{n/2} \left[f(x_i, y_j) - g(x'_i, y'_j) \right]^2 \tag{4.1}$$

where n is the subset size. i, j is the pixel number. $f(x_i, y_j)$ is the grayscale intensity value at pixel (x_i, y_j) in the reference image, and $g(x'_i, y'_j)$ is the grayscale intensity value at pixel (x'_i, y'_j) in the deformed image. Other criteria of SSD family like the Normalized Sum of Squarred Differences (NSSD) and Zero-normalized Sum of squared Differences (ZNSSD) can also be selected in Vic-3D. In the current section, we use the NSSD criterion which has

taken into account the influence of illumination. The Cross-Correlation (CC) criterion is also widely used [Pan et al., 2009].

Once full-field displacements are got from the previous procedures, strain field is calculated by an algorithm similar to finite element method [Manual, 2010].

4.1.3 Subset and step size

To achieve a reliable correlation analysis in DIC, the size of a subset should be large enough so that there is a sufficient grayscale pattern information contained in the subset to distinguish itself from other subsets. On the other hand, however, a larger subset size leads to a reduction in the displacement spatial resolution (for the local method the spatial resolution corresponds to the subset size itself). The choosing of subset size is the result of a compromise. In the current version of Vic-3D, the recommended subset size is 21~29 pixels [Manual, 2010].

The step size controls the spacing of the points (subsets) that are analysed during correlation. If a step size of 1 is chosen, a correlation analysis is performed at every pixel inside the area-of-interest which is very time consuming without much gain. The overlapping subsets won't be independent of each subset. Step size of 1 would significantly increase processing time while typically providing little to no gain. To get independent and non-repetitive data, the recommended step size in Vic-3D is roughly 1/3~1/4 of the subset size.

4.1.4 2D and 3D correlation

There are two major drawbacks of 2D correlation. First, the specimen must be planar or nearly planar. Secondly no motions are allowed in the direction perpendicular to the specimen. The 3D correlation shares similar tracking principle with 2D correlation, while the use of stereovision allows it to obtain 3D field measurement and overcome the drawbacks of 2D correlation. In 3D correlation, subsets are selected in one camera as the reference and compared to subsets in the deformed image pairs to extract the matching image positions. Then, triangulation is performed between the matching subset centers in both cameras using the calibrated camera parameters to locate the 3D spatial position of the object point [Sutton, 2013].

4.1.5 Estimate measurement uncertainty

By correlating two repeatedly acquired images without any rigid body motion, the measurement uncertainty of the calibrated DIC system in terms of strain can be determined. As can be seen in Fig. 4.3 the strain resolution is around $\varepsilon_{yy} = 0.0003$. The scale of this noise does not vary much for a good calibration. This means that the minimum $\Delta\varepsilon$ between the reference image and the current image should be larger than 0.0003. When performing incremental correlations, the interval time Δt should be large enough.

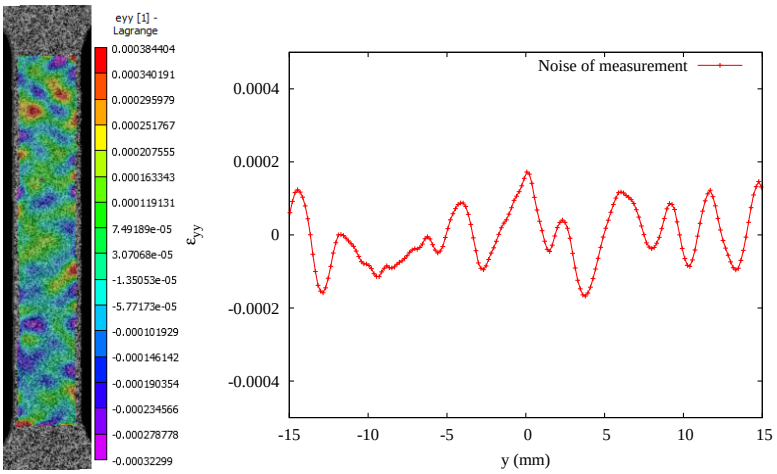

Figure 4.3 – Estimation of measurement uncertainty.

4.2 PLC effect in AA2139-T3 alloy

This section is reproduced from: Ren, S.C., Morgeneyer, T. F., Mazière, M., Forest, S & Rousselier G. (2017). Portevin-Le Chatelier effect triggered by complex loading paths in an Al-Cu aluminium alloy. *To be submitted.*

4.2.1 Introduction

In addition to the characterizations of the PLC effect in terms of the nSRS and serrations, the critical strain for the occurrence of PLC instabilities is another important feature. As far as diffusion of solutes is involved, there is a limited active zone of PLC effect within a certain range of temperature and strain rate. Many experimental observations about the onset of PLC instability are based on constant strain rate tensile tests [Dierke et al., 2007; Fu et al., 2012]. It seems that only a few emphases have been laid on the influence of interruptions on the triggering of PLC effect [Balík et al., 2000; Allain et al., 2011]. However for those studies, the materials (Al-3Mg [Balík et al., 2000] and FeMcC [Allain et al., 2011]) are all very sensitive to PLC instabilities in monotonic tensile tests. A recent work [Gupta et al., 2017] reported the occurrence of Lüders effect after strain rate change on the AA2024 aluminium alloy which does not show highly serrated flow for monotonic tests according to the authors. The triggering effect of the PLC effect by relaxation has also been reported for the AA2024 alloy in [Leacock et al., 2007]. However, the 2024 alloy is different from the industrial alloy addressed in our work. The PLC effect in AA2024 alloy has been widely reported in the literature even for constant strain rate tests such as in [Böhlke et al., 2009]. The tensile test curves of the constant strain rate tests presented in [Leacock et al., 2007] already displayed slight oscillations.

For an Al-Mg alloy that does show PLC effects during constant strain rate tests, it could be shown that the critical strain to trigger the PLC effect can be influenced by prestraining and aging [Balík et al., 2000]. In PLC sensitive FeMnC austenitic steel the critical strain for PLC could be reduced by stress relaxation tests [Allain et al., 2011].

The current work is also motivated by an earlier work on strain intermittency and the presence of multiple strain localization bands in the material bulk around the notch area of a compact tension-like specimen made of the material of the present study [Morgeneyer et al., 2016]. Strain localization and intermittent activity have also been found

for AA2198-T8R material in [Morgeneyer et al., 2014; Buljac et al., 2016] and AA2198-T3R [Buljac et al., 2017] via synchrotron 3D imaging combined with digital volume correlation. The aim of the present study is to gain insight on the origins of the strain intermittency in AA2139-T3. Constant strain rate tests and tests with complex strain rate evolutions are applied to the material to test its susceptibility to PLC effects. This may have important consequences for the understanding and improvement of the mechanical properties of such complex industrial alloys used for structural parts. A DSA model implemented in a finite element framework is used to try to capture the experimental findings.

4.2.2 Material and experimental methods

The tested material is taken from a 4.7 mm thick sheet of AA2139-T3 aluminium alloy (naturally aged). Copper (4.5 – 5.5 wt%) is the primary alloying element in this material. Smaller amount of other elements like Mg, Mn, Si, Fe, Ag, Ti and Zn are also involved (see Table 4.1). All the samples are cut from AA2139-T3 plates with longitudinal direction along the transverse direction (T). The dimension of the gage area is $4.7 \times 6 \times 32$ mm.

Table 4.1 – Chemical composition (wt%) of 2139 alloy.

Cu	Mg	Mn	Si	Fe	Ag	Ti	Zn
4.5-5.5	0.2-0.8	0.2-0.6	<=0.1	<=0.15	0.15-0.6	<=0.15	<=0.25

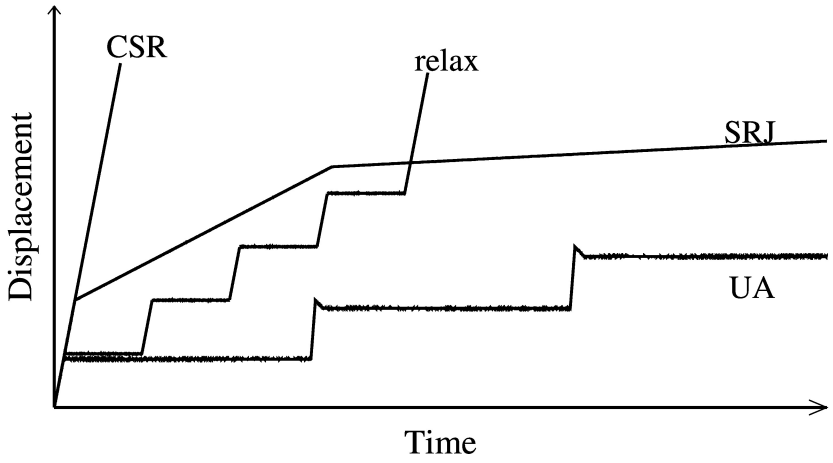

Figure 4.4 – Illustration of strain evolutions of complex loading tests realised in this work as function of time: constant strain rate test (CSR), relaxation test (relax), unloading ageing test (UA) and strain rate jump test (SRJ).

Tests are carried out using a 100 kN MTS machine under displacement control. All the tests are performed at room temperature. Four types of tensile tests are carried out:

1. Usual monotonic constant strain rate tests with prescribed strain rates of $10^{-5}\,s^{-1}$, $10^{-4}\,s^{-1}$, $10^{-3}\,s^{-1}$ and $10^{-2}\,s^{-1}$ (CSR).

2. Strain rate jump (SRJ) tests : increasing or decreasing strain rate at different strain levels.

3. Interrupted at 2%, 4%, 6%, and 8% with 15 seconds of relaxation.

4. Interrupted at 2%, 4%, 6%, and 8% with partial unloading and 120 seconds of ageing (UA).

A schematic diagram concerning the displacement evolution as a function of time for those different loading paths is shown in Fig. 4.4. In addition, a stereo-DIC system using two Manta G419 cameras (4.1 MPixels each) is synchronised with the tensile machine. The image sampling rate is 20 fps (frames per second) for the CSR and relaxation tests under bulk strain rate $10^{-2}\,s^{-1}$; 5 fps for the unloading test; 10 fps for $10^{-3}\,s^{-1}$ CSR; 0.5 fps for $10^{-4}\,s^{-1}$ CSR; 0.067 fps for $10^{-5}\,s^{-1}$ CSR. The sampling rate for the strain rate jump tests ranges from 0.1 to 10 fps. The heterogeneous strain measurement on the surface of the tested specimens was performed via a DIC software VIC-3D. In the current work, a proper subset size of 25×25 pixels is used to achieve an acceptable measurement error [Xu et al., 2015]. The calculation step size is 8 pixels. Using calibration target, the pixel resolution has been determined to be 34 µm/pixel.

4.2.3 Results of constant strain rate tests

The stress-strain curves of constant strain rate tests are plotted in Fig. 4.5(a). The strain rate sensitivity characterised by $m = \log(\sigma_i/\sigma_j)/\log(\dot{E}_i/\dot{E}_j)$ [Picu et al., 2005] , where σ_i and σ_j are the stress measured in tests under bulk strain rates $\dot{E}_i$ and $\dot{E}_j$, shows only a very slight negative strain rate sensitivity from strain 3% to 12%. All the constant strain rate curves are smooth. PLC related serrations are not observed. To better illustrate the evolution of PLC bands, a so called spatio-temporal pattern is used for describing the location of potential strain bands at different stages of experiments [Chmelík et al., 2002; Nogueira de Codes and Benallal, 2011]. A Y-line is positioned in the gage area to measure the incremental axial strain over the whole deformation process. The colour contour is a measure of the ratio between measured strain rate and applied macroscopic strain rate $\dot{\varepsilon}_{yy}/\dot{E}$, where $\dot{\varepsilon}_{yy} = \Delta\varepsilon_{yy}/\Delta t$ is calculated by correlating two successive images with a constant time interval Δt. The maximum ratio is chosen to be 4 as the computed strain rate inside a band is around 5 times of the applied strain rate according to DIC measurement. This result is rather close to that found in [Cai et al., 2016b].

The spatio-temporal pattern of the constant strain rate test at strain rate $10^{-2}\,s^{-1}$ is shown in Fig. 4.5(b). PLC bands were not observed. The absence of PLC effect has also been confirmed in the other 3 constant strain rate tests.

4.2.4 Triggering effect found in non-monotonic loading tests

The loading part of the tensile test interrupted by relaxation is conducted at strain rate $10^{-2}\,s^{-1}$. The stress-strain curve of this relaxation test is superposed with the corresponding constant strain rate curve at strain rate $10^{-2}\,s^{-1}$ in Fig. 4.6(a). Comparing the interrupted test with the constant strain rate curve, the current experimental data show very similar stress levels and ductility. The first stress relaxation was performed at strain = 0.02. When the specimen is re-loaded after 15 seconds of in-situ ageing by maintaining cross-head displacement, a sharp yield point is found. The following 3 relaxations were performed at strain = 0.04, 0.06 and 0.08. A static ageing type plateau appeared after each re-loading followed by PLC type serrations.

As shown in Fig. 4.6(b), the strain rate inside a band is higher than 4 times of applied strain rate. Two bands initiate at the two ends of the specimen after the second re-straining and propagate to the other side of the gage area forming a 'X' type pattern

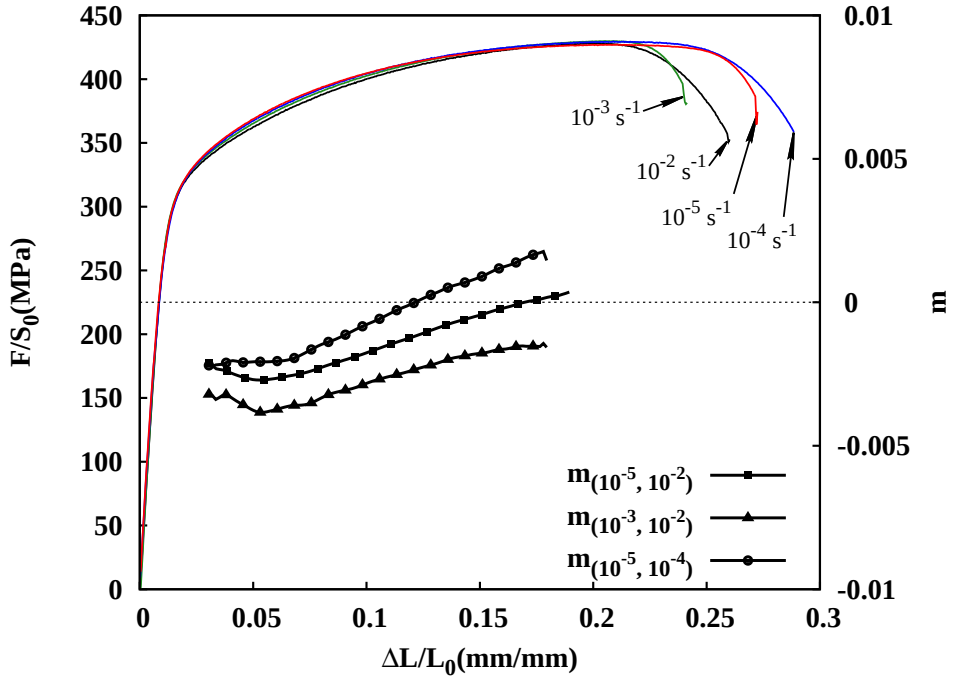

(a)

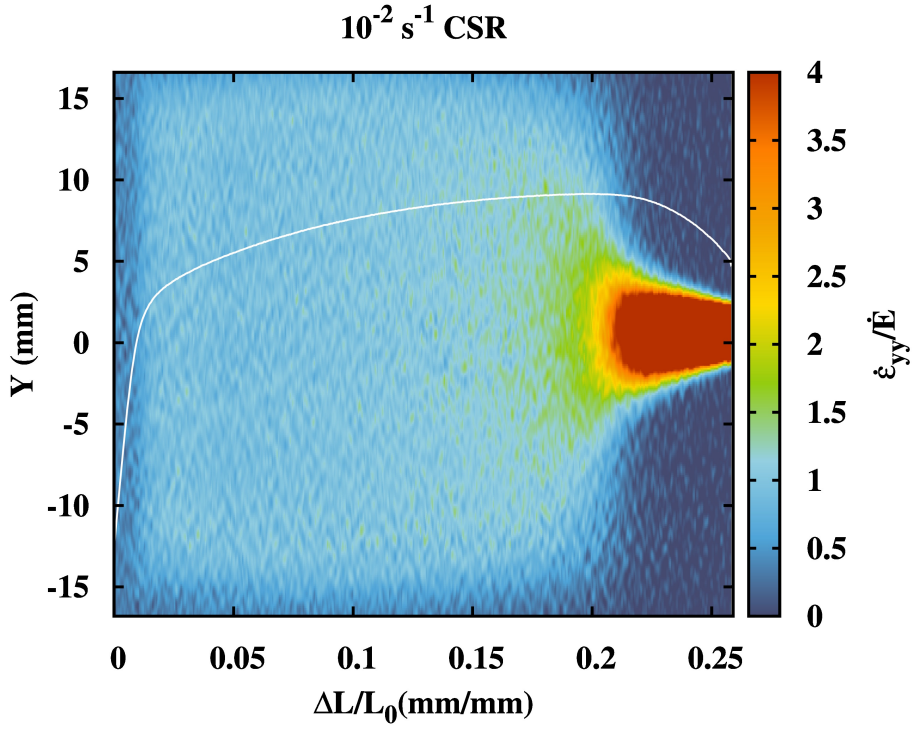

(b)

Figure 4.5 – (a) Stress strain curves for constant strain rate (CSR) tests at different strain rates and the strain rate sensitivity evolution calculated from different strain rate pairs. (b) Spatio-temporal pattern of the CSR test at strain rate 10^{-2} s^{-1} (Δt=0.2 s).

over time. This combination of yield peak and stress plateau is often observed in aluminium alloys. The first band cannot be distinguished from the following PLC bands. We call this initial band associated with stress plateau a Lüders band. After the third relaxation, a stronger single Lüders band propagates from the upper end to the lower end.

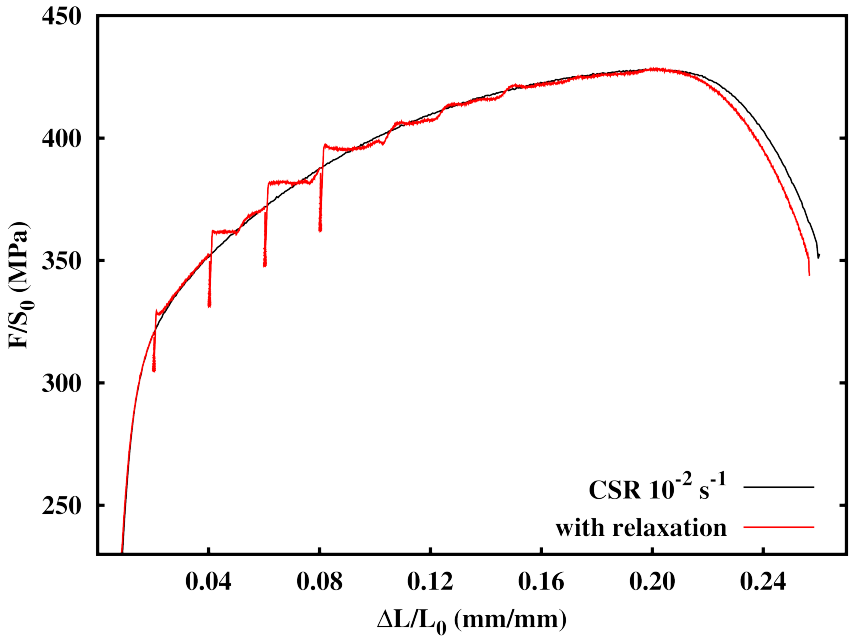

(a)

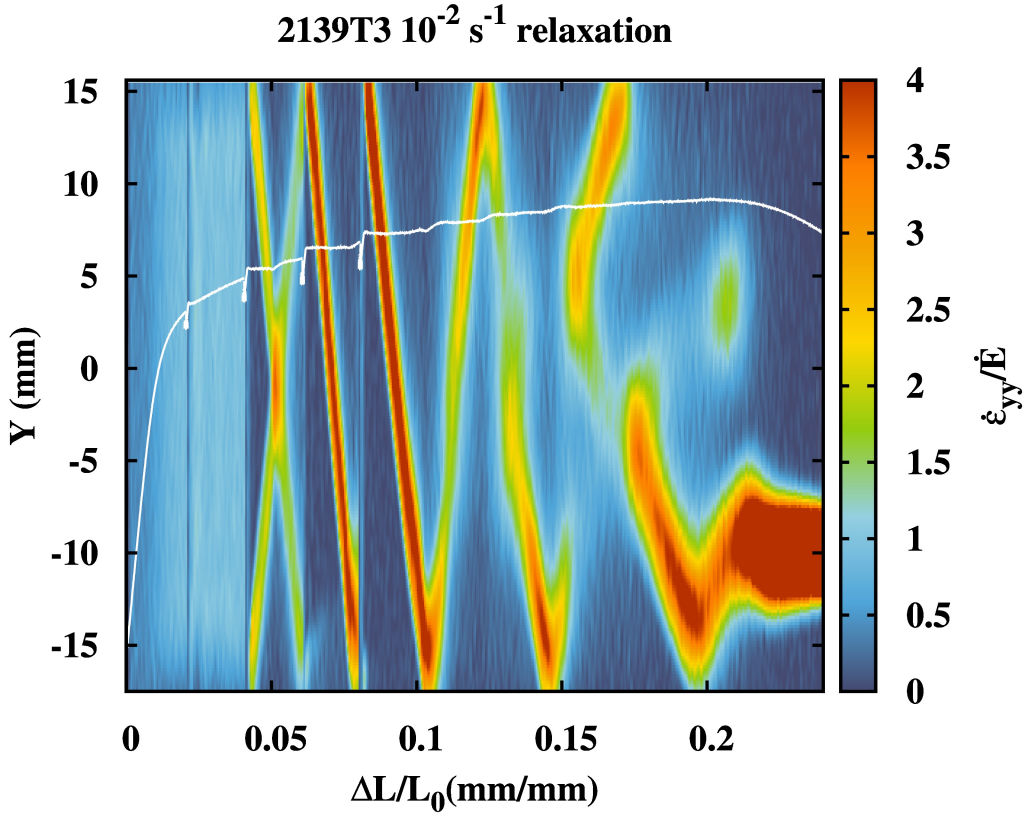

(b)

Figure 4.6 – (a) Constant strain rate tensile test at strain rate $10^{-2}\,s^{-1}$ (black line) superposed with the curve of relaxation test. (b) The spatio-temporal pattern of the relaxation test at strain rate $10^{-2}\,s^{-1}$ ($\Delta t = 0.05\,s$).

During the last stage of deformation, multiple bands appear. At each instant, two bands with different strengths seem to compete with each other. Finally, a single band becomes dominant and causes the final fracture. The corresponding stress-strain curve takes a

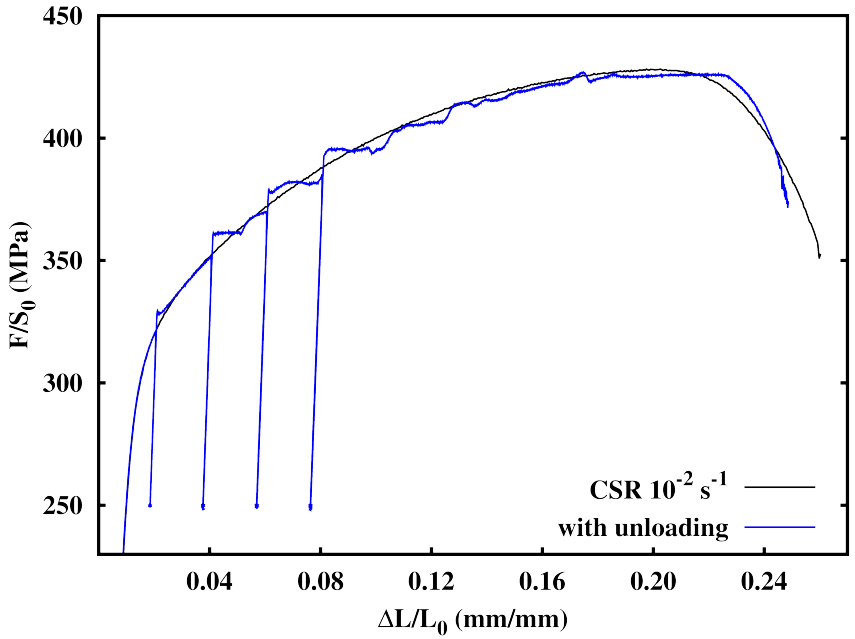

(a)

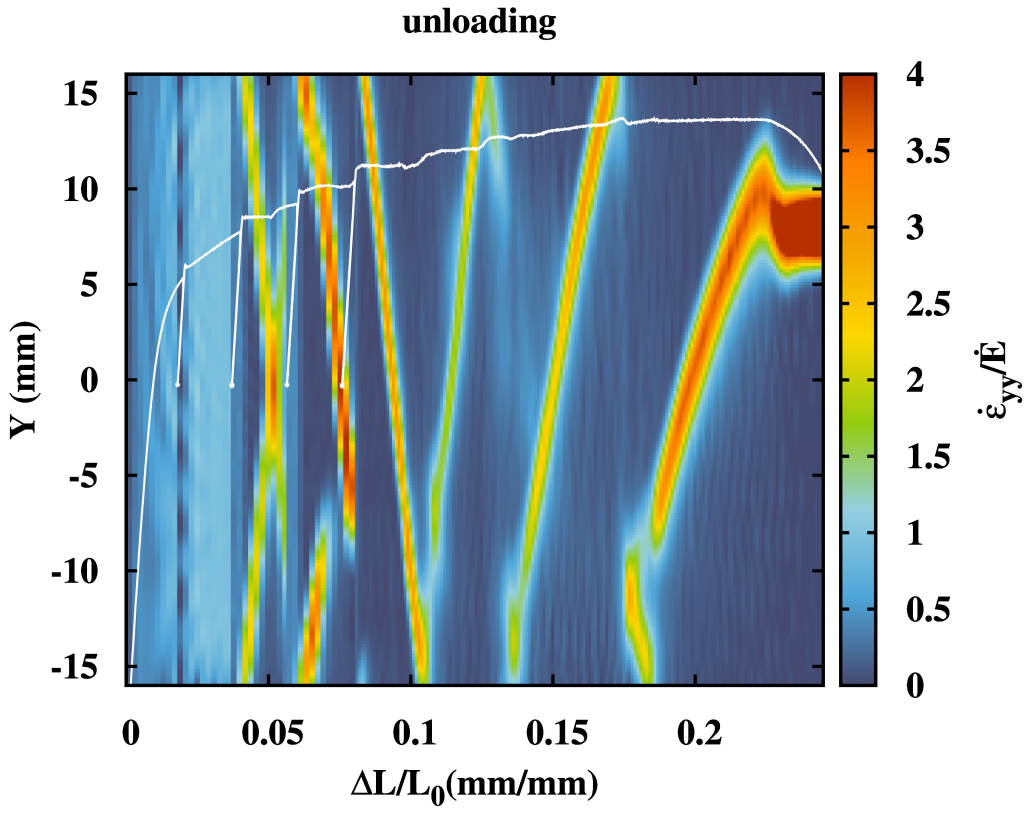

(b)

Figure 4.7 – (a) Constant strain rate tensile test of AA2139-T3 specimens at strain rate $10^{-2}\,s^{-1}$ (black line) superposed with the curve of unloading ageing test (blue curve). (b) The spatio-temporal pattern of the unloading test at strain rate $10^{-2}\,s^{-1}$ (Δt=0.2 s).

stair-like shape. The strain rate field of the gage area is shown in Fig. 4.6(b) as well as the final fracture image. The bands are horizontal which is due to the section geometry as presented in [Nogueira de Codes and Benallal, 2011]. Slant fracture is observed in the

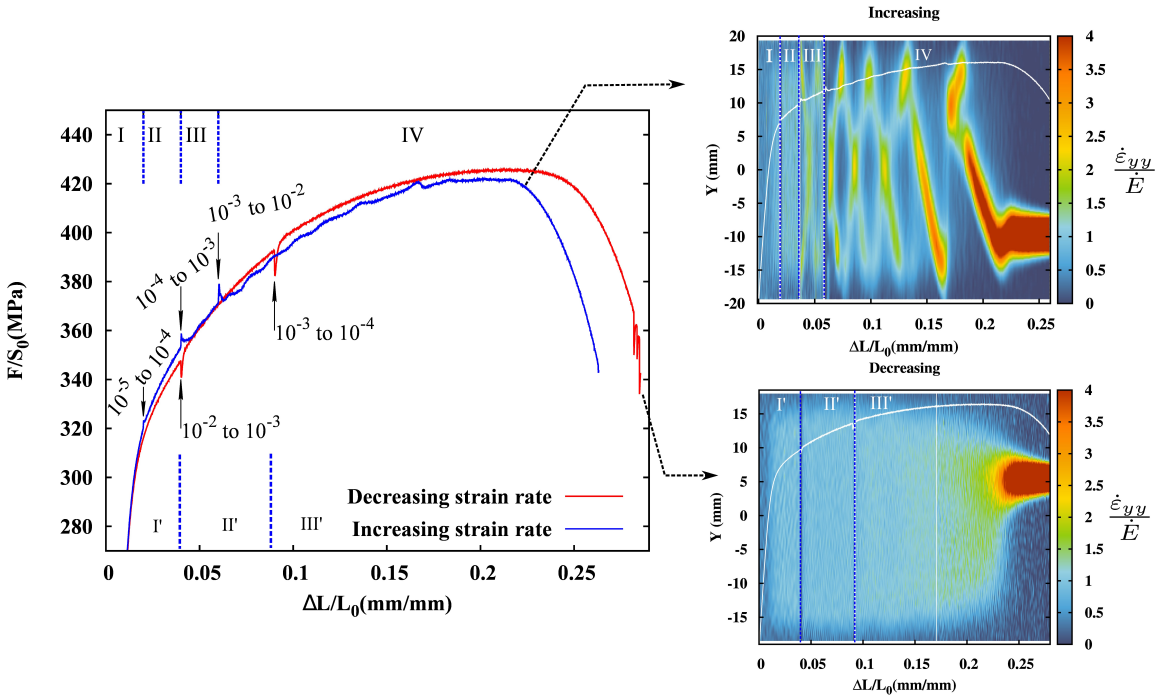

Figure 4.8 – Stress-strain curves of strain rate jump tests: increasing (blue curve) and decreasing (red curve) strain rate jump tests. Right: Spatio-temporal patterns corresponding to these two tests (Δt varies according to strain rate).

thickness plane. A similar fracture mode has also been noticed and discussed by Cai et al. [2016a]. For a thinner specimen, a slant band is favoured in the transverse plane.

For the unloading ageing test (see Fig. 4.7(a)), the 4 unloadings were performed at the same strain level as the relaxation test. For each unloading, the stress is maintained for 2 minutes after descending to 14.1 kN (250 MPa). The serrated flow after reloading is very similar to that found during the relaxation test. The spatio-temporal pattern of the unloading test shows very similar localization (see Fig. 4.7(b)).

Two types of strain rate jump tests, namely the increasing and decreasing strain rate changes, are applied, that are shown in Fig. 4.8. The increasing strain rate curve (start from low strain rate $10^{-5}\,s^{-1}$) is above the decreasing strain rate curve (start from high strain rate $10^{-2}\,s^{-1}$) at the beginning part(< 5% strain) and below in the last part (> 6% strain). This test confirms the slight negative strain rate sensitivity in constant strain rate tests. Each increase in strain rate is accompanied by the occurrence of a yield point, which also indicates that the instantaneous sensitivity is always positive as mentioned in [McCormick, 1988; Ling and McCormick, 1990, 1993; Picu et al., 2005]. It can be noticed that the stress drop of each strain rate jump increases with strain. The steady-state SRS is negative in both of the decreasing and increasing strain rate change tests. The spatio-temporal patterns corresponding to these two strain rate jump tests are illustrated in Fig. 4.8. The pattern is divided into 4 stages correspond to 4 strain rate states for the increasing test: $10^{-5}\,s^{-1}$, $10^{-4}\,s^{-1}$, $10^{-3}\,s^{-1}$ and $10^{-2}\,s^{-1}$. At stage III, the serrations are very slight, however the localization bands can be seen by DIC measurement. From stage IV on, serrations and localization bands are clearly visible. For the decreasing strain rate jump test, there is no sharp yield point nor serrations after reloading. Localisation bands have not been observed through DIC measurement either, see Fig. 4.8.

4.2.5 Simulations for the current Al-Cu alloy

The reloading peak after the relaxation or unloading is sometimes called the "post-relaxation effect"[Drozd et al., 2004; Trojanová et al., 2005]. This transient behaviour has been interpreted using the DSA theory and related constitutive models. The solute composition can not respond to abrupt change of strain rate [Van den Brink et al., 1975; McCormick, 1988]. The instantaneous SRS is always positive due to the usual thermally activated behaviour. The steady state SRS can be negative or positive. These phenomena have been interpreted by the strain ageing models proposed in literature. However, no effort has been made to investigate the triggering effect. In this part, we will present the simulation results about relaxation tests using the McCormick type model.

Constitutive equations and identification of the strain ageing model

The McCormick type model [Mazière et al., 2010] can be presented as

$$F(\underset{\sim}{\sigma}) = \sigma_{eq}(\underset{\sim}{\sigma}) - R(p) - R_a(t_a), \tag{4.2a}$$

$$R(p) = R_0 + Q_1[1 - e^{-b_1 p}] + Q_2[1 - e^{-b_2 p}], \tag{4.2b}$$

$$\dot{p} = \dot{\varepsilon}_0 \sinh\left(\frac{\max(0, F)}{\sigma_0}\right). \tag{4.2c}$$

where F is the yield function, $R(p)$ is one of the conventional hardening functions, and p the cumulated plastic strain. The ageing hardening term R_a reads

$$R_a(t_a) = P_1\left[1 - e^{-\left(\frac{t_a}{t_0}\right)^n}\right], \quad \dot{t}_a = 1 - \frac{t_a}{w}\dot{p}, \quad t_0 = (1/P_2 p^{\alpha})^{1/n} \tag{4.3}$$

where P_1 is the maximal over concentration maximal stress drop magnitude from a fully pinned state to a fully unpinned state; t_0 characterizes the time of diffusion process; n = 0.33 or 0.66 which corresponds to different diffusion mechanisms; w characterizes the strain increment associated with unpinning event.

Table 4.2 – Identified parameters for AA2139-T3 alloy.

E(GPa)	ν	P_1(MPa)	n	w	$P_2(\mathrm{s}^{-n})$	α
69	0.3	33	0.33	5.8×10^{-4}	2.7	0.4
Q_1(MPa)	b_1	Q_2(MPa)	b_2	R_0(MPa)	$\dot{\varepsilon}_0(\mathrm{s}^{-1})$	σ_0(MPa)
64	406	238.5	8.6	225.3	3.5×10^{-6}	3.0

When the strain rate increases, the solute concentration C_s at dislocations has to decrease with ageing time t_a until reaching the new steady-state controlled by strain rate. A drop in flow stress which follows the initial yield peak occurs in the transient region. When the strain rate decreases, dislocations must wait for a moment before acquiring the new steady state for the lower strain rate. A stress drop is seen after abrupt strain rate change. With the increase of ageing time, the flow stress is restored and increased.

Numerical predictions of the spatio-temporal patterns of CSR and relaxation tests

Some finite element simulations are performed here using this model for the CSR and relaxation-reloading process. Parameters are identified based on the current CSR tensile

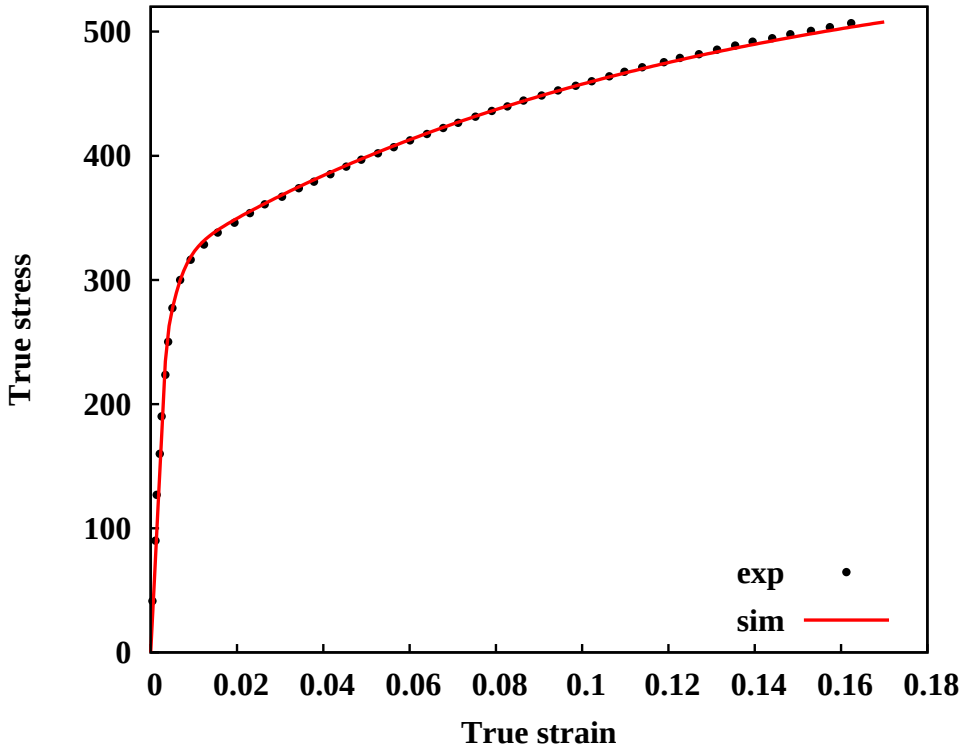

Figure 4.9 – Identification of parameters for AA2139-T3 based on experimental true stress-strain curves.

tests (see Table 4.2). Fig. 4.9 shows the identification result performed on single integration point together with the experimental curve at strain rate $\dot{E}$ =10^{-2} s^{-1}. The identification is satisfactory. The 2D and the 3D finite element meshes are presented in Fig. 4.10. The band morphologies simulated on the 2D and the 3D meshes are different. The band reproduced using 3D mesh is more consistent with experimental observations.

Concerning the premature triggering of the critical strain after interruptions, the mechanism is less clear. Balík et al. [2000] performed prestrain tests for a binary Al-3Mg alloy in order to test the hypothesis that the initial dislocation density governs the critical strain. Their relaxation and unloading test at room temperature is similar to ours except for a much longer waiting time (>17h), while the triggering effect for serrations is very limited. Allain et al. [2011] investigated the influence of different relaxation durations and different prestrain levels on the critical strain in an austenitic FeMnC steel. The longer the duration of the relaxation phase, the earlier the serrations. The different prestrain levels do not make any differences for the onset of serrations for their test condition. The authors attributed this effect to the triggering of twinning during relaxation. However, the 2139 alloy does not present twinning. It is worth noting that the tested austenitic FeMnC steel [Allain et al., 2011] also shows serrations in a regular tensile test without relaxation at strain state higher than 20%.

In the experiments of 2139 alloy, there is no PLC effect at room temperature in the investigated strain rate domain 10^{-5} s^{-1} - 10^{-2} s^{-1} for constant strain rate tests (CSR). Nevertheless, the PLC domain is probably quite close in terms of temperature and/or strain rate and PLC effect. The effect can then be easily triggered by modification of the loading path (relaxation, unloading and ageing, strain rate jumps). This assumption can be confirmed

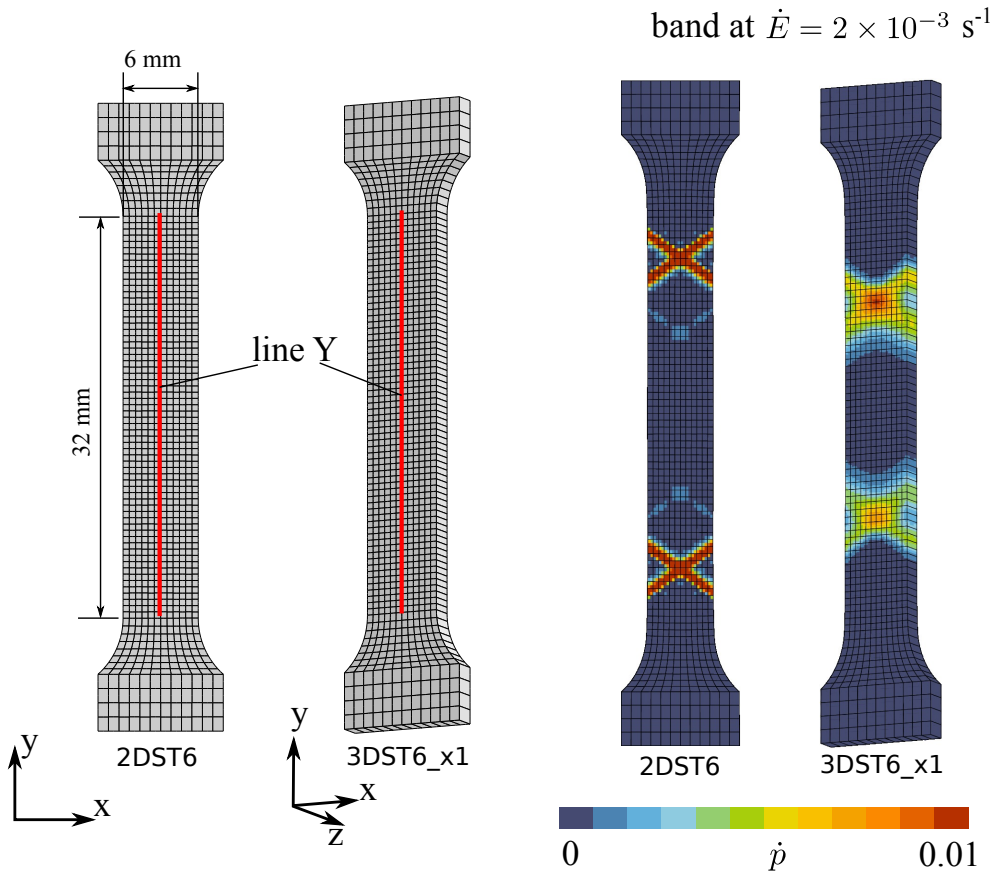

Figure 4.10 – 2D and 3D meshes used for simulations. The spatio-temporal patterns are obtained by measuring strain along line Y. The morphologies of localization bands at $\dot{E}$ =2 × 10^{-3} s^{-1} simulated on these two meshes are shown on the right side.

by simulations at $\dot{E}$ =10^{-2} s^{-1} and 10^{-3} s^{-1}. As shown in Fig. 4.11, for this set of material parameters at strain rate 10^{-3} s^{-1}, some very small serrations on the constant strain rate curve are initiated around strain = 0.14. For the same applied strain rate, when relaxations are involved, serrations appear much earlier following the 4th re-straining (at strain = 0.08). Serrations remain visible until final necking. The second and third re-straining also triggered slight localization bands initiated from the two shoulders of the specimen as shown in the spatio-temporal pattern. At $\dot{E}$ =10^{-2} s^{-1}, no propagating bands can be observed under the constant strain rate condition. Unlike the simulations at 10^{-3} s^{-1}, PLC effect has not been triggered after re-straining for 10^{-2} s^{-1}, although we can still observe localization bands initiated from the shoulder after the 3rd and the 4th re-straining. These bands vanished quickly then.

Actually, the experimental results about AA2139-T3 alloy lie between 10^{-2} s^{-1} and 10^{-3} s^{-1} with present parameter set as presented in Fig. 4.11. PLC effect was not observed for constant strain rate tests, while the serrations are triggered after re-straining. To predict such premature triggering effect during relaxation test as well as a smooth curve for CSR, we have chosen a strain rate between 10^{-3} s^{-1} and 10^{-2} s^{-1}. As shown in Fig. 4.12, both simulation results on 2D and 3D meshes are presented. At this strain rate, we successfully reproduced the triggering effect after relaxation and the absence of PLC effect for CSR condition. It can also be noted that the triggering effect is not influenced by the

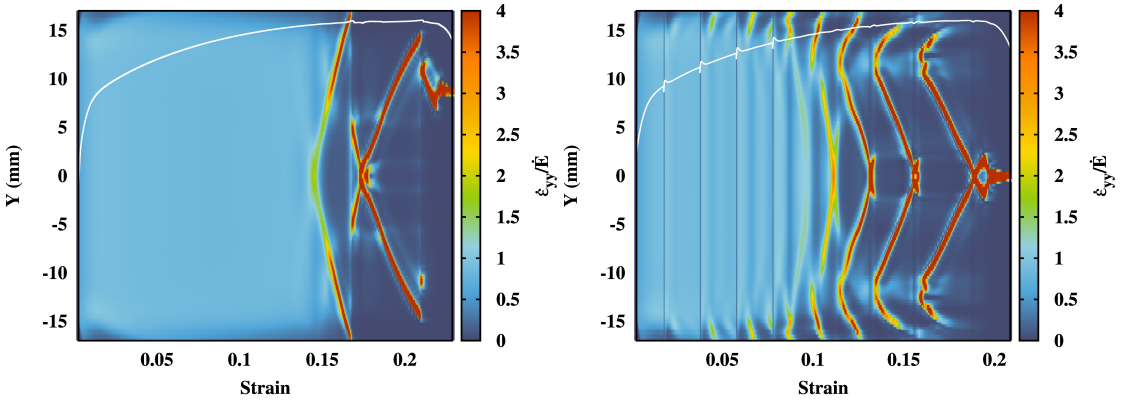

(a) CSR at $\dot{E}$=10^{-3} s^{-1} (b) with 4 relaxations at $\dot{E}$=10^{-3} s^{-1}

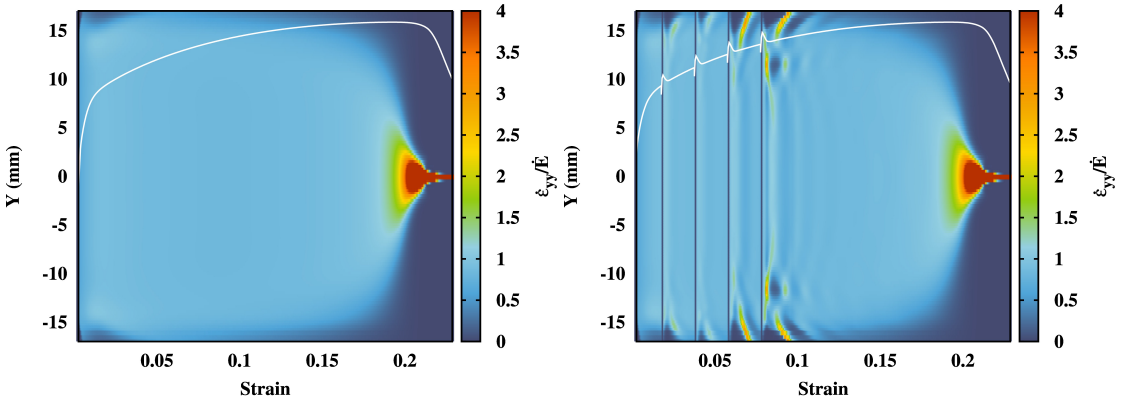

(c) CSR at $\dot{E}$=10^{-2} s^{-1} (d) with 4 relaxations at $\dot{E}$=10^{-2} s^{-1}

Figure 4.11 – Comparison between the simulated spatio-temporal patterns involving 4 relaxations and those without relaxations at 10^{-3} s^{-1} and 10^{-2} s^{-1}. These simulations are performed on 2D mesh (2DST6) (see Fig. 4.10).

difference between 2D and 3D meshes. The 3D results are indeed closer to experimental observations in terms of band width and spatio-temporal characteristics.

Fig. 4.13 gives the evolution of stress as a function of strain rate for different strain levels. The experimental data is also given in this figure. $\dot{E}$ =10^{-3} s^{-1} is located in the centre of negative strain rate sensitivity zone. $\dot{E}$ =10^{-2} s^{-1} is located in the transition area from negative to positive sensitivity. The simulation results are summarized in this figure. If we properly keep a slight negative strain rate sensitivity and choose a proper loading rate around the transition area, we are able to reproduce the premature triggering effect after re-straining while maintaining the absence of serrations at CSR condition.

Perspectives about the triggering effect

The effect found here is of relevance for engineering applications as the forming process might make a material sensitive to the PLC effect. The current standard numerical tools might fail to estimate the actual fracture, considering that the presence of PLC effect could promote the deterioration in mechanical properties, such as a drop of toughness and ductility [Amar and Pineau, 1985; Wang et al., 2012]. In addition, Morgeneyer et al. [2016] reported the occurrence of early stage strain localization bands in the notch area of a CT (compact tension) specimen made of AA2139-T3 alloy through laminography-DVC measurement. They performed stepwise monotonic loading as it is usually done for in situ

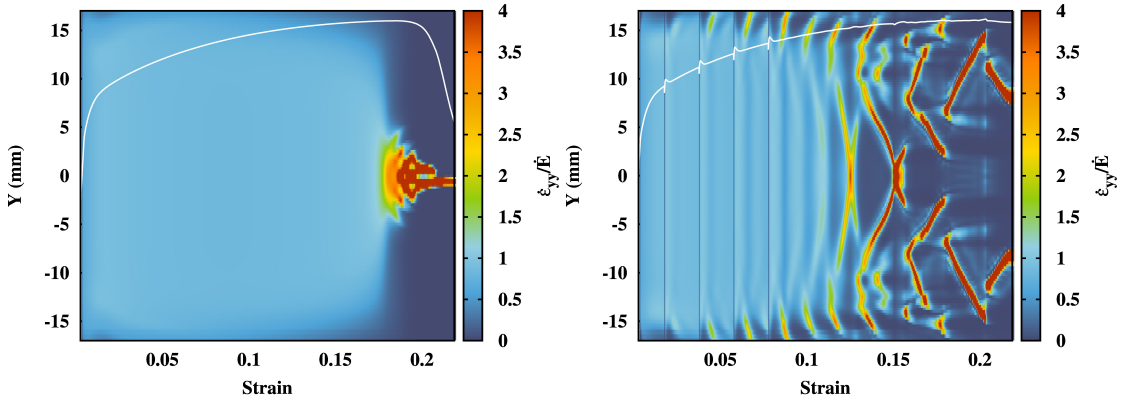

(a) CSR at $\dot{E}$=2 × 10^{-3} s^{-1} (2D)

(b) with 4 relaxations at $\dot{E}$=2 × 10^{-3} s^{-1} (2D)

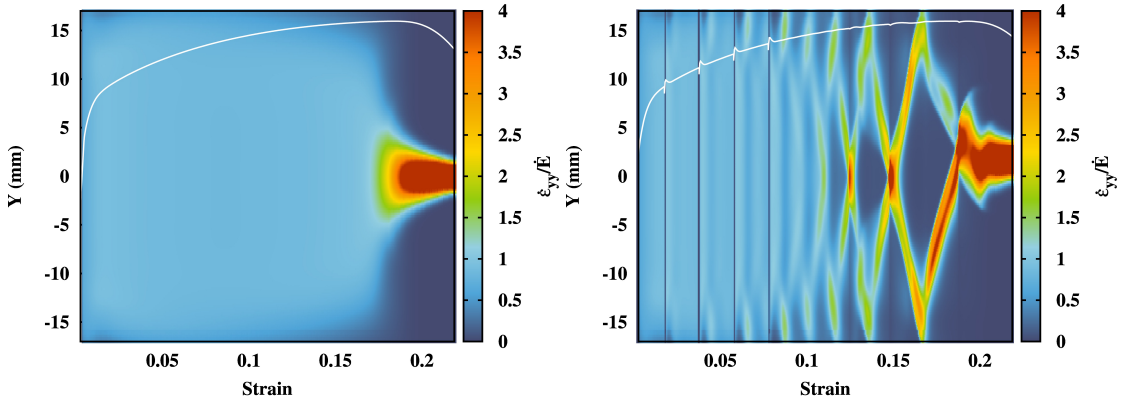

(c) CSR at $\dot{E}$=2 × 10^{-3} s^{-1} (3D)

(d) with 4 relaxations at $\dot{E}$=2 × 10^{-3} s^{-1} (3D)

Figure 4.12 – Comparison between the simulated spatio-temporal patterns involving 4 relaxations and without relaxation at $\dot{E}$ =2 × 10^{-3} s^{-1}. The simulations are performed on 2D (a,b) and 3D (c,d) meshes. Both meshes are shown in Fig. 4.10.

testing procedures. The notch opening displacement is maintained after each load, thus it can be considered as a relaxation test. The results of the present work provide a possible explanation for the localization behaviour observed in Morgeneyer et al. [2016].

More generally, in any tearing test these phenomena may play a role even for monotonic macroscopic loading as the plastic zone and the fracture process zone are subjected to local strain rate changes due to the stress concentration around the notch and due to crack propagation.

Standard J-δa fracture toughness tests involve partial unloading for the sample compliance measurement and could also trigger PLC effects. As relaxation and positive strain rate jumps, as shown in the present work, are able to trigger PLC effects, they might be used as standard procedures to test the sensitivity of a material to PLC. In particular, combined with spatio-temporal graphs a clear picture of the material behaviour can be gained.

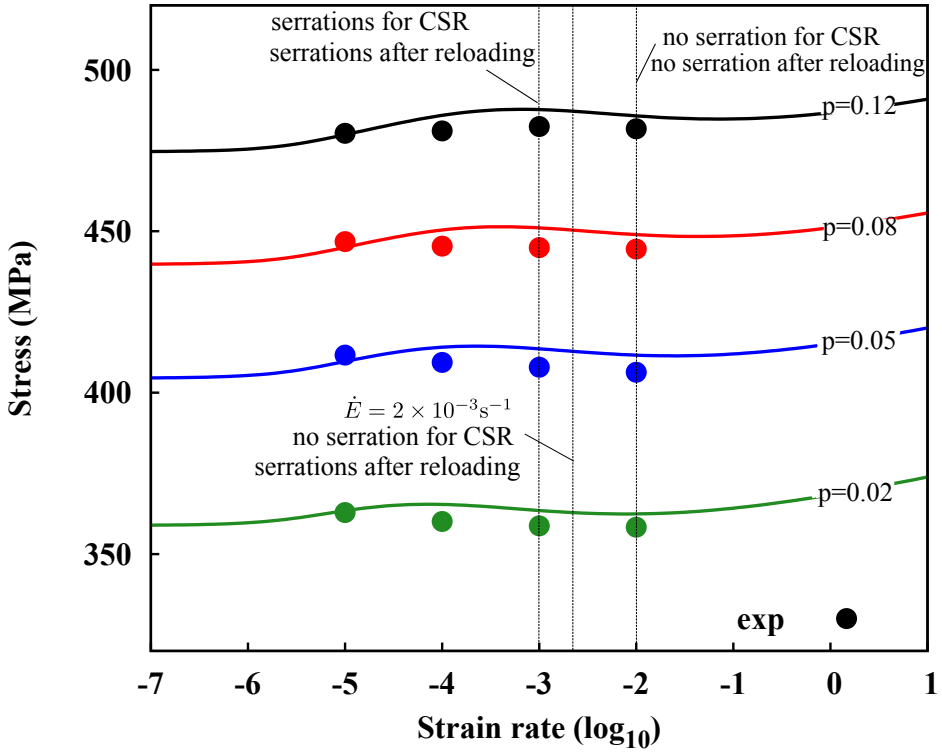

Figure 4.13 – Dependence of stress on strain rate for different strain levels for the current parameter identification. Experimentally observed strain rate sensitivity is compared with the current identification. Numerical results about the triggering effect at different strain rates are summarised here.

4.3 Conclusions about PLC effect in AA2139-T3 alloy

The main findings about the abnormal PLC effect in AA2139-T3 alloy are:

(1) PLC effect is not observed in constant strain rate tests at room temperature for the tested strain rates.

(2) The onset of PLC type serrations and localization is observed in relaxation and unloading ageing tests that involve in-situ ageing.

(3) Comparing the two strain rate jump tests, only the increasing one triggered PLC instabilities.

(4) The temporal evolution of the localization bands after re-straining has been verified by DIC measurements. In addition, according to the DIC measurements, localization bands can be observed even for very weak serrations on the stress-strain curve.

(5) The premature triggering of PLC effects after re-straining has been reproduced by FE simulations for the first time. It seems that the propagation of the Lüders band following relaxations could be responsible for leaving behind a slightly heterogeneous mechanical state which allows the early triggering of the PLC bands.

4.4 PLC effect in AA2198 aluminium alloy

AA2198 alloy belongs to the third generation of low density Al-Cu-Li alloy developed in the past decade, which is starting to be applied for latest aircraft [Warner, 2006]. The addition of Lithium (Li) provides higher strength and damage tolerance along with reduction of density. Li is the major alloying element in term of atomic percentage (see Table 4.3). Li participates in the formation of the T_1 (Al_2CuLi) precipitate which is the main hardening phase in the current material.

The naturally aged 2198 alloy was considered non sensitive to PLC effect by Deschamps et al. [2013]; Ovri and Lilleodden [2015]. Ovri and Lilleodden [2015] found serrated flow for the over aged state. As mentioned in the previous section, we noticed that PLC effect could be neglected without DIC measurement as the serration on the stress-strain curve could be very weak. In the current section, we are going to investigate and verify the possible PLC effect in AA2198 alloy.

Table 4.3 – Chemical composition in weight percent (wt.%) and atomic percent (at.%) of the AA2198 alloy [Chen, 2011].

	Cu	Li	Zn	Mn	Mg	Zr	Si	Ag	Fe
wt.%	2.9 – 3.5	0.8 – 1.1	≤ 0.35	≤ 0.5	0.25 – 0.8	0.04 – 0.18	≤ 0.08	0.1 – 0.5	≤ 0.01
at.%	1.23 – 1.48	3.11 – 4.26	≤ 0.14	≤ 0.25	0.28 – 0.88	0.01 – 0.05	≤ 0.08	0.02 – 0.06	≤ 0.05

4.4.1 Studied material

Two grades of AA2198 alloy are used for experimental study, namely T351 (naturally aged) and T851 (artificially aged). In addition, these material sheets are in the recrystallised state thus also referred to as T3R and T8R respectively.

The grain structure of AA2198-T3R is shown in Fig. 4.14. Pancake shaped grains were observed in the L-T plane. The grain size was measured by Chen [2011] using a mean linear intercept method: 200-300 µm along rolling direction (L) and long transverse direction (T), 25-30 µm in short transverse direction (S). There is no difference in grain structure between T3R and T8R.

TEM investigation results show very different precipitations in these two states [Chen, 2011]. For naturally aged T3 material, precipitates T_1 and θ' are absent. There is no precipitate decoration at grain boundaries or subgrain boundaries. Dispersoids like $Al_{20}Cu_2Mn_3$ or Al_3Zr can be seen. For T8 material, inter-granular precipitations can be found along almost all grain boundary or subgrain boundary areas. Needle shaped hardening precipitates T_1 (Al_2CuLi) and θ' (Al_2Cu) can be seen distributed homogeneously. In addition, the volume fraction of inter-metallic particles and voids content in 2198 alloy is very low (only 0.34%).

4.4.2 Mechanical response

Tensile tests are conduced on these flat specimens under uni-axial loading condition for both grades of 2198 alloy. All the specimens of T3R and T8R are prepared in the L-T plane with axis along the T direction. The geometry is presented in Fig. 4.14. The thickness of these sheets is 2 mm. Tests are carried out using a 100 kN MTS machine under displacement control. Tests are performed at room temperature unless otherwise specified.

Three types of tensile tests are carried out for 2198 alloy:

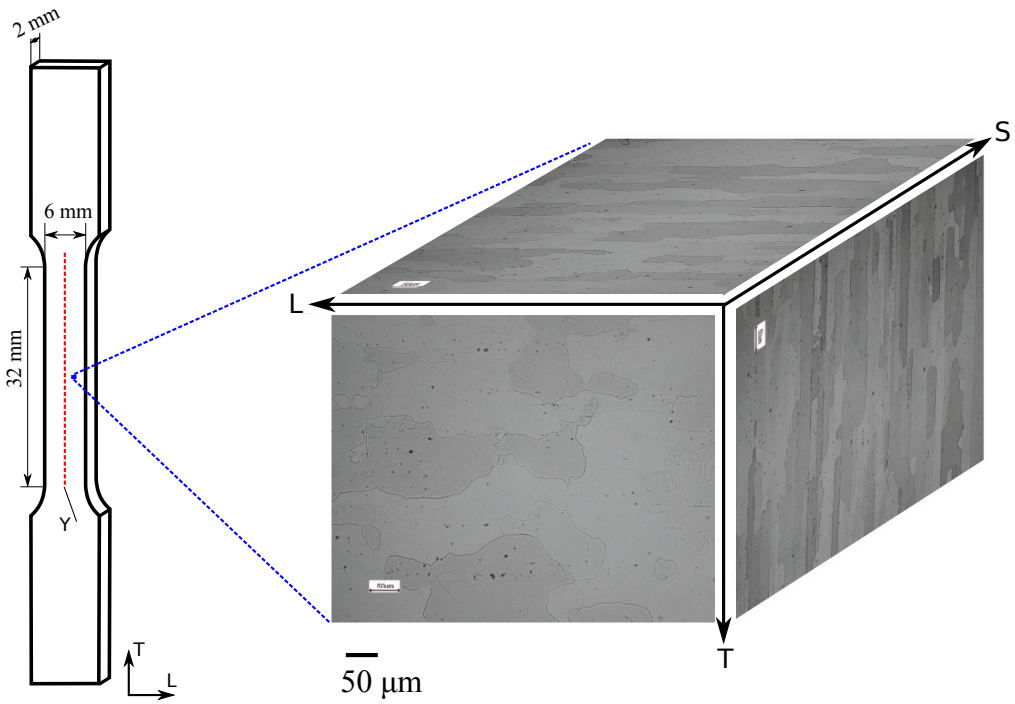

Figure 4.14 – Geometry of smooth tensile specimen. The strain measured by the line Y will be used for creating the spatio-temporal diagram. Optical micrographs of the AA2198-T3R 2 mm-thick recrystallized material in TS, LS, LT planes and pseudo-3D grain structure (L: rolling direction, T: long transverse direction and S: short transverse direction). Optical micrographs reproduced from [Chen, 2011].

1. Usual monotonic constant strain rate tests with prescribed strain rates of $10^{-5}\,s^{-1}$, $10^{-4}\,s^{-1}$, $10^{-3}\,s^{-1}$ and $10^{-2}\,s^{-1}$ (CSR).

2. Tests involving single or multiple relaxations.

3. Strain rate jump (SRJ) tests : increasing or decreasing strain rate at different strain levels.

A schematic diagram concerning the displacement evolution as a function of time for those different loading paths is shown in Fig. 4.4.

4.4.3 Constant strain rate tensile tests

Fig. 4.15 shows the nominal stress-strain curves of T3R specimens under different applied strain rates from $10^{-2}\,s^{-1}$ to $10^{-5}\,s^{-1}$. The strain rate sensitivity between two applied strain rates is calculated by $m_{(\dot{E}_i,\dot{E}_j)} = \log(\sigma_i/\sigma_j)/\log(\dot{E}_i/\dot{E}_j)$, where σ_i and σ_j are the stress values measured in tests under overall strain rates $\dot{E}_i$ and $\dot{E}_j$. As shown by y-axis on the right side, a slight negative strain rate sensitivity can be observed. Similarly, Fig. 4.16 gives the nominal stress-strain curves of T8R specimens tested under different strain rates. It can be noticed that the T8R material presents higher yield and ultimate strength comparing with T3R. In contrast, the ductility of T8R is much lower than T3R. T3R also shows higher negative strain rate sensitivity ($m \simeq -0.005$) than T8R ($m \simeq -0.001$). Type A serrations are observed at $\dot{E}$ =$10^{-2}\,s^{-1}$ and $\dot{E}$ =$10^{-3}\,s^{-1}$ for T3R specimens. These tests have been repeated several times which shows good reproducibility (see Fig. A.3 and A.4).

In contrast to T3R, the stress-strain curves of T8R are rather smooth. The tensile curves for T8R specimens tested at different temperatures from -50°C to +80°C are presented in A.5. There is no significant serration either. As reported in Section 4.2, loading path change can trigger PLC effect in a Al-Cu alloy. Relaxation and strain rate jump tests are also performed for these two grades of AA2198 alloys. The DIC measurement results about the constant strain rate tensile tests will be presented together with that of relaxation tests in order to make a direct comparison.

4.4.4 Triggering of PLC effect after relaxations

Fig. 4.17, 4.18 and 4.19 show the spatio-temporal patterns measured by DIC of the CSR tests and those of single relaxation tests for T3R specimens tested at strain rates $10^{-2}\,s^{-1}$, $10^{-3}\,s^{-1}$ and $10^{-4}\,s^{-1}$. As presented in Chmelík et al. [2002]; Nogueira de Codes and Benallal [2011], the spatio-temporal patterns describe the location of localization bands at different stages of experiment. The idea is to measure incremental axial strain over the whole deformation process along a line positioned in the gage area (see line Y in Fig. 4.14). The colour contour is a measure of the ratio between measured strain rate and applied macroscopic strain rate $\dot{\varepsilon}_{yy}/\dot{E}$, where $\dot{\varepsilon}_{yy} = \Delta\varepsilon_{yy}/\Delta t$ is calculated by correlating two successive images with a constant time interval Δt.

In order to investigate the triggering effect in the T3R material, we compared the spatio-temporal pattern of constant strain rate test with its counterpart involving only one relaxation at $\varepsilon = \Delta L/L_0 = 0.02$. Fig. 4.17 gives the results of AA2198-T3R specimens tested at $\dot{E} = 10^{-2}\,s^{-1}$. For CSR test, PLC effect initiates at $\varepsilon = 0.125$. For relaxation test, bands start to propagate right after the re-straining at $\varepsilon = 0.02$. Fig. 4.18 gives the results at $\dot{E} = 10^{-3}\,s^{-1}$. The PLC effect initiates at $\varepsilon = 0.14$ under CSR condition. The spatio-temporal pattern for relaxation test at this strain rate is very similar to $\dot{E} = 10^{-2}\,s^{-1}$. Fig. 4.19 shows the spatio-temporal patterns of CSR and single relaxation tests at $\dot{E} = 10^{-4}\,s^{-1}$. For CSR test, there is no signal of PLC effect. In contrast to the tests at $\dot{E} = 10^{-2}\,s^{-1}$ or $10^{-3}\,s^{-1}$, localization bands did not appear right after re-straining at $10^{-4}\,s^{-1}$. The critical strain for the onset of PLC effect after re-straining is around $\varepsilon = 0.1$.

The experimental results involving 4 relaxations at strain rate $10^{-2}\,s^{-1}$ for T3R and T8R are compared in Fig. 4.20. For both tests, the 4 relaxations are applied at $\varepsilon = 0.02, 0.04, 0.06$ and 0.08 followed by displacement hold time of 15 s each time. For T3R specimen, localization bands appeared after the first re-straining around the shoulder and propagate through the gauge area. The 2nd re-straining only triggered a single band. The bands after the third and the fourth re-straining start directly from the place where the previous localization bands disappeared. This is the first observation of this phenomenon which shows the influence of localization history on the triggering effect. Unlike T3R specimen, there is no significant localization band after re-straining in T8R specimen. However, we can still observe slight localization behaviour initiated around the shoulder.

The spatio-temporal patterns of T8R specimens under CSR condition are presented in Fig. A.6. There is no PLC effect under CSR condition in T8R specimens.

4.4.5 Strain rate jump tests

Fig. 4.21(a) shows the nominal stress-strain curves of the strain rate jump tests for AA2198-T3R specimens with 2 different jump sequences. The increasing strain rate test (blue curve) started with strain rate $10^{-5}\,s^{-1}$. At $\varepsilon = 0.02$, the applied strain rate is increased to $10^{-4}\,s^{-1}$. At $\varepsilon = 0.04$, strain rate is increased from $10^{-4}\,s^{-1}$ to $10^{-3}\,s^{-1}$. After

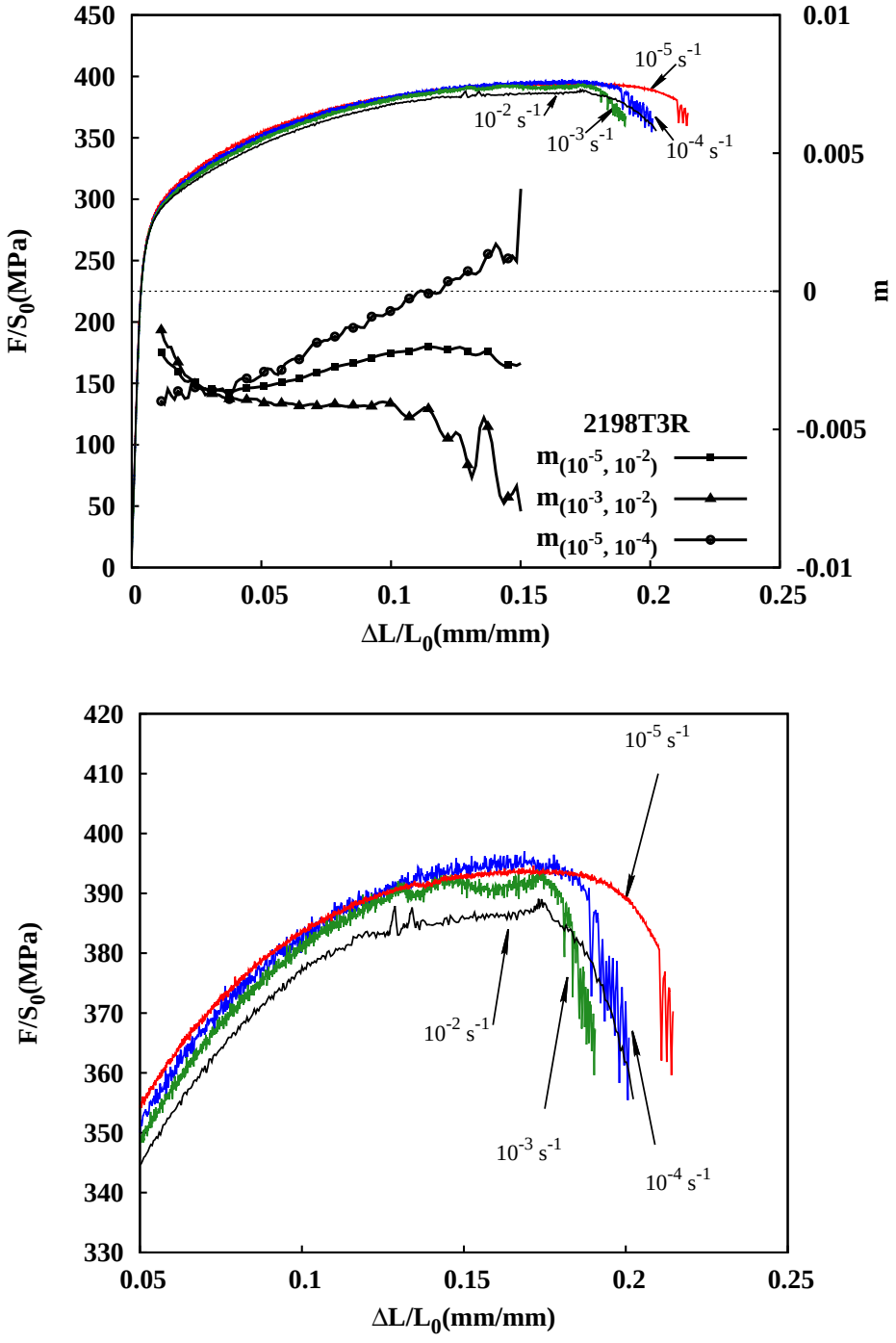

Figure 4.15 – Constant strain rate tensile tests of AA2198-T3R at different strain rates. The strain rate sensitivity indicator m is superposed (right y-axis).

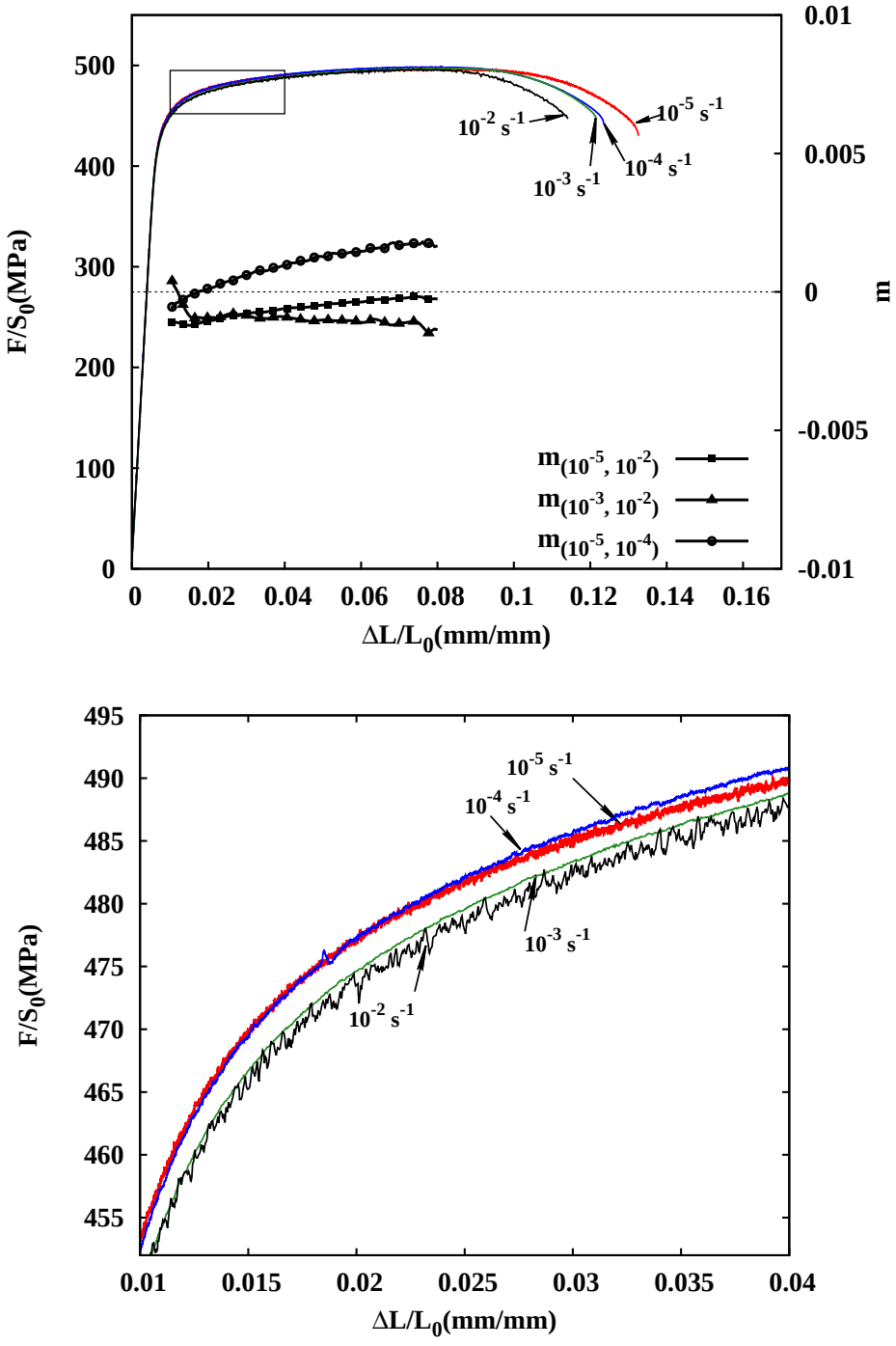

Figure 4.16 – Results of constant strain rate tensile tests of AA2198-T8R at different strain rates. The strain rate sensitivity indicator m is superposed (right y-axis).

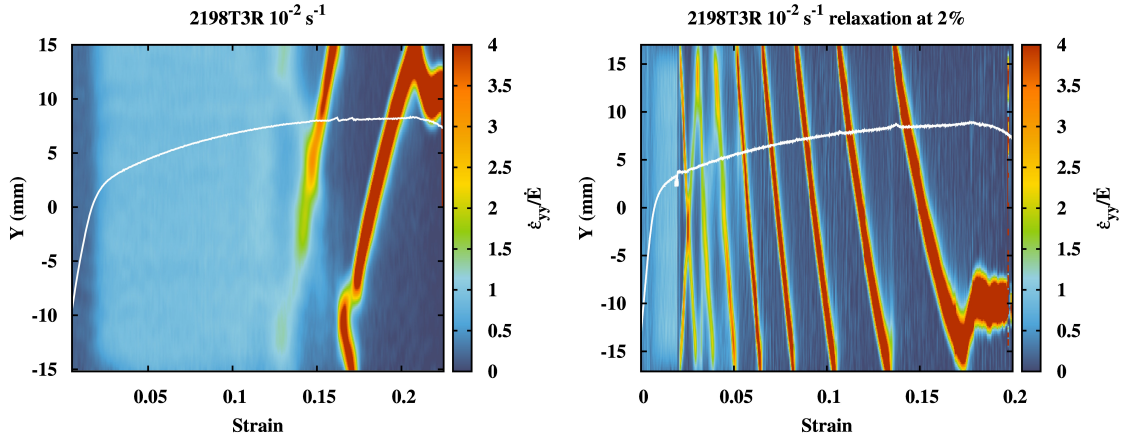

Figure 4.17 – Comparison of the experimental spatio-temporal diagram between the constant strain rate test and the test with a relaxation at strain = 0.02 for AA2198-T3R tested at applied strain rate $\dot{E}$ =10^{-2} s^{-1}.

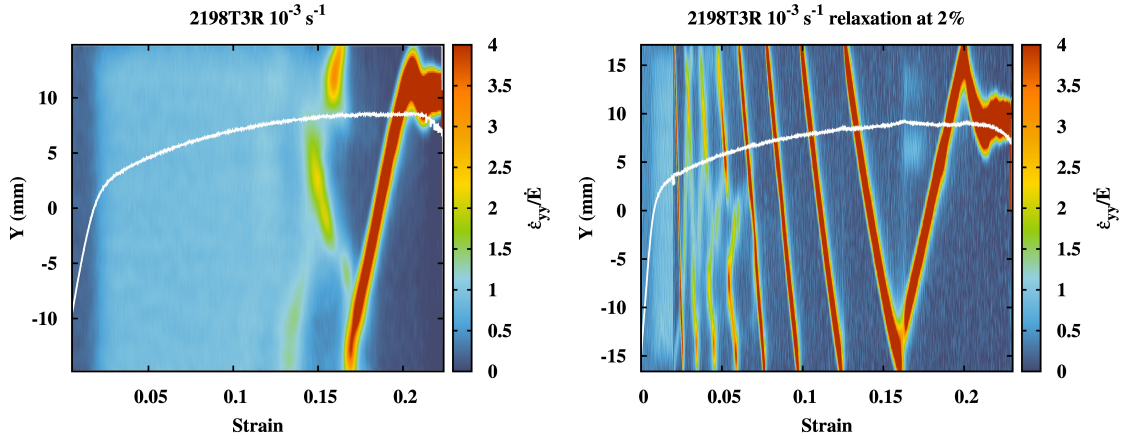

Figure 4.18 – Comparison of the experimental spatio-temporal diagram between the constant strain rate test and the test with a relaxation at strain = 0.02 for AA2198-T3R tested at applied strain rate $\dot{E}$ =10^{-3} s^{-1}.

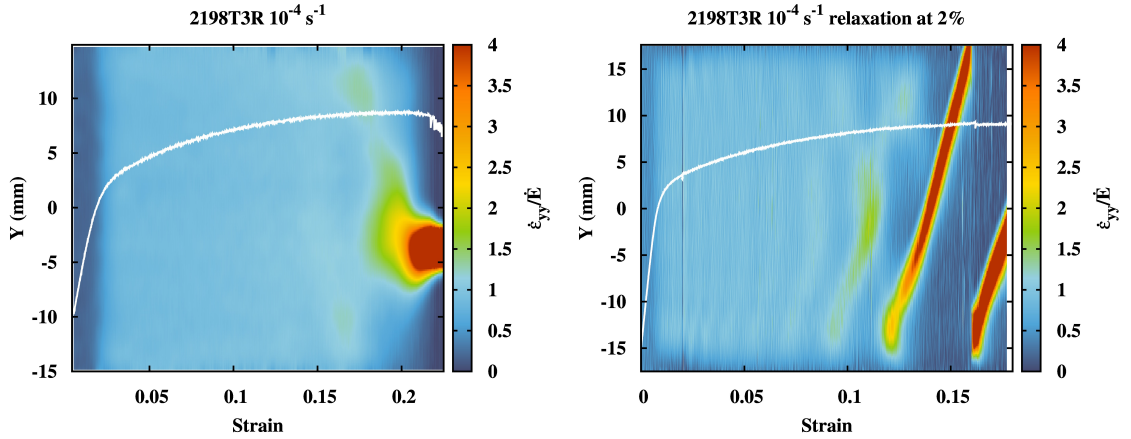

Figure 4.19 – Comparison of the experimental spatio-temporal diagram between the constant strain rate test and the test with a relaxation at strain = 0.02 for AA2198-T3R tested at applied strain rate $\dot{E}$ =10^{-4} s^{-1}.

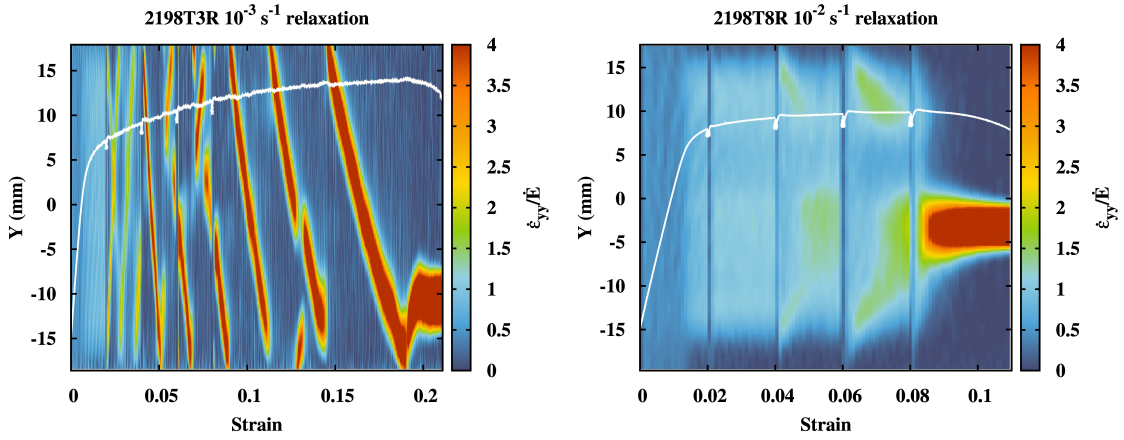

Figure 4.20 – Tensile tests involving 4 relaxations. Left: AA2198-T8R at $\dot{E}$ =10^{-3} s^{-1}. Right: AA2198-T8R at $\dot{E}$ =10^{-2} s^{-1}.

$\varepsilon = 0.06$, applied strain rate is increased to 10^{-2} s^{-1} until fracture.

The decreasing strain rate test (red curve) was conducted in the opposite direction. The first strain rate jump is set at $\varepsilon = 0.04$ where the applied strain rate decreases from 10^{-2} s^{-1} to 10^{-3} s^{-1}. The second jump is set at $\varepsilon = 0.09$ along with a decrease of applied strain rate from 10^{-3} s^{-1} to 10^{-4} s^{-1}.

Fig. 4.21(b) and (c) shows the spatio-temporal diagram of these two strain rate jump tests. In the increasing strain rate test, single localization band started after the second strain rate jump ($\varepsilon = 0.04$) which is earlier than the CSR test at $\dot{E}$ =10^{-3} s^{-1}. In the decreasing strain rate jump test, the triggering effect is less pronounced. We can observe slight bands after the second strain rate change at $\varepsilon = 0.04$. Localization bands showed different behaviour at the same strain rate.

Strain rate jump tests are also performed for T8R specimens. As shown in Fig. 4.22, increasing strain rate test (blue curve) involves 3 strain rate jumps: from 10^{-5} s^{-1} to 10^{-4} s^{-1} at $\varepsilon = 0.02$; 10^{-4} s^{-1} to 10^{-3} s^{-1} at $\varepsilon = 0.04$; 10^{-3} s^{-1} to 10^{-2} s^{-1} at $\varepsilon = 0.06$. Decreasing strain rate test (red curve) involves 2 strain rate jumps: from 10^{-2} s^{-1} to 10^{-3} s^{-1} at $\varepsilon = 0.04$ deformation; 10^{-3} s^{-1} to 10^{-4} s^{-1} at $\varepsilon = 0.65$ deformation. Unlike T3R specimens, moving localization bands are not observed in these strain rate jump tests of T8R specimens. However, for the increasing strain rate test, slight localization bands could be observed initiating from the two shoulders of specimens. The choice of the final necking position seems to be a result of competition between these two early localization spots.

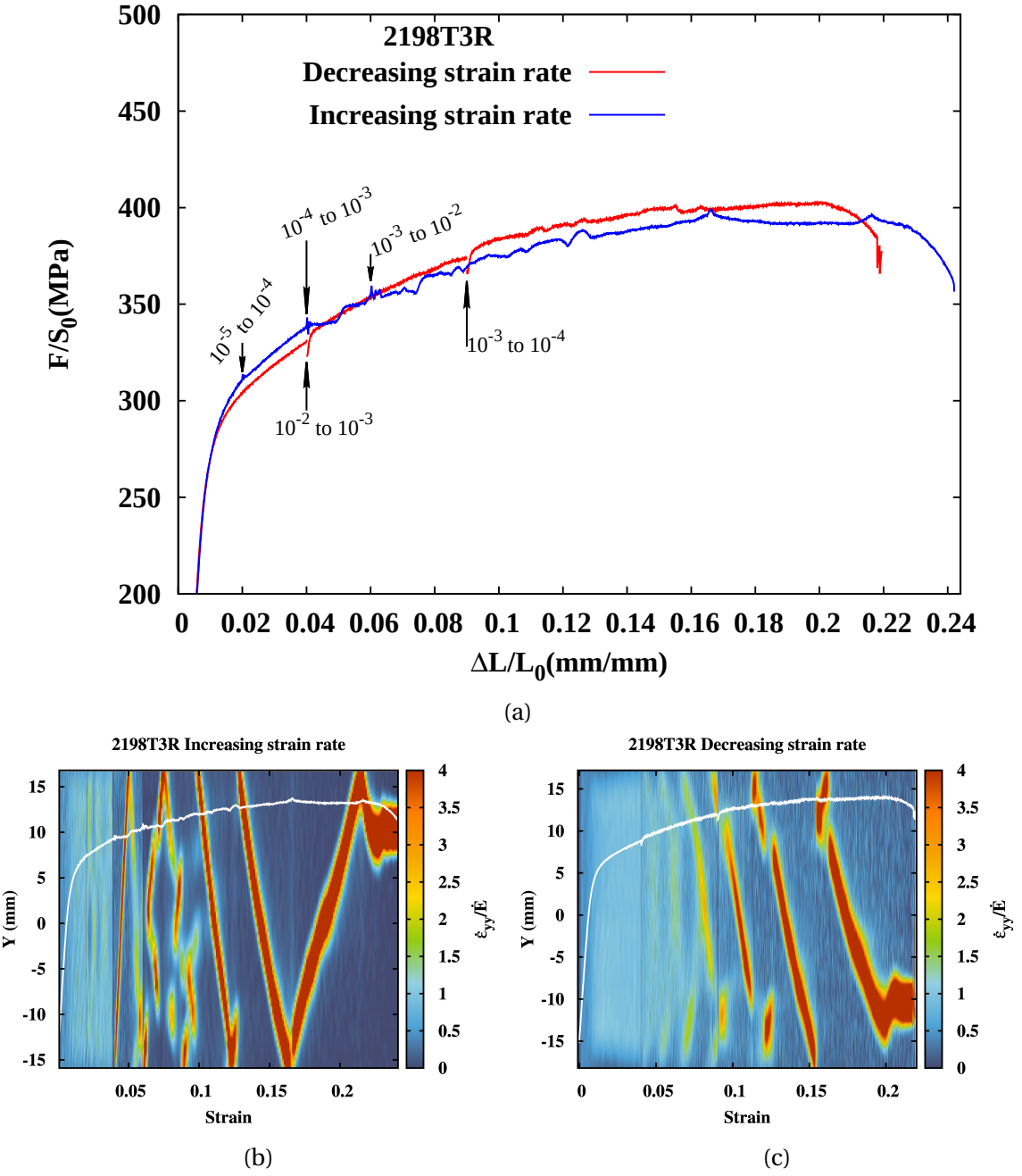

Figure 4.21 – Strain rate jump tests of AA2198-T3R.The spatio-temporal diagram of strain rate jump tests: (b) increasing strain rate test; (c) decreasing strain rate test.

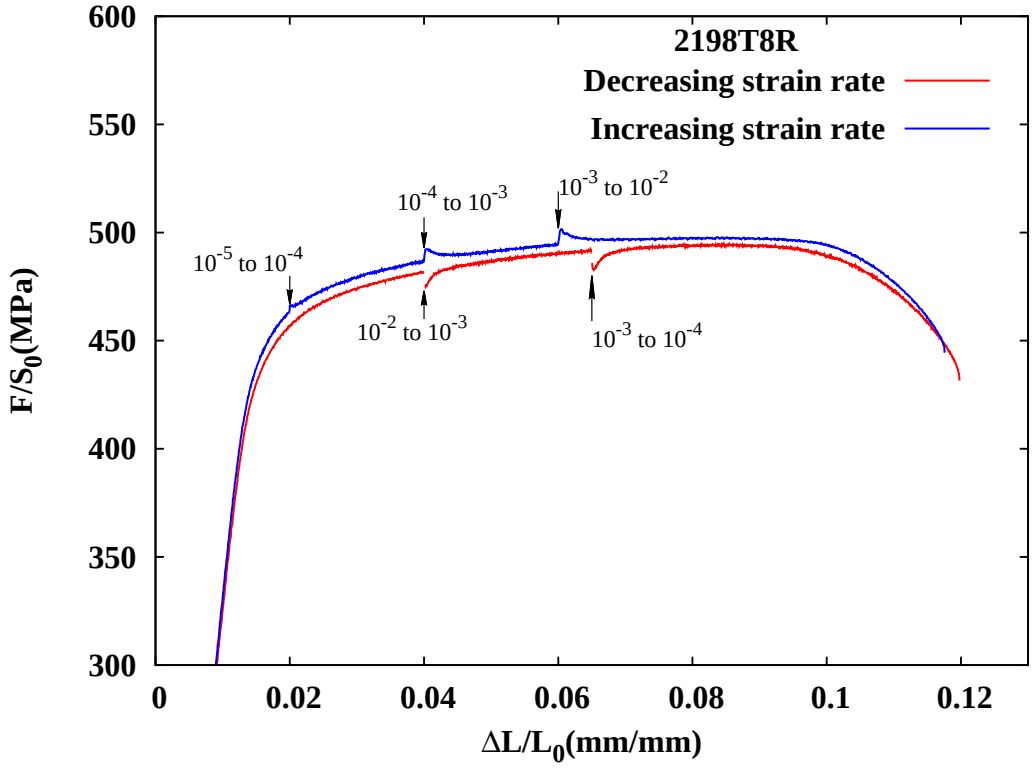

(a)

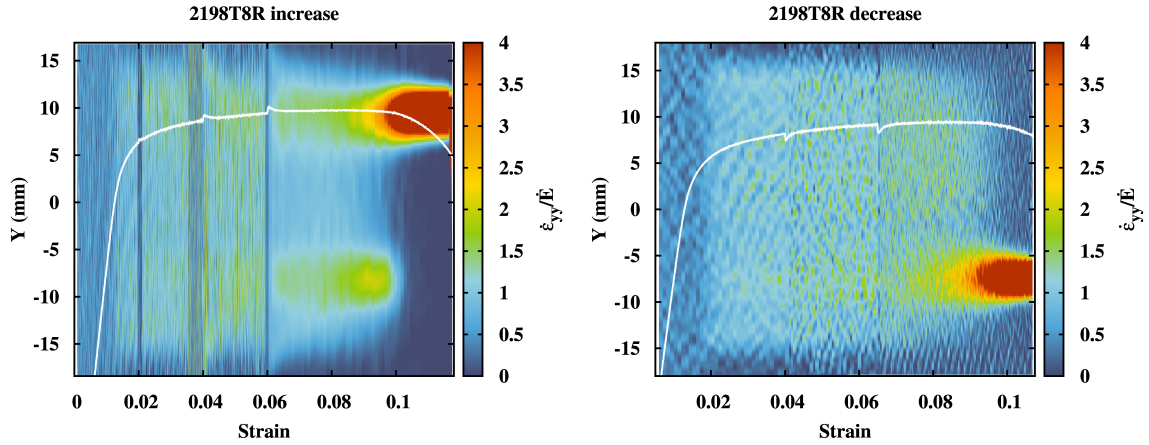

(b) (c)

Figure 4.22 – Strain rate jump tests of AA2198-T8R. The spatio-temporal diagram of strain rate jump tests: (b) increasing strain rate test; (c) decreasing strain rate test.

4.5 Macroscopic strain ageing model and polycrystalline model

In this section, we will present two different models trying to reproduce the experimental observations of the previous sections.

As first, the McCormick type elastoviscoplastic strain ageing model is presented in order to simulate the triggering effect of PLC effect observed in AA2198 alloy during tensile tests (see section 4.5.1).

Secondly, inspired by the work of [Kok et al., 2003], the polycrystalline model proposed by Rousselier et al. [2017] coupled with the McCormick type strain ageing model is used in order to investigate the effect of polycrystalline nature of the material (especially anisotropy) on the localization patterns (see section 4.5.2).

Both of these two models are used for simulating the tearing test of thin sheet CT specimen in 4.6. The obtained localization patterns are compared.

4.5.1 The McCormick type elastoviscoplastic strain ageing model

The McCormick type model [Mazière et al., 2010; McCormick, 1988] can be presented within the finite strain framework using the concept of local objective frames following Besson et al. [2009]. The second and fourth order tensors are defined by a single tilde $\underset{\sim}{Z}$ and a double tilde $\underset{\approx}{Z}$ respectively. Observer invariant stress and strain rate measures $\underset{\sim}{\sigma}$ and $\underset{\sim}{\dot{\varepsilon}}$ are defined by the transformation of the Cauchy stress tensor $\underset{\sim}{T}$ and the Eulerian strain rate tensor $\underset{\sim}{D}$ into the corotational frame characterized by the rotation $\underset{\sim}{Q}$ ($\underline{x}$,t) at each material point:

$$\begin{cases} \underset{\sim}{\sigma} = \underset{\sim}{Q}.\underset{\sim}{T}.\underset{\sim}{Q}^T \\ \underset{\sim}{\dot{\varepsilon}} = \underset{\sim}{Q}.\underset{\sim}{D}.\underset{\sim}{Q}^T \\ \underset{\sim}{Q} \quad \text{such as} \quad \dot{\underset{\sim}{Q}}^T.\underset{\sim}{Q} = \underset{\sim}{\Omega} \quad \text{(corotational)} \end{cases}$$

where $\underset{\sim}{D}$ and $\underset{\sim}{\Omega}$ respectively are the symmetric and skew-symmetric parts of the velocity gradient.

The strain rate is then decomposed into elastic $\underset{\sim}{\dot{\varepsilon}}^e$ and plastic $\underset{\sim}{\dot{\varepsilon}}^p$ parts:

$$\underset{\sim}{\dot{\varepsilon}} = \underset{\sim}{\dot{\varepsilon}}^e + \underset{\sim}{\dot{\varepsilon}}^p, \quad \underset{\sim}{\sigma} = \underset{\approx}{C} : \underset{\sim}{\varepsilon}^e \tag{4.4}$$

where $\underset{\approx}{C}$ is the Hooke tensor of elasticity. The plastic flow is described by the normality rule

$$\underset{\sim}{\dot{\varepsilon}}^p = \dot{p}\,\underset{\sim}{n}, \quad \underset{\sim}{n} = \frac{\partial F}{\partial \underset{\sim}{\sigma}}, \tag{4.5}$$

where p is the cumulative plastic strain and the yield function, F, is taken in the form

$$F(\underset{\sim}{\sigma}) = \sigma_{eq}(\underset{\sim}{\sigma}) - R(p) - R_a(t_a) \tag{4.6}$$

$$R(p) = R_0 + Q_1[1 - e^{-b_1 p}] + Q_2[1 - e^{-b_2 p}] \tag{4.7}$$

$$\dot{p} = \dot{\varepsilon}_0 \sinh\left(\frac{\max(0, F)}{\sigma_0}\right) \tag{4.8}$$

where σ_{eq} can be any of the well known equivalent stress measures associated with classical yield criteria (von Mises, Tresca etc.). $R(p)$ is one of the conventional hardening

Table 4.4 – Parameters of the elastoviscoplastic model identified for T3R and T8R.

AA2198-T3R						
E(GPa)	ν	P_1(MPa)	n	w	$P_2(s^{-n})$	α
71	0.3	43	0.33	10^{-4}	3.49	0.29
Q_1(MPa)	b_1	Q_2(MPa)	b_2	R_0(MPa)	$\dot{\varepsilon}_0(s^{-1})$	σ_0(MPa)
50	456	205	10	196	1.27×10^{-6}	3.0
AA2198-T8R						
E(GPa)	ν	P_1(MPa)	n	w	$P_2(s^{-n})$	α
71	0.3	30	0.33	10^{-4}	3.49	0.22
Q_1(MPa)	b_1	Q_2(MPa)	b_2	R_0(MPa)	$\dot{\varepsilon}_0(s^{-1})$	σ_0(MPa)
70	544	94	20	358	1.27×10^{-6}	3.0

function. R_0, Q_1, Q_2, b_1 and b_2 are hardening parameters. The ageing hardening term R_a reads

$$R_a(t_a) = P_1\left[1 - e^{-\left(\frac{t_a}{t_0(p)}\right)^n}\right], \quad \dot{t}_a = 1 - \frac{t_a}{w}\dot{p}, \quad t_0(p) = (1/P_2 p^{\alpha})^{1/n} \tag{4.9}$$

where P_1 is the maximal over concentration; t_0 characterizes the time of diffusion process; n = 0.33 is usually used for aluminium; The ageing time t_a depends on the plastic strain rate $\dot{p}$. ω represents the strain increment produced when all arrested dislocations overcome local obstacles and move forward to the next pinned configuration. P_2 and n introduced the influence of cumulated plastic strain on the ageing process.

The elastic modulus, Poisson's ratio are kept the same for the T3R and T8R states. Parameters σ_0 and $\dot{\varepsilon}_0$ related to viscosity were determined based on the relaxation test and CSR tests at different strain rates. These values are kept unchanged for T3R and T8R states. The value of $\dot{\varepsilon}_0$ (1.27×10^{-6}) used here is smaller than that ($\dot{\varepsilon}_0 = 3.5\times10^{-5}$) used for the 2024 Al-Cu alloy [Böhlke et al., 2009].

The ageing hardening term R_a involves 5 distinct parameters: P_1, P_2, α, n, w. As shown in Table 4.4, P_2, n, w have the same values for T3R and T8R states. P_1 and α have been optimised to better fit the experimental results. A typical value of $w = 1\times10^{-4}$ for aluminium alloy is used [Benallal et al., 2008] which is smaller than that (6.81×10^{-4}~7.4×10^{-4}) proposed in Böhlke et al. [2009]. The parameter n is fixed at 0.33 as Böhlke et al. [2009] and [Benallal et al., 2008]. The optimised value of P_1 is consistent with that in Böhlke et al. [2009] (19-50 MPa). The resultant t_0 varies from 1.4 to 5 s (t_0 =0.125 s in [Böhlke et al., 2009], t_0 =10 s in [Gupta et al., 2017]).

The hardening parameters Q_1, Q_2, b_1 and b_2 together with P_1 and α are determined by an optimisation procedure. The Levenberg-Marquardt algorithm is used to minimize the deviation between data from material point simulations and that of the smoothed experimental stress-strain curves during the optimisation procedure. This strategy avoids time-consuming FEM simulations on full dimension specimens [Marais et al., 2012].

4.5.2 Reduced texture methodology (RTM) based polycrystalline plasticity model

The RTM can make use of any polycrystalline plasticity model with a very small number of crystallographic orientations. These orientations are determined from mechanical experiments through inverse optimization instead of crystallographic measurements.

In the framework of RTM, each of the N grains represents a set of physical grains with close orientations, also called "phase". In each "grain" g, with a volume fraction f_g, the

stress $\underset{\sim}{\boldsymbol{\sigma}}_g$ and strain $\underset{\sim}{\boldsymbol{\varepsilon}}_g = \underset{\sim}{\boldsymbol{\varepsilon}}^p_g + \underset{\sim}{\boldsymbol{\varepsilon}}^e_g$ represent values for each phase. In the isotropic case, the macroscopic stress and strain are defined as spatial average within N grains:

$$\underset{\sim}{\boldsymbol{\Sigma}} = \sum_{g=1}^{N} f_g \underset{\sim}{\boldsymbol{\sigma}}_g \quad \text{with} \quad \sum_{g=1}^{N} f_g = 1, \quad \underset{\sim}{\boldsymbol{E}}^p = \sum_{g=1}^{N} f_g \underset{\sim}{\boldsymbol{\varepsilon}}^p_g. \tag{4.10}$$

The unique relationship between the stresses at the macroscopic and crystal scale is established by the "β rule"[Cailletaud, 1992; Sai et al., 2006]. It offers a general way of modelling the transition from elastic to plastic accommodation of intergranular deformations by introducing intermediate deviatoric strain tensors $\underset{\sim}{\boldsymbol{\beta}}_g$ with a non-linear equation between $\underset{\sim}{\boldsymbol{\beta}}_g$ and $\underset{\sim}{\boldsymbol{\varepsilon}}^p_g$.

$$\begin{aligned} &\underset{\sim}{\boldsymbol{\sigma}}_g = \underset{\sim}{\boldsymbol{\Sigma}} + C(\underset{\sim}{\boldsymbol{B}} - \underset{\sim}{\boldsymbol{\beta}}_g) \quad \text{with} \quad \underset{\sim}{\boldsymbol{B}} = \sum_{g=1}^{N} f_g \underset{\sim}{\boldsymbol{\beta}}_g, \\ &\underset{\sim}{\boldsymbol{\beta}}_g = \underset{\sim}{\dot{\boldsymbol{\varepsilon}}}^p_g - \underset{\approx}{\boldsymbol{D}} : \underset{\sim}{\boldsymbol{\beta}}_g \parallel \underset{\sim}{\dot{\boldsymbol{\varepsilon}}}^p_g \parallel \quad \text{where} \quad \parallel \underset{\sim}{\dot{\boldsymbol{\varepsilon}}}^p_g \parallel = \sqrt{\frac{2}{3} \underset{\sim}{\dot{\boldsymbol{\varepsilon}}}^p_g : \underset{\sim}{\dot{\boldsymbol{\varepsilon}}}^p_g}. \end{aligned} \tag{4.11}$$

where $\parallel \underset{\sim}{\dot{\boldsymbol{\varepsilon}}}^p_g \parallel$ represents the von Mises equivalent strain rate for each grain. The scalar modulus C is close to the elastic shear modulus $\mu = E/(1+\nu)/2$. The fourth order tensor $\underset{\approx}{\boldsymbol{D}}$ accounts for anisotropy of materials. $\underset{\approx}{\boldsymbol{D}}$ has 10 independent elements: D_{11}, D_{12}, D_{13}, D_{21}, D_{23}, D_{31}, D_{32}, D_{44}, D_{55}, D_{66} (see [Rousselier et al., 2012]).

Let $\underline{\boldsymbol{n}}_s$ be the unit normal vector of a slip plane and $\underline{\boldsymbol{l}}_s$ the unit slip direction vector. The orientation tensor of the slip system number s is defined as:

$$\underset{\sim}{\boldsymbol{m}}_s = (\underline{\boldsymbol{l}}_s \otimes \underline{\boldsymbol{n}}_s + \underline{\boldsymbol{n}}_s \otimes \underline{\boldsymbol{l}}_s)/2. \tag{4.12}$$

The resolved shear stress τ_s of each slip system reads

$$\tau_s = \underset{\sim}{\boldsymbol{\sigma}}_g : \underset{\sim}{\boldsymbol{m}}_s \tag{4.13}$$

The viscoplastic constitutive equations for each slip system takes the following form [Cailletaud, 1992]:

$$\begin{aligned} &\dot{\gamma}_s = \dot{v}_s \mathrm{Sign}(\tau_s - X_s), \\ &\dot{v}_s = \max\left[0, \left(\frac{|\tau_s - X_s| - r_s}{K}\right)^{\kappa}\right], \\ &r_s = r_s(v_s, v_t), \\ &\dot{\alpha}_s = \dot{\gamma}_s - d\alpha_s \dot{v}_s, \quad X_s = c\alpha_s. \end{aligned} \tag{4.14}$$

where $\dot{\gamma}_s$ and τ_s are respectively the slip rate and resolved shear stress of each slip system. The index s is the slip system number (s = 1 to M); In the case of FCC crystallographic structures, $M = 12$. r_s denotes the isotropic hardening which depends on the cumulated slip v_s of each slip system and kinematic hardening α_s. c and d are two parameters related to a non-linear kinematic hardening model.

To distinguish between different contributions to the hardening term, the classical isotropic hardening law for each slip system is noted by r_s

$$\begin{aligned} &r_s = R_0 + Q_1 \textstyle\sum_{t=1}^{M} H_{st}\left[1 - \exp(-b_1 v_t)\right] + Q_2 \sum_{t=1}^{M} K_{st}\left[1 - \exp(-b_2 v_t)\right] + R_a, \\ &R_a = P_1\left[1 - e^{-\left(\frac{t_a}{t_0(v_s)}\right)^n_s}\right], \quad \dot{t}_a = 1 - \frac{t_a}{w}|\dot{\gamma}_s|, \quad t_0(v_s) = (1/P_2 v_s^{\alpha})^{1/n} \end{aligned} \tag{4.15}$$

where R_0 is the initial critical resolved shear stress (CRSS), which is assumed to be identical for all octahedral slip systems. The diagonal terms of matrix $H_{st}(s = t)$ represent the self-hardening of each system, and the non-diagonal terms ($s \neq t$) represent the latent hardening. The term characterised by (Q_2, b_2) on the right side of equation 4.15 is devoted to characterising the evolution of the hardening matrix at large strains. The hardening matrix K_{st} takes the same form as H_{st}, which is a 12×12 symmetric matrix depending on six parameters (h_1 to h_6, see Rousselier et al. [2009] for the detailed elements of H). For FCC crystallographic structures, with four distinct octahedral slip planes {111} and 12 slip systems, the 12×12 symmetric hardening matrix is supposed to depend on six parameters h_1 to h_6 [Méric et al., 1991]: Similarly, the hardening matrix K_{st} can be presented by parameters k_1 to k_6.

The strain ageing term R_a is added to the hardening in each slip system. P_1, P_2, w, n are the parameters related to strain ageing which have the same definitions as in the previous macroscopic model except for that they are on the slip system scale. The cumulated equivalent strain in the KEMC model is substituted here with the cumulated slip v_s of each slip system. The function of ageing time in each slip system is shown in eq. 4.15.

The macroscopic plastic strain rate is:

$$\underset{\sim}{\dot{\varepsilon}}^p = \sum_{g=1}^{N} \sum_{s=1}^{M} \underset{\sim}{\boldsymbol{m}}_{sg} (\dot{\gamma}_s) \tag{4.16}$$

where $\underset{\sim}{\boldsymbol{m}}_{sg}$ is the orientation matrix of each slip system.

The identification procedure of a reduced texture is outlined in Rousselier et al. [2012]. Firstly, model parameters, including those of reduced texture, are identified and optimised from mechanical experiments without the strain ageing model. Only 6 curves including the tensile curves and Lankford coefficients along L (0°)-T (90°)-D (45°) directions are used as experimental database for the identification process as shown in Fig. 4.23.

The mechanical behaviour of an individual slip system is described through the following hardening parameters:

- 5 isotropic hardening parameters (R_0, Q_1, b_1, Q_2, b_2)
- 2 kinematic hardening parameters (c, d)
- latent hardening parameters (h_2 to h_6) and (k_2 to k_6), assuming $h_1 = k_1 = 1$
- 11 localization parameters (C, D_{11}, D_{12}, D_{13}, D_{21}, D_{23}, D_{31}, D_{32}, D_{44}, D_{55}, D_{66})

The identified values of these parameters are presented in Table 4.5. It should be pointed out that the strain ageing term is not taken into account here ($P_1 = 0$).

Another identification is performed together with the strain ageing term. At the scale of slip system, the value of P_1 is taken as half of that at macroscopic scale due to the angle of slip plane to the loading direction (simple tension). To compensate the over hardening due to strain ageing effect, the value of R_0 is reduced as shown in Table 4.6.

Table 4.5 – Identified hardening parameters of the polycrystalline model for AA2198-T3R.

κ	K(MPa s$^{1/\kappa}$)	C(MPa)	E(MPa)	ν					
25	20	20000	74	0.3					
R$_0$ (MPa)*	Q_1(MPa)	b_1	Q_2(MPa)	b_2	c(MPa)	d			
107	82	4.9	38.4	2.86	14.4	0.65			
h_2	h_3	h_4	h_5	h_6	k_2	k_3	k_4	k_5	k_6
0	0.8071	0.0011	0.0014	0.0074	0.1260	0.1437	0.0577	0	0.1037
D_{11}	D_{12}	D_{13}	D_{21}	D_{23}	D_{31}	D_{32}	D_{44}	D_{55}	D_{66}
1000	11.53	146.34	1000	140.36	0	666.14	453.91	1500	1500

Note: *Decreased when strain againg term is activated

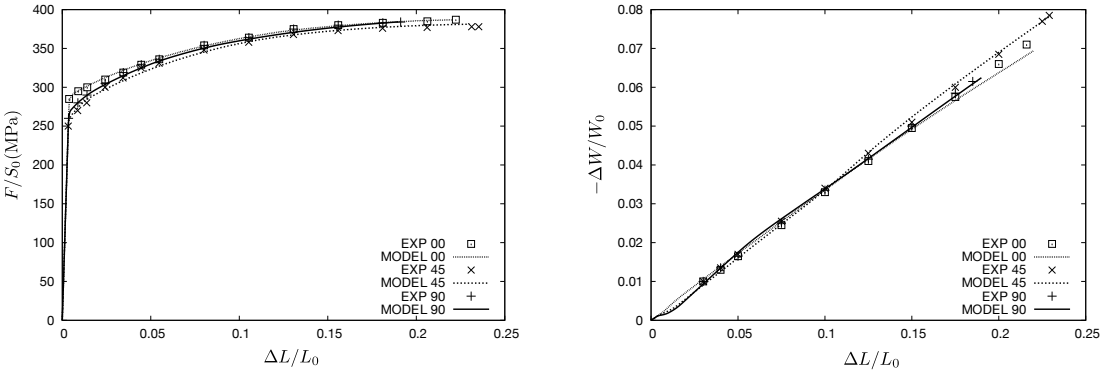

(a) Stress-strain curves

(b) Width reduction-strain curves

Figure 4.23 – Identification of polycrystalline model based on tensile tests of AA2198-T3R material. (a) stress-strain curves along different directions (L (0°)-T (90°)-D (45°); (b) width reduction versus strain. If the material is isotropic the slope in (b) should be 0.5. Experimental data reproduced from [Chen, 2011]

Table 4.6 – Identified strain ageing parameters of the polycrystalline model for AA2198-T3R.

P_1(MPa)	n	P_{2s}(MPa)	w	α	R_0(MPa)
21	0.33	4	10^{-4}	0.1	94

4.6 FEM simulations for AA2198 alloy

4.6.1 FEM simulation of the triggering effect of relaxation using macroscopic strain ageing model

Fig. 4.24 shows the 2D and 3D meshes used for the simulations of CSR and relaxation tensile tests. The 2DST6 mesh contains 1056 C2D8R elements (R denotes reduced). The 3DST6_x1 mesh is completed with 1056 C3D20 elements. 3DST6_x4 mesh has 4 times more elements than 3DST6_x1 due to the partition in the thickness plane. The simulated PLC band at $\dot{E}$ =10^{-2} s^{-1} using these 3 meshes are presented in Fig. 4.25. The band on the 2D mesh is distinct from that on 3D mesh. The band morphology simulated using the mesh with 4 elements in the thickness plane is similar to that using a single element in the thickness plane.

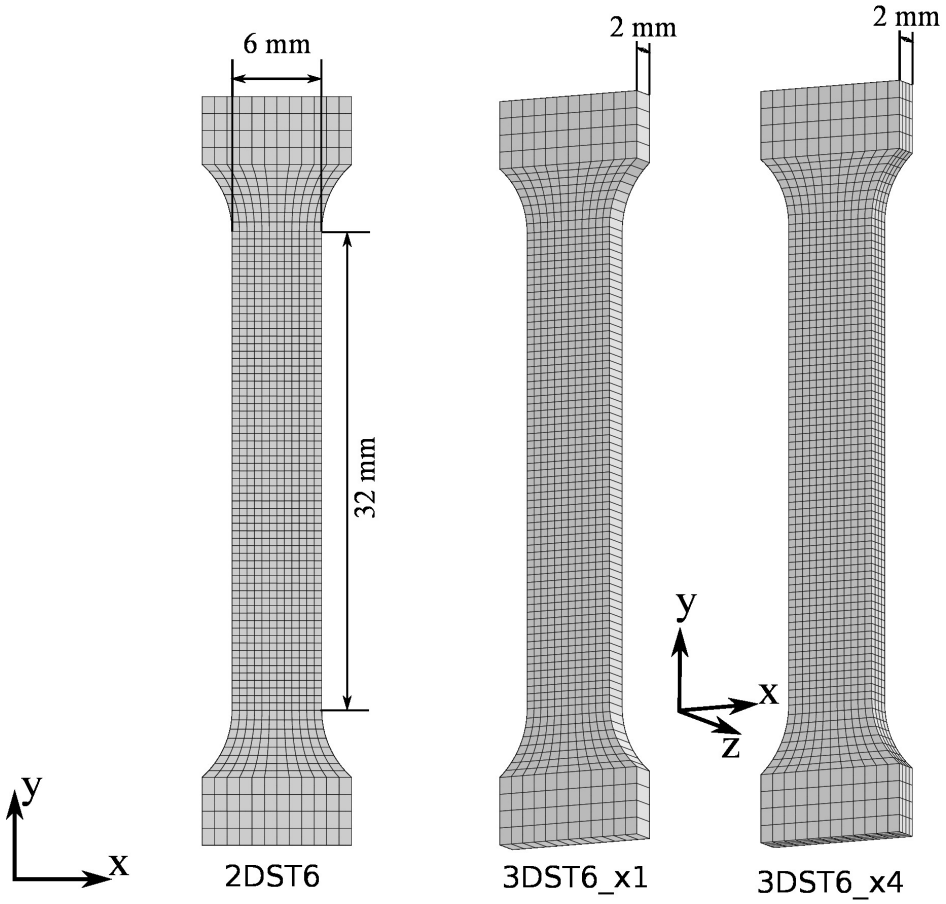

Figure 4.24 – Mesh used for the simulations of CSR and relaxation tensile tests.

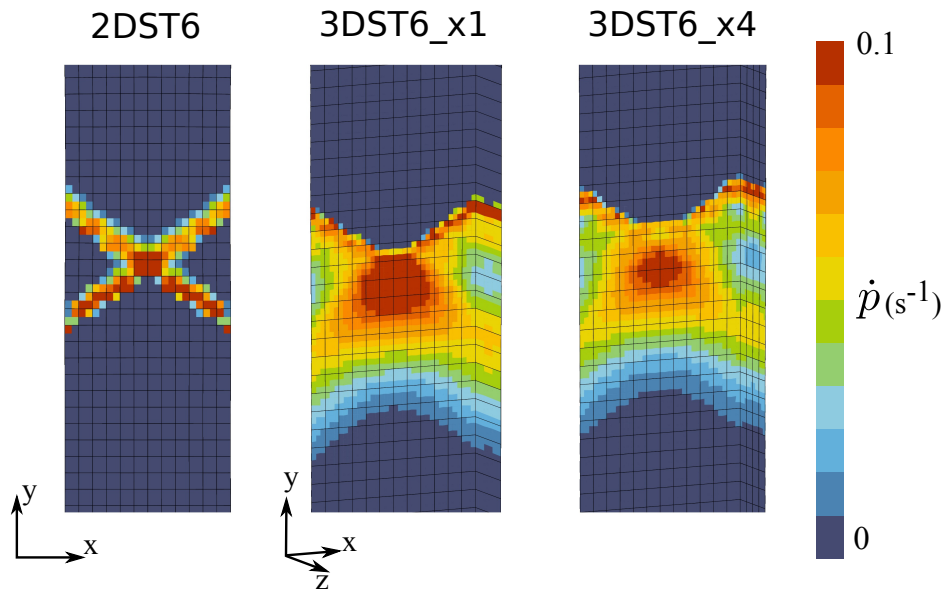

Figure 4.25 – PLC band morphologies at 10^{-2} s^{-1} using different meshes.

Fig. 4.26 shows the simulated macroscopic stress-strain curve for both T8R and T3R states at $\dot{E}$ =10^{-2} s^{-1}. The numerical results are in good agreement with experiments. Fig.

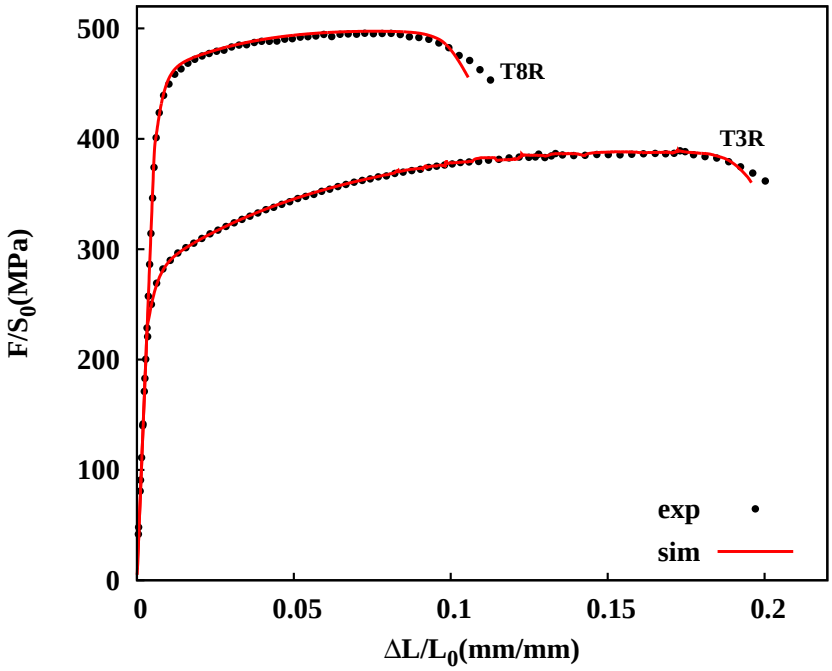

Figure 4.26 – Simulated constant strain rate tensile curves at $\dot{E}$ =10^{-2} s^{-1} for T3R and T8R with the macroscopic model.

4.27(a) and (b) shows the numerical spatio-temporal pattern of the CSR test and single relaxation test using 2D mesh of T3R material. Fig. 4.27(c) and (d) presents the result on the 3D mesh (3DST6_x1). The triggering effect after relaxation is reproduced successfully. 3D simulation is closer to DIC measurement presented in Fig. 4.17. Fig. 4.28 shows the stress-strain curve at strain rate 10^{-2} s^{-1} with one relaxation applied at ε=0.02 (corresponds to Fig. 4.27(d)). The band morphology is also presented.

Fig. 4.29 gives the numerical spatio-temporal patterns of CSR and multiple-relaxation tests of T8R material. There is no localization band that could be found for the CSR condition. However, slight trace of localization bands initiated after re-straining. These results are very similar to the DIC measurement presented in Fig. 4.20(b).

4.6.2 Thin sheet compact tension (CT) specimen

The previous simulation results reproduce the major experimental observations in tensile tests which allows us to apply these models to other specimen geometries. As reported by Morgeneyer et al. [2014]; Buljac [2017], multiple localization bands have been observed in the notch area of CT specimens made by AA2198-T3R and T8R alloys. The final fracture is found to develop following these localization bands. However, the origin of these bands is still obscure. To investigate the localization patterns due to strain ageing and compare with that observed in CT specimen by laminography-DVC [Morgeneyer et al., 2014], we simulated the tearing test of CT specimen with these models presented in the previous parts. Particularly, the relaxation effect in CT specimen is investigated as the stepwise loading mode during in-situ laminography test is closer to the current relaxation test. The specimen is scanned after each loading by maintaining the notch opening displacement [Morgeneyer et al., 2014].

The objective of finite element simulations in this part is to investigate the localization

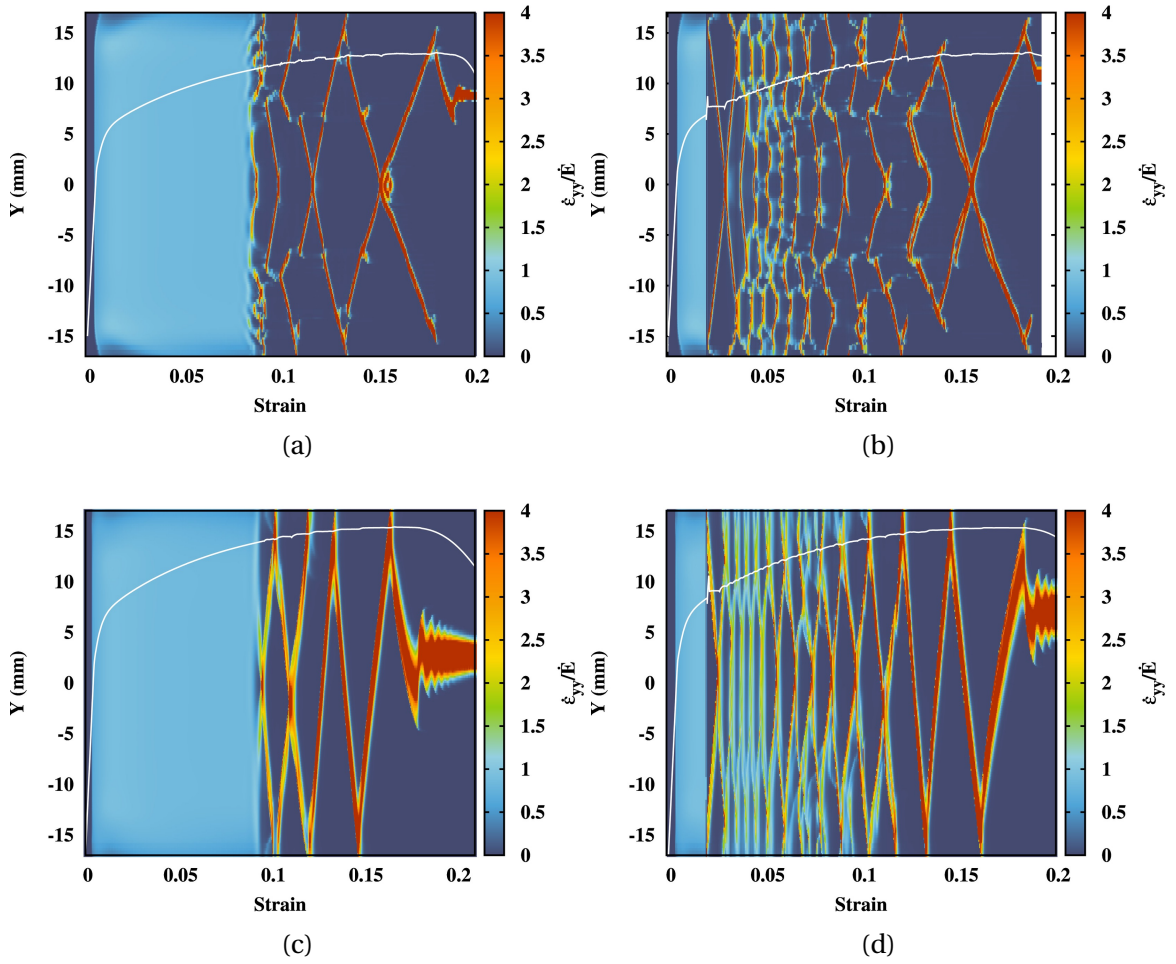

Figure 4.27 – Comparison of the spatio-temporal patterns of CSR and relaxation tests at $10^{-2}\,s^{-1}$ for AA2198-T3R: (a) 2D FEM simulation of CSR test; (b) 2D FEM simulation involving a single relaxation at $\varepsilon = 0.02$; (c) 3D FEM simulation (3DST6_x1) of CSR test; (d) 3D FEM simulation (3DST6_x1) involving a single relaxation at $\varepsilon = 0.02$. These simulated patterns could be compared with experimental results in Fig. 4.17

behaviour around the notch tip of thin sheet CT specimen. The strain rate pattern after re-straining in CT specimen is compared with that under constant strain rate loading. We use the same specimen geometry ($60 \times 70 \times 1$ mm) as that in [Morgeneyer et al., 2014; Rousselier et al., 2017] in order to make a direct comparison with previous laminography and simulation results. Fig. 4.30 shows the detail of the mesh. The total element number is 29360. The design is completed with C3D20R hexahedral elements and C3D15R prismatic elements. The element size in the refined notch region is $0.125 \times 0.1 \times 0.125\,mm^3$. Displacements at a constant velocity of $10^{-3}\,mm\,s^{-1}$ were applied as loading conditions through two "rigid" triangular blocks. The positions of these two blocks are determined according to experimental conditions [Morgeneyer et al., 2014]. To fix the rigid body motion, the point at (x = 60 mm, y= 0 mm, z= 0 mm, the origin of the coordinate system is located at the mid-plane of left side) is fixed ($U_x = 0$, $U_y = 0$, $U_z = 0$). To prevent buckling, the displacement U_z is set to be 0 at the mid-plane z = 0 mm of the area surrounding the critical notch zone.

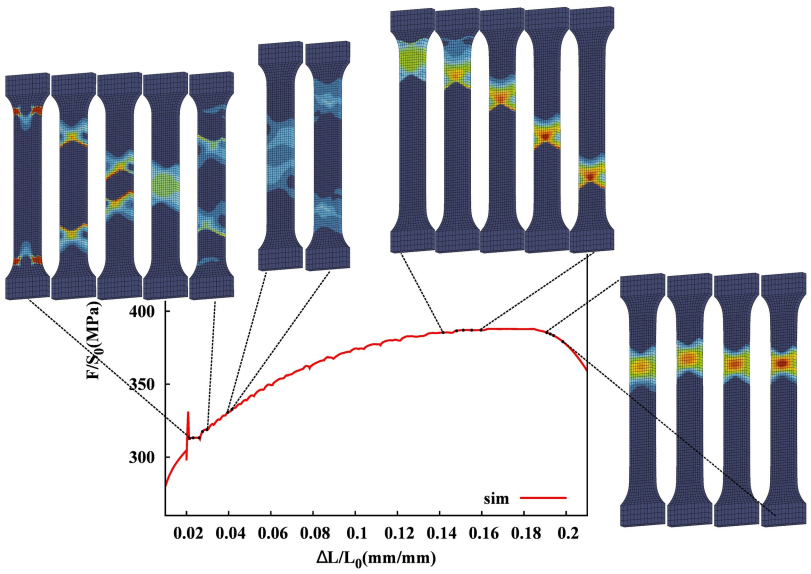

Figure 4.28 – Strain rate bands in 3D tensile specimen (3DST6_x1) at strain rate 10^{-2} s^{-1} with one relaxation at $\varepsilon = 0.02$.

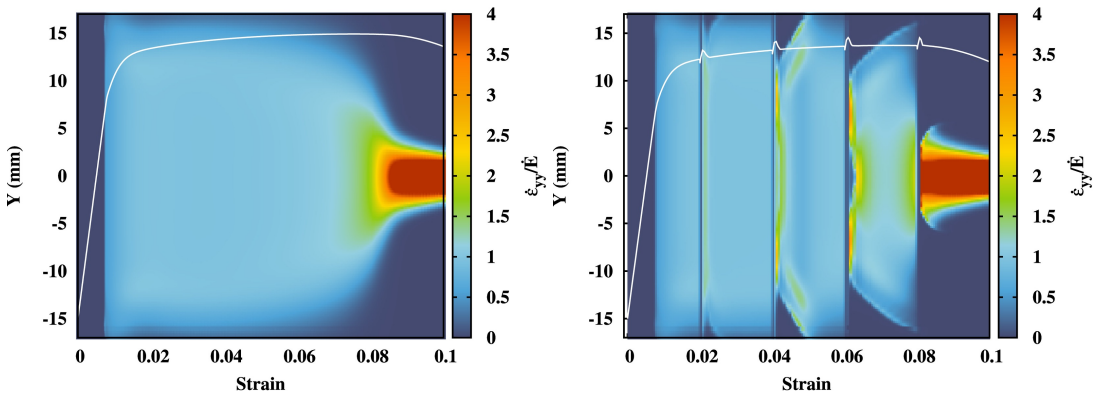

Figure 4.29 – 3D FEM simulation (3DST6_x1) involving relaxation is compared with the constant strain rate (CSR) curve at the same applied strain rate ($10^{-2} s^{-1}$) for AA2198-T8R. These results can be compared with Fig. 4.20(b).

Simulations using the macroscopic strain ageing model on CT specimen

The simulation results of AA2198-T3R CT specimen using the macroscopic strain ageing model are shown in Fig. 4.31. The section located at 1 mm to the notch tip (Δx =1 mm) is extracted for observation. 5 snapshots are selected for both of the CSR and stepwise loading tests whose corresponding time instants are marked on the force-time curves. The "waffle-like"strain rate pattern composed of multiple parallel or orthogonal slant bands are observed for both CSR and stepwise loading conditions. The pattern for CSR condition shows more intermittent behaviour. The pattern is less symmetric compared with that after relaxation. A "X"type pattern is always found after the restraining which is very stable. The strain rate inside these bands is visibly higher than during CSR loading. These "X"type bands split into multiple bands after a very short time and seems try to escape from the notch area. Fig. 4.31 shows the patterns after the first (t= 42 s) and second (t= 83 s) re-straining.

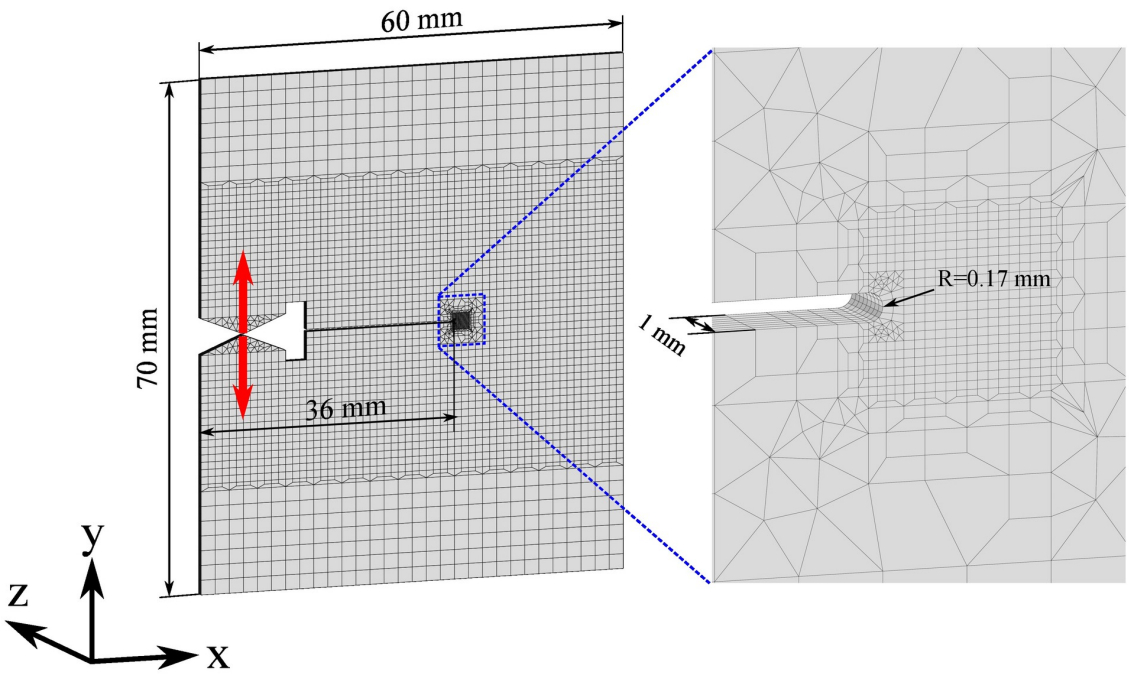

Figure 4.30 – Mesh of the thin sheet CT-like specimen.

CSR and stepwise loading conditions were also performed on the CT specimen using the parameters of T8R material as shown in Fig. 4.32. For this material, there is no PLC effect for the CSR loading which is validated by both of DIC measurement and simulations on tensile specimens. For the relaxation tests, only a very slight tendency for localization band formation can be seen right after re-straining. Compared to T3R specimen, these shallow bands can easily be neglected as shown in Fig. 4.20 and Fig. 4.29. Only two snapshots of the strain rate pattern for CSR loading are presented in Fig. 4.32. There is no multiple band formation in CSR condition which has been checked for the whole deformation process. For the stepwise loading, "X"type localization bands are observed again as in the T3R material. These bands evolved into multiple bands later. Compared to T3R, there are less localization bands in T8R and the pattern is relatively more homogeneous. Once the bands propagate towards the region far from the notch tip, no more band could be seen.

Simulations using the polycrystal model for CT specimen

The simulation results using the polycrystal model (RTM) combined with a DSA term which accounts for material anisotropy are presented here. Fig. 4.33 shows the plastic strain rate patterns at $x = 1$ mm to the notch tip using the polycrystal model without DSA term. Unlike the macroscopic DSA model (see Fig. 4.31), the plastic strain rate pattern is relatively homogeneous without multiple localization bands using the current parameter set with reduced texture.

The DSA term is then activated by using the parameter set presented in Table 4.6. The P_1 used for this polycrystal model is much lower than the macroscopic model. As shown in Fig. 4.34, the DSA term helped generating heterogeneities of plastic strain rate patterns. However, compared to the macroscopic model, the localization bands are not that clear. In addition, the curves of the macroscopic DSA model (in Fig. 4.31) and of the polycrystal

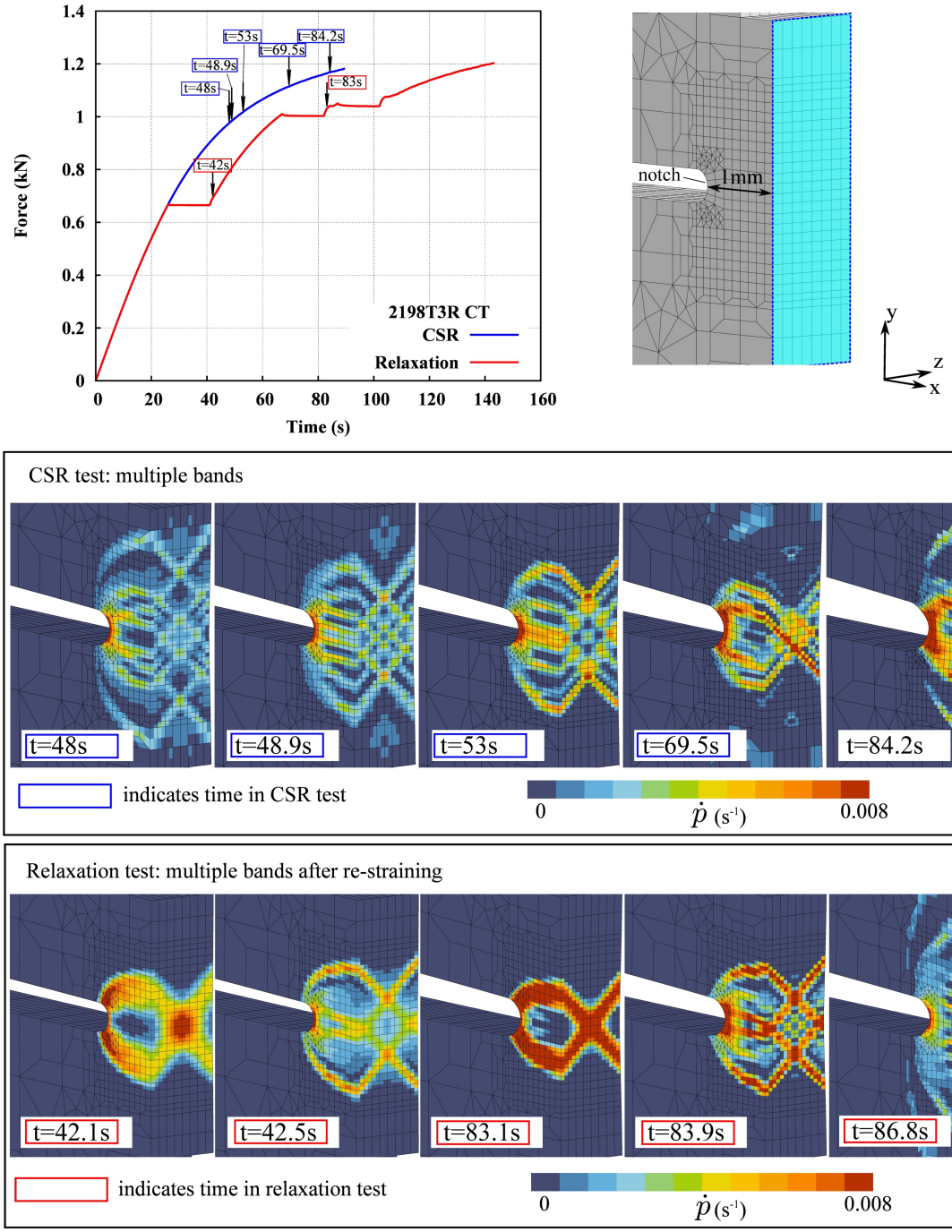

Figure 4.31 – Force-time curves of the CSR and the stepwise loading of AA2198-T3R CT specimen. Strain rate patterns on the surface at Δx =1 mm to the notch tip. The time instant of each snapshot is given and marked on the force-time curves. Simulations are performed with the macroscopic strain ageing model.

model without DSA term (in Fig. 4.33) are superposed with the current curve. The curve predicted by the polycrystal model is slightly lower than the macroscopic model.

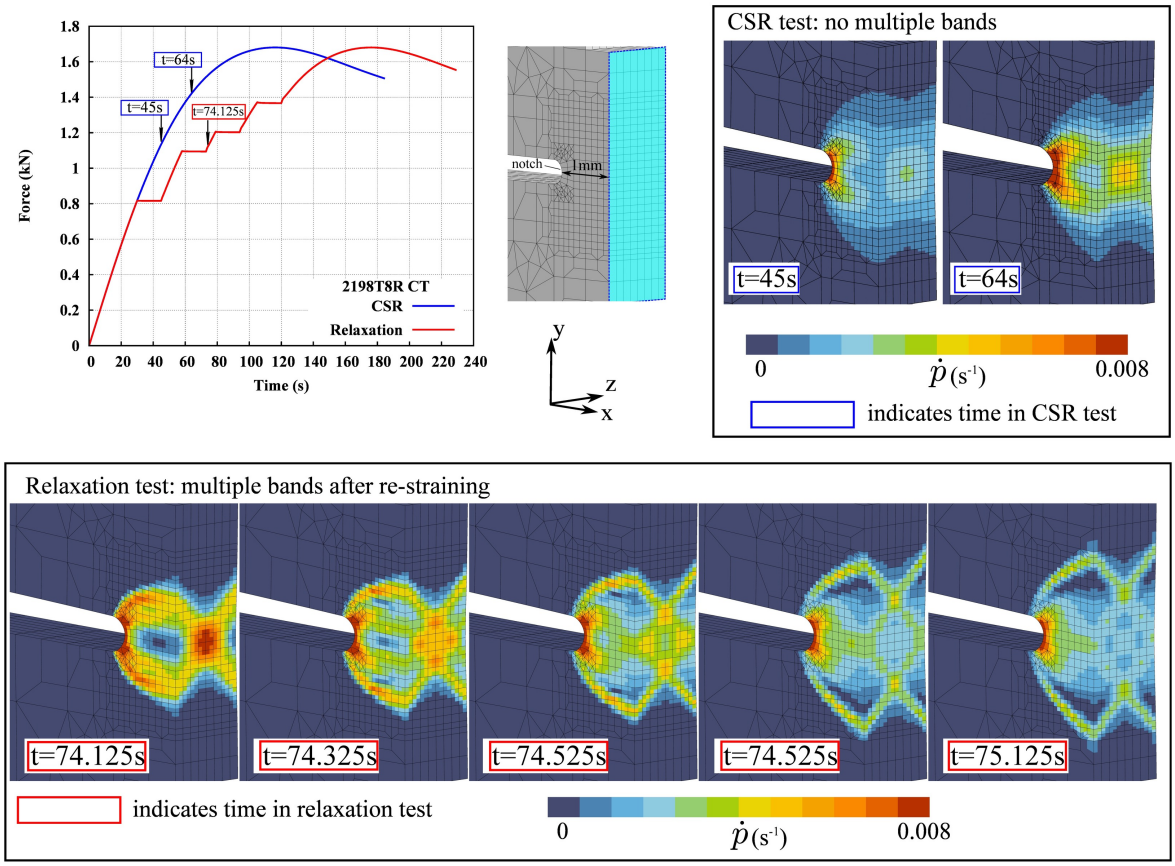

Figure 4.32 – Multiple strain rate localization bands triggered after re-straining in AA2198-T8R compared with constant strain rate loading condition. The corresponding positions of these images are marked on the force-time curve. Simulations are performed with the macroscopic strain ageing model.

4.6.3 Discussions

Experimental results compared with previous studies

Deschamps et al. [2013] did not find PLC effect in the naturally aged AA2198 alloy (T351). Ovri and Lilleodden [2015] also reported the absence of plastic instability in the naturally aged AA2198 alloy in which higher concentration of solute atoms is found. Meanwhile, PLC phenomenon is observed for an overaged temper treatment at a higher temperature (370°C) different from Deschamps et al. [2013]. The authors made the conclusion that DSA is not sufficient to account for the plastic instability in AA2198 alloy. A diffusion-controlled mechanism which involves the operation of a pseudo-locking mechanism that accompanies order hardening was proposed.

Contrary to Deschamps et al. [2013] or Ovri and Lilleodden [2015], we showed that the naturally aged AA2198 alloy is indeed very sensitive to PLC effect. This result can be supported by the work of Alexopoulos et al. [2013], though the author did not pay attention to the plastic instabilities showed on the T351 curve. The artificially aged temper (T8R) is less sensitive to PLC effect. This result suggests that DSA is still the main mechanism for triggering plastic instabilities in AA2198-T3R alloy due to higher Li concentration in this naturally aged state. The T8R state is less sensitive because of the depletion of Li due to precipitation.

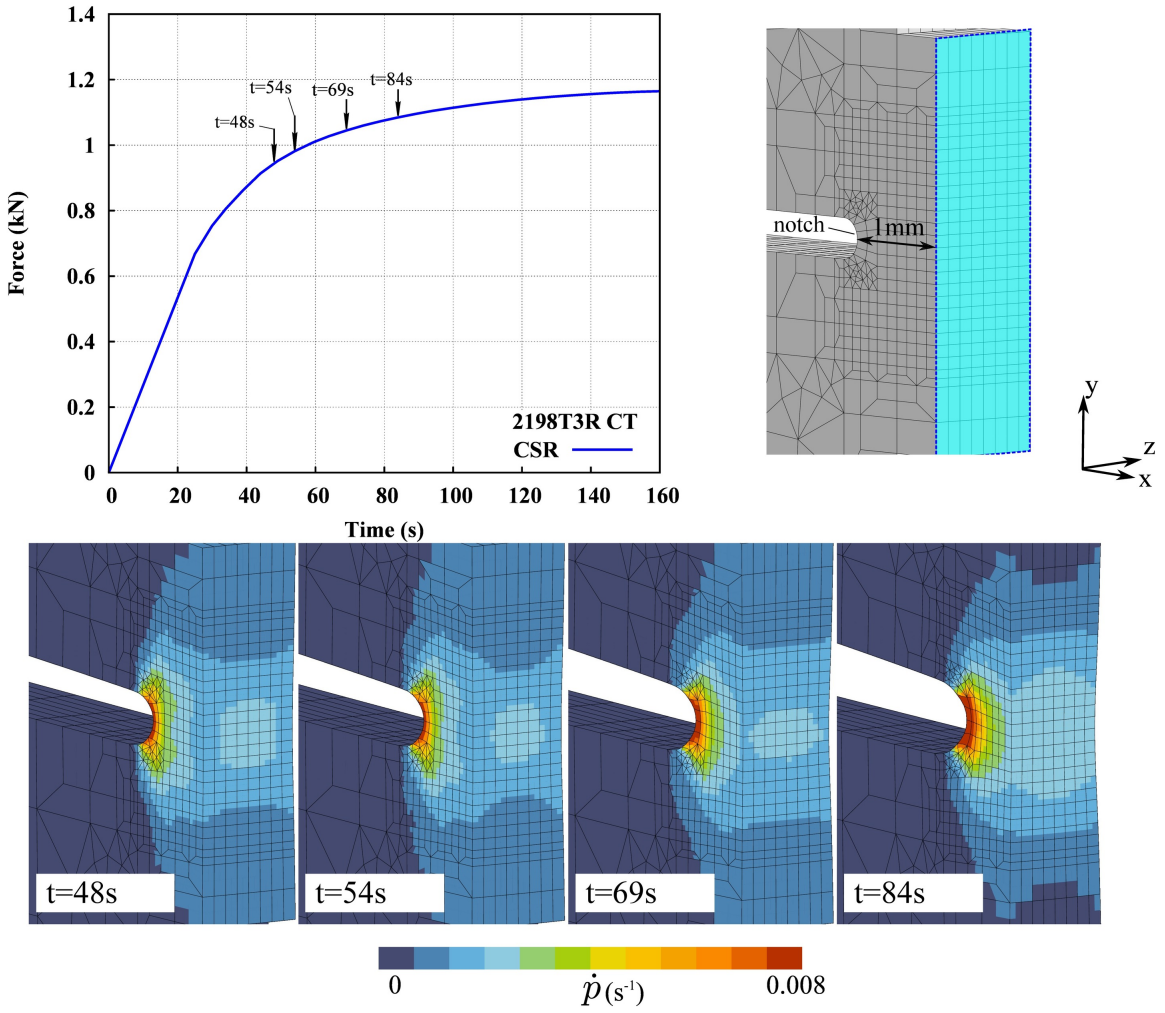

Figure 4.33 – Plastic strain rate patterns simulated by the polycrystalline model without DSA term.

To some extent, the triggering effect after relaxation observed here is very similar to that in a FeMnC alloy [Allain et al., 2011]. There is always a Lüders like plateau after re-straining followed by type A serrations. Allain et al. [2011] attributed this phenomenon in the FeMnC alloy to the triggering of twinning promoted by dislocation pinning during relaxation, whilst this explanation cannot be applied to the current aluminium alloy.

The current relaxation tests and simulations show that the DSA mechanism could explain this premature triggering effect. As shown in Fig. 4.19, the PLC effect did not appear right after the re-straining. Due to solute diffusion, the ageing during relaxation and pre-strain history modified local Li distribution which might result in a modification of the critical strain. In addition, the strain rate heterogeneity due to Lüders effect after reloading could also allow an early triggering of PLC bands.

Perturbation analysis

As presented in [Mazière and Dierke, 2012], the perturbation analysis can be used to predict the critical strain for the onset of PLC effect. Following this method, the influence of relaxation on the prediction of critical strain is investigated here. In Figure 4.35, the instability indicator (SIS = 0 means stable; SIS = 1 means unstable) is detected based on

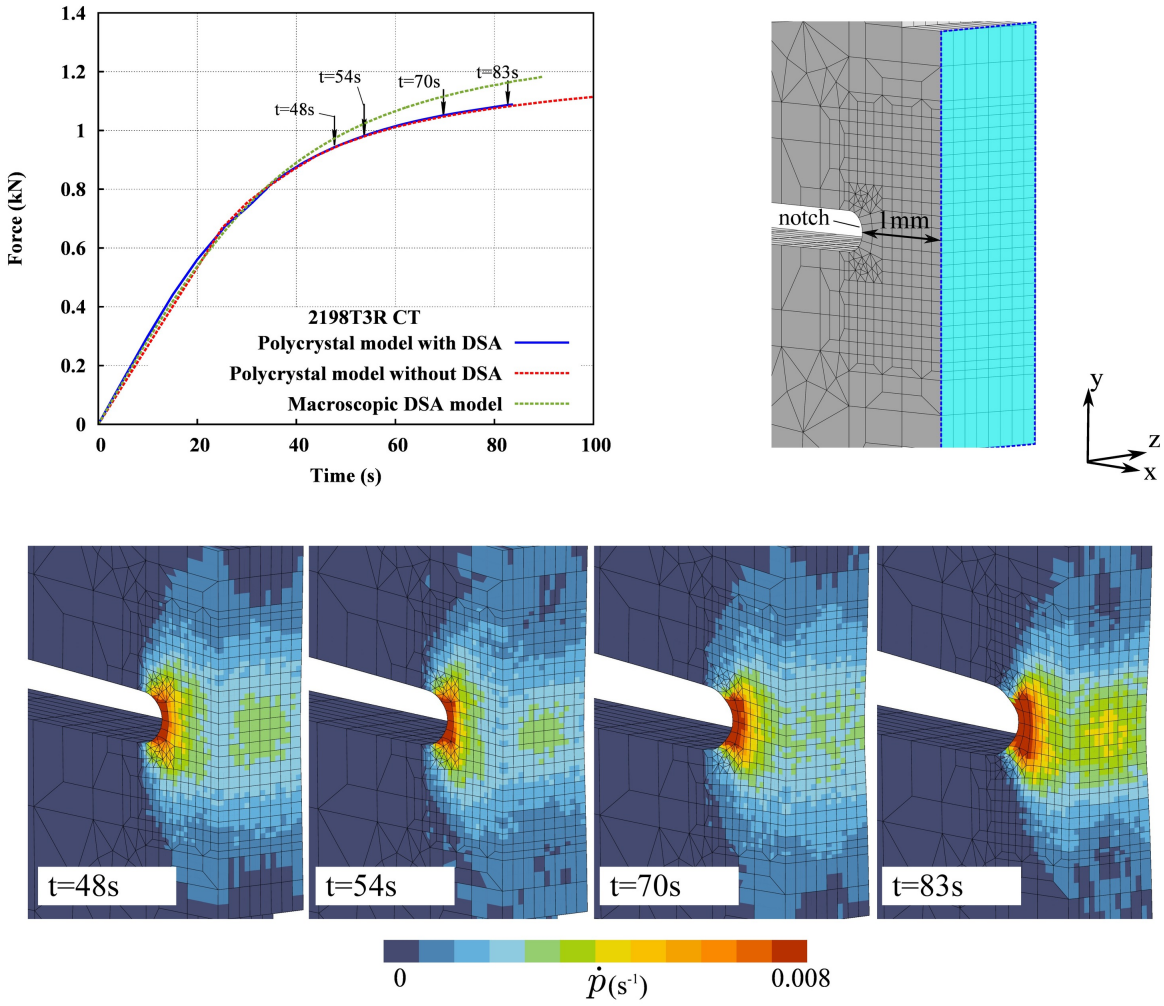

Figure 4.34 – Plastic strain rate patterns simulated by the polycrystalline model combined with DSA term (P_{1s} = 21; R_{0s} = 94) of AA2198-T3R CT specimen. The curves of the macroscopic DSA model (in Fig. 4.31) and of the polycrystal model without DSA term (in Fig. 4.33) are superposed with current curve.

single material point in order to predict the onset of PLC effect (see Mazière and Dierke [2012]). However, we observed that the relaxations have no influence on the critical strain detected by single material point simulation except for a short jump from 0 to 1 after re-straining.

The instability indicator is also detected based on full FEM mesh (see 2DST6 in Fig. 4.24) as long as any integration point attains SIS = 1. As shown in Fig. 4.36, for the relaxation tests, the indicator is activated right after the first re-straining. For CSR test, the indicator shows some fluctuations around strain = 0.11. The detected critical strain by the indicator is slightly lower than that at the onset of visible serrations on the stress-strain curve. This is due to the fact that instabilities firstly occur in the shoulder area before influencing the gauge area. These numerical results suggest that the single material point method can not detect the premature triggering of PLC effect presented in the current section. It also confirms that the heterogeneity occurred after re-straining in the shoulder area is the precursor of Lüders type localization. The propagation of the Lüders band could therefore be responsible for leaving behind a slightly heterogeneous mechanical

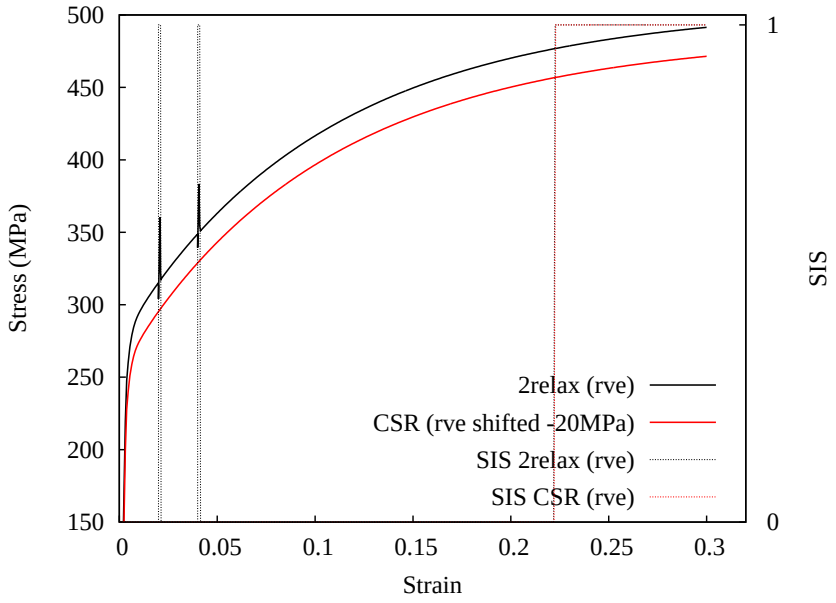

Figure 4.35 – Simulations involving 2 relaxations (black curve) are compared with the constant strain rate curve (red curve) at the same applied strain rate. The relaxation curve is shifted down for 5 MPa. ε_c is detected by the criterion proposed in [Mazière and Dierke, 2012] based on a single material point.

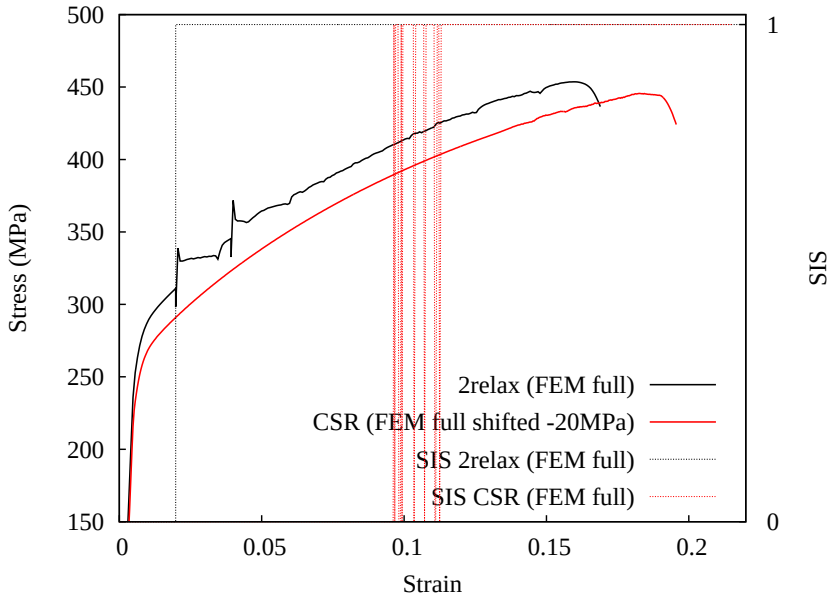

Figure 4.36 – Simulation involving 2 relaxations (black curve) is compared with the constant strain rate (CSR) curve at the same applied strain rate. ε_c is detected by the criterion proposed in Mazière and Dierke [2012]. The detected criterion (SIS) in this figure is based on full FEM mesh including shoulder area.

state which favours the early triggering of the PLC bands.

4.7 Conclusions about PLC effect in AA2198 alloy

From section 4.4 to 4.6, the strain ageing effect in two grades of AA2198 alloy was studied systematically through tensile tests, DIC measurement and finite element simulations.

The PLC effect is observed for AA2198-T3R tensile specimens under constant strain rate loading conditions. It is found that relaxation and a sudden strain rate change can trigger localization bands and significantly advance the onset of PLC effect in T3R material. PLC effect has not been observed for AA2198-T8R specimens. Only shallow localization bands could be seen after re-straining located in the region close to the shoulders of specimens. These bands failed to propagate.

An elastoviscoplastic model accounting for strain ageing is identified based on tensile experiments at different strain rates in order to simulate the strain ageing effect in T3R and T8R specimens. The spatio-temporal evolution of localization in tensile specimen is well captured. The triggering effect of localization bands after re-straining for T3R and the slight immobile bands for T8R are reproduced respectively.

Three-dimensional FE simulations using strain ageing model demonstrated that the triggering effect of PLC effect after re-straining observed in tensile tests can also be noticed in CT specimen. Using the material parameters of T8R, multiple bands are produced after re-straining, whereas the constant strain rate loading can not produce multiple localization bands. These simulations support the idea that the strain bands observed by laminography-DVC are possibly due to strain ageing [Morgeneyer et al., 2014, 2016]. These results may also explain why multiple strain bands can be observed in T8R considering that stepwise loading is applied during in-situ laminography tests. Unlike experiments, the simulated bands using the macroscopic strain ageing model show high mobility. Other softening mechanism might be able to stabilize these localization bands.

There is only a moderate anisotropy found in AA2198 alloy. The simulations using polycrystalline model shows that the polycrystalline frame has little influence on the band formation. Taupin et al. [2016] showed that microstructural heterogeneity can lead to band formation. Nevertheless, the simulated pattern is different from [Morgeneyer et al., 2014]. The current experimental and numerical results suggest that the patterns observed by laminography-DVC in these Al-Cu-Li alloys can be better explained with DSA.

Experiments on CT specimens should be performed with DIC measurement. The observation around the notch tip with high resolution DIC system could validate the assumptions made by the current numerical simulations. The strain bands around notch after re-straining in T8R CT specimens might display different features on the surface compared with CSR condition.

Chapter 5

Observation and simulation of the PLC effect in SENT specimens

Summary

The localization phenomena induced by the Portevin-Le Chatelier effect (PLC) were investigated in single edge notch tension (SENT) specimens of a C-Mn steel (A42). The specimens are tested at room temperature outside the PLC domain and at a higher temperature (175 °C) in the PLC domain. Serrations and corresponding localization bands of plastic strain rate related to the PLC effect are observed at 175 °C. A huge drop of fracture resistance (with a factor of about 2 in ductility) is observed at 175 °C compared with 20 °C. Slant fracture is observed at 175 °C while flat fracture is found at 20 °C. In addition, the Lüders effect is observed for all the test conditions including those at room temperature without PLC effects. The digital image correlation (DIC) analysis revealed very different strain localization kinematics at these two temperatures. With the presence of PLC effects at 175 °C, the strain localization around crack tip showed unstable flip-flop characteristics in particular during crack propagation. The deformation rate inside localization bands was measured. These observations indicate that the abnormal strain localization induced by PLC effect is responsible for the early loss of symmetry of plastic zone evolution which consequently leads to the slant fracture. Simulations are carried out using an elastoviscoplastic model involving dynamic strain ageing. The localization behaviour is qualitatively reproduced.

Résumé

Les phénomènes de localisation dus à l'effet Portevin-Le Chatelier (PLC) dans les éprouvettes SENT (Single Edge Notched Tension) en acier C-Mn (A42) ont été étudiées. Les éprouvettes sont testées à température ambiante en dehors du domaine PLC et à une température plus élevée (175 °C) dans le domaine PLC. Les oscillations et les bandes de localisation de vitesse de déformation plastique associées dues à l'effet PLC ne sont observées qu'à 175 °C. Une perte importante de de ductilité (avec un facteur d'environ 2) est observée à 175 °C par rapport à 20 °C. La rupture en biseau est observée à 175 °C tandis qu'un faciès de rupture plan est observé à 20 °C. De plus, l'effet Lüders est observé pour toutes les conditions d'essai y compris celles à température ambiante. L'analyse de corrélation d'images (DIC) a montré des cinématiques

de bande de localisation très différentes à ces deux températures. Avec la présence d'effets PLC à 175 °C, les localisations autour de la pointe de fissure présentent des caractéristiques d'instabilité du type flip-flop. Le taux de déformation à l'intérieur des bandes de localisation a été mesuré. Ces observations indiquent que l'effet PLC a déclenché la localisation de déformation qui est responsable de la perte de symétrie de l'évolution de la zone plastique et, par conséquent, de la rupture en biseau. Des simulations par éléments finis sont réalisées à l'aide d'un modèle élastoviscoplastique contenant un terme de vieillissement dynamique par la déformation. Le comportement de localisation est correctement reproduit.

This chapter is reproduced from: Ren, S.C., Morgeneyer, T. F., Mazière, M., Forest, S & Rousselier G. (2017). DIC field measurements and simulations of Lüders and Portevin-Le Chatelier bands in notched steel specimens at two temperatures. *To be submitted.*

Contents

5.1 Introduction

The Portevin-Le Chatelier (PLC) has been widely observed in various industrial alloys within a certain range of temperature and strain rate. It is usually evidenced by the stress serrations (or 'jerky flow') and associated propagative localization bands of plastic strain rate at macroscopic scale. The localization bands leave traces on the surface of material sheets during material forming. A good characterization of the PLC sensitive domain is useful for eliminating these manufacturing defects. In addition, the degradation of mechanical properties have been considered to be related to the PLC effect, such as loss of toughness and ductility [Chakravartty et al., 1983; Amar and Pineau, 1985; Gomiero et al., 1992; Kim et al., 2004; Wang et al., 2012]. Microscopically, this effect is due to the dynamic strain ageing (DSA) which is attributed to the pinning/unpinning of mobile dislocations by diffusion of solute atoms [Cottrell and Bilby, 1949], though other mechanisms, such as pseudo PLC mechanism [Brechet and Estrin, 1996] and precipitate shearing [Chmelík et al., 1998], may also influence it.

For aluminium alloys like Al-Mg [Chihab et al., 1987; Clausen et al., 2004; Ait-Amokhtar et al., 2006; Halim et al., 2007] and Al-Cu [Ranc and Wagner, 2005; Böhlke et al., 2009], the PLC effect is usually manifested at room temperature. For ferritic C-Mn steels [Wang et al., 2012; Ranc et al., 2016], it is detected at around 200 °C. It has also been reported in the Nickel based superalloy around 500 °C [Dybiec and Chaturvedi, 1991; Rao et al., 1995; Fournier et al., 2001; Cai et al., 2017], and around 600 °C for Cobalt based super alloy [Mazière and Pujol d'Andrebo, 2015] as well as in titanium alloys around 400 °C [Prasad and Varma, 2008].

Before the wide application of imaging techniques, such as digital image correlation (DIC) and digital image thermography (DIT), the identification of the PLC effect was usually based on the serrations observed on the stress-strain curves of uni-axial tensile tests. However, this method will cause ambiguities as it is hard to identify the small serrations from the measurement noise. Localization bands may occur with nearly invisible serrations (see Chapter 4). It is particularly important for the calibration of models for predicting the critical strain of the onset of PLC effect [Mazière and Dierke, 2012]. Non-contact field measurement method reveals more details about the PLC effect with a good accuracy [Besnard et al., 2006]. In the literature, Al-Mg alloys might be the most popular candidates for the study of the PLC effect which shows intensive serrations at room temperature. This feature makes the experimental set-up less demanding. The band properties like width, propagation speed, carried strain/strain rate and its spatio temporal evolution during smooth tensile tests have been investigated with DIC in many works [Tong et al., 2005; Ait-Amokhtar et al., 2006; Halim et al., 2007; Zdunek et al., 2008; Casarotto et al., 2009; De Codes et al., 2011; Cheng et al., 2015; Cai et al., 2016a; Yuzbekova et al., 2017]. The PLC bands have also been characterised by DIC in Al-Cu alloys via tensile tests at room temperature [Jiang et al., 2005; Zhang et al., 2005] and in Chapter 4. The DIC measurement of PLC effects at high temperature have only been applied for the tensile tests of Nickel based alloys [Swaminathan et al., 2015; Cai et al., 2017]. Recently, Ranc et al. [2016] observed the PLC effect in C-Mn steel tensile specimen at 200 °C with DIT.

In addition, most real structures possess complex geometrical features such as holes and edges for design purposes and they may contain defects and flaws such as fatigue cracks. With the presence of notch, the highly inhomogeneous strain gradient may make these sites more sensitive to the PLC effect. Even in uni-axial tensile tests, the localization bands are usually found to nucleate at the edge of the curved transition zone to the grip section [Klusemann et al., 2015]. In the literature of PLC measurement, little attention

has been paid to other geometries than smooth tensile ones [Graff et al., 2004]. Coër et al. [2013] studied the Lüders and PLC bands during simple shear test. Le Cam et al. [2017] showed the PLC bands during equibiaxial tensile loading. Concerning the compact tension (CT) specimen, only the Lüders bands have been observed by Wenman and Chard-Tuckey [2010] at room temperature. However, many standard fracture toughness tests require notched specimens like CT, SENT and SENB (single edge notched bending). A measurement of the band formation in those cases other than smooth tensile ones could be useful for validating numerical results as the interaction between PLC effect and ductile tearing is unknown at present. As reported by Hickey and Ravi-Chandar [2016], two kinds of plastic strain localized zones that precede fracture were observed and resulted in different fracture modes for 6061 alloy with two different heat treatments. Recent observations by in-situ synchrotron X-ray laminography also reported slant intermittent localization bands at early loading stages ahead of the notch of 2000 alloy CT-like specimens [Morgeneyer et al., 2014, 2016; Buljac et al., 2016]. The damage event was found at the final stage of loading following the trace of localization bands. The bands measured by DIC may provide new insights for understanding fracture events. To the best of our knowledge, this is the first investigation of the localization bands related to strain ageing measured by DIC at high temperature in a SENT specimen.

Based on the DSA theory, theoretical models have been developed for modelling the PLC effect. A phenomenological model that uses the negative strain rate sensitivity (nSRS) to explain the serrations was proposed by Penning [1972] and Kubin and Estrin [1985] which is able to reproduce the main features of PLC effect like serrations and localizations [Benallal et al., 2006]. Another macroscopic model [McCormick, 1988; Mesarovic, 1995; Zhang et al., 2001] is based on a time varying state variable namely the ageing time t_a which controls the mean local concentration of solute atoms at dislocations. This model interpreted the physical DSA mechanism at dislocation scale. A modified version has been implemented into the finite element code Zset [Graff et al., 2004, 2005, 2008; Mazière et al., 2010]. In this work, the McCormick approach will be used for simulations.

The aim of the current section is to investigate the kinematic and mechanical characteristics of PLC bands during ductile tearing at high temperature with C-Mn steel (A42) single edged notch tension (SENT) specimens via DIC measurement. The chosen material has been tested at room temperature and low temperature (from -150 °C to 0 °C) by Marais et al. [2012]. Wagner et al. [2006] and Huang et al. [2015] reported that the minimum nSRS and elongation occurs around 200 °C for A42 steel. The temperature for characterizing the PLC effect is chosen to be 175 °C which is in the nSRS domain.

The chapter is organised as follows. In section 5.2, the results of mechanical tests and DIC measurement at room temperature and 175 °C are presented. The comparison of the spatio-temporal behaviour of localization bands at these two temperatures is drawn. In section 5.3, the formulation of the McCormick type model including the identification procedure is given. 3D finite element simulations are conducted trying to reproduce the experimental observations. In section 5.4, a discussion will be given on the experimental and numerical results especially on the flat and slant fracture modes observed at two temperatures.

5.2 Experimental results

5.2.1 C-Mn steel and specimen geometry

The investigated C-Mn steel (A42) is used for the secondary loop of pressurized water reactor (PWR) [Marais et al., 2012]. The tubes made by this material are subjected to pressure ranging from 70 to 80 bar and temperature from 0 °C up to 280 °C. The chemical composition of A42 steel can be found in Table 5.1. This C-Mn steel is very similar to the

Table 5.1 – Chemical composition (mass fraction) of the A42 steel used for the current study.

C	N	Al	Si	P	S	V	Cr	Mn	Ni	Cu	Nb	Mo	Sn
0.15	0.004	0.019	0.19	0.034	0.021	< 0.002	0.034	0.73	0.05	0.041	< 0.002	0.006	0.003

TU48C [Belotteau, 2009]. The interstitial atoms such as carbon and nitrogen play an important role in the strain ageing. Carbon is involved during the elaboration process. The content of aluminium was kept low to avoid the formation of aluminium nitrides (AlN), so that free nitrogen remains in the crystalline lattice which also makes this steel sensitive to dynamic strain ageing.

The SENT specimens are prepared with the geometry illustrated in Fig. 5.1. This sample geometry was chosen to assess the influence of PLC effect on ductile tearing in a case where the entire ligament undergoes plastic deformation at the beginning of the test. These specimens are cut from a seamless pipe obtained by a circular rolling process with longitudinal direction along the transverse direction (T). The microstructure is composed of ferrite and pearlite. The ferrite grain is equiaxed in the LS and TS plane [Marais et al., 2012].

5.2.2 Mechanical tests for SENT specimens

The mechanical behaviour of this material, especially the Lüders effect, has been investigated by Marais et al. [2012] under simple tension from -150 °C to 20 °C. The Lüders effect can be observed in the whole temperature range. A similar C-Mn steel has been investigated by Belotteau [2009] and Wang et al. [2012] in the temperature range between 20 °C and 350 °C. That material has been found to be very sensitive to the PLC effect between 150 °C and 300 °C. That is the reason for choosing 175 °C for observing the PLC effect. The current work consists in comparing the mechanical behaviour, especially the localization bands around the notch area of these SENT specimens in the PLC sensitive domain and in the non-sensitive domain. Tests are carried out using a 100 kN MTS machine under displacement control. In order to perform high temperature test and monitor the localization evolution, the tensile machine is combined with an environmental chamber and DIC system. Images are acquired through the furnace window. A thermocouple is directly welded on the surface of tested specimens for temperature control. The four test conditions are summarised in Table 5.2. In this table, the existence of PLC effect and fracture mode associated with each specimen are also listed in order to clarify the following results presented in this work.

The variation of the normalised stress, defined by F/S_0 (F: force; S_0: initial notch plane section) as a function of the cross-head displacement is plotted in Fig. 5.2. Fig. 5.2(a) gives a comparison of the stress-displacement curves at 175 °C and room temperature with the same loading rate 0.01 mm/s. Serrations can be observed on the 175 °C curve which is in the PLC sensitive domain. It can also be noticed that the ductility of the material is

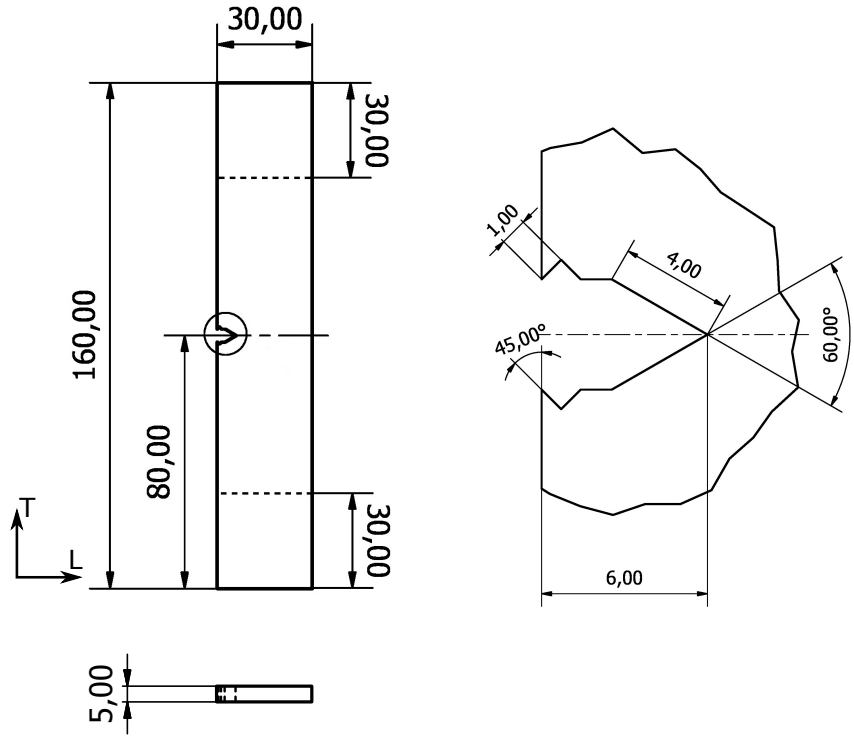

Figure 5.1 – Geometry of the single edge notched tension specimen (SENT) used in the current work. The thickness is 5 mm. The section clamped inside the grip is 30 mm long as marked by dashed line.

dramatically reduced at 175 °C. Very similar phenomenon could be observed for the tests with loading rate 0.002 mm/s. In additon, the stress levels at these two loading rates are similar. The blue point marks the moment a visible crack at the surface could be observed.

Table 5.2 – Summary of experimental conditions and main experimental observations.

	Loading rate (mm/s)	T (°C)	PLC (Yes/No)	Fracture mode
Specimen A	0.01	20	No	Flat
Specimen B	0.01	175	Yes	Slant
Specimen C	0.002	20	No	Flat
Specimen D	0.002	175	Yes	Slant

The current specimen geometry is a non-standard SENT. These specimens are designed for observing the PLC effect with DIC measurement as well as the flat-slant crack transition during propagation. We distinguish the crack initiation energy U_i from the crack propagation energy U_p as shown in Fig. 5.3. The total absorbed energy is therefore $U_t = U_i + U_p$ (see also Buirette et al. [2014]; Dalloz [2007]). As all the 4 tests were performed with the same specimen geometry, the fracture energy could be considered as an indicator for comparing the toughness. Fig. 5.3 shows the fracture energy for specimens tested at different conditions. The fracture energy at room temperature is much higher than that at 175 °C with a factor ranging from 1.72 to 1.98.

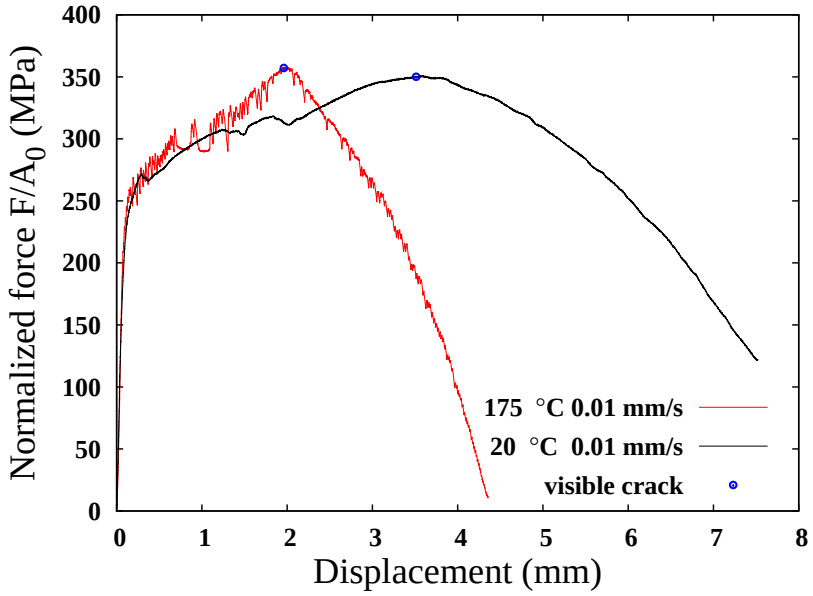

(a) Specimen A and B

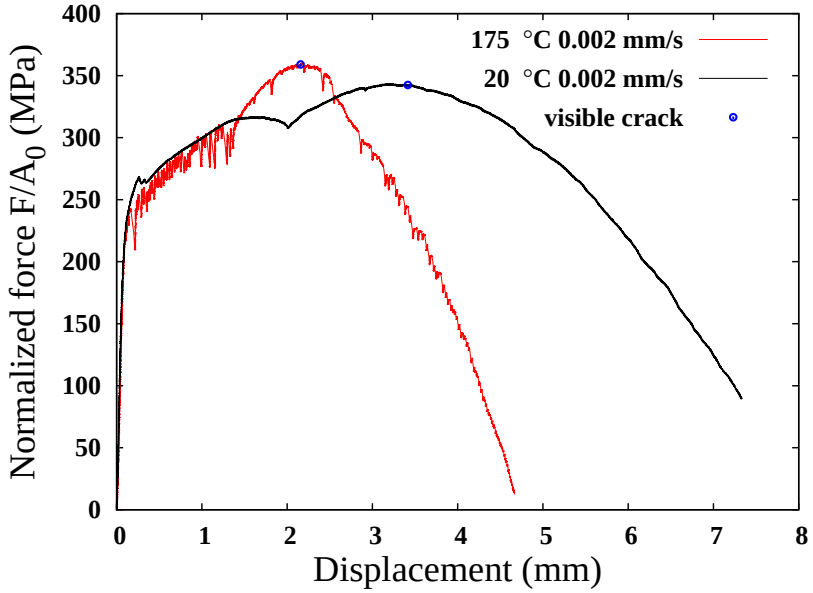

(b) Specimen C and D

Figure 5.2 – The variation of nominal stress against cross-head displacement for the 4 tests under different test conditions. (a) The comparison of the two tests at 175 °C and 20 °C for the same loading rate 0.01 mm/s. (b) The two tests with loading rate 0.002 mm/s.

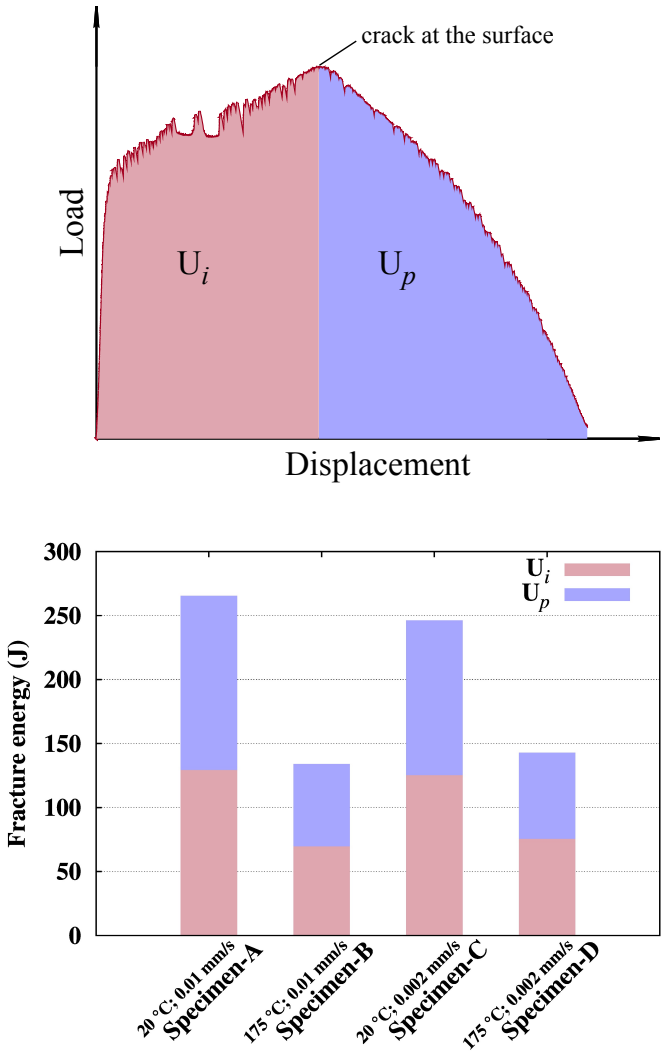

Figure 5.3 – Load-displacement curve and energy partition method. The fracture energy of the 4 tested specimens.

5.2.3 High temperature DIC setup

For the DIC measurement, a stereo-DIC system using two Manta G 419 cameras (2048x2048 pixel each) was synchronised with the tensile machine. The most important point for a successful high temperature DIC measurement is to make a stable contrast pattern. A coating of high temperature resistant (up to 700 °C) black paint was sprayed onto the specimen which forms a uniform bottom colour layer to avoid oxidation. A random white speckle pattern was then sprayed onto the black surface. For the specimens tested at room temperature, ordinary white paint was used as bottom colour layer. Black speckle was then sprayed onto the white surface.

The calibration of the DIC measurement at high temperature is more complex than room temperature. The minimum distance between the cameras and the specimen is limited by the door of the environmental chamber. The calibration is made at room temperature by removing the door. Using calibration target, the spatial resolution is 77.6 µm/pixel for these four tests. A subset size of 25×25 pixels is used for correlation. The calculation step size (spacing of subsets for correlation) is 8 pixels. These settings are within the optimal range of configurations in Vic-3D [Manual, 2010]. More details of DIC technique can be found in [Sutton, 2008]. The image acquisition rate during loading was 2.5 fps (one image every 0.4 seconds) for the two tests with loading rate 0.01 mm/s and 1.0 fps for those with loading rate 0.002 mm/s. The heterogeneous strain on the surface of the tested specimens was calculated via a commercial image correlation software Vic-3D. We chose Lagrangian strain tensor, also known as the Green-Lagrangian strain tensor, for strain computations, which is a finite strain measure including nonlinear terms. The term ε_{yy} mentioned later in DIC measurement is the second component of the Green-Lagrangian strain tensor.

The measurement noise is detected by the correlation between two images in the undeformed case. Fig. 5.4 gives a comparison of the measurement noise at two temperatures. The maximum noise is around ±0.0006 for high temperature and ±0.0002 for room temperature. The noise is 3 times higher at high temperature than room temperature. This is due to the influence of air heating haze, which can cause local changes in the refraction, distorting the view of the surface [Lyons et al., 1996].

5.2.4 Localization band morphology

The PLC bands can be attributed to a strain rate softening phenomenon [Graff et al., 2008; Kubin and Estrin, 1984]. These bands can be directly assessed by plastic strain rate $\dot{p}$ in a FEM simulation, while for DIC measurement, we can only obtain the incremental strain between the reference image and the current one. To reveal the plastic strain rate localization bands, an incremental correlation strategy is involved by correlating two successive images with a constant time interval Δt. The strain rate $\dot{\varepsilon}$ can approximately be calculated by $\Delta\varepsilon/\Delta t$. Theoretically, the smaller the time interval, the closer the strain rate will be to the instantaneous value. However, the measurement noise will be a problem with small time intervals as the signal-to-noise ratio will be degraded.

The time increment is chosen to be Δt =4 s for the two tests with loading rate v = 0.01 mm/s. To make a direct comparison between the tests at 20 °C and 175 °C, the incremental strain fields ($\Delta\varepsilon_{yy}$) corresponding to 22 different stages for each case are displayed in Fig. 5.5 and 5.6 respectively. The strain maximum scale is fixed at 0.003 for both tests which indicates a strain rate $\dot{\varepsilon}$ = 0.003/4 s^{-1} = 0.00075 s^{-1}. With the marked numbers, the corresponding incremental strain pattern could be associated with the stress-time curve. For the test at 20 °C, the propagative bands are only observed before the stage

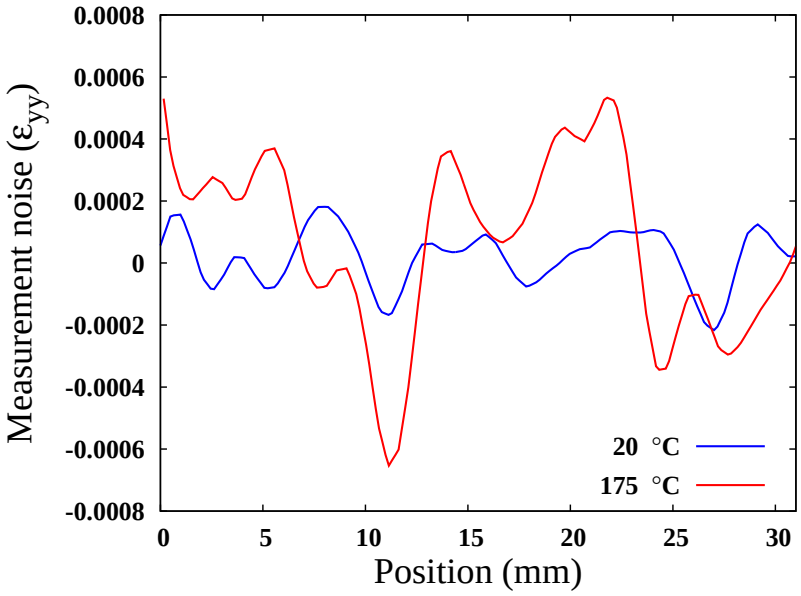

Figure 5.4 – Comparison of the DIC measurement noise of strain (ε_{yy}) at two temperatures.

No.11. There are two stress drops at No.6 and 9 on the stress time curve. These two stress drops are related to the propagating localization bands reaching the grips. In addition the angle of propagating bands to the loading direction is around 54° as indicated in No.5.

For the test at 175 °C, the localization bands also initiated around the notch area then propagated to the grip area (see Fig. 5.6). The two stress plateaus (stage No.6 and 8) on the stress-time curves correspond to the two propagating localization bands. After the stage No.8 at 175 °C, the localization events are mostly concentrated around the notch flipping up and down. No more propagative bands could be observed. In contrast to 175 °C, the plastic zone is very stable at 20 °C after stage No.11. No significant flipping behaviour could be seen. In addition, the visible cracks at the surface are observed around stage No.14 at 20 °C and around stage No.12 at 175 °C.

Another comparative group contains the two tests with loading rate v=0.002 mm/s. The time increment of correlation is Δt = 20 s for these two tests. The maximum scale is also chosen to be 0.003 which indicates a strain rate $\dot{\varepsilon} = 0.003/20 = 0.000\,15\,\mathrm{s}^{-1}$ that is 5 times smaller than the previous tests at loading rate v = 0.01 mm/s. The incremental strain patterns corresponding to different stages are shown in Fig. 5.7 and 5.8. For the test at 20 °C, the propagative bands were annihilated after stage No.9 which corresponds to the end of a stress drop on the stress-time curve. Comparing with the homologous test with higher loading rate (see Fig. 5.5), there is only one significant stress drop on the curve. This is certainly linked to the two propagating bands that arrive at the grip simultaneously. Similarly, the plastic zone is very stable during the crack propagation after stage No.11. At 175 °C, even the main propagating bands (from No.8 to No.10) showed more flipping behaviour than the test at v=0.01 mm/s. These two bands seem to compete with each other by alternating up and down. Similar flipping behaviour of localization bands can also been noticed during crack propagation.

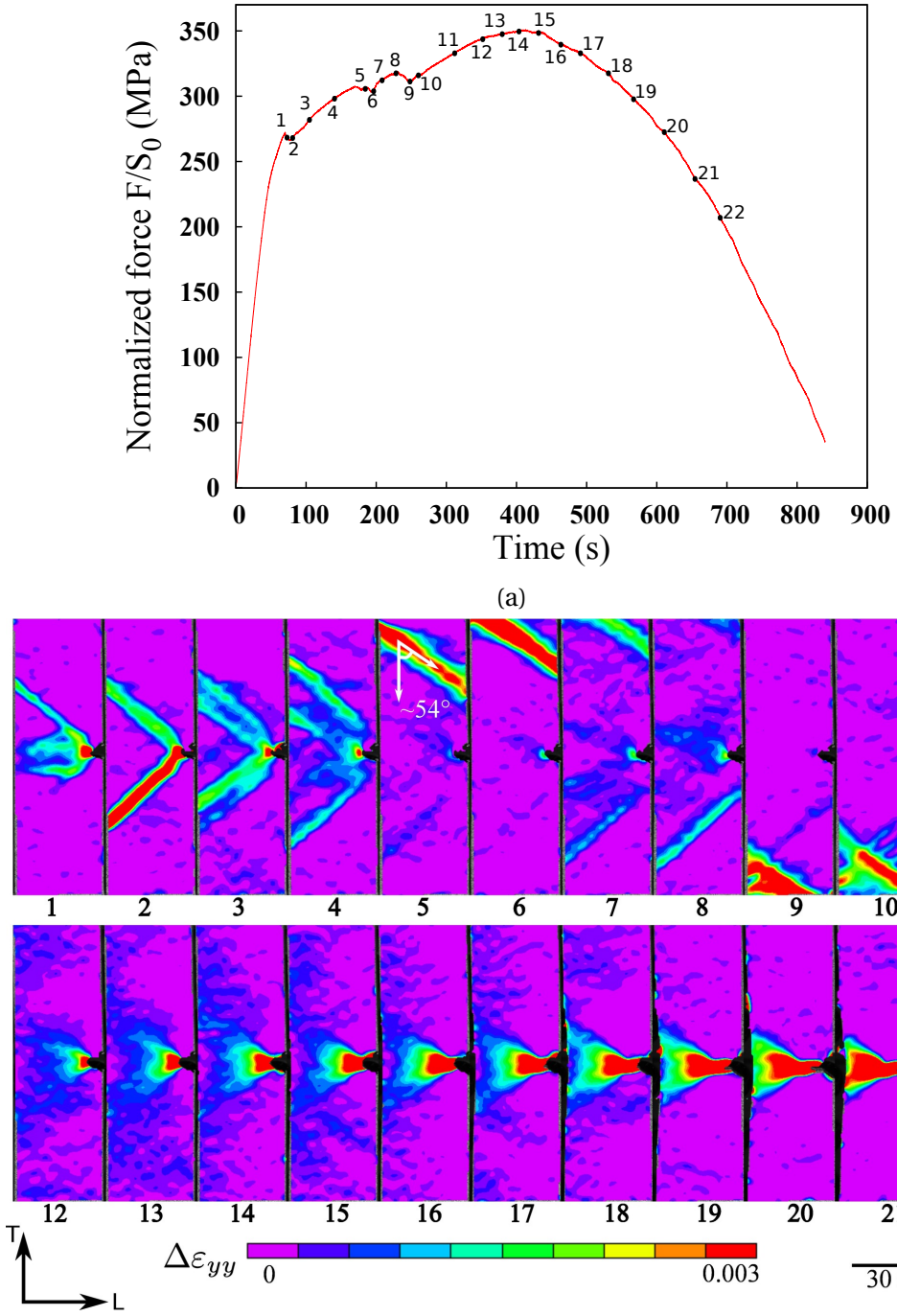

Figure 5.5 – Stress-time curve and incremental strain field (maximum scale fixed at 0.003; $\Delta t = 4$ s corresponding to strain rate 7.5×10^{-4}) measured by DIC of specimen A at 20 °C with loading rate v = 0.01 mm/s.

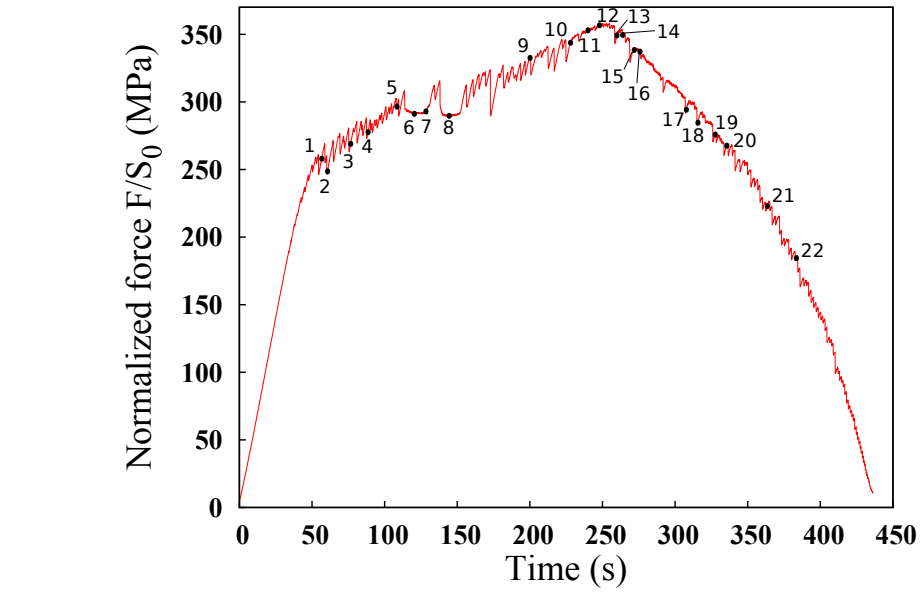

(a)

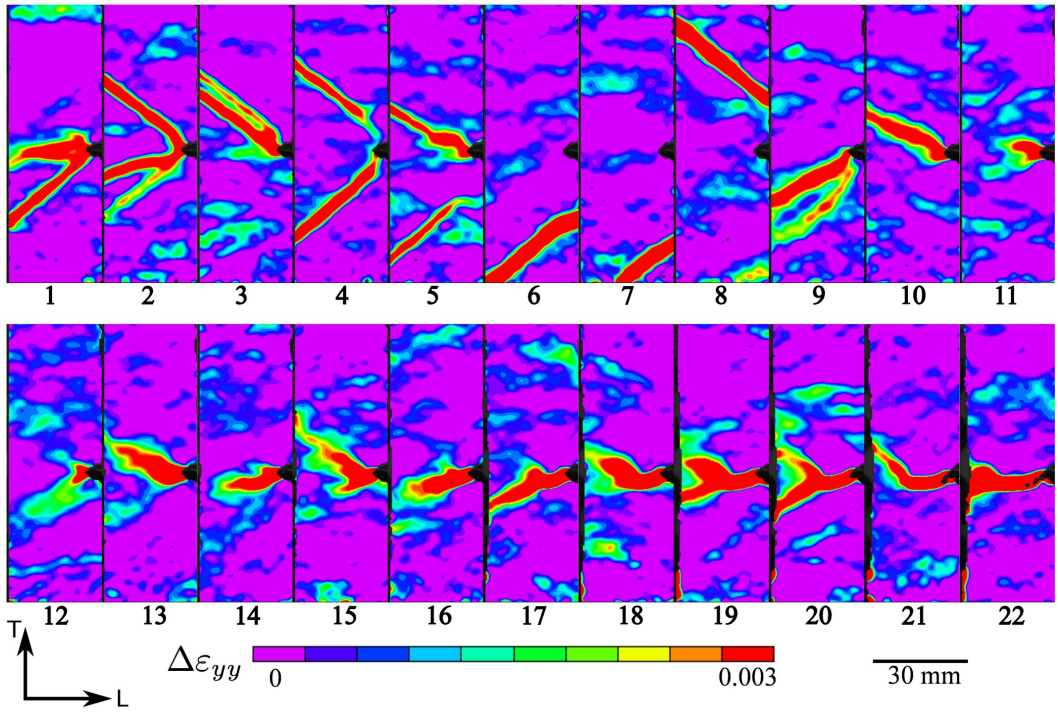

(b)

Figure 5.6 – Stress-time curve and incremental strain field (maximum scale fixed at 0.003; $\Delta t = 4$ s corresponding to strain rate 7.5×10^{-4}) measured by DIC of specimen B at 175 °C with loading rate v = 0.01 mm/s.

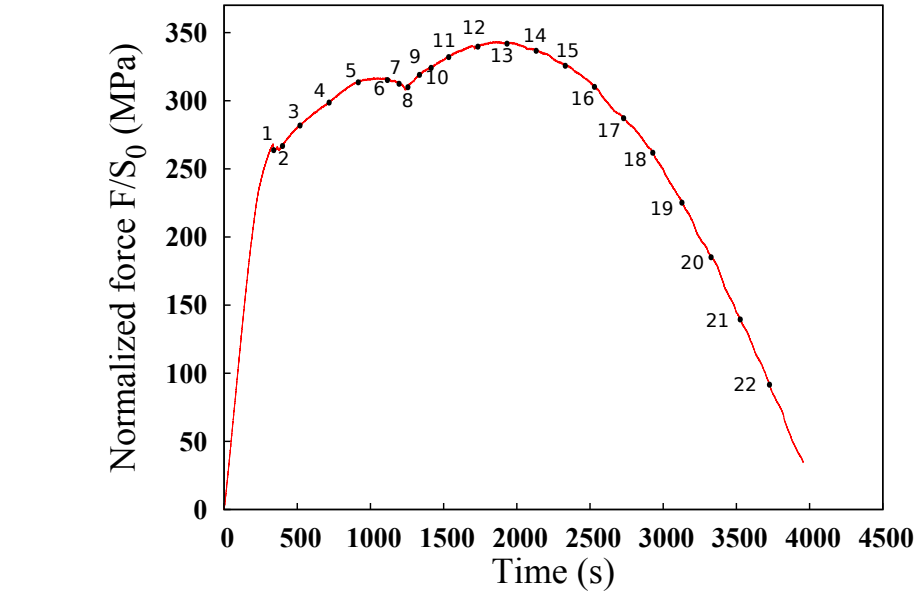

(a)

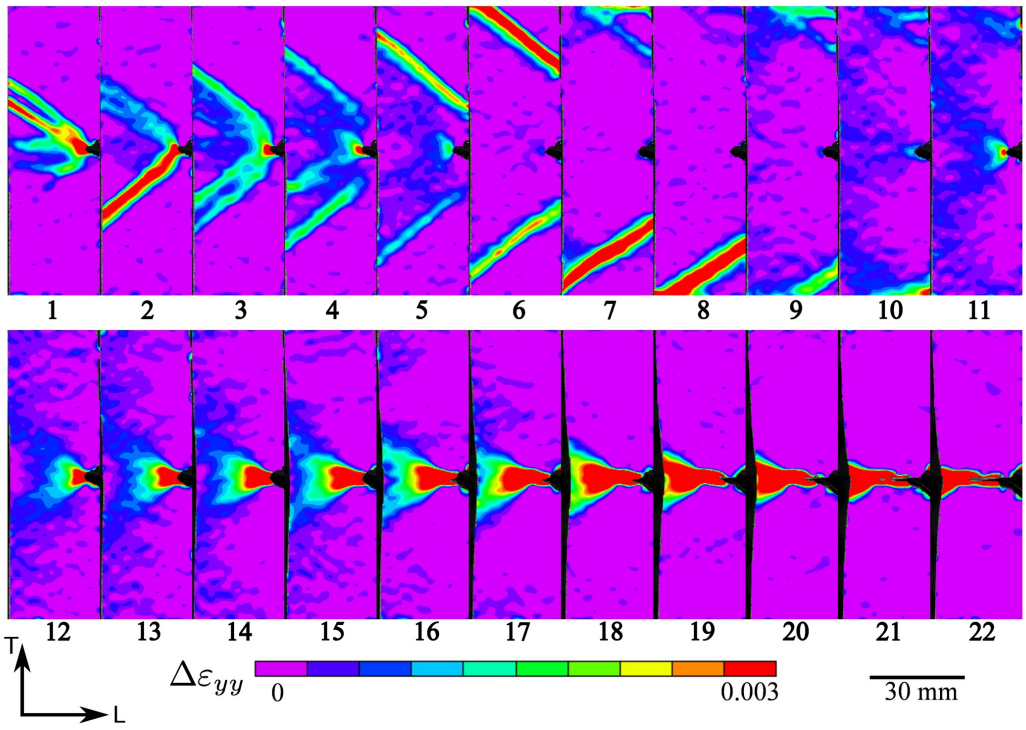

(b)

Figure 5.7 – Stress-time curve and incremental strain field (maximum scale fixed at 0.003; $\Delta t = 20$ s corresponding to strain rate 1.5×10^{-4}) measured by DIC of specimen C at 20 °C with loading rate v = 0.002 mm/s.

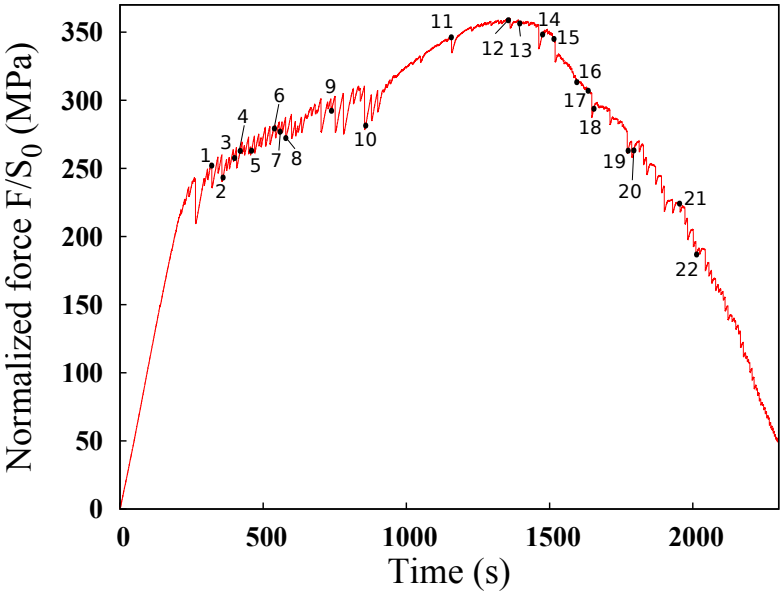

(a)

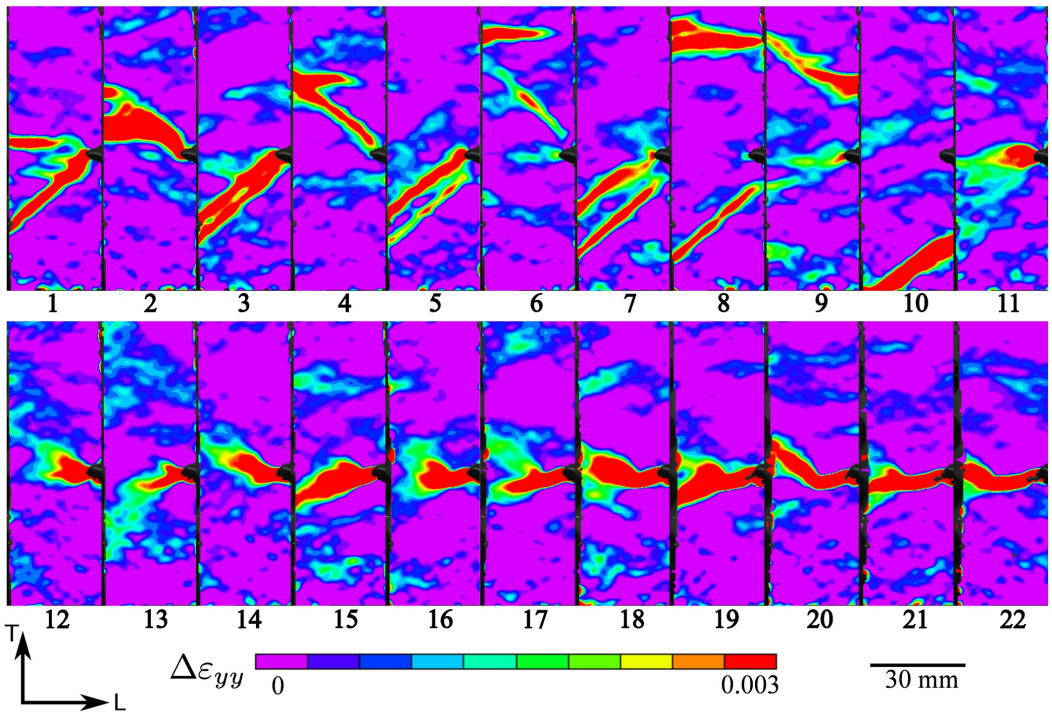

(b)

Figure 5.8 – Stress-time curve and incremental strain field (maximum scale fixed at 0.003; $\Delta t = 20$ s corresponding to strain rate 1.5×10^{-4}) measured by DIC of specimen D at 175 °C with loading rate v = 0.002 mm/s.

5.2.5 Spatio-temporal kinematics of localization bands

To better illustrate the evolution of localization bands, so-called spatio-temporal patterns are used for describing the location of bands at different stages of experiments as practised by many authors [Chmelík et al., 2002; Benallal et al., 2008] and in Chapter 4. A line (Y_{mid}) is positioned in the centre of the specimen in order to measure the incremental strain evolution along this line over the whole deformation process (see Fig. 5.9(a)). The spatio-temporal patterns of these 4 tests are shown in Fig. 5.9 together with the corresponding stress-time curves. The colour contour is a measure of the strain rate $\dot{\varepsilon}_{yy} = \Delta\varepsilon_{yy}/\Delta t$. It can be noticed that the bands propagate under two significantly different velocities. At the beginning, the Lüders bands initiate at notch tip (see Fig. 5.5(b) 1-3 or Fig. 5.6(b) 1-4). Due to the higher concentration of deformation around notch, the bands propagate to the two grips with one side trapped by the notch area which reduced the propagation velocity. Once escaped from the notch area, the band accelerates. Thus, we can observe two different slopes of bands in the spatio-temporal patterns. The velocity of the free propagating bands is 3-4 times higher than the bands around notch. The acceleration of band propagation is also associated with the nearly constant stress plateau (No.6-8) on the stress time curve. After the stress plateau, the propagating bands disappeared. At 20 °C, no more bands could be observed after the propagating bands. At 175 °C, PLC bands continue to initiate around the notch tip. In addition, at 175 °C, the nucleation of localization bands is always associated with stress drops. The flipping behaviour of localization bands during crack propagation at 175 °C, as shown in Fig. 5.6 and 5.8, is also confirmed.

To make a quantitative comparison, the evolution of maximum strain rate along a line Y_{mid} (see Fig. 5.9(a)) is presented in Fig. 5.10. At 20 °C, the first stress drop yields strong localization bands around the notch. Then the strain rate inside the bands gets weaker until reaching the stress plateau. During the free propagation, the strain rate inside localization bands is higher than the bands trapped by notch tip area. At 175 °C, the strain rate inside localization bands did not decrease too much due to the simultaneously occurring PLC effect. The strain rate level inside a band at 175 °C is significantly higher than that at room temperature. The measured maximum strain rate profiles at 175 °C show many peaks due to the intense serrations of PLC effect. A direct comparison of the strain rate in a single band will be made in section 5.3.3.

The strain fields in a region of interest (ROI) at maximum force for specimen A and at the same displacement (=1.96 mm) for specimen B are presented in Fig. 5.11(a) and (b). With the same strain scale, the plastic zone of “butterfly" shape during crack initiation at 20 °C is less concentrated than that at 175 °C. The angle between the two “wings" of the plastic zone is smaller at 175 °C than 20 °C. It can also be noticed that the plastic deformation at 175 °C is cumulated by the passage of previous localization bands which left behind a flame-like plastic zone. Fig. 5.11(c) and (d) also give a measurement of the strain evolution along a line near the notch. The line is perpendicular to the crack propagation direction at 4 mm from the notch tip. The profile of cumulated strain along this line from the initial state to the moment that crack reaches this area (then the correlation cannot be done due to paint cracking) is plotted. Different evolutions at 175 °C and at 20 °C can be noticed. At 175 °C, the evolution of strain is less symmetric. The lower extent of plastic zone (left peak) becomes dominant after reaching ε_{yy} =0.061. At 20 °C, the two peaks keep growing until ε_{yy} =0.165 followed by a stronger plastic zone in the central area between the two “wings". This phenomenon has also been found in the tests with loading rate v=0.002 mm/s. A reasonable explanation for the loss of symmetry of plastic zone evolution at 175 °C would be the key for explaining the slant fracture at 175 °C.

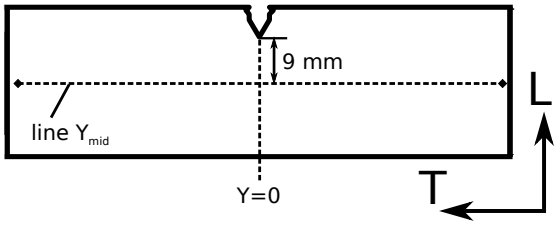

(a) Line Y_{mid} positioned in the middle of specimens along the loading direction.

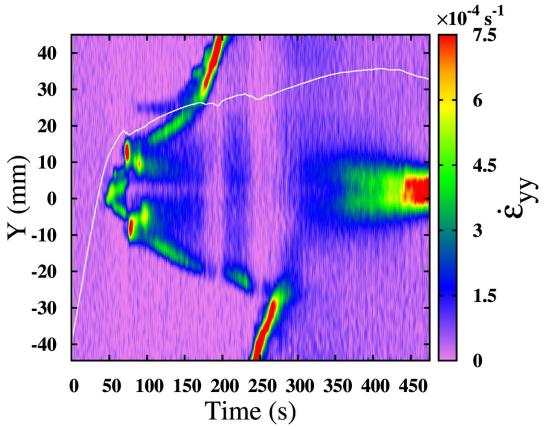

(b) Specimen A: 20 °C; v = 0.01 mm/s.

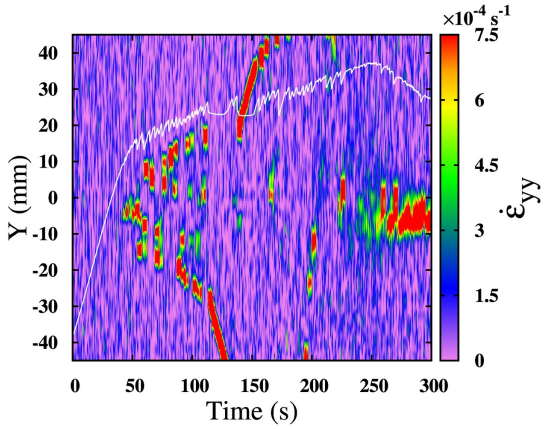

(c) Specimen B: 175 °C; v = 0.01 mm/s.

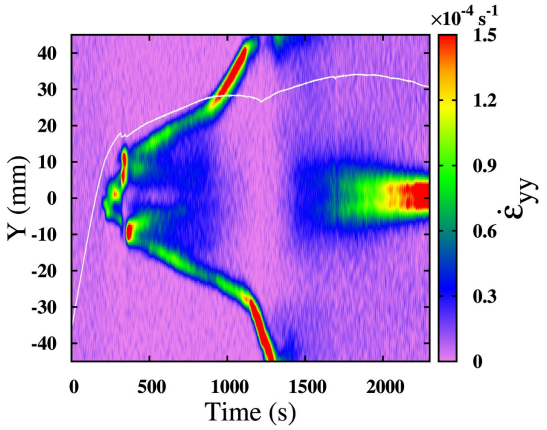

(d) Specimen C: 20 °C; v = 0.002 mm/s.

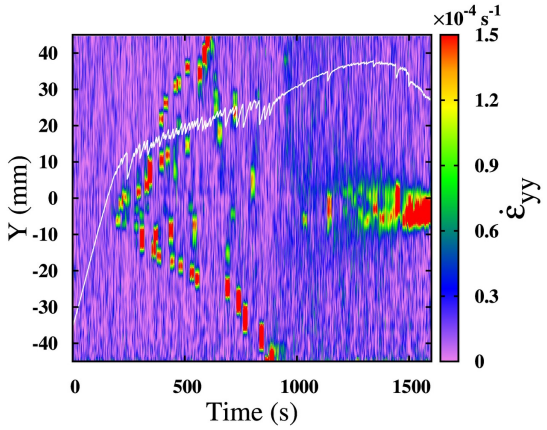

(e) Specimen D: 175 °C; v = 0.002 mm/s.

Figure 5.9 – Spatio-temporal patterns of the four tests measured along line Y_{mid}.

The corresponding position on the global stress-displacement curve denoting the onset of non symmetric plastic zone is marked in the zoom view of Fig. 5.11. For 175 °C, this point appears before the visible crack propagation. However, at 20 °C, this point appears almost at the same time as crack propagation. Considering that the line Y is placed at 4 mm to the notch tip, the loss of symmetry at actual notch tip occurs even earlier. The visible crack indeed propagates along the dominant lower wing (in the current image) of plastic zone at 175 °C. At 20 °C, the crack propagates following the middle plane of the "butterfly" shape plastic zone.

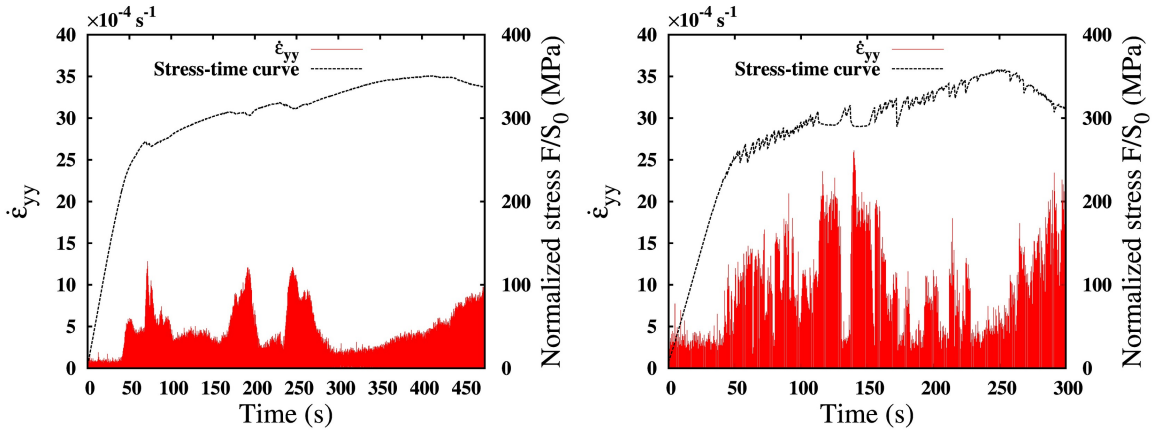

(a) Specimen A: 20 °C; v = 0.01 mm/s.

(b) Specimen B: 175 °C; v = 0.01 mm/s.

(c) Specimen C: 20 °C; v = 0.002 mm/s.

(d) Specimen D: 175 °C; v = 0.002 mm/s.

Figure 5.10 – Maximum strain rate ($\dot{\varepsilon}_{yy}$) along the line Y_{mid} in Fig. 5.9(a).

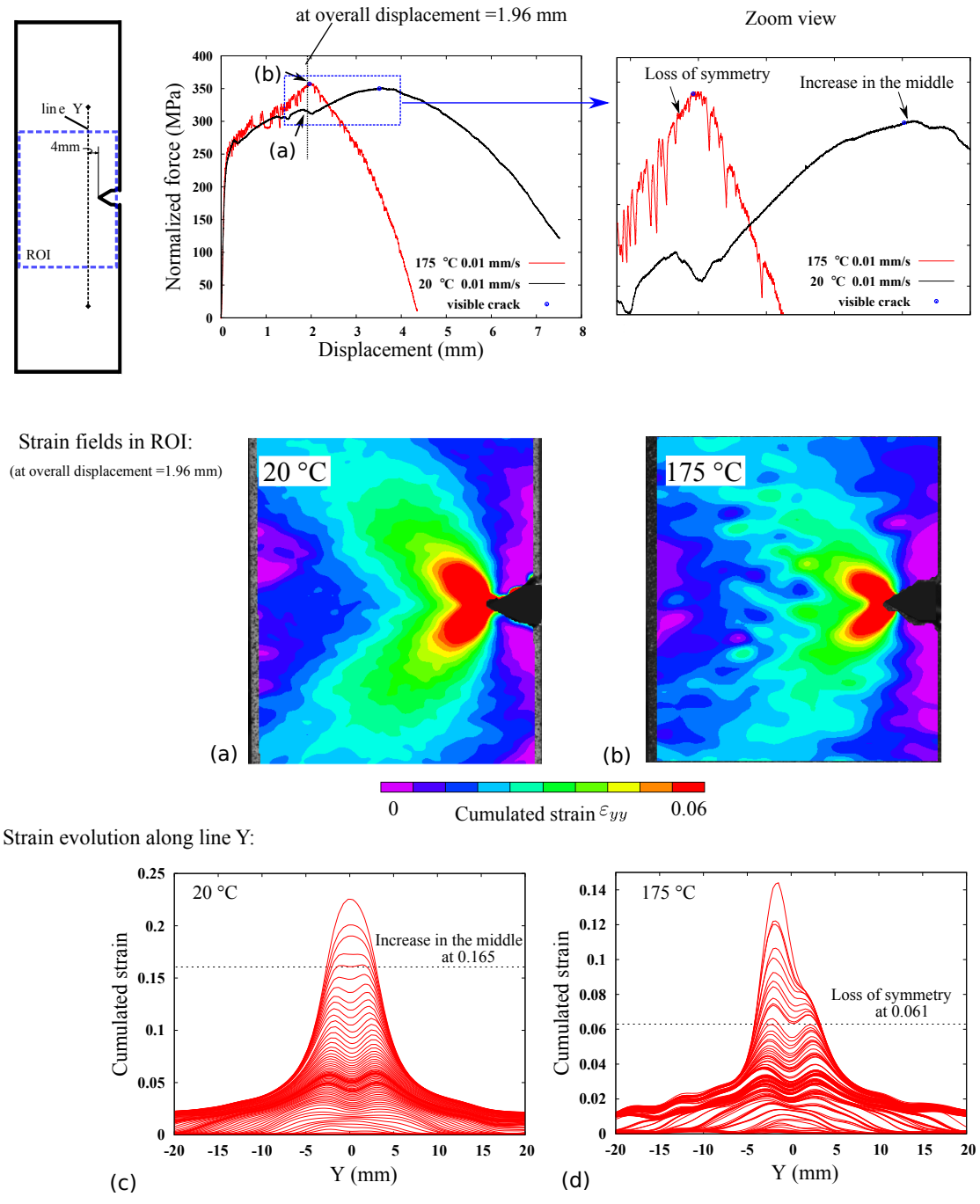

Figure 5.11 – Comparison of the strain fields in ROI at overall displacement=1.96 mm for specimen A in subfigure (a) and B in subfigure (b). Comparison of the evolution of cumulated strain along line Y near the notch tip for 20 °C (specimen A) in subfigure (c) and 175 °C (specimen B) in subfigure (d).

5.3 Finite element simulations of SENT tests

5.3.1 Constitutive equations of strain ageing model

In the current section, in order to simulate the bands characteristics observed via DIC, the constitutive equations proposed by Graff et al. [2008] and Mazière et al. [2010] have been retained. The constitutive model is presented within the finite strain framework using the concept of local objective frames following Besson et al. [2009]. The second and fourth order tensors are defined by a single tilde $\underset{\sim}{\square}$ and a double tilde $\underset{\approx}{\square}$ respectively. Observer invariant stress and strain rate measures $\underset{\sim}{\boldsymbol{\sigma}}$ and $\dot{\underset{\sim}{\boldsymbol{\varepsilon}}}$ are defined by the transformation of the Cauchy stress tensor $\underset{\sim}{\boldsymbol{T}}$ and the Eulerian strain rate tensor $\underset{\sim}{\boldsymbol{D}}$ into the corotational frame characterized by the rotation $\underset{\sim}{\boldsymbol{Q}}$ ($\underline{\boldsymbol{x}}$,t) at each material point:

$$\begin{cases} \underset{\sim}{\boldsymbol{\sigma}} = \underset{\sim}{\boldsymbol{Q}}.\underset{\sim}{\boldsymbol{T}}.\underset{\sim}{\boldsymbol{Q}}^T \\ \dot{\underset{\sim}{\boldsymbol{\varepsilon}}} = \underset{\sim}{\boldsymbol{Q}}.\underset{\sim}{\boldsymbol{D}}.\underset{\sim}{\boldsymbol{Q}}^T \\ \underset{\sim}{\boldsymbol{Q}} \quad \text{such as} \quad \dot{\underset{\sim}{\boldsymbol{Q}}}^T.\underset{\sim}{\boldsymbol{Q}} = \underset{\sim}{\boldsymbol{\Omega}} \quad \text{(corotational)} \end{cases}$$

where $\underset{\sim}{\boldsymbol{D}}$ and $\underset{\sim}{\boldsymbol{\Omega}}$ respectively are the symmetric and skew-symmetric parts of the velocity gradient. The strain rate is then decomposed into elastic and plastic parts:

$$\dot{\underset{\sim}{\boldsymbol{\varepsilon}}} = \dot{\underset{\sim}{\boldsymbol{\varepsilon}}}^e + \dot{\underset{\sim}{\boldsymbol{\varepsilon}}}^p, \quad \underset{\sim}{\boldsymbol{\sigma}} = \underset{\approx}{\boldsymbol{C}} : \underset{\sim}{\boldsymbol{\varepsilon}}^e \tag{5.1}$$

where $\underset{\approx}{\boldsymbol{C}}$ is the Hooke tensor of elasticity. The plastic flow is described by the normality rule

$$\dot{\underset{\sim}{\boldsymbol{\varepsilon}}}^p = \dot{p}\,\underset{\sim}{\boldsymbol{n}}, \quad \underset{\sim}{\boldsymbol{n}} = \frac{\partial F}{\partial \underset{\sim}{\boldsymbol{\sigma}}}, \tag{5.2}$$

where p is the cumulative plastic strain and the yield function, F, is taken in the form

$$F(\underset{\sim}{\boldsymbol{\sigma}}, \rho, t_a) = \sigma_{eq}(\underset{\sim}{\boldsymbol{\sigma}}) - R(p) - R_a(t_a), \tag{5.3}$$

where the isotropic hardening term $R(p)$ is

$$R(p) = Hp + Q((1 - e^{-bp}), \tag{5.4}$$

$$\dot{p} = \dot{\varepsilon}_0 \sinh\left(\frac{\max(0, F)}{\sigma_0}\right). \tag{5.5}$$

The ageing hardening term $R_a(t_a)$ reads

$$R_a(t_a) = P_1\left[1 - e^{-(\frac{t_a}{t_0})^n}\right], \quad t_0(p) = \left(\frac{1}{P_2 p^\alpha}\right)^{1/n}, \quad \dot{t}_a = 1 - \frac{t_a}{w}\dot{p}, \tag{5.6}$$

where P_1 is the maximalthe maximal stress drop magnitude from a fully pinned state to a fully unpinned state; t_0 characterizes the time of diffusion process; n = 0.33 or 0.66 which corresponds to pipe or bulk diffusion mechanisms; w characterizes the strain increment associated with unpinning events.

To describe the mechanical response up to fracture, an attempt has been made to couple the current DSA model with damage induced by void growth. The yield function 5.3 is replaced by following form [Rousselier, 1987, 2001; Rousselier et al., 2017]

$$F = \frac{\sigma_{eq}}{1 - f} + s_1 D_1 f \exp\left[\frac{\sigma_m}{s_1(1 - f)}\right] - R(p) - R_a(t_a) \tag{5.7}$$

where f is the void fraction. In the current section, we only consider the void growth f_g thus we have $f = f_g$. Rousselier's model gives a void growth rate almost identical to Rice and Tracey's formula [Rousselier and Quilici, 2015]:

$$\dot{f} = \dot{f}_g = \dot{p}(1-f)D_1 f \exp\left(\frac{\sigma_m}{s_1(1-f)}\right). \tag{5.8}$$

D_1 is a material independent constant, fixed at $D_1 = 2$ here. Parameter s_1 is chosen to be 275 MPa ($\frac{2}{3}R_m$), and represents the resistance of the metal matrix to void damage. The initial void volume fraction is 0.001.

5.3.2 Identification of the parameters

The parameters related to the ageing term R_a, such as P_1, P_2, n, w, α were based on that given in Wang [2011] as the TU48C steel studied by Wang [2011] is very similar to the current A42 steel. The other hardening parameters at 175 °C are also taken from the function proposed by Wang [2011] due to lack of experimental tensile data of A42 steel at 175 °C. The hardening parameters at 20 °C are identified with experimental tensile curves [Marais et al., 2012]. An optimisation procedure using the Levenberg-Marquardt algorithm is used to minimize the deviation between data from material point simulations and that of the smoothed experimental stress-strain curves of tensile tests. This strategy avoids time-consuming FEM simulations on full dimension specimens. The complete constitutive model parameters used for the current section are presented in Table 5.3.

Fig. 5.12 shows the uni-axial tensile curve at room temperature with applied strain rate $10^{-2}\,s^{-1}$. At this temperature, there is no PLC effect. The Lüders yield peak and plateau can be observed. The simulation result on a 2D mesh is also plotted in Fig. 5.12. The simulated curve is in good agreement with the experimental one.

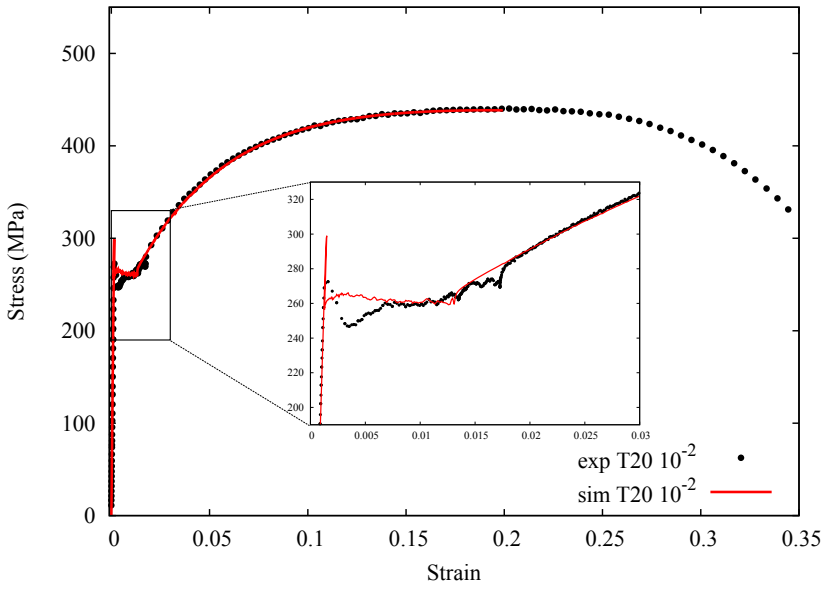

Figure 5.12 – Experimental and simulated stress-strain curves of the tensile test carried out at room temperature at strain rate $10^{-2}\,s^{-1}$.

Table 5.3 – Parameters used at 20 °C and 175 °C for C-Mn steel A42.

20 °C						
E(GPa)	ν	P_1(MPa)	n	w	$P_2(s^{-n})$	α
210	0.3	94	0.66	2×10^{-4}	0.01	0.26
R_0(MPa)	Q(MPa)	b	H(MPa)	$\dot{\varepsilon}_0(s^{-1})$	σ_0(MPa)	t_{a0}(s)
200	256	20	360	9.16×10^{-4}	4.11	5×10^{6}
175 °C						
E(GPa)	ν	P_1(MPa)	n	w	$P_2(s^{-n})$	α
199.83	0.3	84.84	0.66	2×10^{-4}	0.46	0.19
R_0(MPa)	Q(MPa)	b	H(MPa)	$\dot{\varepsilon}_0(s^{-1})$	σ_0(MPa)	t_{a0}(s)
178.86	273.5	29.6	360	9.45×10^{-4}	4.50	10^{4}

5.3.3 3D FEM simulations with strain ageing model

Fig. 5.13 shows the 3D mesh used in the current section, which contains 6184 elements (C3D20R element with reduced number of integration points) and 29499 nodes in total. A piece of the upper half specimen is shown beside. In the refined area, there are 8 elements ($0.625\times0.625\times0.625$ mm^3) through the thickness. Outside this region, coarse meshes are used for saving computation time.

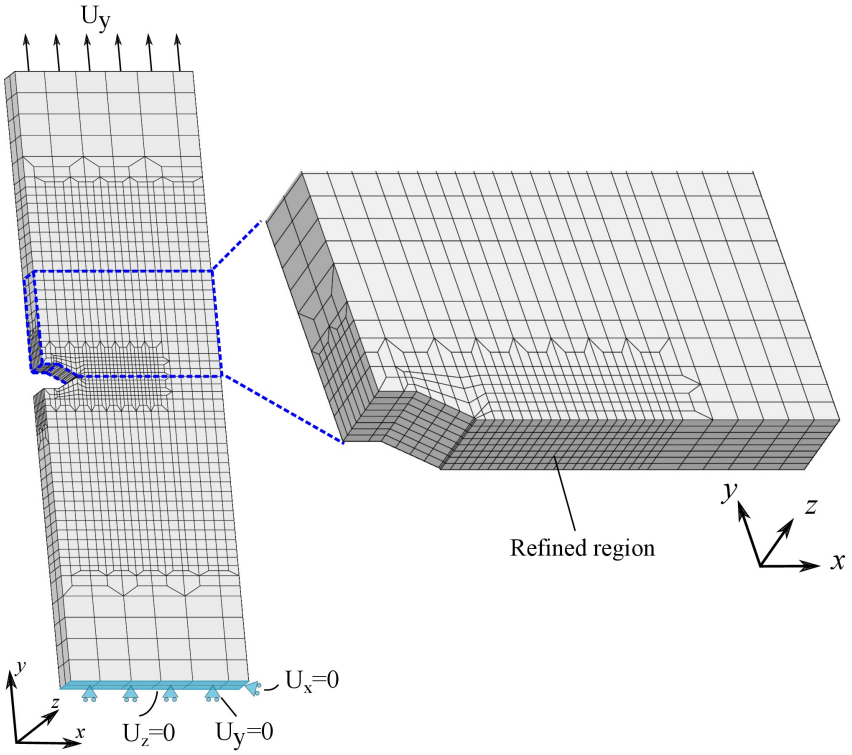

Figure 5.13 – 3D mesh with refined area around the notch.

Firstly, the Lüders effect is studied numerically in order to determine its influence on the overall hardening. The Lüders effect in the current SENT specimen is not characterized by a stress plateau in contrast to tensile tests. Fig. 5.14 compares the result by artificially deactivating the Lüders effect (t_{a0} =0 s) with that showing Lüders effect. With Lüders effect ($t_{a0}\neq$0 s), an over hardening is observed after the yield point followed by a stress plateau. The influence of initial ageing time on the over hardening by Lüders effect

is presented in Fig. 5.14. A longer initial ageing time results in a larger range of Lüders effect on the stress-displacement curve. This simulation result confirms the characteristics of Lüders effect in such kind of specimen geometry. In the following simulations, t_{a0} is set to be 10^4 s for 175 °C and 5×10^6 s for 20 °C. These values are obtained by comparing with experimental curves in the current section.

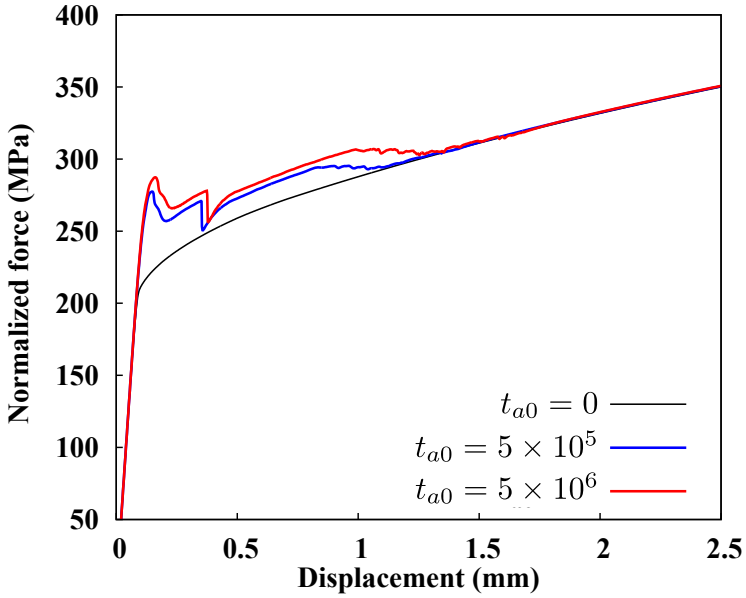

Figure 5.14 – Comparison of the FEM simulation results with and without Lüders effect for SENT tests.

As the tests at loading rate 0.002 mm/s generally showed similar results with those at 0.01 mm/s, only the comparison between experimental and numerical results with loading rate 0.01 mm/s is presented here. Fig. 5.15(a) presents the 3D simulation curves of SENT specimen at 20 °C with loading rate v = 0.01 mm/s. The experimental curves are superposed with numerical ones. It can be noticed that the initial yield peak is overestimated by the FEM simulation. The stress drop reproduced by the simulation occurs earlier than in the experiment. The simulated hardening before fracture is consistent with experimental curve. Without damage mechanism, the current constitutive model is not able to describe the descending part of the global stress-displacement curve. The void damage could occur at very early state due to the notch tip. Therefore, the stress-displacement curves produced by the strain ageing model coupled with damage are also presented in Fig. 5.15. The prediction has been improved significantly at 20 °C. The 3D simulation results of the test at 175 °C with v = 0.01 mm/s are presented in Fig. 5.15(b). The huge ductility loss at 175 °C is not well predicted with the same damage parameters. A more detailed study will be presented in a following chapter concentrated on the ductile fracture.

5.3.4 Spatio-temporal patterns and localization bands from FE simulations

The spatio-temporal patterns of FE simulations with loading rate v=0.01 mm/s are plotted in Fig. 5.16. These simulations are carried out only with the strain ageing model without damage. There are considerable similarities between these numerical patterns and

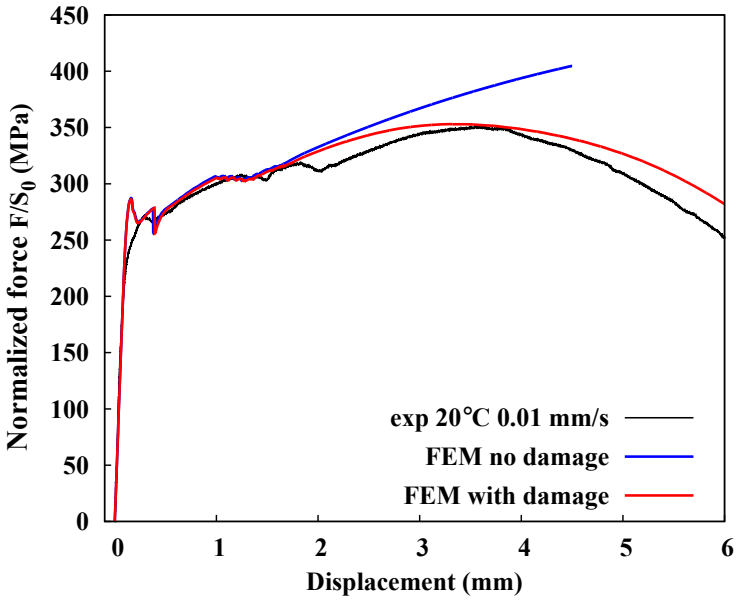

(a) FE simulation results of specimen A.

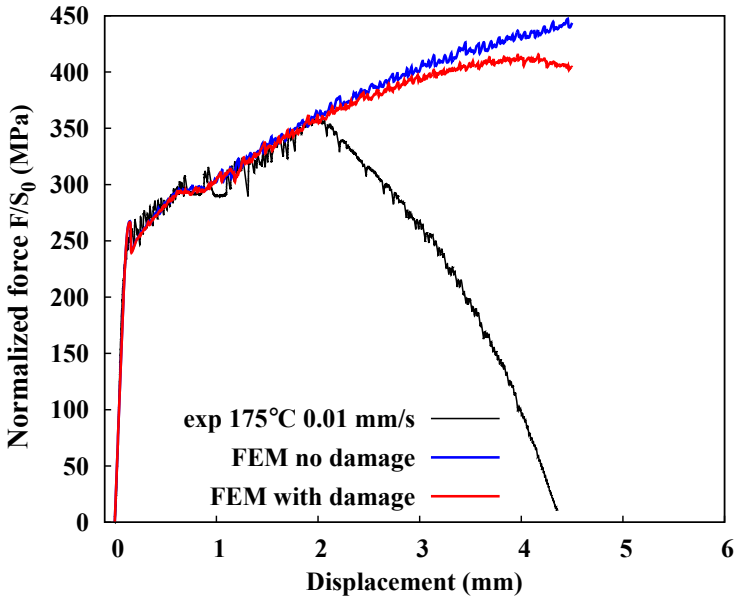

(b) FE simulation results of specimen B.

Figure 5.15 – Stress-displacement curves of FE simulation for the two tests at loading rate 0.01 mm/s.

the ones measured by DIC (see Fig. 5.9). The evolution of localization bands produced by FE simulation at 20 °C is almost identical to the experiment. The effect of notch area for slowing down band propagation is predicted properly. Two different velocity slopes can be seen in the spatio-temporal patterns for both temperatures. In addition, the two propagating localization bands propagate symmetrically and arrive at the two grips at the same time which is not always the case for experiments. At 175 °C, the flipping behaviour of localization bands during propagation has also been reproduced. However, the localization bands around the notch (after the annihilation of propagating bands) show more propagative behaviour in the simulation. In the experiment, theses bands are more intermittent without propagation. Fig. 5.17 gives the band velocities measured from the

spatio-temporal patterns of DIC and simulations. The velocities of two types of propagating bands at 175 °C are in good agreement with DIC measurement. The velocity of free propagating bands at 20 °C is slightly underestimated.

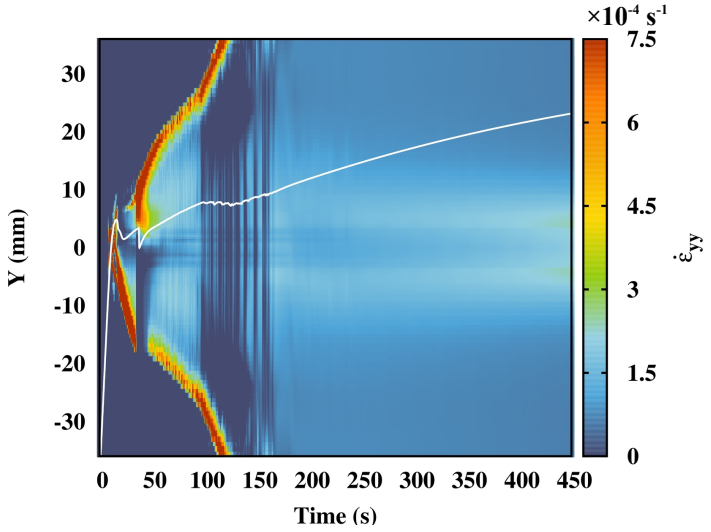

(a) 20 °C; v = 0.01 mm/s.

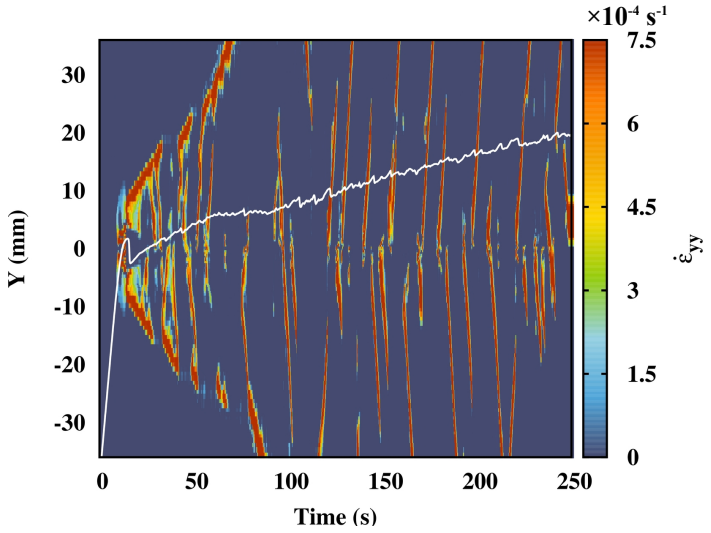

(b) 175 °C; v = 0.01 mm/s.

Figure 5.16 – Spatio-temporal patterns obtained from FE simulations to be compared with the experimental results in Fig. 5.9(a) and (b).

Fig. 5.18 shows the band morphology produced by FE simulations with loading rate v = 0.01 mm/s. At 20 °C, only two propagating bands are obtained. These two bands propagate to the two ends of the specimen simultaneously. As indicated at t=117 s, the angle of the propagating band is 51.25° which is very close to the DIC measurement presented in Fig. 5.5. The plastic zone around the notch is very stable after the annihilation of these initial bands. At 175 °C, the band shape as well as the alternating behaviour are captured.

To compare with Fig. 5.10, Fig. 5.19 shows the evolution of maximum strain rate along line Y_{mid} produced by FE simulations. The strain rate in the band of first stress drop is higher than the following bands which is consistent with DIC measurement. However, the amplitude is overestimated compared with experiments. When the bands start to propagate without the influence of notch tip area, associated with a stress plateau, the

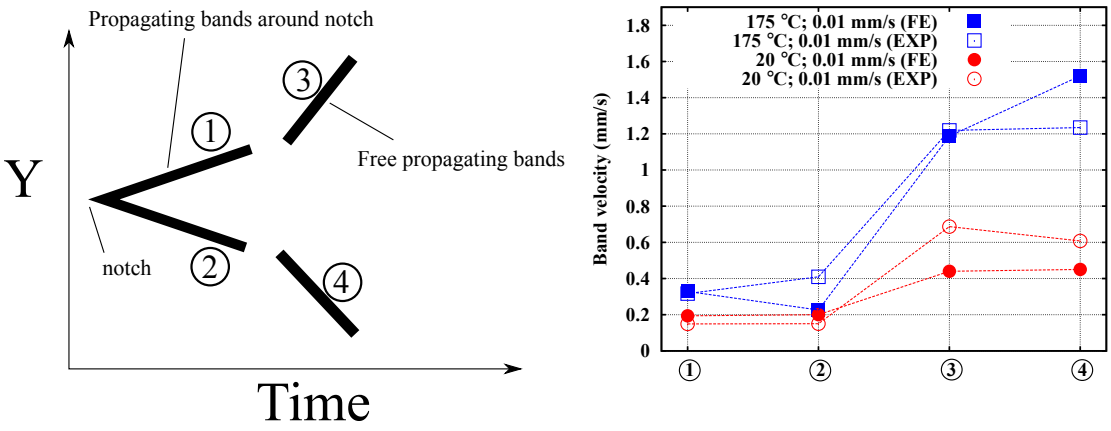

Figure 5.17 – Schematic of the band evolution in a spatio-temporal pattern and comparison of velocities of band propagation measured by DIC and simulations at v = 0.01 mm/s.

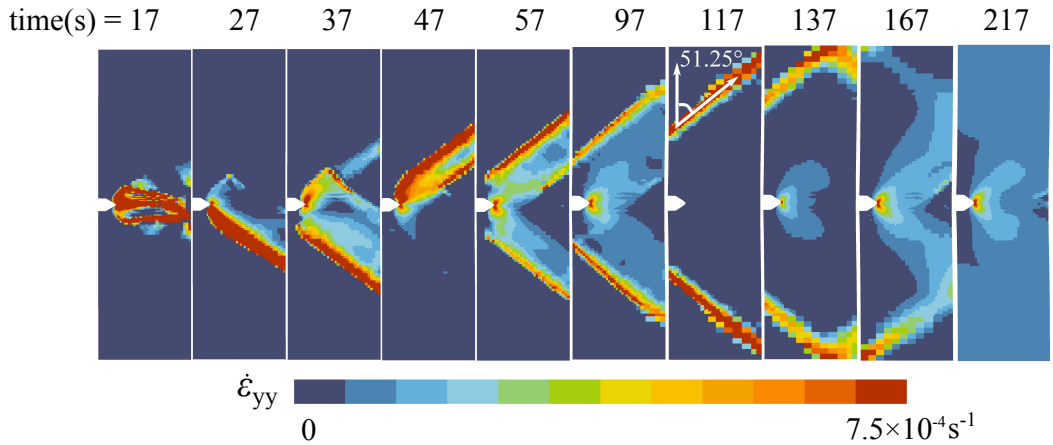

(a) 20 °C; v = 0.01 mm/s.

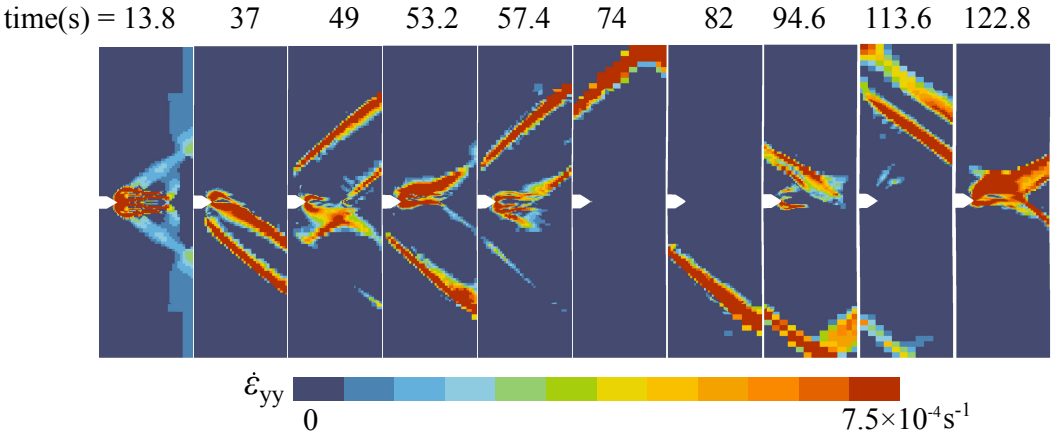

(b) 175 °C; v = 0.01 mm/s.

Figure 5.18 – Localization bands produced by FE simulations with loading rate v = 0.01 mm/s.

strain rate in bands attains again a peak level. The strain rate in bands at 175 °C is higher than 20 °C. At 175 °C the maximum strain rate did not decrease to a lower level after first stress drop, which is due to the continuously propagating PLC bands. These results are in agreement with DIC measurement.

To make a quantitative comparison of the characteristics of localization bands, we selected two typical bands, namely the initial propagating bands around notch ("Band

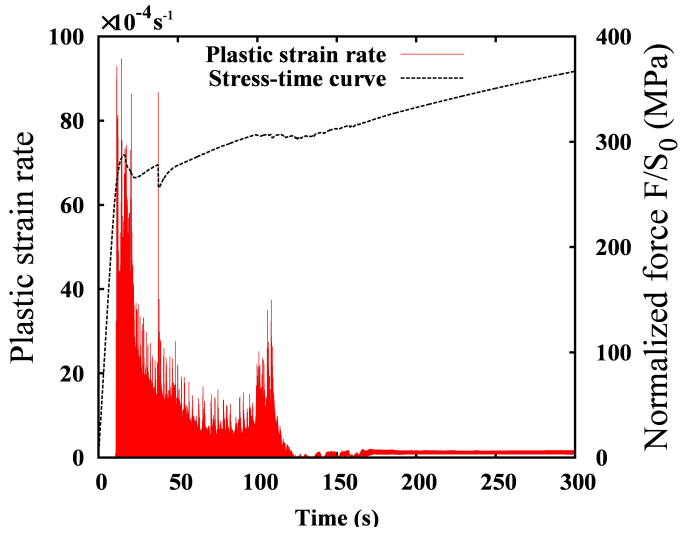

(a) 20 °C; v = 0.01 mm/s.

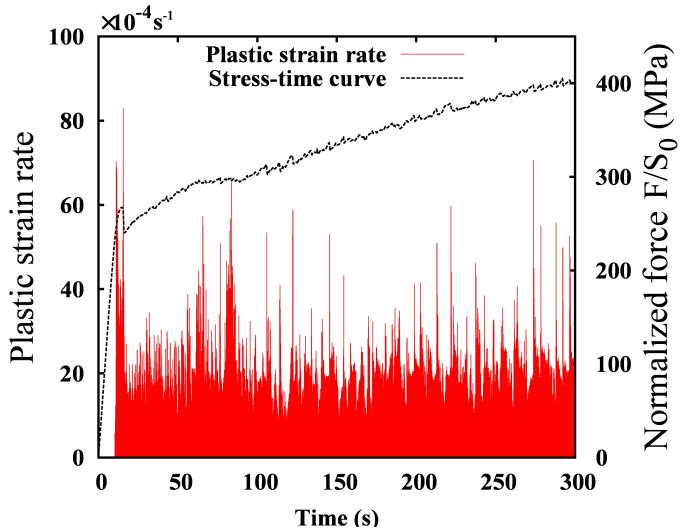

(b) 175 °C; v = 0.01 mm/s.

Figure 5.19 – Maximum strain rate evolution along centre line Y. To compare with DIC results in Fig. 5.10(a) and (b).

around notch" in Fig. 5.20) and the free propagating bands (“Propagating band" in Fig. 5.20) corresponding to the two different slopes in the spatio-temporal patterns. The schematic view of these two kinds of bands is presented in Fig. 5.17. Fig. 5.20(a) and (c) give the DIC measurement of the tests with loading rate v = 0.01 mm/s. The corresponding initiation time of these bands is given. As the experimentally observed propagating bands did not appear simultaneously (see Fig. 5.9(b) and (c)), we measured two propagating bands at different moments that are presented separately by the green and blue curves. By referring to Fig. 5.9(b) and (c), the position of these bands can be found according to the time. It is worth noting that the deformation rate inside a propagating band at 20 °C is higher than the initial bands around the notch. At 175 °C, the deformation rate inside localization bands is much higher than that at room temperature. This observation confirmed the comments about Fig. 5.10. It can be concluded that the localization bands related to the Lüders effect have been enhanced by the PLC effect that occurred at the same time. This interaction also explains the intermittent temporal behaviour of the

Lüders bands at 175 °C presented in Fig. 5.9. In addition, the band width at middle height ranges from 3.5 to 6.5 mm.

The corresponding simulation results are plotted in Fig. 5.20(b) and (d). To make a quantitative comparison, we adopted the same strategy in DIC for measuring the strain rate in FE simulations. The Green-lagrange incremental strain ε_{yy} is calculated for each time increment Δt = 4 s. Then the strain rate $\dot{\varepsilon}_{yy}$ is obtained dividing by Δt. The band width reproduced by simulations is slightly narrower than in the experiments which ranges from 2.5 to 4.5 mm. At 175 °C, the strain rate inside an initial propagating band is higher than at 20 °C due to the simultaneously occurring PLC effect, which is in agreement with experiments. It could also be noted that, the strain rate inside a free propagating band of the simulation at 175 °C is not much higher than that at 20 °C. In addition, the experimentally measured strain rate in a band is higher than the simulated one.

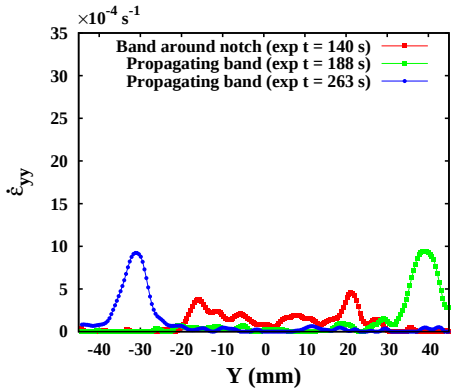

(a) Experiment: 20 °C; v = 0.01 mm/s.

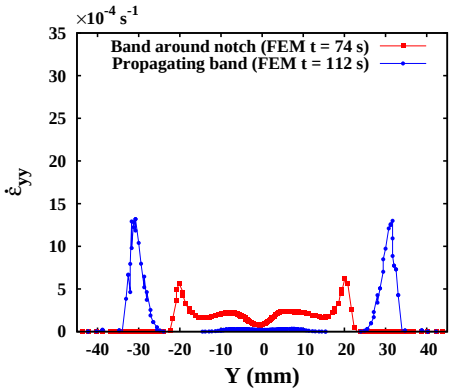

(b) FEM simulation: 20 °C; v = 0.01 mm/s.

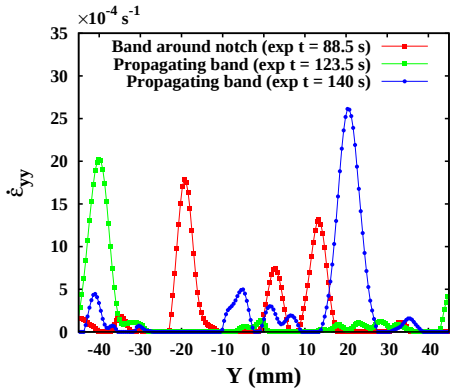

(c) Experiment: 175 °C; v = 0.01 mm/s.

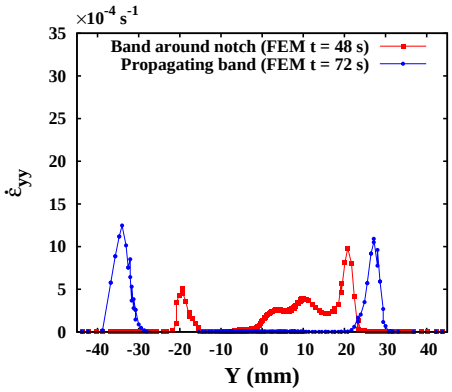

(d) FEM simulation: 175 °C; v = 0.01 mm/s.

Figure 5.20 – Comparison of the deformation rate inside localization bands. It is measured along the line Y placed in the centre of specimen as shown in Fig. 5.9.

5.4 Discussion

The kinematics and mechanical properties of localization bands due to strain ageing were studied by DIC and finite element simulations in this chapter. The DIC measurements revealed, for the first time, the kinematics of PLC bands around the notch tip of C-Mn steel SENT specimen at high temperature. The room temperature experiments also demonstrated the characteristics of Lüders effect different from ordinary smooth tensile specimens. In this discussion, the DIC and simulation results obtained in the previous sections

are compared with the literature.

5.4.1 The global stress-displacement curve

The Lüders effect in tensile tests is characterised by an upper yield stress at elastic-plastic transition point followed by a stress plateau with lower constant stress level. In the current SENT tests, a stress drop can still be observed at 20 °C, but it occurred later than the elastic-plastic transition point (see Fig. 5.5). Unlike the tensile test, the yield stress of the SENT specimen increases during the yield stage. This phenomenon is related to the notch tip effect. The area around notch bears serious plastic deformation. Lüders band initiates in this region earlier than the rest of specimen which results in a nonlinearity on the global stress-displacement curve without visible stress drop. In the less deformed area, the initially pinned dislocations are not able to break away from the Cottrell atmosphere which results in an increase of global stress. When the front of Lüders band reaches the whole width of specimen, a stress drop becomes visible on the global stress curve. This notch effect on the global stress due to Lüders effect has also been observed by Han et al. [2011] in the Q345 steel at room temperature. The DIC measurement presented in the current section confirmed the assumption about the Lüders band initiation around notch tip discussed by Han et al. [2011]. In the work of Han et al. [2011], due to a lack of DIC measurement, the author did not provide any information about the spatio-temporal evolution of Lüders band.

At 175 °C, it is more difficult to identify the Lüders stress drop due to the superposition of PLC serrations. At this temperature, the serrations started right after the elastic-plastic transition point. The PLC serrations did not change the shape of global stress curve.

If considering only the experimental curves, we are still not able to determine the end of Lüders effect. The full 3D simulations shed light on the information needed to determine the range of Lüders effect in such a specimen geometry (see Fig. 5.14). The Lüders effect only affects a limited range on the stress-strain curve and always ends with a stress plateau (or stress drop). This result has not been mentioned in Han et al. [2011] though a small stress plateau is visible on the global stress curve. The simulations also reproduced the yield peak, however the shape is too sharp compared with experiments. This could be related to the out of plane movement during the experiments. As presented in the appendix (Fig. 5.24, 5.25 and 5.26), we simulated three possible specimen movements during test. The mode III loading shows a significant influence on the shape of Lüders peak and results in a more realistic shape. The amplitude of PLC serrations in the current simulations is weaker than experimental results. It is due to the fact that the current simulations did not take into account the influence of the testing machine stiffness on the PLC effect. As shown in Wang et al. [2012], incorporating machine stiffness into the model gives a more realistic amplitude of PLC serrations.

The huge drop of ductility and toughness at 175 °C is observed for both tested loading rates (0.01 mm/s and 0.002 mm/s) which proved the reproducibility of this result. The factor around 2 of toughness drop at 175 °C is consistent with the results reported by Wang et al. [2012]. The simulations using the DSA model only work well for describing the hardening before fracture. The descending part of simulated curves is not in agreement with experiments which is due to the lack of proper damage mechanism. With the addition of void growth, better results are obtained for describing the descending part of experimental curves at 20 °C. Actually, the damage mechanism start to influence the global curve before attaining the maximum force. The pre-matured fracture at 175 °C has not been reproduced using the same damage parameters for both temperatures.

5.4.2 Strain field

In ordinary tensile specimens, Lüders bands initiate at the edge of the curved transition zone to the grip section of the specimen and propagates through the length of the sample. Different types of PLC bands can occur depending on the strain rate and temperature such as the continuously propagating type A band, intermittent type B band and randomly nucleated type C band. The influence of stress concentration areas on the band behaviour was less reported compared to tensile tests.

The Lüders band morphology in double notched tensile specimens was studied by Beardsmore et al. [2013]; Xiao et al. [2016]; Graff et al. [2004]. In this specimen type, Lüders bands initiate from the ends of specimens for small notches as in tensile tests. For large notches, Lüders bands initiate from the notch tip. These bands propagate through the whole specimen length. The Lüders band morphology in compact tension (CT) specimen has been studied by Wenman and Chard-Tuckey [2010] with DIC measurement and 3D finite element simulations. The Lüders bands in CT specimen are confined to the notch area.

The PLC band features in double notch tensile specimens were investigated by Nogueira de Codes and Benallal [2011] using digital infrared thermography and DIC. Bands are observed to be trapped in the vicinity of the minimal cross section for double notched specimen. As the tested material does not show Lüders effect, no more information could be given for it. In contrast, simulations showed the PLC bands could occasionally escape from the minimum section area in double notched specimen [Benallal et al., 2008]. The PLC band morphology in CT specimens is predicted by Belotteau et al. [2009] with the McCormick type DSA model with 2D mesh, and by Rousselier et al. [2017] with 3D mesh, though an experimental validation is still absent. For single crack tensile specimen, the PLC bands are found to remain at the notch area as Lüders bands [Nogueira de Codes and Benallal, 2011].

In the current SENT specimen, the band kinematics showed different features. We clarified the behaviour of simultaneously occurring Lüders and PLC effects. With DIC measurement, the different scenarios of band propagation at two temperatures can be summarised as:

- 20°C: Lüders band initiation around notch tip → Continuous band propagation with one side trapped in notch area → Accelerated continuous free propagation → No PLC bands
- 175°C: Lüders and PLC band initiation around notch tip → Intermittent band propagation with one side trapped in notch area → Accelerated intermittent free propagation → PLC bands flip-flop around notch

Unlike CT specimens (see Wenman and Chard-Tuckey [2010]), the Lüders bands can propagate through the whole specimen length in the current SENT specimen which is similar to the double notched tensile specimens with small notch.

The stress concentrator has a strong influence on the Lüders band propagation (see Fig. 5.9). It will slow down the propagation velocity for these bands with one side trapped in the notch area. The numerical results capture the notch effect on band propagation as shown in Fig. 5.17. The velocities at two stages of band propagation are reproduced by numerical simulations, in good agreement with DIC measurement.

The strain rate in propagating bands is higher than that in the bands with one side trapped in the notch area. This could explain the stress plateau at the end of Lüders effect. When the bands propagate with one side in the notch area, the deformation is still

concentrated in the notch tip area. The dislocations in the less deformed area are not fully unpinned which results in an increasing global stress. When the bands started to propagate without the influence of notch tip, deformation is concentrated in the moving band front which results in a stress plateau.

The flip-flop behaviour of PLC band around notch tip observed in the current section is to some extent in agreement with that reported in double U-notched specimen by Nogueira de Codes and Benallal [2011]. However, the influence of PLC effect on the Lüders band which results in an intermittent propagation has not been observed before. These scenarios are reproduced successfully with finite element simulations, though the simulated PLC bands showed more propagative feature rather than intermittency.

5.4.3 Fracture mode and SEM observations

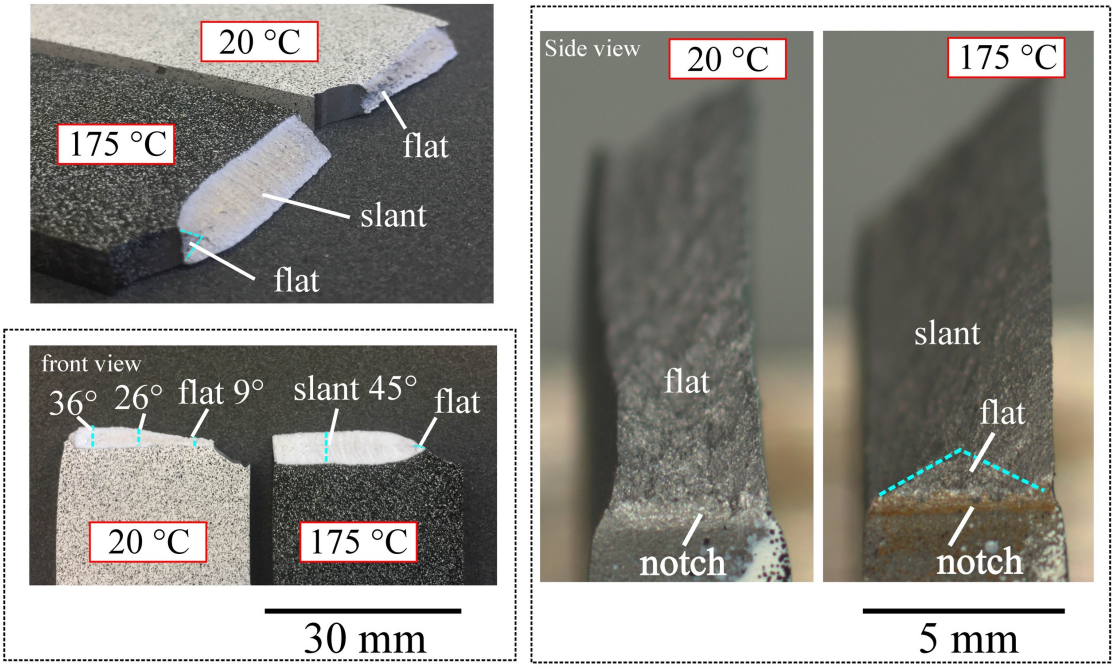

Figure 5.21 – Fracture surfaces of specimens tested at 175 °C and 20 °C for loading rate 0.01 mm/s. A typical slant fracture with a triangular flat transition zone is observed at 175 °C, while flat fracture is found at 20 °C. The same fracture surfaces are found for the loading rate 0.002 mm/s at corresponding temperatures which are not shown here.

As shown in Fig. 5.21, another interesting discovery in the current section is that two different modes of fracture are observed at 20 °C and 175 °C. At 20 °C, the crack remains flat until very late stages. In contrast, at 175 °C, a flat to slant transition is observed. The reduction of section thickness is significant at 20 °C. The slant fracture is certainly related to the early loss of symmetry of plastic zone (see Fig. 5.11d). A reasonable explanation for this phenomenon is that one slant shear band in the thickness plane is enhanced by PLC bands. Then the damage will develop in this slanted localization band and result in a slant crack. This damage mechanism due to early localization has been reported by Morgeneyer et al. [2014] in thin sheet CT specimen using laminography combining digital volume correlation. The slant fracture is simulated in 6.3 with a polycrystalline model incorporating DSA and damage. The flip-flop fracture reported by Simonsen and Törnqvist

[2004] could also be related to the PLC effect considering that the 5083 aluminium alloy is known to be sensitive to the PLC effect.

The fractographic studies at microscopic level are carried out on these SENT specimens using a ZEISS DSM982 scanning electron microscope. Fig. 5.22(a) shows four different areas of the specimen tested at 175 °C. Typical spherical dimples can be observed in the triangular area. Void growth is the controlling damage mechanism. Many dimples can also be observed in the slant regions close to the triangular region or in the further slant region. The dimples appear to be of two distinct sizes in these slant areas. The size of larger dimples is similar to that in the triangular area. A very slight shearing effect can be noticed in these slant areas. In addition, the shearing effect seems to be stronger beside the triangular area than in the further slant region. We can conclude that shearing effect occurred at very late stage.

Fig. 5.23 shows the areas around the notch and the final shear lip of the specimen tested at 20 °C. The dimples also show two different sizes around the initial notch area. The average size of these secondary dimples is larger than that found in the final shear lip area as well as in the slant region of 175 °C test.

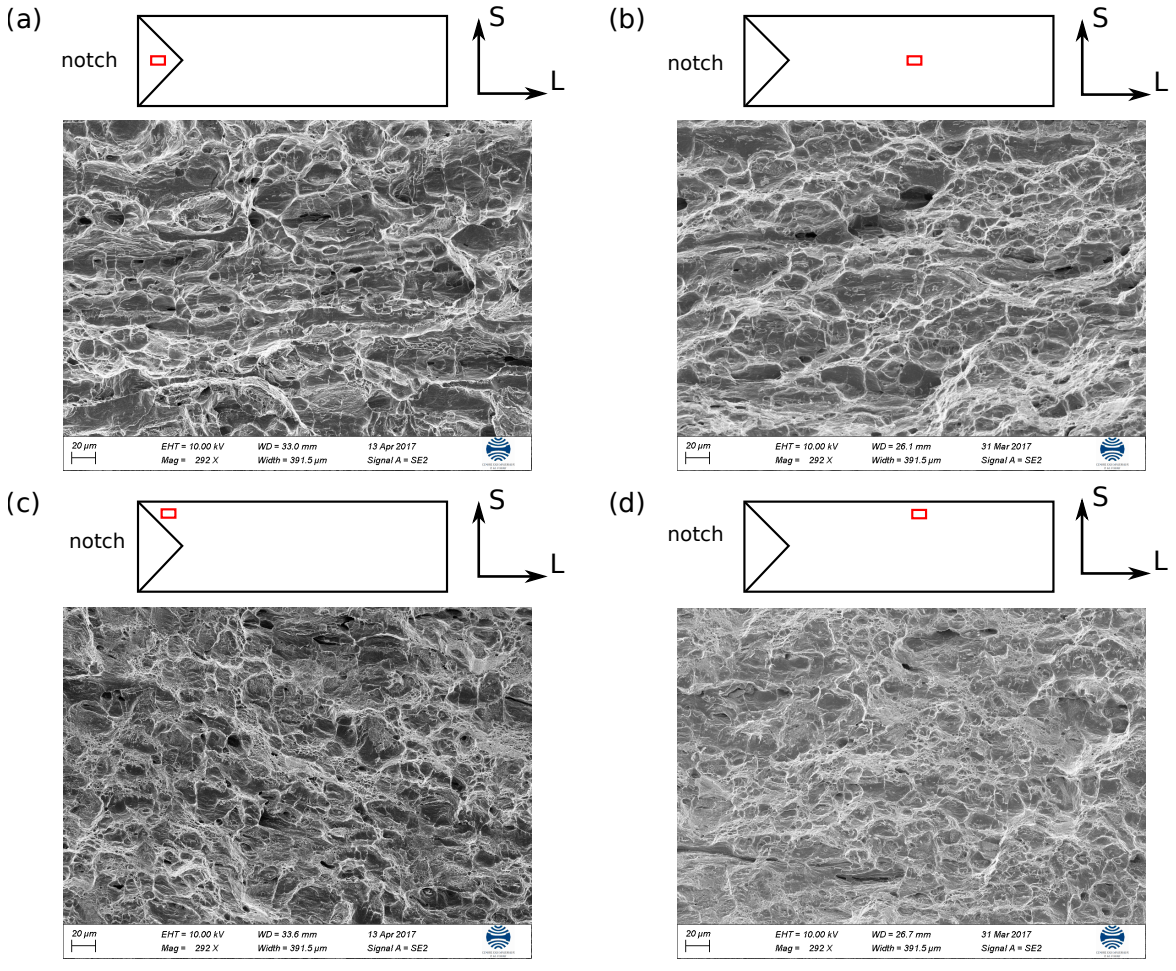

Figure 5.22 – Comparison of the fractography with SEM of specimens tested at 175 °C with loading rate 0.01 mm/s. 4 zones of the fracture surface: (a) triangular flat zone; (b) central area of slant zone; (c) slant area near to the triangular zone; (d) slant zone close to border.

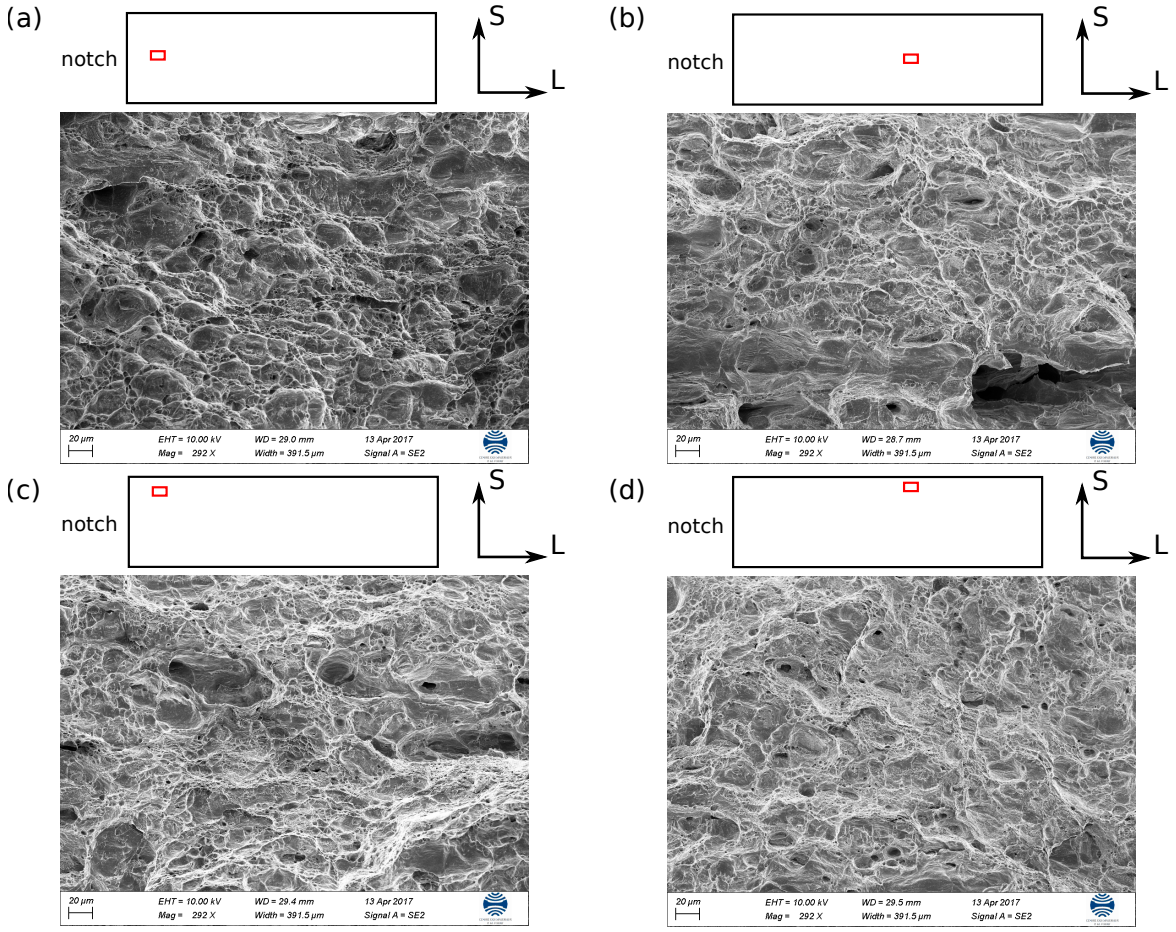

Figure 5.23 – Comparison of the fractography with SEM of specimens tested at 20 °C with loading rate 0.01 mm/s. 4 zones of the fracture surface: (a) middle area of the flat crack around notch; (b) middle area far from the notch; (c) area near to the border around notch; (d) border area far from the notch.

5.5 Conclusions

In this chapter, the DIC method is used for observing the strain ageing effect in C-Mn steel SENT specimens at different temperatures. The result shed light on the different evolution of Lüders and PLC bands in the presence of a notch. The main results are summarized below:

(1) The Lüders effect is observed for all the test conditions. The Lüders band propagation is found to be slowed down by the notch tip area when one side of the band is trapped in it. The propagation velocity in the area far from the notch tip is higher.

(2) The PLC effect is only observed at 175 °C. The DIC measurement at high temperature showed that, due to the presence of PLC effect, the specimen displayed different localization behaviour compared with room temperature. At 175 °C, the propagating Lüders bands display intermittent properties. The PLC bands during crack propagation are stuck in the crack tip area flipping up and down. In contrast, at room temperature there is no PLC band during crack propagation. In addition, the deformation rate inside a Lüders band at 175 °C (with PLC) is much higher than its counterpart at 20 °C (without PLC) due to the superposition of PLC effect.

(3) The cumulated plastic zone at 175 °C exhibits loss of symmetry much earlier than 20 °C. A slant crack is developed following one side of the plastic zone at 175 °C. At 20 °C,

as the plastic zone always develops in the middle plane, a flat crack is observed. The non-symmetric development of plastic zone at 175 °C shown in Fig. 5.11 is the precursor of slant fracture which consequently leads to a reduction of fracture resistance.

(4) The localization bands are reproduced successfully with the elastoviscoplastic model involving strain ageing. With a coupled model involving void growth, the mechanical response of specimens could be better described compared to the pure elastoviscoplastic model. However, the loss of fracture resistance can not be predicted thereby indicating that another damage mechanism, such as secondary nucleation and void sheeting may be at play in this case.

5.6 Appendix 1: Simulations of non-symmetric conditions during SENT tearing test

5.6.1 The effect of torsion due to grip misalignment

The out-of-plane movement is checked by DIC. Fig. 5.24 shows the torsion movement after closing grip. A very slight torsion induced z-direction displacement around 30 µm could be found due to the grip alignment.

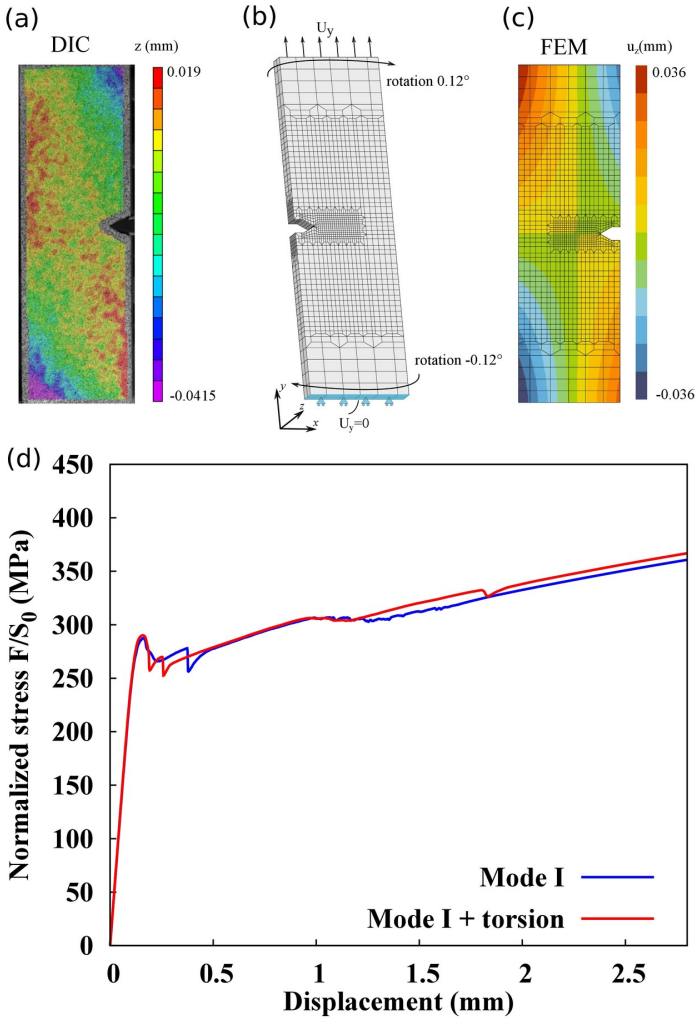

Figure 5.24 – Influence of torsion due to grip alignment: (a) Out-of-plane rotation measured by DIC; (b) Corresponding simulation boundary conditions; (c) u_z displacement field after torsion by FEM simulation; (d) Comparison of stress-displacement curves with mode I loading and with additional torsion.

The influence of this out-of-plane movement has been investigated numerically. An initial rotation of ±0.12° is applied on the upper and lower surfaces (see Fig. 5.24). The simulated u_z field after initial rotation is close to DIC measurement. A comparison of the stress-displacement curves of pure mode I loading and that with a slight torsion is presented in Fig. 5.24. A slight change of the Lüders yield peak could be seen.

5.6.2 The effect of non-symmetric loading

According to experimental measurement, the section length clamped inside the grip could vary from 1 mm to 3 mm when mounting specimens. We tested the influence of this non-symmetric loading by eliminating one layer of elements on the top (~3.5 mm shorter on the upper side). Fig. 5.25 gives the simulated stress-displacement curve which showed negligible influence of non-symmetric loading.

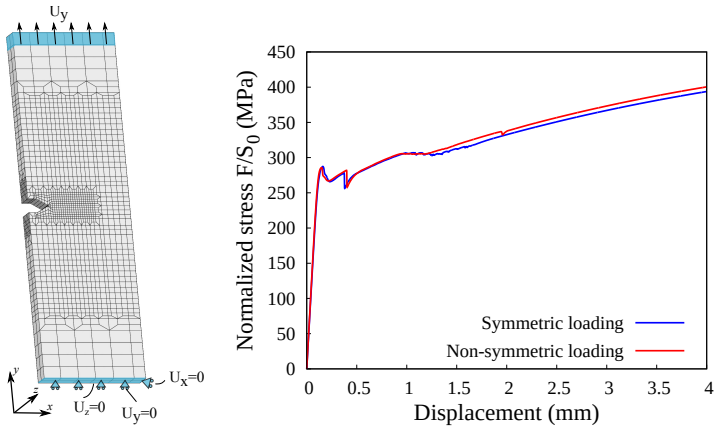

Figure 5.25 – FEM simulation of non-symmetric loading.

5.6.3 The effect of mode III loading

Another numerical test is made by applying mode III loading. Fig. 5.26 shows the schematic of boundary conditions and the stress-displacement curve. It can be noticed that this mode of loading has a significant influence on the initial yield peak. The shape of mode III loading curve is more realistic than that of pure mode I loading.

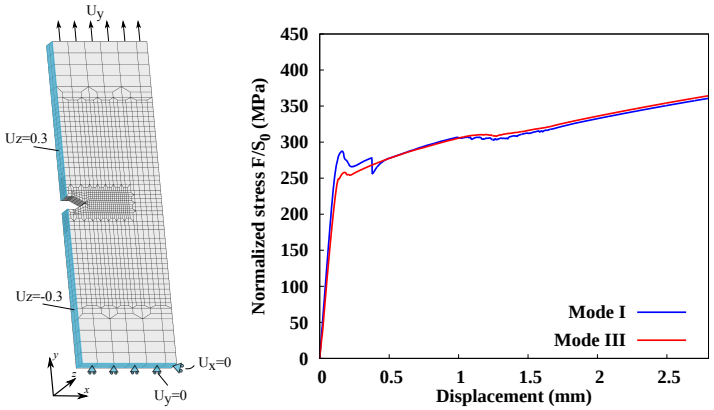

Figure 5.26 – FEM simulation of mode III loading.

Chapter 6

Prediction of fracture based on damage models coupled with DSA

Summary

This chapter is dedicated to numerical simulations of slant fracture.

In the first part, the simulation results using a modified Rousselier damage model are presented. The Gaussian curve used for describing void nucleation [Chu and Needleman, 1980] is replaced by a linear curve in order to describe the fast nucleation in localization bands. This damage model is also coupled with a DSA term. Simulations are performed on 2D and 3D tensile specimens using the material parameters of TU48C C-Mn steel. Results with and without DSA term are compared. This coupled model is then applied for simulating SENT tests presented in Chapter 5. The slant fracture in flat tensile specimens is reproduced. The prediction in round bar and SENT specimens remain challenging with this model.

In the second part, an attempt is made to capture numerically slant ductile fracture and its early slant strain precursors in CT specimens via combining a dynamic strain ageing (DSA) model with ductile damage models in the framework of polycrystalline models. In recent experimental studies it has been shown that in an AA2198 alloy strain localization in slant bands preceded the onset of damage, originating slant fracture ahead of a notch. A McCormick-type DSA model in conjunction with a Rousselier damage model, a reduced polycrystalline plasticity model and a Coulomb fracture criterion for slip systems have been used. Full 3D finite element simulations using this model and typical parameters for aluminium alloys capture the early strain localization in slanted bands, their intermittent activity and the final slant fracture. Prior simulation results without the DSA model and others using the von Mises plasticity or the GTN model did not capture the early slant strain localization thereby suggesting that DSA may well be the physical origin of the early slant strain localization and final slant fracture phenomena in this alloy.

Résumé

Ce chapitre est dédié aux simulations numériques de rupture en biseau.

Dans la première partie, les résultats de simulation utilisant un modèle d'endommagement de Rousselier modifié sont présentés. La loi normale utilisée pour décrire la germination des cavités [Chu and Needleman, 1980] est

remplacée par une loi linéaire afin de décrire la germination rapide dans les bandes de localisation. Ce modèle d'endommagement est également couplé avec le modèle DSA. Les simulations sont effectuées sur des éprouvettes de traction 2D et 3D en utilisant les paramètres de l'acier TU48C C-Mn. Les résultats avec et sans le terme DSA sont comparés. Ce modèle couplé est ensuite appliqué à la simulation de la rupture dans l'éprouvette SENT. La rupture en biseau dans des éprouvettes planes a été reproduite. La prédiction dans des éprouvettes cylindriques et SENT reste difficile avec ce modèle.

Dans la deuxième partie, une tentative est faite de capturer numériquement la rupture ductile en biseau et ses précurseurs de déformation inclinée précoce en combinant un modèle de vieillissement dynamique (DSA) avec des modèles d'endommagement ductile dans le cadre de modèles polycristallins. Dans les études expérimentales récentes, il a été montré que dans un alliage AA2198, les localisations dans des bandes inclinées précédait l'apparition d'endommagement, provoquant une rupture en biseau devant une entaille. Un modèle DSA de type McCormick associé à un modèle d'endommagement de Rousselier, un modèle de plasticité polycristalline réduite et un critère de rupture de Coulomb pour les systèmes de glissement ont été utilisés. Les simulations par éléments finis 3D utilisant ce modèle et les paramètres typiques pour les alliages d'aluminium capturent la localisation précoce dans des bandes inclinées, leur activité intermittente et la rupture en biseau finale. Des résultats de simulation dans la littérature sans le modèle DSA et d'autres utilisant la plasticité de von Mises ou le modèle GTN n'ont pas pu capturer la localisation inclinée précoce, suggérant que le DSA pourrait bien être l'origine physique de la localisation inclinée précoce et des phénomènes de rupture en biseau.

Contents

6.1 Introduction

The understanding and prediction of strain and damage interactions in ductile alloys remain a crucial topic e.g. due to the need for weight reduction without compromising passenger safety in transport applications. The development of novel alloys and enhanced joining techniques [Le Jolu et al., 2014, 2015] make ductile alloy candidates for future structural applications. This understanding of strain and damage interactions is important for micromechanics-based development of new materials and the assessment of structural integrity.

Ductile fracture is commonly linked to ductile fracture micromechanisms which are: the nucleation of voids, their growth and final coalescence. However, failure in cases where strain localization takes place and also in cases where the triaxial stress, the driving force of void growth during ductile deformation, is low, i.e. typically below 1 [Papasidero et al., 2014] is poorly understood. An insufficiently understood phenomenon linked to localization and strain and damage interactions during ductile tearing is slant fracture [Mahgoub et al., 2003].

As mentioned in Chapter 2, slant fracture is hard to reproduce numerically in general [Besson, 2010]. This could be linked to numerical problems due to mesh dependence of local models [Besson et al., 2001b]. Slant fracture has successfully been simulated using shear void nucleation based on the Lode parameter [Morgeneyer and Besson, 2011] that actually resembles the shear modification of the Gurson model [Nahshon and Hutchinson, 2008]. In [Morgeneyer et al., 2016], this model has been used. Slant fracture was reproduced successfully but the early strain localization could not be captured. In [Besson et al., 2013] it has been shown via a computational cell simulation that the dissipated energy reaches a minimum when the crack is slanted. Experimentally, slant fracture is widely observed in thin walled structures [Pardoen and Hutchinson, 2003] and can also lead to flip-flopping phenomena [El-Naaman and Nielsen, 2013b; Simonsen and Törnqvist, 2004] that are neither understood nor reproduced numerically, although out-of-plane loading in thin sheets is a possible explanation.

Two different models are used in the current chapter to simulate slant fracture. In 6.2, a macroscopic DSA model is coupled with a modified Rousselier damage model. A rapid nucleation term is added. The tensile and SENT tests are simulated with this model. In 6.3, a fully coupled polycrystal model involving DSA and Coulomb criterion in the slip system is used for simulating slant fracture in CT-like specimens of AA2198-T8R alloy.

6.2 Prediction of fracture with modified Rousselier damage model coupled with DSA

6.2.1 Presentation of the coupled macroscopic model

Ductile fracture in metals can be characterised by three simultaneous or successive mechanisms: nucleation, growth and coalescence of voids. The evolution of void volume fraction can be represented as:

$$\dot{f} = \dot{f}_n + \dot{f}_g, \tag{6.1}$$

where f_n is the contribution of void nucleation to total void fraction and f_g the contribution of the growth of existing voids. Rousselier's model gives a void growth rate almost

identical to Rice and Tracey's [Rousselier and Luo, 2014]:

$$\dot{f}_g = \dot{p}(1-f)D_1 f \exp\left(\frac{\sigma_m}{s_1(1-f)}\right). \tag{6.2}$$

D_1 is a material independent constant, fixed at $D_1 = 2$ here. s_1 represents the resistance of the metal matrix to the growth and coalescence of cavities, for which the recommended value is $\frac{2}{3}R_m$. In the Rousselier model [Rousselier and Luo, 2014], the void nucleation rate can be described by a Gaussian curve as introduced by Chu and Needleman [1980]

$$\dot{f}_n = \dot{p}\frac{f_N}{s_N\sqrt{2\pi}}\exp\left(-\left(\frac{p-e_N}{s_N\sqrt{2}}\right)^2\right), \tag{6.3}$$

where f_N is the volume fraction generated by nucleation, e_N is the mean plastic strain at maximal nucleation, s_N the standard deviation of Gaussian distribution as shown in Fig. 6.1(a). The coalescence of voids doesn't need any additional function in Rousselier's model. It is embedded by relation the necessary kinematic coalescence condition (NKCC) [Rousselier and Luo, 2014].

The fracture process is translated by a critical value f_c. When $f > f_c$, the material is considered to be "broken". The material parameters will be set to be near zero after reaching this value, thus the material will lose its mechanical strength because of almost complete stress softening. Unlike the f_c in Gurson type model, f_c in the Rousselier model has little effect on the results [Rousselier and Luo, 2014]. It can be used for visualising the crack path.

As mentioned in Section 5.3, an attempt has been made to couple the DSA model with void damage. The new yield surface can be written in the following form [Rousselier, 1981, 1987; Rousselier and Luo, 2014]:

$$\Phi = \frac{\sigma_{eq}}{1-f} + s_1 D_1 f \exp\left(\frac{\sigma_m}{s_1(1-f)}\right) - R(p) - R_a(p,t_a). \tag{6.4}$$

The irreversible deformation rate $\dot{\underset{\sim}{\varepsilon}}_p$ is obtained assuming the normality rule, so that:

$$\dot{\underset{\sim}{\varepsilon}}_p = \dot{p}\frac{\partial\Phi}{\partial\underset{\sim}{\sigma}}. \tag{6.5}$$

The conventional isotropic hardening term $R(p)$ in eq. (6.4) can be presented as

$$R(p) = R_0 + Q\left(1-e^{-bp}\right) + Hp, \tag{6.6}$$

$$\dot{p} = \dot{\varepsilon}_0 \sinh\left(\frac{\max(0,\Phi)}{\sigma_0}\right), \tag{6.7}$$

where p is the cumulated plastic strain. The strain ageing hardening term R_a reads

$$R_a(p,t_a) = P_1\left(1-e^{-P_2 p^\alpha (t_a(p))^n}\right), \quad \dot{t}_a = 1 - \frac{t_a}{w}\dot{p}, \tag{6.8}$$

where P_1 represents the maximal stress drop from a fully pinned state to a fully unpinned state; t_0 characterizes the time of diffusion process; n is selected depending on different diffusion mechanisms; w characterizes the strain increment associated with unpinning event.

Fast nucleation model

As presented in Section 5.4.3 and by Wang et al. [2012], according to the fractography of the tested C-Mn steel, spherical dimples with similar sizes can be observed on both slant and flat surfaces which indicates that the final fracture is driven by a sudden nucleation of voids at very late stage. This fast nucleation is possibly related to the localization bands observed by Morgeneyer et al. [2016].

A modified nucleation law is introduced in eq. (6.1) in order to take into account such phenomenon:

$$\dot{f} = \dot{p}\left((1-f)D_1 f \exp\left(\frac{\sigma_m}{s_1(1-f)}\right) + \underbrace{\mathrm{H}(p-p_c)k_c(p-p_c)}_{\dot{f}_{na}} \right) \tag{6.9}$$

where the void growth evolution f_g has been retained [Rousselier and Luo, 2014]. The Gaussian curve for nucleation ($\dot{f}_n$) has been replaced by a linear curve ($\dot{f}_{na}$) in order to model the rapid nucleation process as shown in Fig . 6.1(b). In summary, the parameters involved in the present constitutive model could be classified into the following categories:

-parameters characterising DSA in KEMC model: P_1, P_2, α, n, ω,

-parameters of the damage model:

$$\begin{cases} \text{Nucleation:} & (f_N, e_N, s_N) \quad \text{replaced by} \quad (p_c, k_c); \\ \text{Growth:} & D_1, s_1; \\ \text{Coalescence:} & f_c, \end{cases}$$

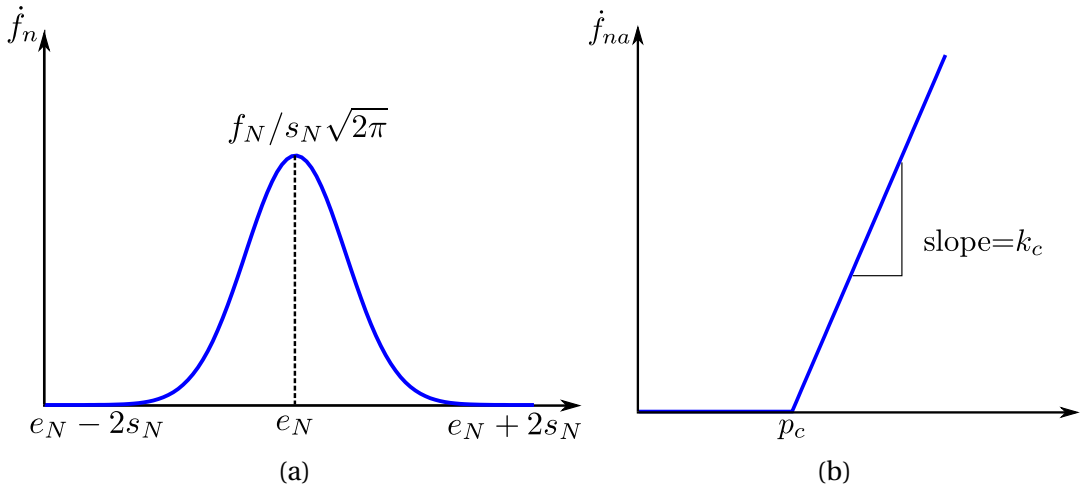

Figure 6.1 – Example of void nucleation laws: (a) Chu and Needleman [1980]. (b) the linear function used for the current study.

Influence of k_c and p_c

p_c is the threshold value for which massive nucleation happens. In tensile specimens, as can be seen in Fig. 6.2(a), higher p_c values result in a later fracture. k_c denotes the nucleation rate. Higher nucleation rate results in an earlier fracture and a faster descending curve (see Fig. 6.2(b)).

Table 6.1 – Parameters of TU48C steel at 200 °C for the current simulation.

E(GPa)	ν	P_1(MPa)	n	w	$P_2(s^{-n})$	α
198	0.3	83	0.66	2×10^{-4}	0.85	0.17
R_0(MPa)	Q(MPa)	b	$\dot{\varepsilon}_0(s^{-1})$	σ_0(MPa)		
176	287	29.3	9.47×10^{-4}	4.55		
D_1	s_1	f_c	k_c	p_c		
2	275	0.99	-	-		

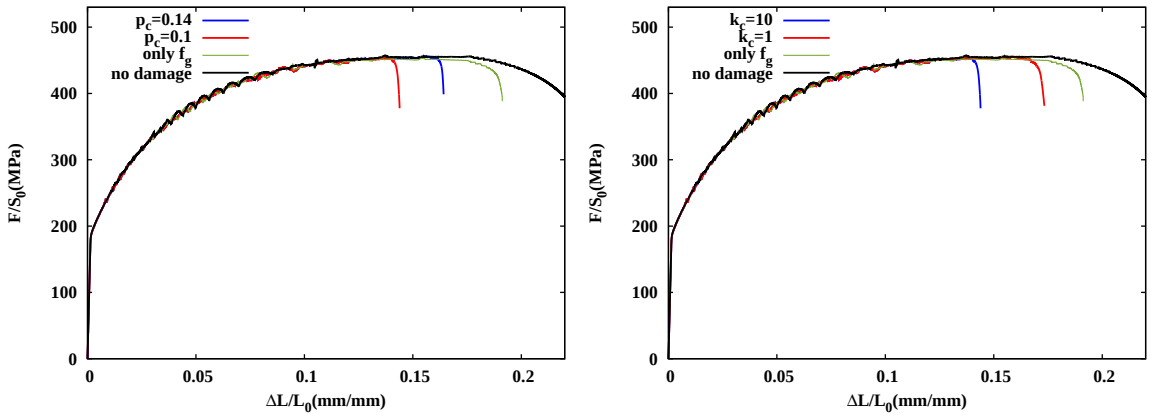

(a) Influence of p_c ($k_c = 10$). (b) Influence of k_c ($p_c = 0.1$).

Figure 6.2 – Influence of parameters related to the fast nucleation term on the tensile curve. Simulations performed at 10^{-3} s^{-1}.

6.2.2 Finite element simulations of tensile tests

2D simulations with and without DSA

We compared the simulations with and without DSA term under plane stress condition in order to investigate its influence on ductile fracture. Simulations are conducted on a 2D mesh with 12 elements (C2D8R element with reduced integration point number) in the transverse direction. Strain rate 10^{-4} s^{-1} is chosen for the current numerical tests because slanted PLC bands can be produced under this condition with the parameter set shown in Table 6.1. $k_c = 20$ and $p_c = 0.1$ are used to generate a fast nucleation.

Fig. 6.3 shows the cumulated plastic strain field simulated without the DSA term ($P_1 = 0$). By setting $P_1 = 0$, the contribution of strain ageing on the hardening is also eliminated. Therefore, a term R_a with $t_a = \frac{w}{\dot{E}}$ is added to compensate the total hardening. The broken elements are deleted in post-processing by setting a threshold value at $f = 0.045$. We can notice that the damage initiates from the centre of the specimen and expands to the boundary along the transverse direction.

Fig. 6.4 shows the cumulated plastic strain field simulated with the activated DSA term ($P_1 = 83$). The damage (f) is found to develop following a PLC band in a slanted plane.

Orientation of localization band and fracture

Two different 2D meshes with different element sizes have been investigated under plane stress assumption as shown in Fig. 6.5. The first one contains 8 elements (0.75 mm × 0.75 mm C2D8R) through the transverse direction. The second one has 12 elements (0.5 mm×0.5 mm C2D8R) through the transverse direction. The final angle of fracture

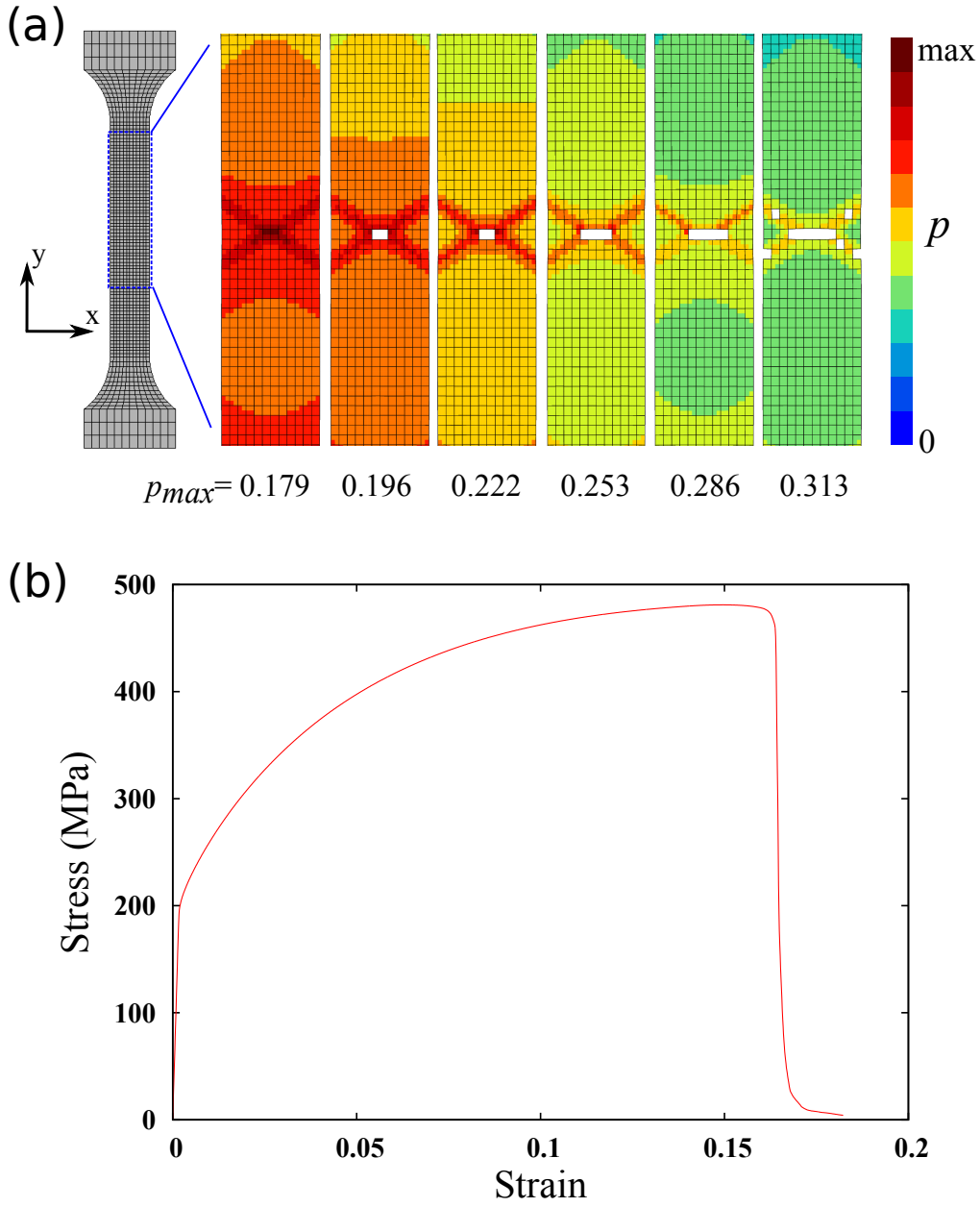

Figure 6.3 – Simulations without the DSA term ($P_1 = 0$): (a) plastic strain field and development of void damage. A stress compensation is considered as the DSA term has been eliminated; (b) simulated tensile curve.

surface is presented by the void fraction (f). The propagative PLC band in terms of plastic strain rate ($\dot{p}$) is presented beside the pattern of void fraction. It can be noticed that the angle of final fracture ($\sim 64°$ in the initial configuration) is different from that of PLC band $\sim 58°$. With a finer mesh, this difference is reduced.

3D plate specimens

This model is then applied for 3D plate specimens with different layers (from 1 to 4) of elements in the thickness as shown in Fig. 6.6. C3D20 elements are used for constructing

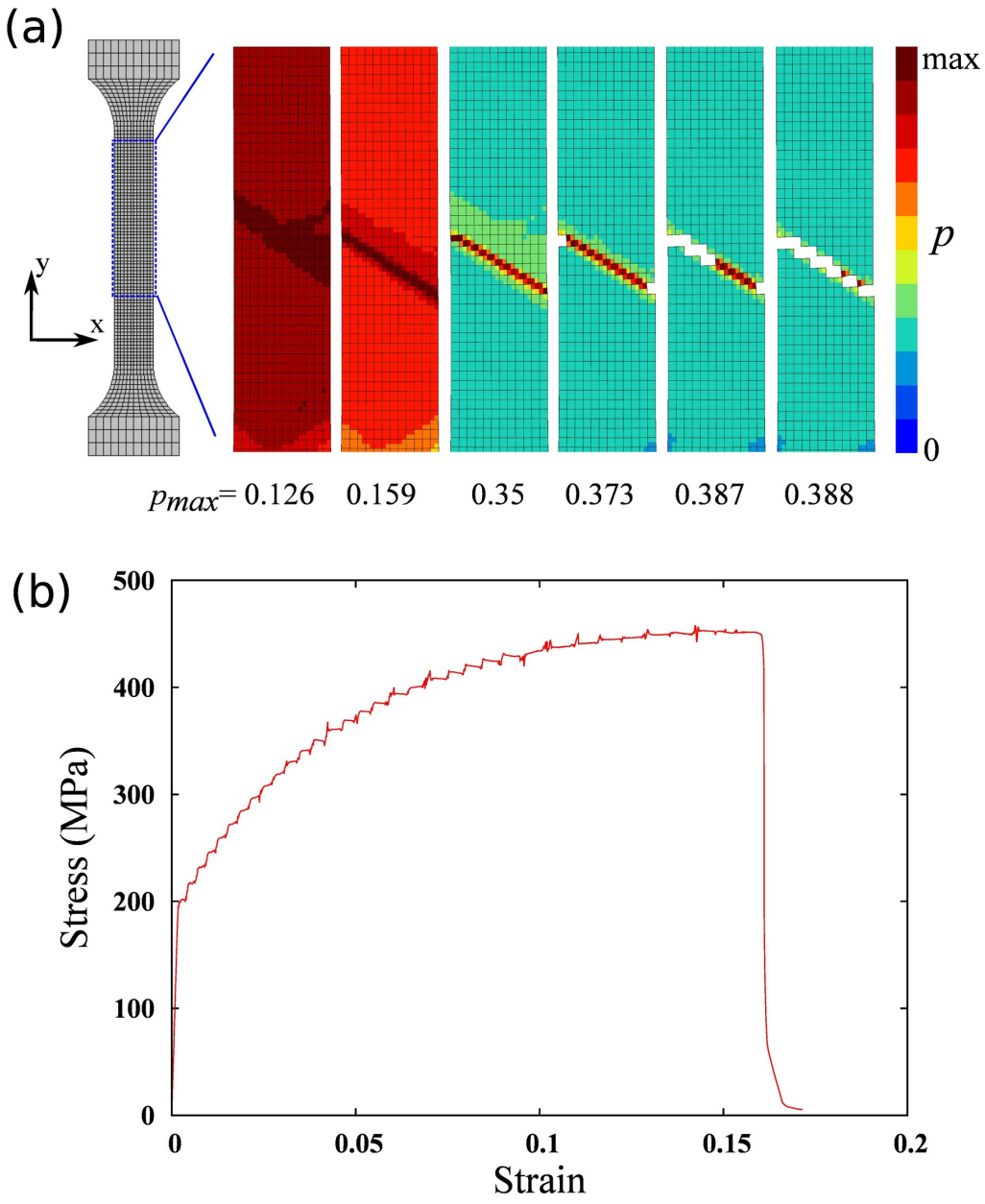

Figure 6.4 – Simulations with the DSA term (P_1 = 83): (a) plastic strain field and development of void damage; (b) simulated tensile curve.

these meshes. k_c = 20 and p_c = 0.1 are used as in the 2D cases. Propagating slanted PLC band in the transverse plane is found for all the simulations as shown in Fig. 6.6. A cup-cone shape is observed in the thickness plane. Slant fracture is obtained for the meshes with more than one layer of elements in the thickness plane. Flat fracture is found in the single layer mesh.

3D round bar specimens

The same parameter set is then applied for round tensile bar tests. The mesh is constructed by 6696 C3D20R elements. Fig. 6.7 show the simulation results at strain rate

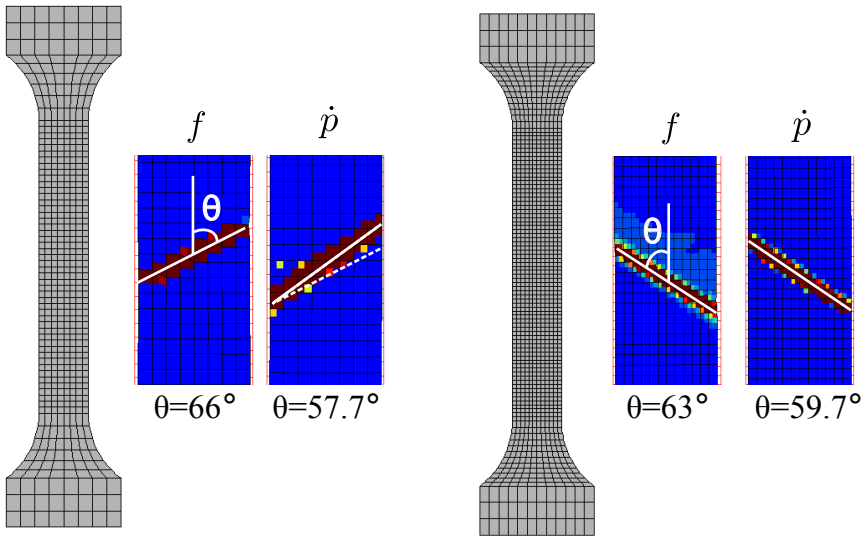

Figure 6.5 – The angles of localization band and final fracture. Simulations are performed on the meshes with 8 elements (left) and 12 elements (right) along the transverse direction respectively. These simulations are performed at strain rate $10^{-4}\,s^{-1}$.

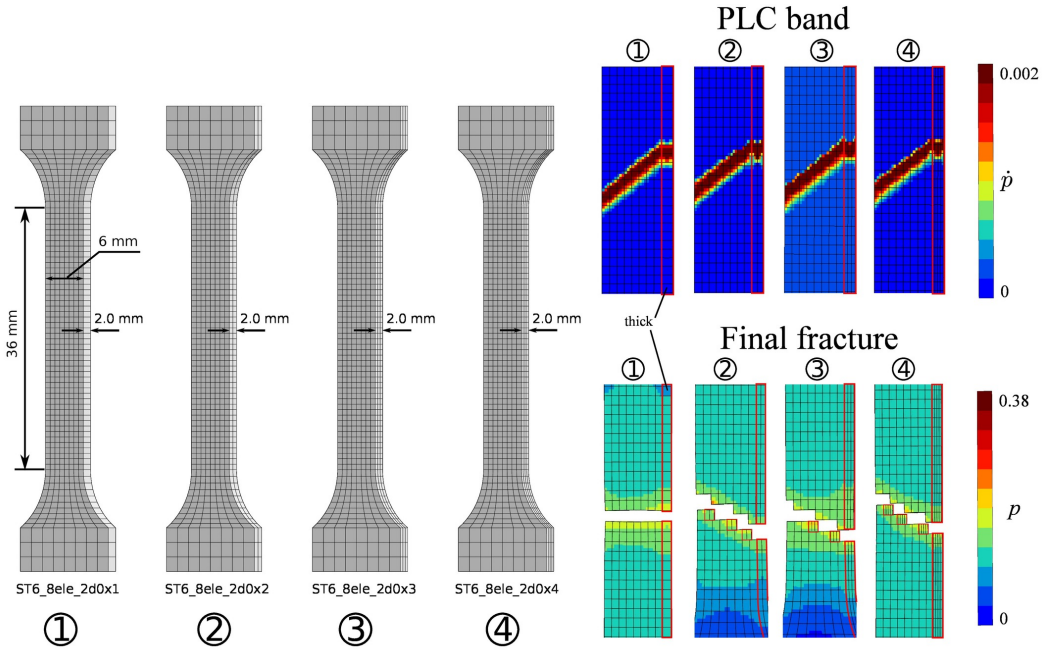

Figure 6.6 – Simulations with the modified damage model at strain rate $10^{-4}\,s^{-1}$ on 3D plate tensile specimens with increasing number of element through thickness: PLC band and final fracture.

$10^{-4}\,s^{-1}$. It can be noticed that PLC band oscillates around the necked area showing high mobility. These bands rotate around the y axis and occasionally appear outside the necking area. Along with the development of the necking area, the strain rate bands begin to concentrate in the minimum section and become flat. Though the slanted PLC band is produced at the beginning, the current simulation failed to capture the slant fracture observed experimentally by Wang et al. [2012].

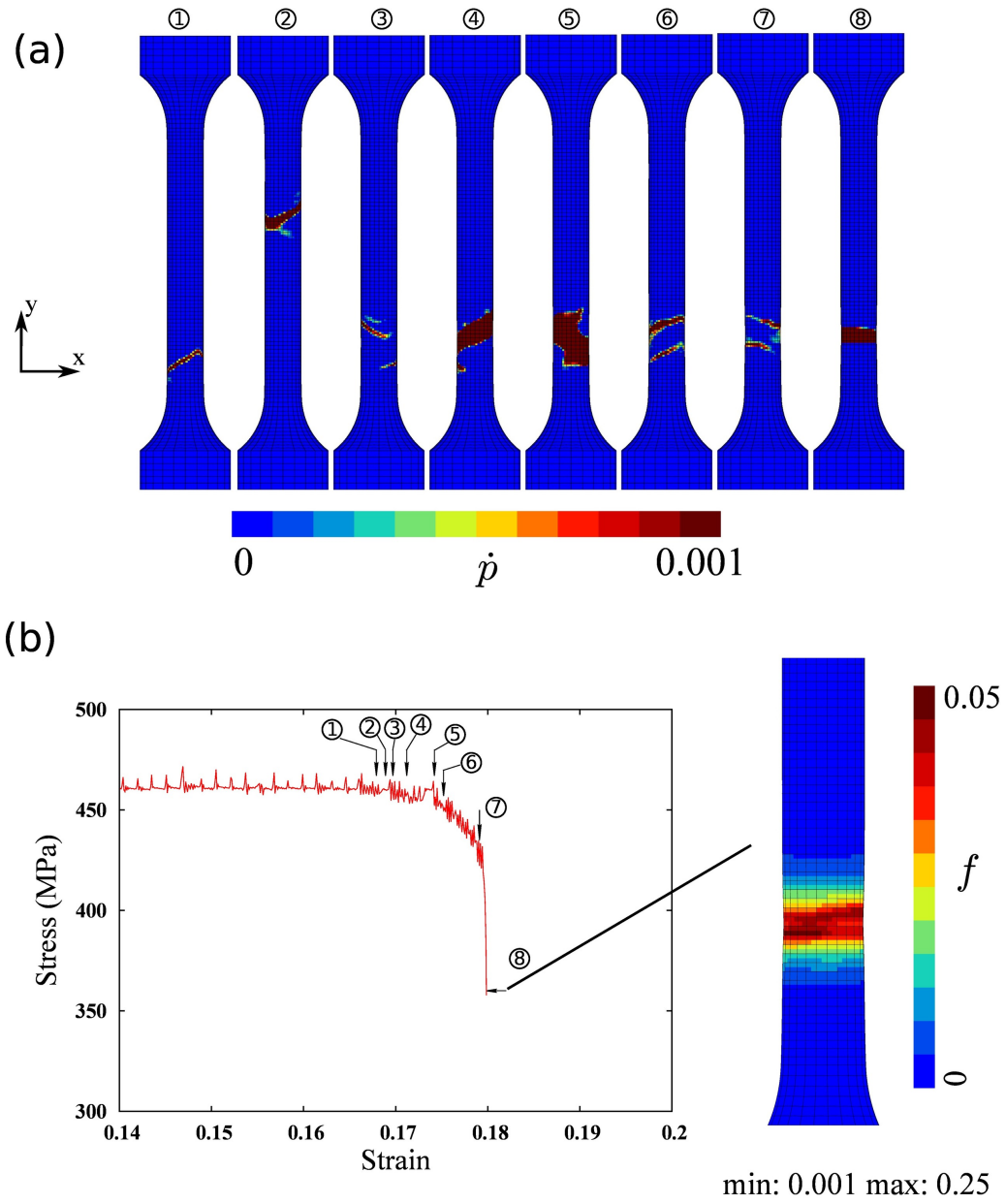

Figure 6.7 – Simulations with the modified damage model on 3D round bar specimens. (a) The plastic strain rate bands at strain rate $10^{-4}\,s^{-1}$ around the necking area. (b) the stress-strain curve and void fraction at the last step of current calculation.

6.2.3 Simulation of fracture in A42 SENT specimens

In the previous Chapter 5, it has been shown that slant fracture is found in a C-Mn SENT specimen tested at 175 °C with the presence of PLC effect, whereas flat fracture is observed at 20 °C. The modified damage model coupled with DSA term is applied for simulating the tearing test of SENT specimens at 20 °C and 175 °C. The material parameters can be found in Table 5.3. Fig. 6.8 shows the upper part of the 3D SENT mesh. $k_c = 10$ and $p_c = 0.3$ are used. A flat crack in a single layer of elements is finally obtained at 175 °C as shown in 6.8(b) indicated by broken Gauss points (red). This is not in agreement with experimental results at 175 °C. The simulation at 20 °C obtains a flat crack which is very similar to Fig. 6.8.

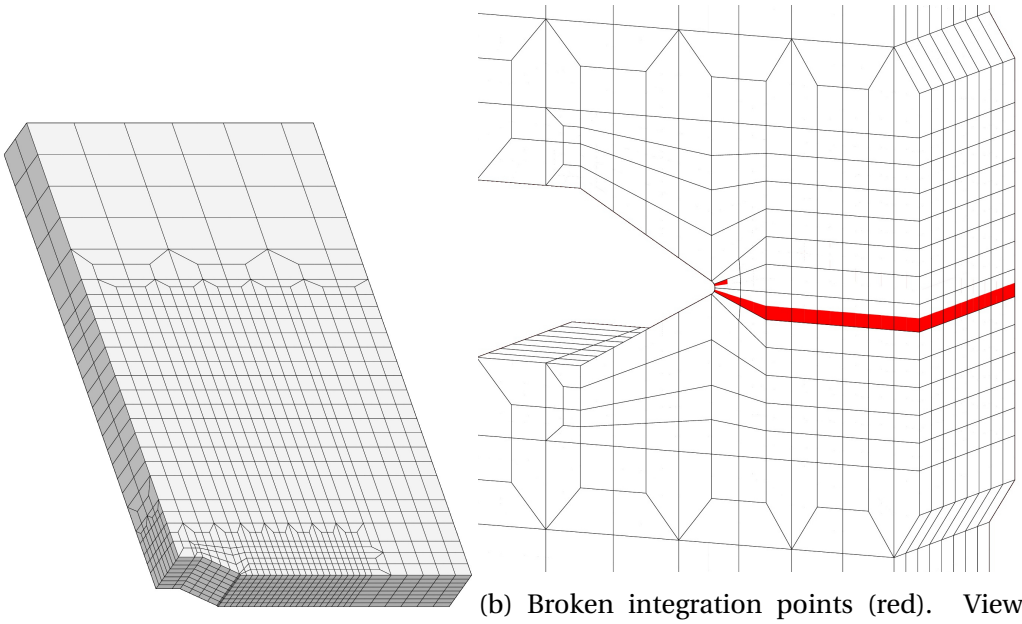

(a) Upper half of SENT mesh.

(b) Broken integration points (red). Viewed from x = 5 mm.

Figure 6.8 – Simulations of SENT test at 175 °C with fast nucleation and DSA.

In order to produce slant fracture at 175 °C, different methods for promoting non-symmetric distribution of the plastic zone have been applied as shown below.

Introduction of soft zones

We tried to impose soft zones in order to reduce the mobility of PLC bands. As shown in Fig. 6.9(a), three lines of elements forming a 45° angle to the loading direction in the thickness plane are selected as soft zones. In theses zones, the material is considered 10% softer than the bulk region as studied in Morgeneyer et al. [2016]. Fig. 6.9(b) shows the broken Gauss points. Although this soft zone results in slight asymmetric strain band, the final fracture mode is not influenced. Compared to Fig. 6.8, the fracture developed to another element layer due to the asymmetry.

Different damage parameters in the selected shear lip region

Another attempt is made by introducing different damage parameters in the shear lip and further crack propagation regions and in the initial flat fraction region as done in section 6.3. The different regions are indicated in Fig. 6.10(a). In the initial flat fracture region a larger $p_c = 0.3$ is used, whereas a lower value $p_c = 0.2$ is used in the shear lip and further crack propagation regions. Similar to the "mesh orientation effect ", this artificial modification might limit the crack propagation in the flat plane. However, as shown in Fig. 6.10(b), the crack is still confined in two layers of elements even though the asymmetric effect is stronger than the previous two methods.

6.2.4 Conclusions of simulation results using the fast nucleation model

In section 6.2, a rapid nucleation term is added to Rousselier's damage model in order to simulate the slant fracture in SENT specimens. A DSA term is coupled with this modified damage model. The results of numerical tests on different specimens are summarised below:

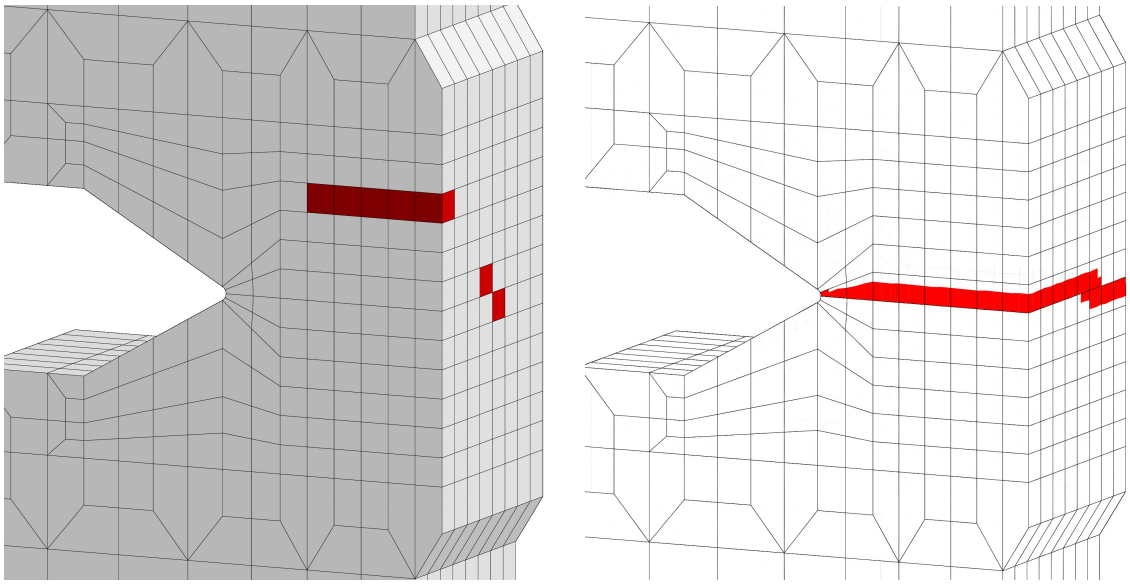

(a) Selected soft zones. (b) Broken integration points (red).

Figure 6.9 – Simulations of SENT test at 175 °C with fast nucleation and DSA involving soft zones. Viewed from x = 5 mm.

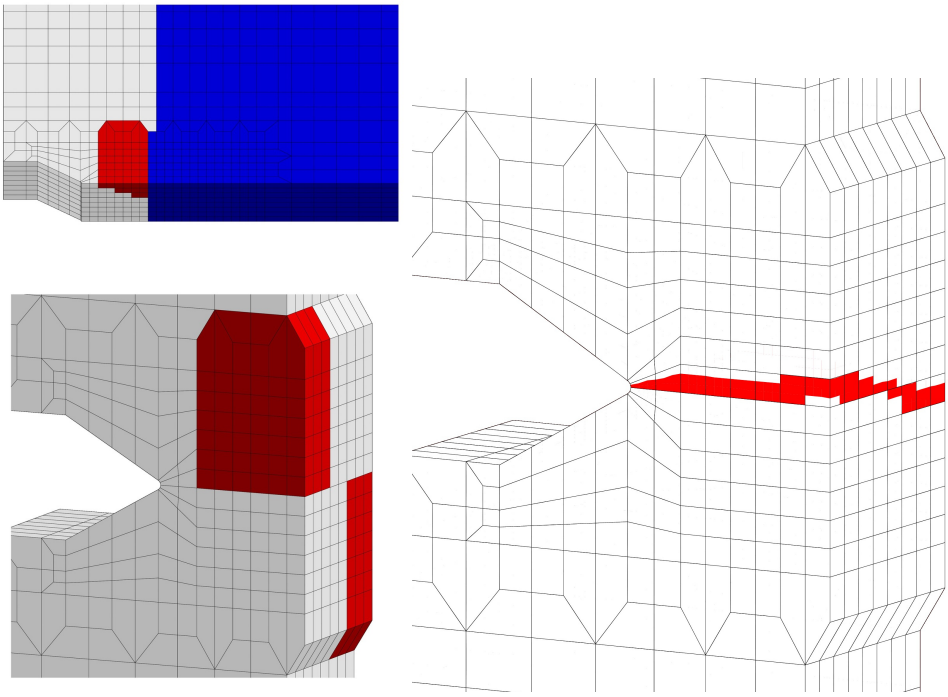

(a) (b)

Figure 6.10 – Simulations of SENT test at 175 °C with different parameters in the selected shear lip region. (a) Different fracture parameters are used in the selected shear lip region (red) and further crack propagation region (blue); (b) broken integration points (red). Viewed from x = 5 mm.

- 2D simulation of tensile test under plane stress condition shows that a slanted PLC band could lead to slant fracture. The final fracture angle is slightly different from that of PLC band.
- Slant fracture can be produced in 3D plate tensile specimens with multiple layers

of elements in the thickness plane. The fracture is found to initiate in a slanted PLC band as same as 2D simulations.

- The current modified model can not reproduce the slant fracture observed in 3D round bar specimen or in SENT specimen.

The current simulations show that the fast nucleation model is not able to capture slant fracture in notched specimens. As shown in Chapter 5, the simulated localization bands showed higher mobility compared to experimental results. The strong measured localizations flipping around notch tip should be reproduced in the future, which may promote slant fracture.

In the next section, we will present the results about flat-to-slant crack in CT-like specimens using a polycrystal model involving DSA in the slip system.

This part is reproduced from: Rousselier, G., Morgeneyer, T. F., Ren, S., Mazière, M., & Forest, S. (2017). Interaction of the Portevin–Le Chatelier phenomenon with ductile fracture of a thin aluminum CT specimen: experiments and simulations. *International Journal of Fracture*, 206(1), 95-122.

6.3 Simulation of slant fracture in AA2198 compact tension (CT) specimen with the polycrystal model

With recent advances in synchrotron imaging [Maire et al., 2011; Maire and Withers, 2014] and strain measurement techniques via digital volume correlation [Morgeneyer et al., 2013], it has become possible to measure damage and strain evolution in situ and in three dimensions non-destructively. For the observation of damage and strain interaction during ductile tearing of sheet materials synchrotron laminography is particularly adapted Helfen et al. [2012].

For an Al–Cu–Li alloy with low work hardening (AA2198-T8R) it has been shown with these techniques that slant strained bands precede the onset of damage and the slant crack [Morgeneyer et al., 2014]. This region of the sample has been shown to be in a plane strain state with respect to the crack propagation direction [Buljac et al., 2016]. It has also been shown that the ratio between the strain in the band and outside of the band was of the order of 2 [Morgeneyer et al., 2014]. In other words, the material outside the bands also deforms during every load step, except for the very last ones, but to a lesser extent than the material within the band. For the last load step deformation only occurs within the band. Strain concentrations in a slant band were observed very early on and the scene for localization and fracture was already set. For another 2XXX alloy with initial porosity and strong work hardening (AA2139-T3), the early strain localization in slanted bands ahead of a notch has been confirmed via the mentioned techniques [Morgeneyer et al., 2016]. Intermittent band activity and their relative stability in space could be confirmed. Von Mises plasticity or a GTN type model did not manage to reproduce the above mentioned findings in terms of slant bands or slant fracture [Morgeneyer et al., 2014].

One objective of this section is to investigate whether the multiple and intermittent crossing strain bands observed by laminography-DVC in CT-like specimens could be related to dynamic strain ageing (DSA) via simulations. In aluminium alloys at room temperature, DSA can also be involved in ductile fracture. Shear banding in aluminium alloys at room temperature has also been attributed to DSA and the Portevin–Le Chatelier (PLC) effect [Le Chatelier, 1909; Portevin and Le Chatelier, 1923]. It led to equally spaced rough bands on the surface of a Kahn tear test specimen made of Al–Li alloy [Delafosse et al., 1993]. In [Clausen et al., 2004], it was noted that shear failure only occurred inside the PLC domain. The macroscopic KEMC model has been used for DSA in many papers [Zhang et al., 2001; Graff et al., 2004; Benallal et al., 2008; Belotteau et al., 2009; Mazière et al., 2010; Wang et al., 2011]. In the present section, the polycrystalline framework enables to use this model at the slip system scale, which seems more appropriate [Rousselier and Quilici, 2015; Marchenko et al., 2016]. The limitation is numerical: for a fixed loading rate, the KEMC model is intrinsically unstable when the so-called waiting time $t_w = w/|\dot{\gamma}|$ decreases, where $\dot{\gamma}$ is the slip rate (or the strain rate in a macroscopic model) and w is the strain parameter of the model. Very small time steps are then required to describe the transient behaviour of PLC. Also, when the parameter w is very small for a given loading rate, the numerical integration fails in some finite elements.

Another objective is to investigate the transition from flat to slant fracture in a thin

aluminium CT specimen. In some aluminium alloys, fracture surfaces do not show the dimples related to void damage and another mechanism is involved, in particular in slant and shear fracture [Rousselier and Luo, 2014; Morgeneyer et al., 2014]. In [Rousselier and Luo, 2014], the Coulomb fracture model [Coulomb, 1773] was combined with the Rousselier damage model in the framework of polycrystalline plasticity. In the present work, the combination of these models with the KEMC model enables to investigate the interactions of DSA with ductile fracture. The combination of all the above-mentioned models is required to match the whole set of experimental measurements and observations. It leads to several difficulties and the calculations are at the limit of what is reasonably achievable. In finite element (FE) analyses, the CPU time is very long because of the small time steps required by the DSA model. For most of the calculations, a relatively coarse finite element mesh is used to limit the CPU time. Another difficulty is the mesh dependence in fracture predictions, in particular the propagation of a slant crack in a Cartesian mesh for which a pragmatic method is used. The modelling choices can be discussed but they succeeded in reproducing qualitatively and quantitatively the localized strain pattern found experimentally and the main features of physical damage and of flat to slant fracture transition.

This section is structured as follows: material data and experimental results from tensile tests are given to assess the PLC effect for the material. Experimental findings for strain and damage interaction during tearing measured by laminography and digital volume correlation (DVC) are recalled. Fracture mechanisms are discussed. The combined models are presented and the material parameters are calibrated with the existing observations and data. The numerical strain patterns are compared to the measured ones. The flat to slant fracture transition is shown for coarse and fine meshes. The achievements and limitations of the current work are then discussed and the main conclusions are drawn.

6.3.1 Experimental results for AA2198-T8R

Material

The 2.0 mm thick aluminium sheet was provided by Constellium in the recrystallized state and after an artificial ageing treatment (T8) generating nanometric hardening precipitates. The composition is 2.9-3.5Cu, 0.8-1.1Li, 0.25-0.8Mg, 0.1-0.5Ag, 0.04-0.18Zr (in wt.%), balance Al. The intermetallic particles volume fraction is $0.3-0.4\%$, their size is $2-3\,\mu m$. Almost no initial porosity was found (< 0.03 vol%). The grains are elongated to $200-300\,\mu m$ in the longitudinal L direction and to $60\,\mu m$ in the transverse T direction. The typical grain size in the short transverse S direction is $25-30\,\mu m$. The yield strength is 440 MPa and the ultimate tensile strength is 500 MPa, showing relatively low work hardening. The material has moderate texture and hardly any anisotropy measured in stress–strain curves.

The room temperature experimental tensile curves in the transverse direction are plotted in Fig. 4.16, using the nominal strain measured by the extensometer (ΔL: elongation, L0: extensometer gage length = 25 mm, specimen width = 6 mm, thickness = 2 mm). A small but significant negative strain rate sensitivity equal to 4 MPa is observed in this alloy between $10^{-4}\,s^{-1}$ and $10^{-2}\,s^{-1}$. Repeated tests at the same strain rate give a scatter smaller than 1 MPa.

The strain rate measured by 2D digital image correlation (DIC) on the specimen surface is non- homogeneous in the gauge length. It can be seen in the space-time figures for 10^{-4} and $10^{-3}\,s^{-1}$ (Fig. 6.11: in this figure, the strain along a line in the specimen length direction Y is plotted vs. time). The tests at $10^{-2}\,s^{-1}$ show the same features. The heterogeneities are significantly larger than the estimated measurement noise, equal ap-

proximately to 10^{-5} and $10^{-4}\,s^{-1}$ in Fig. 2a, b, respectively. They have more or less fixed locations. For $10^{-3}\,s^{-1}$, the locations are more mobile. The characteristic length of the heterogeneities is larger than ~ 1 mm. In this AA2198-T8R alloy, DIC does not reveal the mobile inclined strain rate bands that can be seen for example in AA2198-T3R with the same chemical composition but with a different heat treatment. For nominal strains ΔL/L0 larger than 0.1, the strain rate concentrates in some fixed regions of the gauge length and eventually in a fixed horizontal band corresponding to through-the-thickness slant fracture.

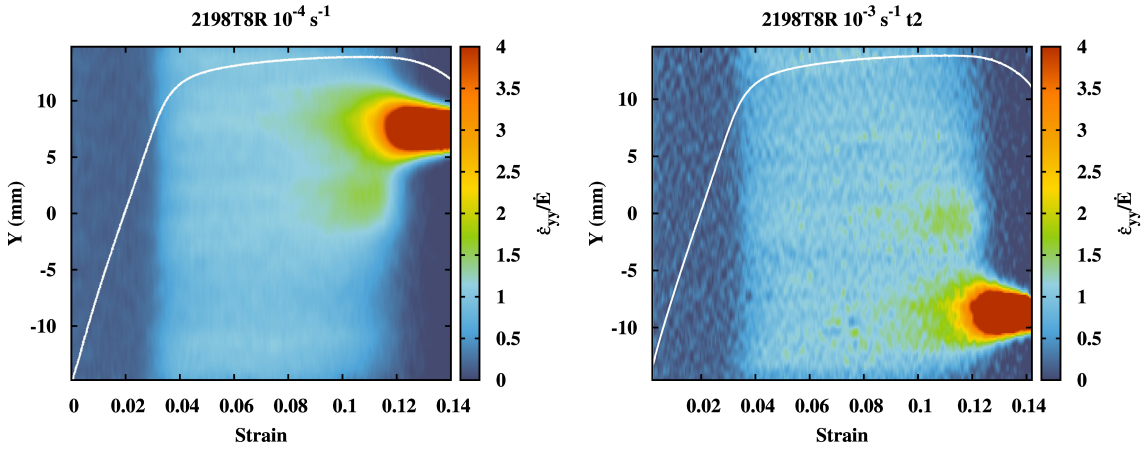

(a) (b)

Figure 6.11 – Tensile tests in T-direction, strain rate (s^{-1}) along the specimen gage length (coordinate Y) versus time (s), elongation rates: (a) $10^{-4}\,s^{-1}$, noise ~$10^{-5}\,s^{-1}$, (b) $10^{-3}\,s^{-1}$, noise ~$10^{-4}\,s^{-1}$. The normalised strain rate scale is on the right of each figure

Laminography (CT specimen)

A CT-like specimen with dimensions: width W = 60 mm, height H = 70 mm, thickness B = 1 mm, notch length a = 36 mm, ligament W-a = 24 mm, notch radius ρ = 0.17 mm, was investigated by in situ X-ray laminography at the European Synchrotron Radiation Facility (ESRF, Grenoble, France) [Morgeneyer et al., 2014]. A schematic view of the laminography experimental set-up is shown in Fig. 6.12(a). An anti-buckling device was used to limit out-of-plane displacements. A 3-D reconstructed volume of the notch region in the initial unloaded state is also shown in Fig. 6.12(a). The gray levels give the notch geometry, the voids and the cracks in plane sections and in reconstructed volumes. The specimen is loaded in the T-L configuration. The coordinates x, y, z correspond to L, T, S, respectively. The two regions of interest (ROI 1 and ROI 2) defined in Fig. [Morgeneyer et al., 2014](b) were analyzed with digital volume correlation (DVC). Sections normal to L and S-axes are referred to as L and S-sections in the sequel. The results are presented and discussed in [Morgeneyer et al., 2014; Buljac et al., 2016].

A stepwise loading was applied on the crack with screws (Fig. 6.12(a)). Each loading step is applied within several seconds. The displacement is kept constant during the laminography scans. More details are given in [Morgeneyer et al., 2014]. The notch opening was measured at a mid-thickness point in the notch ~ 200µm in front of the initial notch tip using the laminography images (e.g. Fig. 6.12). The notch opening displacement (NOD) is obtained by subtracting the initial notch opening (Table 6.2). The time is the one of the FE calculations; it is defined in Sect. 6.3.3.

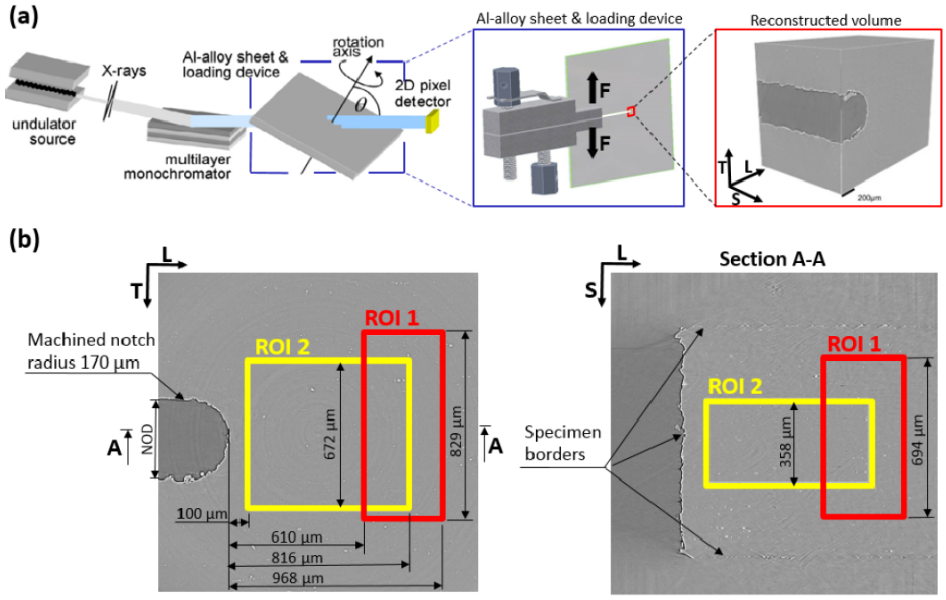

Figure 6.12 – (From [Buljac et al., 2016]). (a) Schematic view of the laminography experimental setup with scanned region in front of the notch root (red) and reconstructed volume. (b) Reconstructed volume sections with ROI positions and relevant dimensions for DVC analyses. ROI 1 corresponds to the analysis reported in [Morgeneyer et al., 2014]. The approximate notch opening displacement (NOD) measurement location is shown (initial value $2\rho = 340\,\mu m$ has to be subtracted).

Strain fields

Figure 6.13(a) shows the incremental equivalent strain fields in the ROI 1 for the previously described loading steps: 1-2, 2-3 and 3-4 (the correlation quality was insufficient for step 5). The incremental activity of the localization bands can be seen more clearly in this representation than for the total equivalent strain fields. (Incremental strain fields calculated by FE analysis are shown for comparison. The used model combines a Rousselier damage model with dynamic strain aging, a reduced polycrystalline model and a Coulomb model at the slip system scale for damage. The model and the simulations are discussed in Sect. 6.3.3) For steps 1-2, the main experimentally measured band is approximately oriented at minus 45° in the yz plane and several parallel bands appear at plus and minus 45° with "hot spots"at band intersections. The band pattern is not symmetric with respect to mid-height (notch plane) and mid-thickness. These features are preserved for steps 2-3 and 3-4 but strain is more and more localized in the main band region. The band activity is highly variable but the bands locations do not change much, perhaps due to the large load steps.

The spacing between the bands ranges from 100 to 300 µm. By contrast, the strain heterogeneities that appear in the DIC images of the tensile specimens tested at $10^{-2}\,s^{-1}$, $10^{-3}\,s^{-1}$ and $10^{-4}\,s^{-1}$ are separated by more than 1 mm (the specimen width is 6 mm). The length scale of the strain heterogeneities seems to depend on the specimen geometry.

With the hypothesis of a one minute duration for each load step, the maximum strain rate in the bands increases approximately from $5 \times 10^{-4}\,s^{-1}$ in steps 10^{-2} and 2-3 to $10^{-3}\,s^{-1}$ in steps 3-4 (Fig. 6.13(a)). Outside the bands, the strain is still increasing in steps 1-2 and 2-3, with an approximate rate of $2 \times 10^{-4}\,s^{-1}$ ([Morgeneyer et al., 2014; Buljac et al., 2016]). In the case of damage-related strain localization, the strain rate contrast between

the band and the adjacent material is expected to be larger. Moreover, damage could not be found at micrometer resolution [Morgeneyer et al., 2014]. By contrast, a smaller incremental strain rate, approximately $10^{-4}\,s^{-1}$, is observed outside the bands in the right figures for steps 3-4; it corresponds to the localization that will lead to the final slant fracture. With the hypothesis of 5 s duration for each load step, probably closer to the real one, the strain rates still lie in the range 10^{-2} to $10^{-4}\,s^{-1}$.

Note that for steps 1-2-3-4 of Table 6.2, the dam- age is very small in ROI 1 Morgeneyer et al. [2014]. In the simulations (Sect. 6.3.3, fine mesh), the crack tip is at 0.06-0.2-0.3-0.8 mm from the notch tip, respectively. The front section of ROI 1 at 0.968 mm is not yet reached by the crack.

Table 6.2 – Applied NOD measured on laminography images for loading steps 1 to 5 and at unstable fracture [Morgeneyer et al., 2014].

Load step	0	1	2	3	4	5	Failure
NOD (µm)	0	56	101	127	177	210	245
Time (s)	0	277	386	436	517	564	609

The corresponding time values are obtained with the FE analyses in Sect. 6.3.3

Figure 6.14(a) reveals the traces of the incremental strain bands in S-sections parallel to the specimen faces. (Incremental strain fields calculated by FE analysis are shown for comparison. They are discussed in Sect. 6.3.3.) Depending on the section (only mid-thickness sections are shown here) and on the loading step, one, two or three bands can be seen. A more quantitative assessment is given in Fig. 8 of Buljac et al. [2016]. In their paper, it is also shown that at distances larger than ~ 250µm from the notch tip, the strain in the crack propagation direction L is very small and deformation is mainly shear in the T-S plane. It can be concluded again that the band activity is highly variable but that the band locations do not change much; they are fixed by the presence of the notch.

Fracture results

The fracture surface scanning electronic microscopy (SEM) images of Fig. 6.15 show a typical flat-to-slant crack transition in a thin sheet made of the same material teared in similar conditions as in [Morgeneyer et al., 2014]. The crack initiates at the notch tip or very close to it and it first propagates in the notch plane in a flat triangular region. At a small distance from the notch, two shear lips form at the specimen surfaces. They join each other after ~ 1 mm propagation and the crack becomes fully slanted. Large dimples corresponding to the intermetallic particles can only be seen in the flat triangular crack Fig. 6.15, but they are mixed with flat zones without visible dimples. The shear lips and slant zones could correspond to transgranular fracture. Similar fracture zones without dimples were already observed with SEM on the same alloy in the slanted cracks of Kahn and M(T) specimens [Chen, 2011].

In Fig. 12 of [Buljac et al., 2016], the overlay of L- section strain fields and final crack path reconstructed images shows that, at distances larger than ~ 250µm from the notch tip, the “flat”crack triangle actually is made of “zigzagged” failure patterns at the locations of the very early strain bands. Associated with the limited void damage, it supports the occurrence of an additional shear transgranular fracture mechanism in some aluminium alloys.

These features are confirmed in Fig. 6.16(a), (b) showing the final damage ahead of the notch. In Fig. 6.16(a), the reconstructed image of the damage (in blue) shows mainly

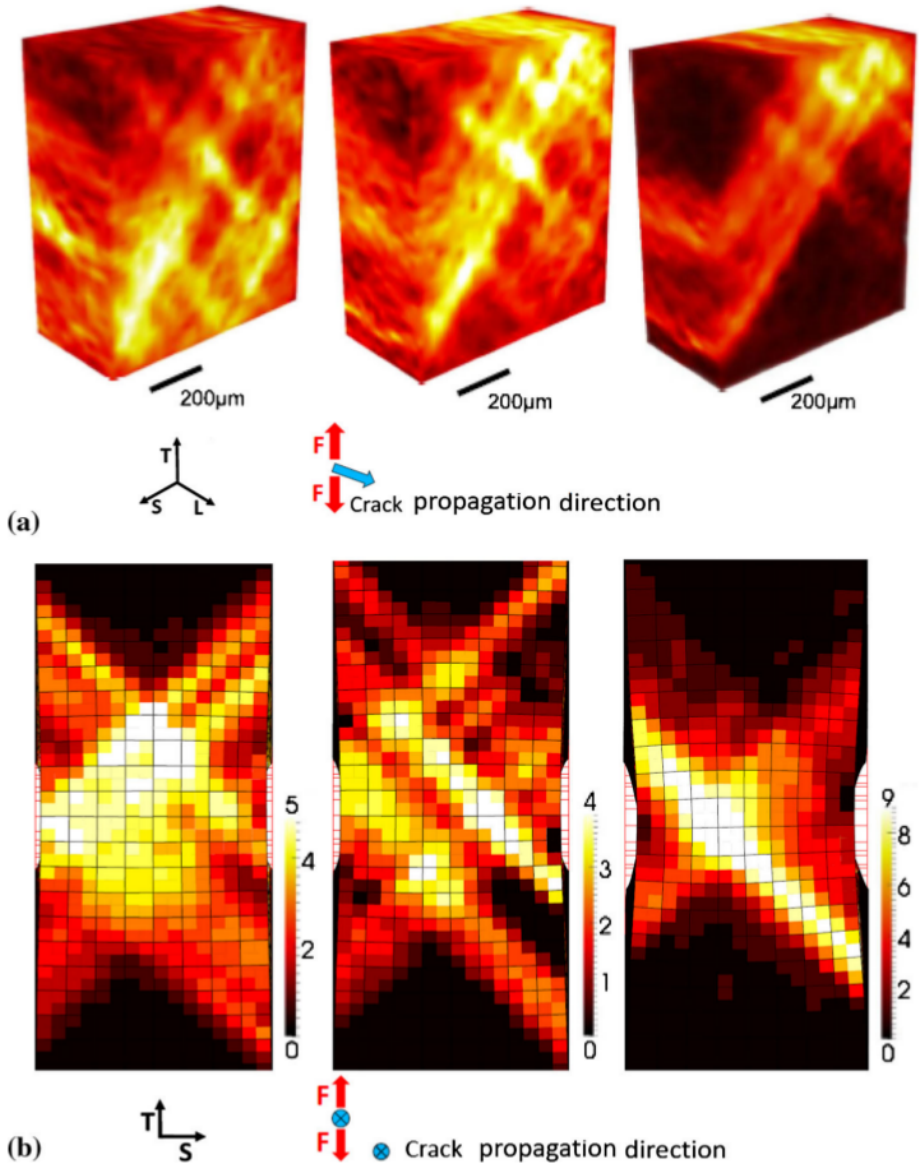

Figure 6.13 – Incremental von Mises equivalent strain fields: (a) DVC results in the ROI 1 (reduced thickness 0.694 mm), front L-section at x = 36.968 mm, undeformed geometry (from Morgeneyer et al. [2014]), (b) FE analysis with the fine mesh, L-section x = 37 mm viewed from x+, full thickness 1 mm, deformed geometry, the initial mesh is in red lines. From left to right: loading steps 1-2, 2-3 and 3-4 (3-4* for FE analysis, stopped at NOD = 171 instead of 177 µm in Table 6.2). The scales in % are the same for DVC and FE

the flat crack, together with some transgranular damage in the elongated grains in the L-direction (perpendicular to the notch round tip). In Fig. 6.16(b), damaged zones are selected at a smaller scale. The slant crack appears at some distance from the notch (the elevation of each point is represented by a color scale). In the reconstructed S-sections of Fig. 6.16(c), transgranular cracking is more visible than void damage; a small shear crack can be seen at the notch tip, corresponding to the additional fracture mechanism.

In Fig. 10 of [Morgeneyer et al., 2014], 3D rendering of the very small initial porosity and of the void/damage shows no evolution in ROI 1 after the first and second loading steps. Some damage appears for steps 3 and 4 but only in the regions of strain localization and the void volume fraction is still very limited (Fig. 6.17(a)). Final failure is character-

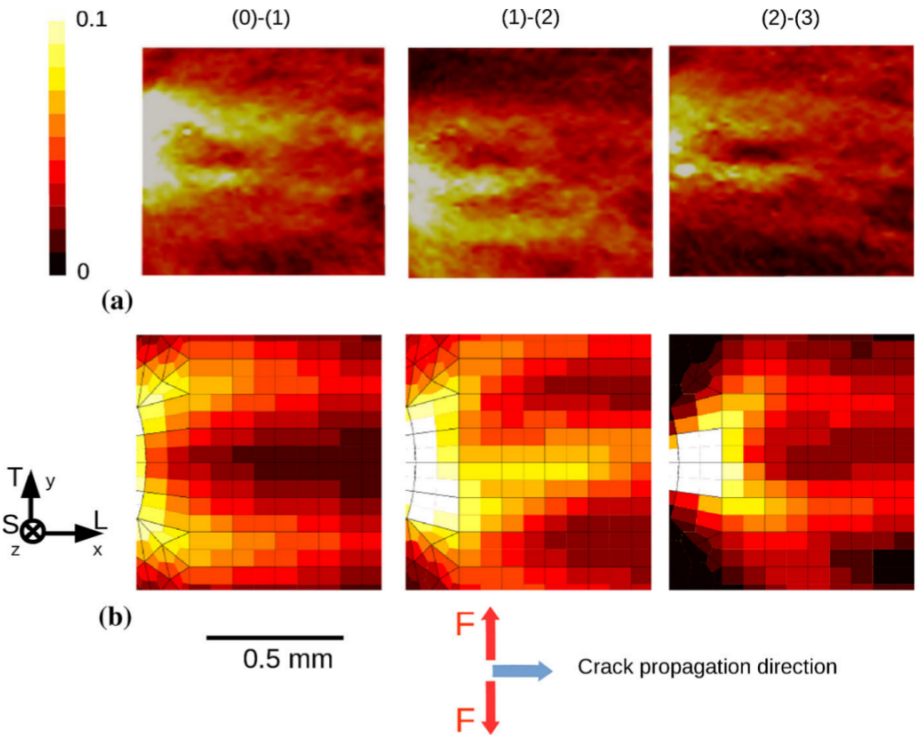

Figure 6.14 – Incremental von Mises equivalent strain fields, ROI 2, mid-thickness S-sections (z = 0), undeformed geometry with the notch on the left: (a) DVC analyses (from [Buljac et al., 2016]), (b) FE analysis with the fine mesh. From left to right loading steps 0-1, 1-2 and 2-3. The scale 0-0.1 is the same for DVC and FE

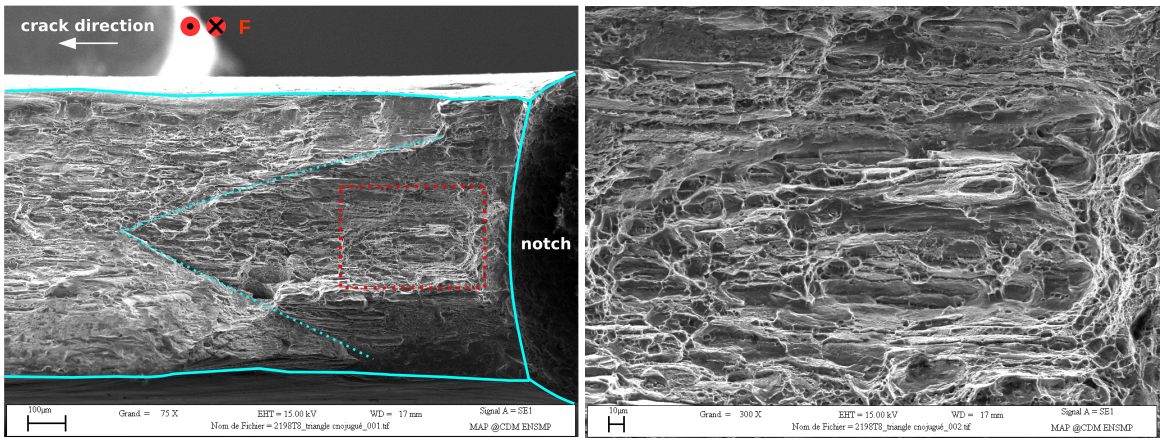

Figure 6.15 – SEM of the full thickness fracture surface (left, triangular flat zone) and of the flat zone (right, enlargement of the red quadrangle in left figure). The horizontal bars represent 100 and 10 µm, respectively

ized by a burst of localized damage forming a slanted crack (Fig. 6.17(b)). The slanted crack is very straight and seems to be transgranular. No damage can be seen after failure in the vicinity of the slanted crack. The nanometric dimples on the slant fracture surface are much smaller than the intermetallic particles (Fig. 6.17(c)). Slant strain localization is the critical event and nanometric voids only appear in the localization band after a large amount of deformation. Similar tomography results without dimples were obtained by

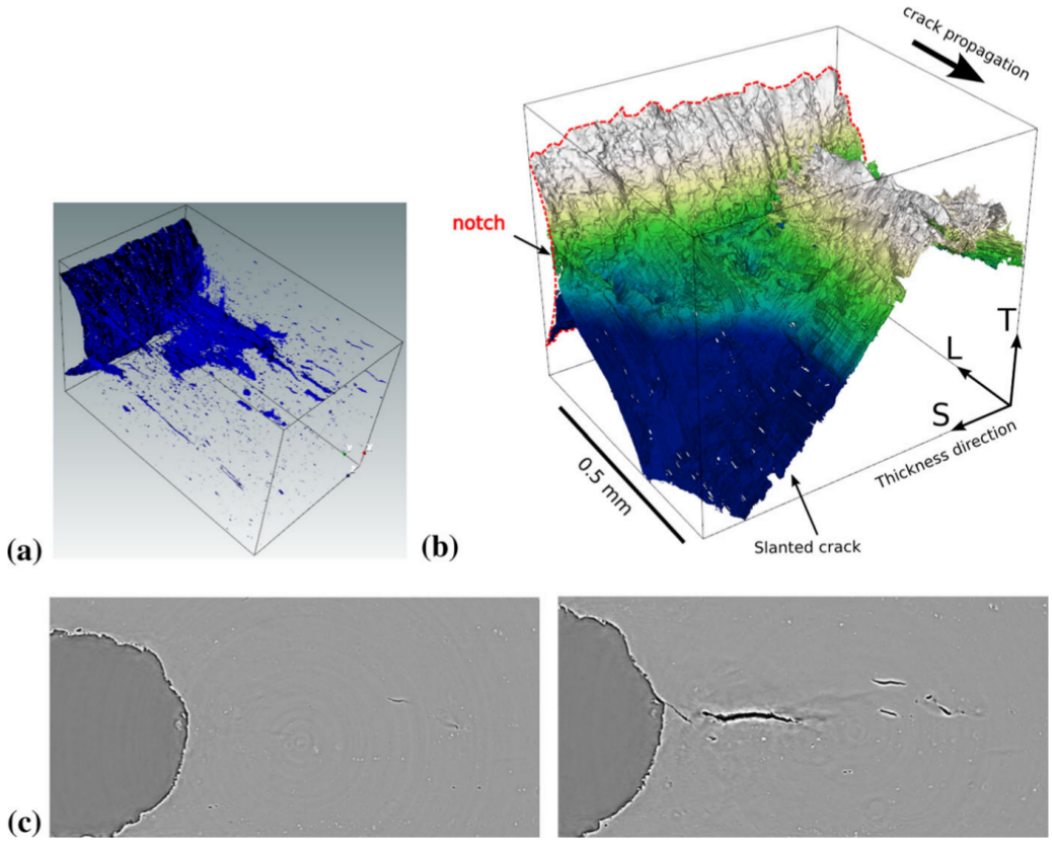

Figure 6.16 – Voids/cracks at the notch: (a) 3D rendering of damage in the laminography images investigated by DVC, (b) height map of the final crack, (c) 2D slices of reconstructed laminography data at mid-thickness normal to the S-direction for steps 4 (left) and 5 (right).

[Chen, 2011] in the slanted cracks of Kahn specimens made of the same alloy.

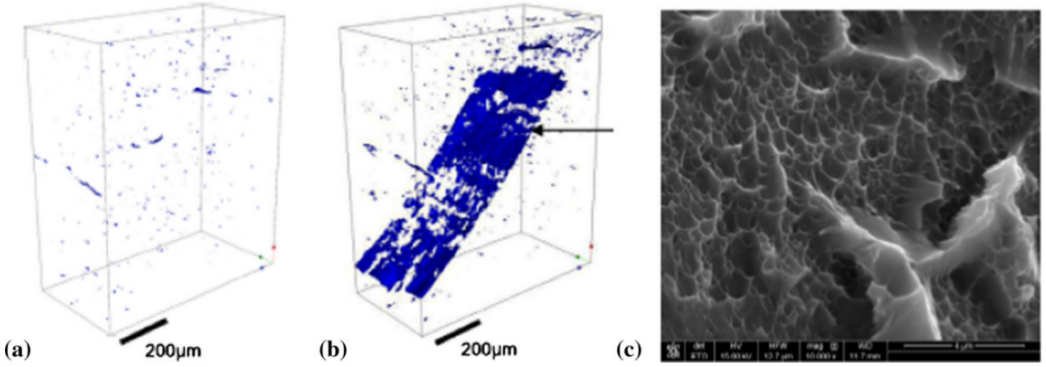

Figure 6.17 – Voids/crack in the ROI 1: (a), (b) laminography images investigated by DVC for step 4 and after unstable fracture, respectively, (c) SEM of the slant fracture surface showing nanometric dimples, the horizontal bar represents 4 µm [Morgeneyer et al., 2014].

6.3.2 Models

The results of Sect. 6.3.1 reveal two original features: (I) plastic deformation is heterogeneous at the macroscopic scale with the early formation of several intermittent shear

strain bands ahead of the notch, (II) ductile fracture mechanisms in the CT specimen are not only void nucleation, growth and coalescence but also transgranular fracture with limited diffuse damage development. Prior calculations using von Mises plasticity or the GTN porous plasticity and ductile fracture model did not capture localization bands neither slant fracture [Morgeneyer et al., 2014; Ren et al., 2016]. This indicated that plasticity modeling need to be enhanced to be able to capture the experimental findings in simulations. To make an attempt to improve the plasticity model and associated simulations, a well-known dynamic strain aging (DSA) model Kubin and Estrin [1985]; McCormick [1988]; Kubin and Estrin [1990]; Estrin and McCormick [1991]; McCormick and Ling [1995]; Zhang et al. [2001] is used in the present analyses. This so-called KEMC model is formulated here at the slip system scale [Rousselier and Quilici, 2015]. In addition, to account for fracture mechanisms not related to void damage, the Coulomb fracture model at the slip system scale Rousselier and Luo [2014] is combined with porous plasticity [Rousselier, 1981]. It is emphasized that these combined models are all necessary to match the numerous experimental observations, as detailed in Sect. 6.3.3. The quantitative agreement is the result of parameter calibration, Sect. 6.3.3.

Plasticity

A polycrystalline plasticity model is the backbone of the present work. The framework of physically based polycrystalline metal plasticity has intrinsic advantages in describing the anisotropy and distortion of the yield surface, as well as realistic anisotropic hardening. Moreover, crystal plasticity is required to introduce the DSA and Coulomb models at the slip system scale. Besides, void nucleation and growth models have to be reformulated in the polycrystalline framework. A particular self-consistent polycrystalline model [Cailletaud, 1992] was improved to model with accuracy the anisotropic behaviour at large strain [Luo and Rousselier, 2014]. For brevity, only key ingredients of the polycrystalline plasticity model are presented here.

The polycrystal is composed of N grains (single crystals) that differ only by their crystallographic orientation. The single crystal model relates the slip rate $\dot{\gamma}_s$ and the resolved shear stress τ_s of each slip system (s = 1 to M, M = 12 for the FCC aluminum alloy). A phenomenological viscoplastic model [Cailletaud, 1992] is used as the constitutive equations for each slip system:

$$\begin{aligned} &\dot{\gamma}_s = \dot{v}_s \mathrm{Sign}(\tau_s - X_s), \\ &\dot{v}_s = |\dot{\gamma}_s| = \mathrm{Max}\left[0, \left(\tfrac{|\tau_s - X_s| - r_s}{K}\right)^{\kappa}\right], \\ &r_s = r_s(v_s, v_t), \quad \forall t \neq s, \\ &\dot{\alpha}_s = \dot{\gamma}_s - d\alpha_s \dot{v}_s, \quad X_s = c\alpha_s. \end{aligned} \tag{6.10}$$

For each slip system, two scalar internal variables are introduced: $r_s = r_s(v_s, v_t)$ for isotropic hardening, depending on the cumulated slips v of the M slip systems, and α_s for kinematic hardening. Equation 6.10 defines a nonlinear kinematic hardening model [Armstrong and Frederick, 1966; Chaboche, 1977] with two parameters c and d. Viscoplastic flow reaches the rate independent limit for large n and small K. Two constant hardening matrices H and K are introduced in the isotropic hardening equation:

$$r_s = R + Q_1 \sum_{t=1}^{M} H_{st} \left[1 - \exp(-b_1 v_t)\right] + Q_2 \sum_{t=1}^{M} K_{st} \left[1 - \exp(-b_2 v_t)\right], \tag{6.11}$$

In Eq. 6.11, R is the initial critical resolved shear stress (CRSS) and the two hardening terms Q_1 and Q_2 depend on the cumulated slips of the M slip systems (self and latent

hardening) through the two hardening matrices H and K . More details are given in [Luo and Rousselier, 2014]. The 12×12 symmetric hardening matrices only depend on six parameters h_1 to h_6 and k_1 to k_6, respectively. Readers are referred to Rousselier et al. (2009) for the detailed elements of H (they are the same in K).

To establish a unique relationship between the stresses at the macroscopic and microscopic (i.e. crystal) scales, the so-called "β-rule"generalized for anisotropic materials is used [Cailletaud, 1992; Sai et al., 2006]. It requires a scalar modulus C of initial elastic accommodation close to the elastic shear modulus $\mu = E/(1+\nu)/2$, in accordance with Kröner's theory [Kröner, 1961] and a fourth-order tensor of orthotropic anisotropy $\underset{\approx}{\boldsymbol{D}}$. With the Voigt notation for the symmetric second order tensors, $\underset{\approx}{\boldsymbol{D}}$ has 10 independent elements D_{ij}.

DSA modelling

The physical origin of PLC is DSA, the pinning of dis- locations by solute atoms that diffuse during straining. The dislocations are temporarily arrested at obstacles such as forest dislocations. Stress softening due to dislocation unpinning could be the cause of strain localization. It is postulated that each slip system has its own history of dislocation pinning and unpinning by solute atoms, corresponding to different ageing times [Rousselier and Quilici, 2015]. For the KEMC model, the DSA term is added to the hardening Eq. 6.11 of each slip system (to shorten the equation, H and K are substituted with H_1 and H_2):

$$r_s = R + \sum_{i=1}^{2} Q_i \sum_{t=1}^{M} H_i \left[1 - \exp(-b_i v_t)\right] + P_1 \left[1 - \exp\left(-P_2 v_s^{\alpha} (t_a)_s^{n}\right)\right]. \tag{6.12}$$

The cumulated equivalent strain in the KEMC model is substituted here with the cumulated slip v_s of each slip system. P_1 and P_2 are multiplicative constants, α and β are exponents. The DSA term mainly depends on the ageing time variables t a (one for each slip system s), the rate equation of which is:

$$\dot{t}_a = 1 - \frac{|\dot{\gamma}|}{w} t_a. \tag{6.13}$$

Ductile fracture

Contrary to the GTN model, the Rousselier model: (i) fulfills the necessary kinematic condition for flat or slant macroscopic localization [Rousselier and Quilici, 2015], (ii) has the ability to model ductile fracture in shear, (iii) can be reformulated in the polycrystalline framework [Rousselier and Leclercq, 2006] with the plastic potential:

$$F = \frac{\sigma_{eq}}{1-f} - \left(\sum_{g=1}^{N} f_g \underset{\sim}{\boldsymbol{\sigma}}_g \right)_{eq} + D_1 f \sigma_1 \exp\left(\frac{\sigma_m^*}{(1-f)\sigma_1} \right) \tag{6.14}$$

In Eq. 6.14, $\sigma_{eq}$is the macroscopic von Mises equivalent stress, f is the void volume fraction, the grains of the matrix material $g = 1$ to N have the volume fractions $(1-f)f_g$and the stress tensors $\underset{\sim}{\boldsymbol{\sigma}}_g$ (the equation for $\underset{\sim}{\boldsymbol{\sigma}}_g$ is not recalled here). D_1 and σ_1 are constants. As proposed in [Morgeneyer et al., 2009], the mean macroscopic stress σ_m is substituted with σ_m^* to model 3D anisotropic void growth in an orthotropic material (principal axes of orthotropy: L, T, N). For isotropic void growth, $\alpha_L = \alpha_T = \alpha_N = 1/3$ and $\sigma_m^* = \sigma_m$:

$$\sigma_m^* = \alpha_L \sigma_{LL} + \alpha_T \sigma_{TT} + \alpha_N \sigma_{NN} \quad \text{with} \quad \alpha_L + \alpha_T + \alpha_N = 1. \tag{6.15}$$

The void volume fraction rate is the sum of a first term due to the mass conservation law and a second p term for void nucleation; ε_{eq} is the macroscopic von Mises equivalent strain rate:

$$\dot{f} = (1-f)\dot{\varepsilon}^p_{eq} D_1 f \exp\left(\frac{\sigma^*_m}{(1-f)\sigma_1}\right) + A\dot{\varepsilon}^p_{eq}. \tag{6.16}$$

In this work, the factor A is a Gaussian function of p the cumulated equivalent plastic strain ε^q_{eq} with parameters f_N , σ_N and ε_N [Chu and Needleman, 1980]:

$$A = \frac{f_N}{\sigma_N\sqrt{2\pi}} \exp\left[-\left(\frac{\varepsilon^p_{eq}-\varepsilon_N}{\sigma_N\sqrt{2}}\right)^2\right]. \tag{6.17}$$

For the Coulomb fracture model at the slip system scale, an additional slip rate $\dot{\gamma}^C_s$ activated at large strains is added to the slip rate $\dot{\gamma}_s$ of Eq. 6.10. The total slip rate is: $\dot{\gamma}^{tot}_s = \dot{\gamma}_s + \dot{\gamma}^C_s$. For $|\tau| + c_0\sigma_n \geq R_0$, the Coulomb slip $\dot{\gamma}^C_s$ and cumulated Coulomb slip are given by the viscoplastic rate equations:

$$\dot{\gamma}^C_s = \text{Max}\left[0, \left(\frac{|\tau| + c_0\sigma_n - R_0\exp(-b_0\gamma^C_{cum})}{K}\right)^\kappa\right]\text{Sign}(\tau), \quad \dot{\gamma}^C_{cum} = \dot{\gamma}^C\text{Sign}(\tau). \tag{6.18}$$

In Eq. 6.18, the index s of the slip system is not written. At the slip system scale, the only two stress components are the resolved shear stress τ and the normal stress σ_n. The Coulomb model depends on the two parameters R_0 and c_0. The novel feature in Eq. 6.18 is a slow decrease (small parameter b_0) of the critical stress with σ^C_{cum}, resulting in stress softening and strain localization.

To sum up, the macroscopic plastic strain rate tensor is:

$$\underset{\sim}{\dot{\boldsymbol{\varepsilon}}}^p = (1-f)\sum_{g=1}^{N} f_g \sum_{s=1}^{M} \underset{\sim}{\boldsymbol{m}}_{sg}\left(\dot{\gamma}_s + \dot{\gamma}^C_s\right) + f\frac{D_1}{3}\exp\left(\frac{\sigma^*_m}{(1-f)\sigma_1}\right)\dot{\varepsilon}^p_{eq}\underset{\sim}{\mathbf{1}}. \tag{6.19}$$

In Eq. 6.19, $\underset{\sim}{\boldsymbol{m}}_{sg}$ is the orientation matrix of each slip system; $\underset{\sim}{\mathbf{1}}$ is the unity matrix; $\dot{\varepsilon}^p_{eq}$ is calculated by taking the second invariant of the first right-hand term. The second right-hand term of Eq. 6.19 is the volumetric strain rate, obtained by derivation of the porous plastic potential Eq. 6.14; the DSA model is included in $\dot{\gamma}_s$; the Coulomb fracture model corresponds to $\dot{\gamma}^C_s$.

6.3.3 Finite element analyses

Objectives, constraints, limitations

As mentioned at the beginning of Sect. 6.3.2, the objective of finite element analyses in this work is to model the particular features of plastic deformation and slant ductile fracture of the AA2198-T8R CT specimen. As far as possible, the constitutive models are based on physical mechanisms and provide a quantitative agreement with the available experimental data. In ductile fracture, a large amount of plastic deformation is involved. Therefore, a suitable modelling of large strain plasticity is a prerequisite for the analysis of the CT specimen. Moreover, both crack initiation at the notch tip and crack propagation generate highly non-proportional loading paths. At large strains and in non-proportional loading, the complex distortion of the yield locus is related to the activation and cross-hardening of different slip systems, depending on crystallographic

orientations. Advanced macroscopic models give a good description of the initial plastic behaviour of most metallic materials, in particular of initial anisotropy. However, the modelling of anisotropic hardening still is a difficult task for these models. By contrast, anisotropic hardening and non-proportional loadings are well captured using self-consistent polycrystalline plasticity, physically-based at the slip system scale.

A first constraint is the computation time in the numerical integration of the polycrystalline constitutive model. An accurate modelling of the material texture requires at least hundreds crystallographic orientations and thousands internal variables. Fortunately, a promising modelling of a large database of mechanical tests can be obtained with a significant reduction of the number of representative crystallographic orientations [Luo and Rousselier, 2014]. Usually, $N/4 = 3$ texture components and $N = 12$ orientations are sufficient for an initially orthotropic metal. This so-called reduced texture methodology (RTM) consists in applying a specific calibration procedure. The reduced texture parameters ($3N/4$ Euler angles and $N/4-1$ volume fractions) are calibrated with the mechanical tests only [Rousselier et al., 2009, 2010]. It can be verified a posteriori that the reduced texture matches the real texture. A limitation of the present work is that tensile tests in 3 directions only were available to calibrate the model. Although the reduced texture is not accurately representative of the material, it is expected that the intrinsic qualities of the polycrystalline model are preserved. Another limitation is that crystallographic texture evolution is not modelled, although a few total slips $\gamma_s^{tot} = \gamma_s + \gamma_s^C$ can be very large near fracture.

In [Kok et al., 2003], a DSA model was already introduced at the slip system scale in a polycrystalline model (using a Taylor-type assumption) for FE simulations of Al–2.5%Mg tensile specimens. The N-crystal aggregates assigned to the integration points have random orientations, with $N = 1$, 8 or 16 (same orientations in a given finite element). The objective is to introduce material heterogeneity with a length scale equal to the element size when $N = 1$ and smaller when $N = 8$ or 16. It generates stress gradients and enables to model the complex spatio-temporal dynamics of jerky flow. In our simulations, the material is homogeneous and the length scale that spontaneously appears in the strain band patterns seems to be more related to the specimen geometry and size. Moreover, the KEMC model is more advanced than the "crude"one used in [Kok et al., 2003].

To model crack initiation and propagation, it is also necessary to use ductile fracture models. In its broad- est sense, ductile damage may be defined as the cause of failure processes involving a significant amount of dissipation. Various mechanisms can be involved (adiabatic softening at high strain rates and creep fracture mechanisms at high temperature are not considered in this work):

1. plastic deformation diffuse macroscopic localization, like necking in round tensile specimens or in thin sheets,

2. shear fracture due to micro-shear bands localization at the slip system scale,

3. dimple fracture due to micro-voids initiation, growth and coalescence.

The first item is modelled provided the plasticity model is accurate enough. In aluminium alloys, no dimples are observed on some fracture surfaces, for example in AA6260 notched tension and shear specimens [Rousselier and Luo, 2014]. In the present AA2198 alloy, dimples are observed in the flat fracture zone only and even in this zone they are mixed with transgranular fracture surfaces without dimples. Therefore, the mechanism 2 can be involved. A specific model is required. The Coulomb fracture model at the slip

system scale was used with success in [Rousselier and Luo, 2014]. It is based on the resolved shear and normal stresses on the slip plane. Alternatively, a model based on a critical cumulated slip associated with a stress softening equation could be used, similar to the maximum shear strain model of [Kim and Yoon, 2015]. In the analyses, the Coulomb fracture model competes with the porous plasticity model for the mechanism 3. Because of the very low initial porosity and the early intermetallic particle damage of the present alloy [Morgeneyer et al., 2014], a void nucleation model also is necessary.

Model parameters

Table 6.3 – Hardening, viscosity, localization and elasticity parameters

R(MPa)	Q_1(MPa)	b_1	Q_2(MPa)	b_2	c(MPa)	d	h_i
101.0	23.9	6.41	9.9	3.51	49.3	1.065	1
k_i	κ	K(MPa s$^{1/\kappa}$)	D_{ii}(MPa)	D_{ij}(MPa)	C (MPa)	E (MPa)	ν
1	25	20	200	0	20,000	74,000	0.3

Table 6.4 – KEMC model parameters

P_1(MPa)	$P_2(s^{-\beta})$	α	n	ω
80	4	0.1	0.33	0.002

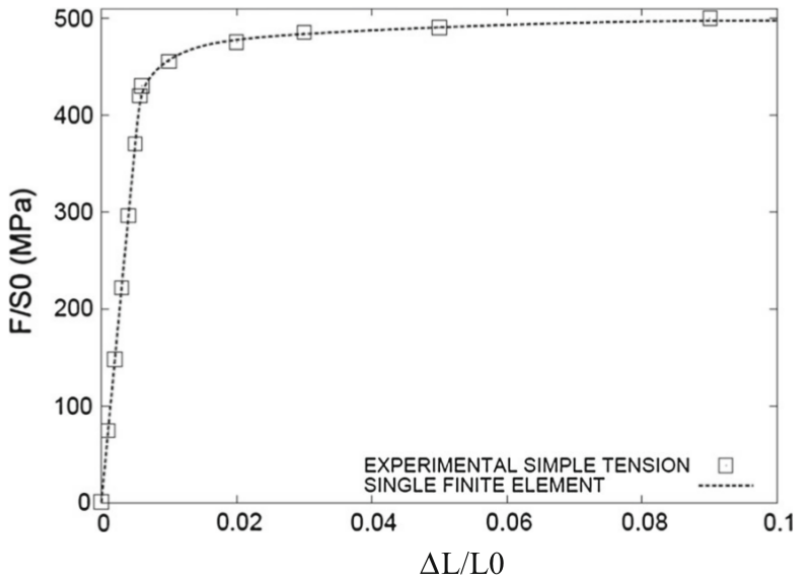

Figure 6.18 – Tensile curve in T-direction: F/S0 (MPa) versus ΔL/L0, experimental points and calibrated model curve. The maximum ΔL/L0 = 0.1 is applied in 100 s.

The combined models of Sect. 6.3.3 involve a large number of parameters. The lack of appropriate number and kind of mechanical tests made it impossible to calibrate the initial anisotropy and the parameters of the KEMC model for the present material. Realistic values or parameters taken from the existing literature are used. By contrast, the experimental data enables a good calibration of the fracture parameters.

6260 and the present AA2198-T8R aluminum alloys have the same small anisotropy of the tensile stress-strain curves in the sheet plane. That is why the available reduced texture parameters of AA6260 with $N = 12$ crystallographic orientations are used [Luo and Rousselier, 2014]. The calibration of the reduced texture (11 parameters for $N = 12$) would need at least additional tensile tests and shear tests in the sheet plane. For the same reason, the two hardening matrices terms are supposed to be all equal to one: $h_i \equiv 1$ and $k_i \equiv 1$. Because of the small positive strain rate effect of aluminum alloys at room temperature, the viscosity parameters n and K of Eqs. 6.10 and 6.18 are chosen to give a small effect of the viscoplastic stress $K\dot{\gamma}^{1/n}$ for a large range of shear rates $\dot{\gamma}$. The "β-rule"matrix is supposed to be isotropic with equal diagonal terms D_{ii} and zero non-diagonal terms D_{ij}. The remaining hardening parameters are the first seven ones in Table 6.3: from R to d. These parameters are calibrated with the tensile curve in the T-direction (single finite element calculation, Fig. 6.18). An optimization software is used with the Levenberg-Marquardt algorithm [Levenberg, 1944]. Because no tension-compression test was available, the kinematic hardening parameters c and d of Eq. 6.10 are calibrated like a third isotropic hardening term at large strain (exponent coefficient d smaller than b_1 and b_2). These two parameters are not representative of the real kinematic hardening of the material. Note that in Luo and Rousselier [2014], initial values of the back resolved shear stresses (kinematic hardening) at the slip system scale were implemented to model the small deviation from orthotropy resulting in tension-compression asymmetry (the so-called differential stress effect) and distinct shear curves in the two diagonal directions of the sheet plane. These values are equal to zero here.

In the calibration with the tensile test, the ductile damage parameters have a negligible effect: no significant damage softening can be seen in Fig. 6.18. The dislocations are pinned because a large value $\omega = 0.04$ of the DSA strain parameter in Eq. 6.13 has been used, giving large waiting times $t_w/|\dot{\gamma}|$. In that case, the calibrated initial CRSS is $R + P_1$, i.e. 181 MPa for $P_1 = 80$ MPa. The values of P_1 in the polycrystalline model are larger than the ones in a macroscopic model because unpinning only impacts simultaneously a small fraction of the model $N \times M = 144$ slip systems. Experimental data were not designed to calibrate the DSA model. The three DSA parameters $P_2 = 4s^{-\beta}$, $\alpha = 0.1$, $\beta = 0.33$ in Table 6.4 are taken from the literature for aluminium alloys [Estrin and McCormick, 1991; Graff et al., 2004; Benallal et al., 2008; Böhlke et al., 2009]. In these papers, $\omega = 10^{-4}$ is used.

According to Eq. 6.12, the PLC domain approximately corresponds to $0 < t_a < 1s$; see also Fig. 12a in [Rousselier and Quilici, 2015] obtained with $R + P_1 = 69$ MPa and $P_1 = 30$ MPa (same ratio R/P_1 as for the present alloy). The asymptotic value $t_a = t_w = \omega/|\dot{\gamma}|$ of Eq. 6.13 decreases when strain rate increases with plastic deformation and t_a decreases abruptly when it crosses this value. Therefore, for slip rates in the order of $10^{-3}\,s^{-1}$, the PLC domain can be obtained for $\omega < 0.001$, approximately. In aluminium alloys, it corresponds to the PLC domain lower limit in strain rate and to the upper limit in temperature. For smaller values of P_1, at the same strain rates, t_a and ω have to be decreased simultaneously. The CT specimen has been calculated mainly with $P_1 = 80$ MPa. In that case, $\omega = 0.002$ is the smallest value for which the calculation does not diverge early (it diverges for $\omega = 0.0015$). Other couples (P_1, ω) have also been investigated ("Appendix 1").

The fracture parameters are given in Table 6.5. The rather flat tensile curve enables to define a flow stress σ_Y and the porous plasticity parameter $\sigma_Y = 2\sigma_Y/3 = 350$ MPa. $D_1 = 2$ is the value given by early void growth measurements Rousselier [1987]. The measured intermetallic particles volume fraction and initial porosity give f_N and f_0. Because of the very small initial porosity volume fraction, the mean nucleation strain $\varepsilon_N = 0.1$ is the decisive parameter; this value is representative of the intermetallic particles and it matches

well the experimental crack growth. Nucleation is concentrated around this mean value with a small scatter $\sigma_N = 0.02$. Without experimental data for anisotropic void growth, $\alpha_L = \alpha_T = \alpha_N = 1/3$ is retained.

Table 6.5 – Coulomb fracture model and porous plasticity parameters

D_1	σ_1(MPa)	f_0	f_N	ε_N	$\varepsilon_N$slant	σ_N	f_c
2	350	0.0001	0.0034	0.1	0.05	0.02	0.15
c_0	R_0(MPa)	R_0 slant (MPa)	b_0	γ_c^C	α_L	α_T	α_N
0	260	240	2	2	0.3333	0.3333	0.3333

In this work, we only use the Coulomb model with $c_0 = 0$, because the single fracture experiment does not enable to calibrate this parameter and also because the computational cost is reduced with a fully associated model (the Coulomb model with $c_0 \neq 0$ is non associated). The experimental balance between dimples and transgranular fracture in the triangular flat zone is obtained with $R_0 = 260$ MPa. To deal with the mesh orientation effect in local approach to ductile fracture, smaller values for $R_0 = 240$ MPa and $\varepsilon_N = 0.05$ are used in the shear lips and in the slant fracture zones defined in Sect. 6.3.3 (refer to this section and to Sect. 6.3.3 for a more complete discussion and reference to similar methods). These values for R_0 are calibrated to match the experimental crack growth. Although it is reduced to 0.05, the nucleation parameter ε_N has no significant effect in these zones because void damage is very small (Fig. 6.15).

The material is considered as "broken"when the void volume fraction exceeds some critical value: $f > f_c$ or when a first cumulated Coulomb slip exceeds some critical value: $\gamma_{cum}^C > \gamma_c^C$. A quadratic cumulative rule $(f/f_c)^2 + (\text{Max}(\gamma_{cum}^C)/\gamma_c^C)^2 = 1$ is used when porous plasticity and the Coulomb fracture model are combined. The material behaviour is then replaced by an elastic behaviour with a very low stiffness (Young's modulus $E_c = 1$ MPa). Gauss integration points where this condition is met are referred to as "broken Gauss points"[Morgeneyer et al., 2009]. It is shown in Fig. 11 of [Rousselier and Luo, 2014] that displacements at failure of a notched tensile specimen differ by $< 1\%$ with parameters in the ranges $0.15 < f_c < 0.25$ and $2 < \gamma_c^C < 3$. At these large values: $f = f_c = 0.15$ and $\text{Max}(\gamma_{cum}^C) = \gamma_c^C = 2$, the material has lost its mechanical strength because of almost complete stress softening, see for example Eq. 6.18 with $b_0 = 2$. Consequently, these two parameters have very little effect on the results and we must emphasize that they are not fracture parameters (contrary for example to f_c in the GTN model). They do not participate in strain localization. Their single function is to alleviate the calculation.

At the FE mesh level, when $nc = 4$ Gauss points of a reduced integration quadratic hexahedral element C3D20R (for example) are "broken", the element is removed from the calculation. It is not realistic to remove an element when only $nc = 3$ Gauss points out of the total number $n = 8$ are broken. It has been checked theoretically and with FE analyses that the removal criterion with $nc \geqslant 5$ gives no element deletion: with 4 out of 8 broken Gauss points, C3D20R elements have lost their load carrying capacity. That is why in some figures of Sect. 6.3.3 unbroken Gauss points (in white) are visible in the cracked areas, mixed with red broken points.

In conclusion, the only decisive parameters that could not be calibrated with experimental and literature data are the PLC parameters P_1 and ω.

Meshes

The element numbers are 13,000 and 29,360 in the coarse and fine meshes, respectively (6.19). The Cartesian grid in the notch region, Fig. 6.19(b), (d), is designed with equal size C3D20R hexahedral elements to prevent the well-known "mesh size effect "in local approach to fracture. For the coarse mesh, the element size in the notch region is$0.25 \times 0.20 \times 0.25 mm^3$ (four elements in the 1 mm thickness, z direction). For the fine mesh, it is $0.125 \times 0.10 \times 0.125 mm^3$ (eight elements in the thickness). The elements are smaller in the y-direction to account for their elongation in the deformed state. For the same mesh size effect prevention, a special design is chosen at the notch tip, so that the element height in the deformed state is as close as possible to that of the Cartesian mesh, 6.19(c), (e). The design is completed with C3D15R prismatic elements. The Cartesian mesh is 2 mm long; it enables approximately 2 mm crack propagation with limited mesh size effect. The coarse and fine meshes are used to quantify the mesh size effect. With the fine mesh and the unstable DSA model, the calculations are very long; the coarse mesh also enables preliminary calculations at a reasonable cost. An accurate calculation of the mechanical fields can only be obtained with the fine mesh, remember the ~ 100−300 µm experimental band spacing in Figs. 6.13 and 6.14.

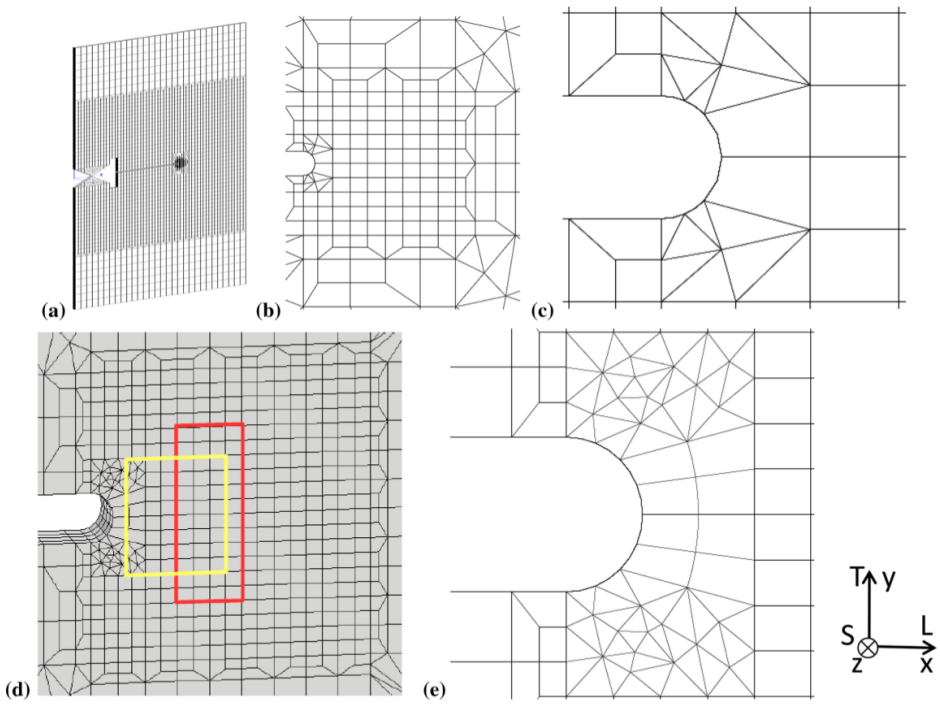

Figure 6.19 – 3D meshes: (a)-(c) coarse mesh, four elements through the thickness; (d), (e) fine mesh, eight elements through the thickness. Meshes (a) and (d) are tilted. In (d), the positions of ROI 1 (red) and ROI 2 (yellow) are shown (at mid-thickness section, half geom- etry). The coordinates of the notch tip are x = 36 mm, y = 0.

Displacements U_y and $-U_y$ are imposed to the upper and lower rigid elastic triangles attached to the crack in Fig. 6.19(a) (Young modulus 10^7 MPa). The applied rate is 10^{-3} mm/s and the final value is $U_y = 1$ mm (U_y = time/1000). To prevent rigid-body motion, the point $x = W = 60$ mm, $y = z = 0$ (mid-height, mid-thickness) is fixed. To prevent buckling and mode III crack loading, $U_z = 0$ is imposed to the specimen mid-thickness $z = 0$, except a large zone surrounding the notch tip ($30 < x < 50$, $-5 < y < 5$). Without this kind

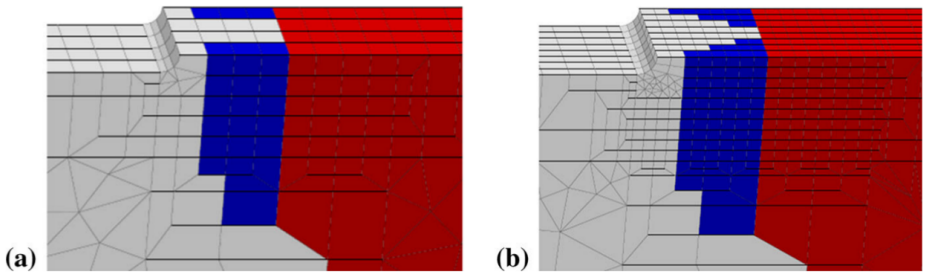

Figure 6.20 – Slant region (red) and shear lip region (blue), half meshes, sections $y = 0$, notch on the left: (a) coarse mesh and (b) fine mesh.

of condition, buckling is effectively observed.

The NOD is calculated from the vertical displacements of mid-thickness nodes at 301 µm (coarse mesh) and 292 µm (fine mesh) from the notch tip (radius 170 µm). The NOD determined at 200 µm from the notch tip is smaller by less than 5 µm. The NOD is used in the comparisons with experimental obser- vations, because the variable "time"does not correspond to the real loading history and because the load is not measured during the tests. (For that reason, the numerical load–displacement curves of Sect. 6.3.3 could not be compared to the experimental one.) In Table 6.2, the correspondence between NOD and time is obtained with the coarse mesh. It depends on numerical crack propagation. With the fine mesh, crack propagation is earlier and the time values are slightly different.

It has been shown, for example in [Rousselier and Quilici, 2015] with the same models, that crack propagation is much more rapid in one of the Cartesian mesh directions than at 45° of it. It is the "mesh orientation effect"in local approach to fracture. It can be prevented with the so-called non-local models [Forest et al., 2004; Bargellini et al., 2009; Feld-Payet et al., 2011; Bergheau et al., 2014]. These models increase the computational cost and they are beyond the scope of the present work. A more pragmatic way is to use different fracture parameters in the flat fracture region on the one hand and in the shear lips and slant fracture regions on the other hand (R_0 = 260 and 240 MPa in Table 6.5, respectively). These regions are known a priori from the SEM fractographies of Fig. 6.15. This approach is not entirely predictive but it is effective in the present case. The regions are defined in Fig. 6.20.

The method used in [Morgeneyer and Besson, 2011] is not so different. The authors have introduced an additional strain-based void nucleation model with a Lode angle dependence that promotes shear fracture. Consequently, this ad-hoc model gives the shear lips. The two lips eventually join at mid-thickness, forming slant fracture. Instead of different parameters for the same models in the present work, the authors use different models in the flat and slanted fracture zones. This method is not convenient here because there is no void nucleation in the shear lips and slant fracture regions. In [Chen, 2011], the Cartesian mesh of a Kahn specimen is gradually slanted to follow the experimental flat-to-slant transition, successively avoiding the mesh orientation effect. As the two preceding ones, this third method is not entirely predictive.

An order-2 Runge–Kutta algorithm with automatic time stepping is used for the material model. The tan- gent matrix is the elastic one. The finite strain formula- tion is based on the so-called co-rotational frame associated with the rotation tensor (e.g. [Rousselier and Luo, 2014], Appendix 1). The equilibrium is solved with a Newton–Raphson algorithm.

Load serrations and PLC bands

According to Table 6.2, the applied NOD rate increases from 0.2 to 0.8 µm ⊥ s. In Fig. 6.13(b), the numerical strain rate is between 5×10^{-4} and $2 \times 10^{-3}\,s^{-1}$ for load steps 1-2, 2-3 and 3-4, with time increments ~ 100, 50 and 50 s, respectively. The experimental load steps are applied in less than 10 s, i.e. the stain rate is larger, but still in the PLC range 10^{-4} to $5 \times 10^{-4}\,s^{-1}$ (Sect. 6.3.1).

In the load–displacement curves of Fig. 6.21, a small scatter can be seen for several runs of the same configuration (coarse or fine mesh), even with the same single processor and therefore the same rounding errors correction algorithm, because of the unstable characteristic of the DSA model, Eq. 6.13. The different results are probably seeded by the random exchanges between the two cores used in the calculations or by the random share between several users of the processor. Load inflexions appear in Fig. 6.21 for $U_y \sim 0.300$ mm (time = $U_y/1000 \sim 300$s). Before this displacement, there is no difference between the coarse and fine mesh curves because damage is small and it is limited to a very small zone at the notch tip. The first broken Gauss point and the first removed element appear in the two fine mesh calculations at time = 250-250 and 301-311 s, respectively. In the five coarse mesh calculations, the time ranges of these two events are 295-300 and 454-467 s, respectively. Classically, crack growth is more rapid in the fine mesh which results in a lower load curve and slightly delayed load oscillations. (The first removed element appears much later in the coarse mesh also because two layers of elements are involved in flat fracture vs. a single layer in the fine mesh, see Sect. 6.3.3. Thus, by contrast with the broken point events, the removed element events are not mechanically relevant.)

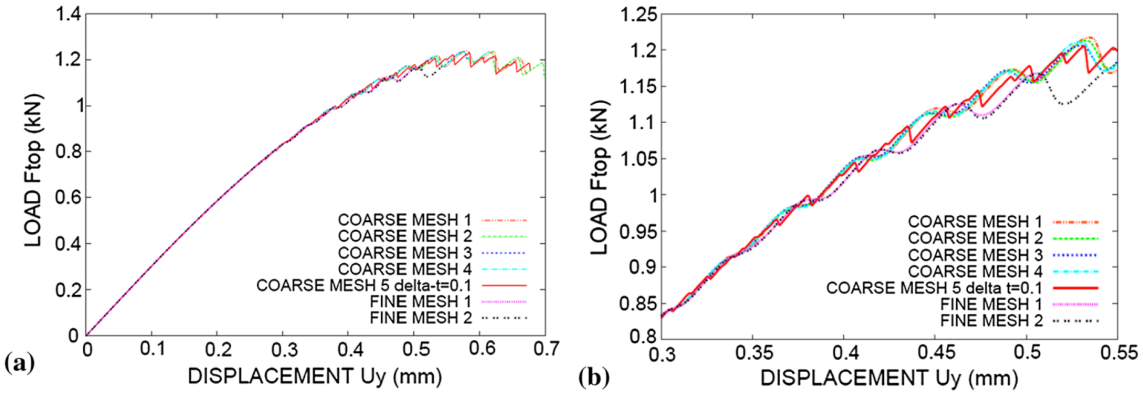

Figure 6.21 – Load (kN) versus displacement curves: (a) U_y range$0-0.7mm$, (b) U_y range $0.3-0.55mm$. The MESH numbers correspond to several calculations with the same coarse or fine meshes and with the same material parameters $P_1 = 80$ MPa and $\omega = 0.002$. The maximum time increment is $\Delta t = 1$ s, except for COARSE MESH 5 ($\Delta t = 0.1$ s).

The large sinusoidal oscillations of Fig. 6.21 are not commonly observed in experimental load–displacement curves. The maximum time increment $\Delta t = 1$ s can be too large to capture well the instabilities generated by the DSA model (the automatic time stepping algorithm is not activated by the DSA model in the present calculations). With $\Delta t = 0.1$ s (COARSE MESH 5), the red curve shows more realistic serrations. For example, the load decreases for $U_y = 0.3046$ to 0.3064 mm. This range exactly corresponds to the appearance and disappearance of strain rate bands ahead of the notch. The same correspondence is observed for the following load decreases. In this 5 calculation, the broken Gauss points appear at the notch tip in the inter- vals $U_y = 0.2981 - 0.3062$ mm (4 points),

0.3800 – 0.3812 mm (+4 points), 0.4063–0.4079 mm (+6 points), etc. They form two layers of broken integration points on each side of the symmetry plane y = 0. The broken point events always fall in the load decrease events but with $\Delta t = 0.1$ s the latter are much more numerous in the range $U_y = 0.3 - 0.45$ mm. For $U_y > 0.475$ mm, load decreases, strain rate bursts and broken points always coincide. It shows that the intermittent PLC bands and the broken point events are strongly related. PLC may well be the initiator of broken point events.

The coarse mesh calculations with $\Delta t = 1$ and 0.1 s give very close crack propagation rates. Both give crack growth during strain rate band bursts. The difference is that for $\Delta t = 1$ s these events are much longer and consequently the load oscillations are much larger.

Smaller values P_1 = 40 and 30 MPa have been investigated using the coarse mesh, with$\omega = 0.0005 - 0.0003$ and 0.0001, respectively. The results are given in "Appendix 1". In the rest of this Sect. 6.3.3, we only consider $P_1 = 80$ MPa and $\omega = 0.002$ for both coarse and fine meshes with the maximum time step $\Delta t = 1$ s.

The strain rate bands are better visible with the fine mesh. The occurrence of 2 or 3 horizontal bands on the specimen surface is emphasized in Fig. 6.22. The figures are slightly tilted around the y axis (positive rotation angle) to show the notch tip inner surface on the left. The strain rate is zero at mid-thickness in the notch tip because the Gauss points are broken, but the small flat crack does not yet extend to the surfaces (similar to the left inset in Fig. 6.27, "Appendix 1"). At time = 385 and 425 s (U_y = 0.385 and 0.425 mm), the successive strain rate bursts are clearly shown, both on specimen surface and through the thickness (section AA at 1 mm from the notch tip). As in the coarse mesh, they coincide with discontinuous crack propagation steps: no broken integration points for time = 350-376 s, 14 additional broken points for time = 377-393, no broken points for time = 394-417, etc. At time = 425 s, the crack forms a flat triangle shorter than 0.4 mm, it shows that the strong interaction between strain rate and crack propagation bursts begins in the flat fracture regime. The load has two minima at time = 385 and 430 s, in accordance with the strain rate bursts of Fig. 6.22 The calculated incremental strain fields (FINE MESH 1) are compared to the measured ones in Fig. 6.13 of Sect. 6.3.1. The full thickness (1 mm) is shown because the small number of Gauss integration points cannot be reduced without an important loss of information. The deformed mesh is used to evidence the small displacements of the incremental bands, which seem to be immobile in the DVC figures. In the latter, the ROI 1 thickness only is ~ 0.7 mm and the initial geometry is used. The large load increments 1-2, 2-3 and 3-4 encompass several load oscillations with slightly different locations of the calculated strain rate bands, which could explain this difference. Nevertheless, the same experimental method was applied to another aluminium alloy with much smaller load steps and no significant band motion was detected [Morgeneyer et al., 2016]. The large PLC amplitude P_1 in the analyses could also increase the band motion.

Apart from the band mobility, which is slightly larger in the numerical simulations, there are strong similarities between the band patterns: several parallel bands at plus and minus 45° with "hot spots"at band intersections, no symmetry with respect to mid-height ($y = 0$) and mid-thickness ($z = 0$), similar strain levels although there are no "black zones"(very small values) in the two left DVC figures. The hot spots correspond to distinct micro-mechanical mechanisms, as evidenced in the infrared thermography measurements of [Delpueyo et al., 2016], and to distinct slip systems in the numerical analyses, which accumulate at the crossing points. The inter-band spacing of several hundred microns cannot be related to crystallographic heterogeneities. It strongly suggests that

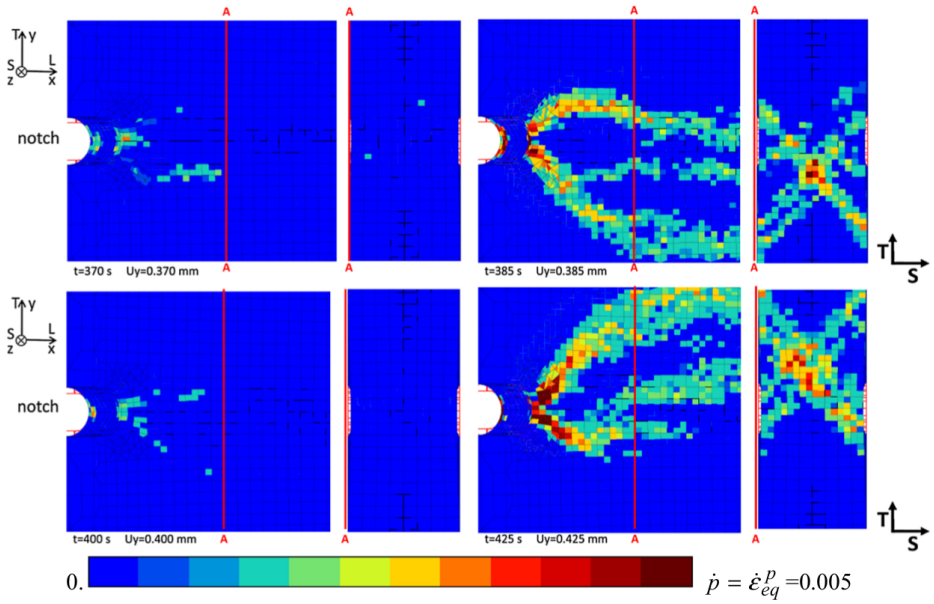

Figure 6.22 – Strain rate fields, fine MESH 1 calculation, front surface z = +0.5 mm tilted mesh (Cartesian mesh region, 0-2 mm from the notch) with the notch on the left and section AA at Δx = 1 mm from the notch (view from x+) for time = 370-385-400-425 s. The strain rate range is 0-0.005 s^{-1}, navy blue to dark red). The initial meshes are in red lines.

DSA is the cause of multiple banding. Anyway, DSA is not a completely deterministic phenomenon and a strictly identical band pattern was not expected. For steps 3-4, the localization in a single band is more advanced in the calculation, probably because with the fine mesh the crack is larger than the experimental one, see Sect. 6.3.3. When the crack approaches the section $x = 37$ mm of Fig. 6.13, the crack geometry imposes a single band, flat or slanted depending on the specimen geometry (the thickness in particular that impacts the mechanical fields) and on the parameters of the various fracture mechanisms. Note that in Fig. 6.13(b) the numerical main band is at plus 45° in the yz plane, i.e. perpendicular to the experimental main band of Fig. 6.13(a). Because of the random characteristic of the DSA model, the result plus or minus 45° depends on the calculation.

Figure 6.23 enables a more quantitative comparison. The cumulated equivalent strain in the main localiza- tion band is about twice as large as in the surrounding area for load steps (1), (2) and (3), in DVC as in FE analysis. For load step (4), the ratio is larger than 2 and the band is narrower for DVC. In FE analyses, the strain rate bands are more mobile than in the measurements and consequently the total cumulated strain is less localized. This early PLC-related strain localization is distinct from the late damage-related strain localization where plastic yielding takes place within the band only and the outer region undergoes elastic unloading. In the AA2198-T8R alloy, the latter localization is linked to the former. This mechanism could be general for this class of aluminium alloys [Morgeneyer et al., 2016]. By contrast with Fig. 6.13, the total strain for the whole history is shown in Fig. 6.23; that is why the main band only is clearly visible, particularly in the finite element calculation with slightly moving strain rate bands. Figure 6.23 also does not show the strain rate band mobility.

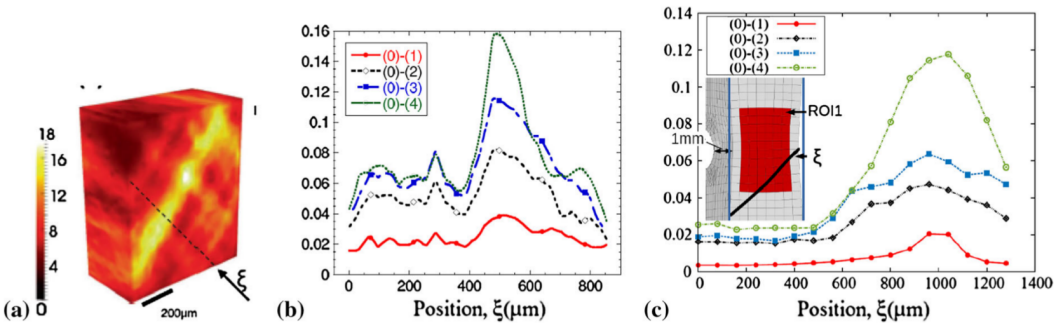

Figure 6.23 – Total cumulated von Mises equivalent strain along a line perpendicular to the localization band for load steps 1-4, deformed geometry for the abscissa ξ: (a), (b) measured by DVC along line ξ in the plane at $\Delta x = 1$ mm from the notch (ste 4 in Fig. 6.23(a)), initial reduced thickness 0.694 m (ROI 1), from Fig. 8 in [Morgeneyer et al., 2014] and (c) fine MESH 1 calculation, initial full thickness 1 mm

Ductile fracture

The results for both coarse and fine meshes are presented. The DSA model parameters are $P_1 = 80$ MPa and $\omega = 0.002$. In Fig. 6.24, the damage variables are shown on the surface $y = 0$. The notch is on the right, the thickness S-direction is vertical. The flat crack and the intersection of the slant crack with the plane $z = -0.5$ mm can be seen in some figures (because of thickness reduction in Fig. 6.24(c), (d). The void volume fraction is large in the triangular flat fracture zone only: Fig. 6.24(a), (e) for the coarse and fine meshes, respectively. It is negligible in the shear lips and in the slant crack although a smaller value for the void nucleation strain ε_N was used in these regions. It is not homogeneous because it competes with transgranular fracture, according to the SEM images of Fig. 6.15. As mentioned in Sect. 6.3.3, a good balance between dimples and transgranular fracture in the flat zone is obtained with the Coulomb critical resolved shear stress $R_0 = 260$ MPa. A few maps of the Coulomb slips are presented for both meshes. The critical Coulomb slip depends on the local stress and strain tensors; that is why several slip systems are involved in crack growth.

Some of the ones with the larger Coulomb slips are shown in Fig. 6.24(g). For example, at the notch tip, the critical Coulomb slip index is 85 (Fig. 6.24(h)) which means grain $g = 8$ and slip system $s = 1$ ($7 \times 12 + 1 = 85$); it corresponds to the normal to the slip plane $0.773, -0.599, 0.212$ and slip direction $-0.440, -0.649, -0.227$ (undeformed geometry values) that give a pure shear strain in a plane close to the xy plane, parallel to the specimen surface (the shear plane is the one formed by the first two eigenvectors of the orientation matrix $\underset{\sim}{\boldsymbol{m}}_{sg}$, they are close to the directions x and y). The crack initiates with this Coulomb slip, in agreement with the small shear crack in Fig. 6.16(c) and with the small stress triaxiality σ_m/σ_{eq} in the vicinity of the notch free surface that limits void damage. Void damage only prevails at some distance from the notch, Fig. 6.24(e). Note that $\sigma_m/\sigma_{eq} \leqslant 1$ in the whole specimen. This small value for a CT specimen is due to the very small relative thickness B/W = 1/60. In the standard CT specimens with B/W = 25/60, maximum stress triaxiality is larger than 2.5. It partly explains the limited void damage in the experiment and the prevalence of the Coulomb model in the numerical analyses.

The damaged zones are smaller in the fine mesh figures because they correspond to a smaller applied NOD (the calculation incidentally stopped at NOD = 199 μm). This displacement corresponds to the ~ 1 mm crack of Fig. 6.24(j): the white integration points

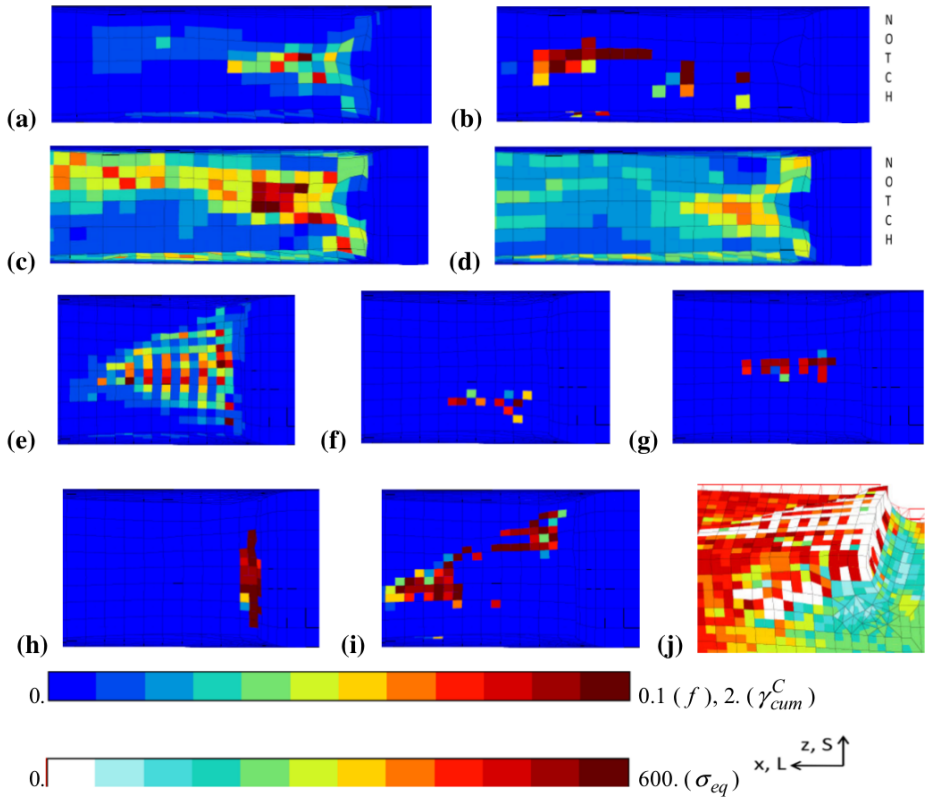

Figure 6.24 – (a)-(d) coarse MESH 2 calculation, lower half of the specimen $y < 0$, the notch is on the right, time = 698, NOD = 335 µm: a void volume fraction, scale 0-0.1, (b)-(d) Coulomb slips 99, 116, 126, respectively, scale 0-2. (e)-(j) fine MESH 2 calculation, upper half of the specimen $y > 0$, the notch is on the right, time = 542, NOD = 199 µm: (e) void volume fraction, scale 0-0.1, f-i Coulomb slips 13, 71, 85, 116, respectively, scale 0-2, (j) von Mises equivalent stress, scale 0-600, tilted mesh, the initial mesh is in red lines.

are broken (zero stress). The shear lips are already well developed; the front one can be seen on the specimen surface (the mesh is tilted). In the fine mesh, unbroken points are visible on the surfaces. The reason why was explained at the end of Sect. 6.3.3: only 4 broken points out of 8 integration points are possible in one element, some of them are hidden. This mixed pattern is not seen in the coarse mesh because the element thickness is twice larger in the perpendicular direction and the damage concentrates in two layers of integration points adjacent to the plane $y = 0$ (Fig. 6.25(a)); the four broken points are all visible on this plane.

For the applied NOD = 242 µm the coarse mesh L-sections of Fig. 6.25(a) give the experimental flat zone length of ~ 1 mm. The right transition from flat to slant fracture is obtained with R_0 = 240 MPa (Table 6.5) in the shear lips and in the slant region of Fig. 6.20(a). With R_0 = 245 MPa, slant fracture is delayed and the slant crack is not as nice as the one in Fig. 6.25(b). With R_0 = 250 MPa, shear lips and slant fracture are not obtained. The transition from flat to slant fracture is also shown in Fig. 6.25(c) with the intersections of the crack and the surfaces $y = 0$ (mid-height) and $z = -0.5$ mm (specimen surface).

The three values $R_0 = 240 - 245 - 250$ MPa in the shear lips—slant crack regions have also been tested in the coarse mesh without DSA (ω = 0.020 instead of 0.002, that suppresses the load serrations and the strain rate bands). Slant fracture is obtained with R_0 = 240 and 245 MPa, not with R_0 = 250 MPa. Because of the completely pinned dis-

locations with $\omega = 0.020$, the stresses and the load are slightly larger and consequently the Coulomb model gives earlier crack propagation than with $\omega = 0.002$. By contrast, the load is smaller after crack initiation. Void damage is much smaller than the experimental one in the flat crack. Without DSA, slightly larger values of R_0 in both the flat crack and the shear lips—slant crack regions should be used to match physical damage and experimental crack path and growth rate.

The CT specimen has also been calculated with the same R_0 parameter in the whole mesh (coarse mesh). With $R_0 = 260$ MPa, the crack does not quit the direction of the Cartesian mesh, it remains flat. With $R_0 = 250$ MPa, a shear lip forms on one side of the specimen and after 2 mm propagation it encompasses only the half of the specimen thickness. With $R_0 = 240$ MPa, the flat crack stops too early, slant crack propagation is obtained but it is too rapid and the maximum load is much smaller. These results do not fit experimental data and observations. Two distinct values for the R_0 parameter are necessary in the present calculations.

Figure 6.26 is for the fine mesh. The MESH 1 and MESH 2 calculations incidentally stopped at time = 508 and 542 s, respectively (Fig. 6.21(b)). The flat crack terminates in L-section $\Delta x = 0.875$ mm from the notch tip. The deformed mesh shows that a single layer of finite elements is involved in flat fracture, with two discontinuous layers of broken points. The unbroken points in the removed elements make the "discontinuous crack artifact"not visible in the coarse mesh.

Figure 6.26(b) shows the intermittent crack growth in relation with the DSA model. The figures at time = 465 and 483 s correspond to the beginning and the end of a PLC band event and they show a large crack propagation causing a load decrease in Fig. 6.21. On the contrary, there is almost no crack propagation from time = 483-498 s, only one additional broken point can be seen in the shear lip. The next strain rate burst and intermittent crack growth occur at time = 500-520 s. In Fig. 6.26(b), the broken point patterns are somewhat different for MESH 1 (time = 498) and MESH 2 (time = 542). As expected, the NOD increase rate is larger during the crack propagation periods. In the laminography experiments on the ductile 2139T3 aluminum alloy [Morgeneyer et al., 2016], smaller load increments were applied to a CT specimen and experimental stepwise crack growth was observed, similar to the one in the present calculations.

6.3.4 Discussion

The laminography observations of a AA2198-T8R aluminium alloy CT-like specimen revealed unexpected deformation patterns and early strain localization in slant bands in the slant fracture region [Morgeneyer et al., 2014]. It was a challenge to simulate this experiment because the material database is limited and not designed for this purpose and because the calculations are at the limits of numerical capabilities. In the future, a new experimental program should include both laminography and a comprehensive characterization database. Moreover, the experimental results showed complex interactions between plastic behavior and ductile fracture. Ductile fracture itself resulted from various mechanisms. The backbone of the present work is to contribute to the understanding of the heterogeneous deformation ahead of the sharp notch using enhanced plasticity models.

First, the physical origin of the strain bands is not straightforward. On the one hand, the intermittent character of the bands seems to exclude the microstructural heterogeneity hypothesis. Also, the length scale, larger than 1 mm in tensile specimens (6 mm width) and smaller than 0.3 mm in the CT specimen (1 mm thickness), is not in favour of this

hypothesis. Clearly, the length scale is related to the specimen geometry and dimensions and to the mechanical fields resulting from the boundary conditions. With infrared thermography measurements of 5052 aluminium-magnesium alloy tensile specimens loaded at strain rates larger than $10^{-2}\,s^{-1}$, Delpueyo et al. [2016] observed moving and intermittent band patterns similar to the ones in the present CT specimen but with a ~ 5 mm length scale related to the large 40 mm width of the specimens.

On the other hand, the AA2198-T8R alloy is at the limit of the PLC domain in tensile tests at room temperature and for the usual constant strain rates considered in the present work. Also, the intermittent bands seem to be fixed ahead of the notch of the CT specimen, which is not usual for the PLC phenomenon. This could be explained by the physical origin of the PLC phenomenon: DSA first takes place inside the grains and because DSA is limited in this material and testing conditions, it could be hardly visible at the macroscopic scale in tensile tests. The strain heterogeneities could remain related to the grain microstructure and/or be seeded by it, which could explain the fixed bands in Figs. 6.13 and 6.14 and also the fixed strain localization patterns in a 2139T3 aluminum alloy Morgeneyer et al. [2016]. This latter alloy has more work-hardening than AA2198-T8R and equiaxed grains (mean sizes $60-52-24\,\mu m$ in the L-T-S directions), nevertheless the band spacing is the same in the CT specimen: 150-250 µm. This explanation would perhaps conciliate the "DSA"and "microstructural heterogeneity"points of views. The latter is modelled in Taupin et al. [2016]: the enforcement of tangential continuity conditions of the distortion rate along grain boundaries spontaneously gives shear bands patterns in the L-S plane of AA2198 rolled sheets. Nevertheless, these patterns are different from the ones in Fig. 6.13.

For these aluminium alloys and this large in-plane dimensions CT specimen (W/B = 60), the plastic deformation is concentrated in a small region ahead of the notch. That is why, by contrast with smooth tensile specimens, the PLC phenomenon is not expected to give large serrations of the load–displacement curve. In the notch region, numerical simulations show a strong interaction between PLC and flat or slant ductile fracture and consequently the load inflexions and oscillations are also due to crack initiation and propagation. The coarse mesh calculations with sufficiently small time steps $\Delta t = 0.1$ s give realistic load serrations (Figs. 6.21, 6.27). Unfortunately, a satisfactory modelling of the strain rate bands could only be obtained with the fine mesh and in that case only $\omega = 0.002$ and $\Delta t = 1$ s were within affordable computation times. The combination of small ω and large time steps gives early divergence of the calculation (In the present work, the smallest ratio without divergence is $\Delta t/\omega = 500$ s for the applied loading rate. It corresponds approximately to $1 > \Delta t/t_w > 0.2$ with the waiting time $t_w = \omega/p$ and the equivalent strain rate $2\times10^{-3}\,s^{-1} < \dot{p} < 5\times10^{-4}\,s^{-1}$ in the bands).

Although the AA2198-T8R alloy is at the limit of the PLC domain in classical tensile tests at room temper- ature and the KEMC model parameters were not cal- ibrated with these tests, it does not really impact the results of this work. Actually, the stepwise loading of the CT specimen was performed with a screw system that results in relaxation between load steps. Recently, relaxation periods were shown to give PLC-type serrations and localization in tensile specimens made of AA2139-T3 aluminium alloy although no PLC effect is observed in constant strain rate tests (see Chapter 4). Both the present KEMC model and the parameter calibration with constant strain rate tests can be questioned for complex loading paths [Böhlke et al., 2009]. It was beyond the scope of this work to simulate the complex loading history of the CT specimen. The simulation results are to be considered in relation with laminography to support the role of DSA in the observed strain patterns.

Special care was given to the mesh design in order to limit mesh effects in ductile fracture modeling. Two mesh sizes are used to quantify the mesh size effect. Comparing Figs. 6.25(a) and 6.26(a), it can be seen that in both meshes the thickness of the fracture process zone is equal to one element size in both flat and slant cracks, i.e. twice larger in the coarse mesh, which delays crack initiation and propagation. In the flat crack, there are two parallel layers of broken integration points in both meshes, but they are located differently, in one and two layers of finite elements for the fine and coarse meshes, respectively. These mesh effects could be eliminated with regularized models. They include non-local models or higher-order continua models. The combination of DSA and PLC modelling with strain gradient plasticity has been shown in various publications [Aifantis, 1987; Hähner, 1993; Mazière and Forest, 2015; Mazière et al., 2017].

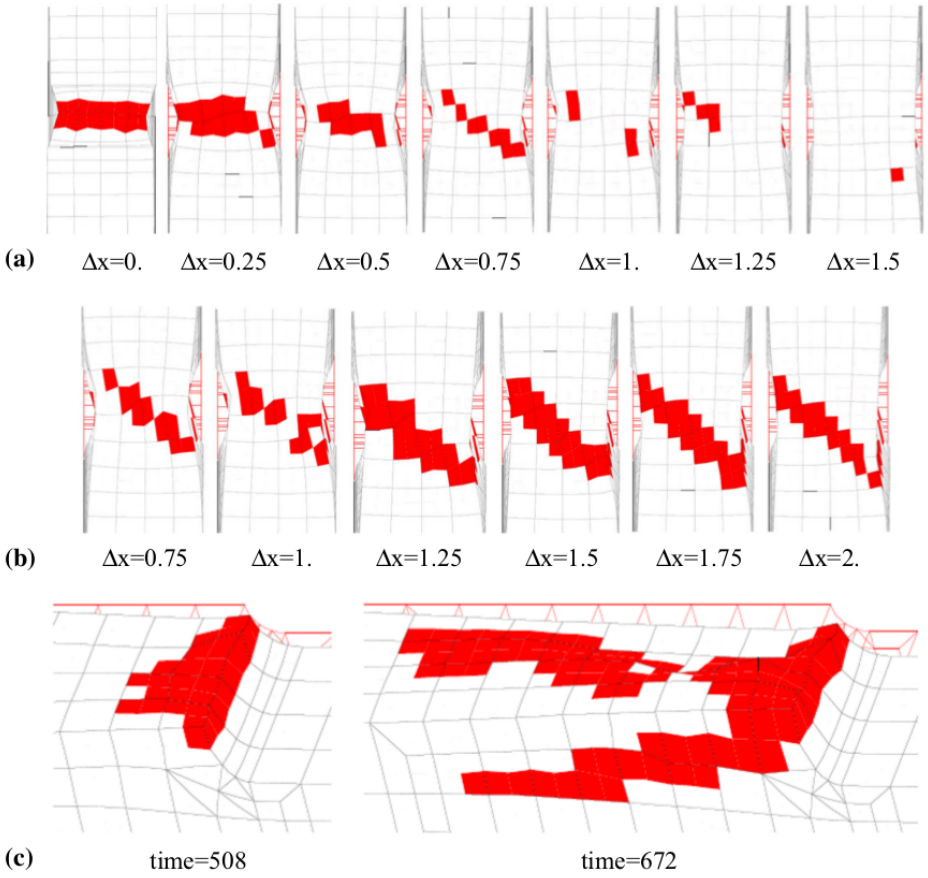

Figure 6.25 – Broken Gauss points. (a) Coarse MESH 2 calculation, time = 610, NOD = 242 µm, notch tip x = 36 mm (Δx = 0). Viewed from x = 0 and L-sections viewed from $x+$ at Δx = 0.25 – 0.50 – 0.75 – 1 – 1.25 – 1.50 mm from the notch. (b) Coarse MESH 2 calculation, time = 698, NOD = 335 µm,, L-sections at Δx = 0.75 – 1 – 1.25 – 1.50 – 1.75 – 2mm from the notch. (c) Coarse MESH 1 calculation, lower half of the specimen $y < 0$, tilted mesh with the notch on the right, time = 508 and 672, NOD = 171 and 302 µm respectively. The initial meshes are in red lines.

The two micro-mechanisms of ductile fracture are modeled with two distinct models: porous plasticity and Coulomb fracture model. These mechanisms do not correspond to flat and slant fracture. Dimples and trans-granular fracture are both observed in the flat crack of Fig. 6.15 as well as in the slant fracture surface of a notched tensile specimen made of AA6260 Rousselier and Luo [2014]. The balance seems to be material dependent and the mechanisms should be carefully checked in ductile fracture experiments.

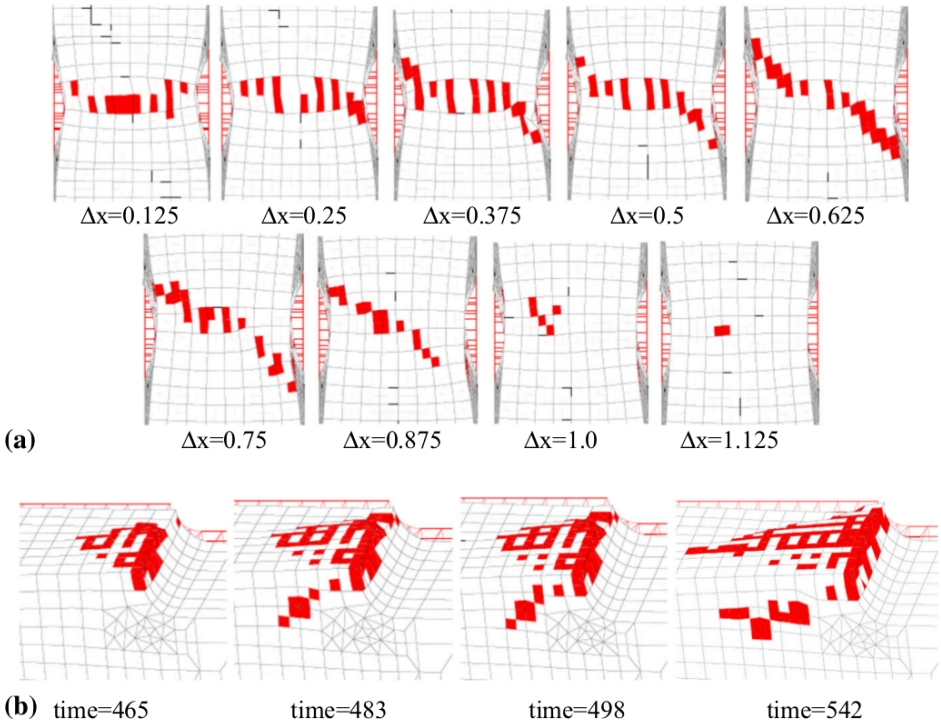

Figure 6.26 – Broken Gauss points, a fine MESH 2 calculation, time = 542, U_y = 0.542, NOD = 199 µm, L-sections at Δx = 0.125 – 0.25 – 0.375 – 0.5 – 0.625 – 0.75 – 0.875 – 1.0 – 1.125 mm from the notch, view from $x+$, (b) fine MESH 1 (time = 465-483-498, U_y = time/100, NOD = 142 – 160 – 163 µm respectively) and fine MESH 2 (time = 542, NOD = 199 µm) calculations, upper half of the specimen $y > 0$, tilted mesh with the notch on the right. The initial meshes are in red lines.

6.3.5 Conclusions of simulation results using the fully coupled polycrystal model

At room temperature, tensile tests on many aluminium alloys show evidence of dynamic strain ageing (DSA), resulting in the Portevin–Le Chatelier (PLC) effect. It is the case for the Al–Cu–Li recrystallized AA2198-T8R alloy that exhibits serrations on the tensile curves, an inverse strain effect, non-homogeneous strain rates in the gauge length of the tensile specimens and through-the-thickness slant fracture. On the tensile specimen surface, digital image correlation (DIC) does not reveal mobile inclined strain rate bands, contrary to some other aluminium thin sheets. Large compact tension (CT) specimens were also tested with high-resolution in situ synchrotron X-ray laminography combined with digital volume correlation (DVC) to measure the plastic strain fields and the damage ahead of the crack-like notch. The main experimental observations are several parallel inclined strain bands at ±45° in L-sections perpendicular to the crack plane, flat to slant fracture transition without micrometric dimples in the shear lips and in the slant crack and no damage outside the slant crack Morgeneyer et al. [2014].

These observations suggest some interaction between PLC and fracture for this thin aluminium sheet. To further investigate this point, finite element analyses of the CT specimen have been performed. Prior calculations using von Mises plasticity or the GTN porous plasticity and ductile fracture model did not capture the localization bands neither slant fracture [Morgeneyer et al., 2014; Ren et al., 2016]. Contrary to the GTN model, the Rousselier model fulfils the necessary kinematic condition for flat or slant macro-

scopic localization and it has the ability to model ductile fracture in shear [Rousselier and Quilici, 2015]. Moreover, it can be reformulated in the framework of polycrystalline plasticity. This model is combined with the [Chu and Needleman, 1980] model for void nucleation and with the Coulomb fracture model formulated at the slip sys- tem scale to account for transgranular fracture mechanisms not related to void damage. The Kubin-Estrin-McCormick (KEMC) model at the slip system scale is used for DSA. The main conclusions are:

- Although the fracture models involve many material parameters, most of them can be determined with the available material data. The main remaining parameters are the mean strain ε_N for void initiation and the Coulomb critical shear stress R_0 . They are calibrated to match stable crack growth before final failure and the balance between void-related and void-free ductile fracture mechanisms. To account for the mesh orientation effect, different values are used for the flat fracture region and for the shear lips and slant fracture regions.

- The PLC parameters are taken from the literature for aluminium alloys, except the stress amplitude $P_1 = 80$ MPa and the time parameter $\omega = 0.002$. For $P_1 = 0$ or for a large value $\omega = 0.020$ (pinned dislocations), DSA is not activated; the load–displacement curve displays neither serrations nor oscillations. Nevertheless, slant fracture is obtained with the calibrated Coulomb stress $R_0 = 260 - 240$ MPa (flat-slant). For a quantitative and qualitative modelling, DSA activation with $\omega \leqslant 0.005$ is necessary. For this material, the combination of all the above-mentioned models is required to match the whole set of experimental measurements and observations.

- For $P_1 = 80$ MPa and $0.002 \leqslant \omega \leqslant 0.005$, bursts of strain rate bands are obtained, corresponding to the decreasing part of the load oscillations or serrations. Crack growth takes place during these time periods. Strain rates could not be determined exper- imentally because of the small number of loading steps in laminography, but the measured incremental strain fields between successive steps are in good agreement with the numerical incremental strain fields. If DSA is not activated, multiple bands can not be obtained.

- This early PLC-related strain localization is distinct from the late damage-related strain localization where plastic yielding takes place within the band and the outer region is plastically inactive. In the present AA2198-T8R alloy, the latter is linked to the former. This mechanism could be general for this kind of materials. Nevertheless, the numerical strain rate bands are slightly moving whereas the experimental ones seem to be fixed. The DSA activation could be related to some microstructural features. The microstructure alone cannot be the main origin of the bands because they are intermittent. Moreover, the inter-band spacing is well predicted with the DSA model.

- The increasing crack growth rates corresponding to the successive strain rate bursts could lead to “pop- ins” or even to unstable slant fracture like the one in the experiment, but this result could not be achieved in the present calculations because of numerical divergence for $\omega \leqslant 0.0015 (P_1 = 80$ MPa) or too large computation times for $P_1 < 80$ MPa$(\omega \leqslant 0.0003)$.

The numerical analyses have important limitations:

- Mechanical tests were not available to calibrate the anisotropic plasticity model (reduced crystallographic texture and mechanical parameters) and the PLC model. Nevertheless, the results support the interaction of PLC with both plasticity and ductile fracture for this material.

- Numerical problems have not been addressed in the present work: (i) convergence accuracy, (ii) first stress invariant accuracy in relation with the volumetric plastic strain constraint (incompressibility or void growth), (iii) divergence and increasing computation times with decreasing PLC parameter ω and the related small time step Δt, (iv) mesh dependence (size, orientation, other characteristics). The mesh size effect has been observed with the coarse and fine meshes. The mesh orientation effect has been accounted for in a pragmatic way with two sets of fracture parameters R_0 and ε_N . The experimentally observed unstable slant fracture could probably be modelled with smaller values of ω as in [Rousselier and Quilici, 2015].

Future studies are required for a better understanding and modeling of the interaction between DSA and ductile fracture:

- The DSA model could be enhanced to account for non-monotonic loading.

- The numerical integration of the DSA model could be improved to reduce the computation time and to avoid early divergence.

- A numerically efficient method has to be developed for the unresolved problem of the mesh effect in the transition from flat to slant fracture.

- The PLC effect is temperature and loading history dependent. Future studies would better include these factors.

- DSA and ductile fracture are highly dependent on microstructure. The present modeling methodology could be applied to other aluminium alloys and heat treatments.

- For the present aluminium alloy, the existing Kahn tests could be used to calibrate the two parameters of the Coulomb fracture model (R_0 and c_0).

6.4 Appendix 1

Smaller values P_1 = 40 and 30 MPa have been investigated using the coarse mesh, with $\omega = 0.0005 - 0.0003$ and 0.0001, respectively (the calculations diverge early for smaller values of ω). The parameter R is increased from 101 to 141 and 151 MPa (same $R + P_1$), respectively, to account for the smaller PLC amplitudes P_1. Although they assume completely pinned dislocations, these corrections approximately give the same load levels in Fig. 6.27 up to $U_y \sim 0.580$ mm. Therefore, the damage models (porous plasticity and mainly the Coulomb fracture criterion which is very sensitive to the stress level) are not much impacted and the crack growth is almost the same. Note that for ω = 0.0003 and 0.0001 (pink and red curve), the maximum time step had to be reduced (from Δt = 1 s to Δt = 0.1 s) to catch the sharp variations of the ageing time, Eq. 6.13. With this small time increment, the CPU time already is 24 days for the coarse mesh (The clock time is 13.5 days with two cores. It is not significantly reduced with 4 or 8 cores). Although the coarse mesh only gives poor images of the strain rate band patterns, fine mesh calculations have not been attempted with these small values of the ω parameter.

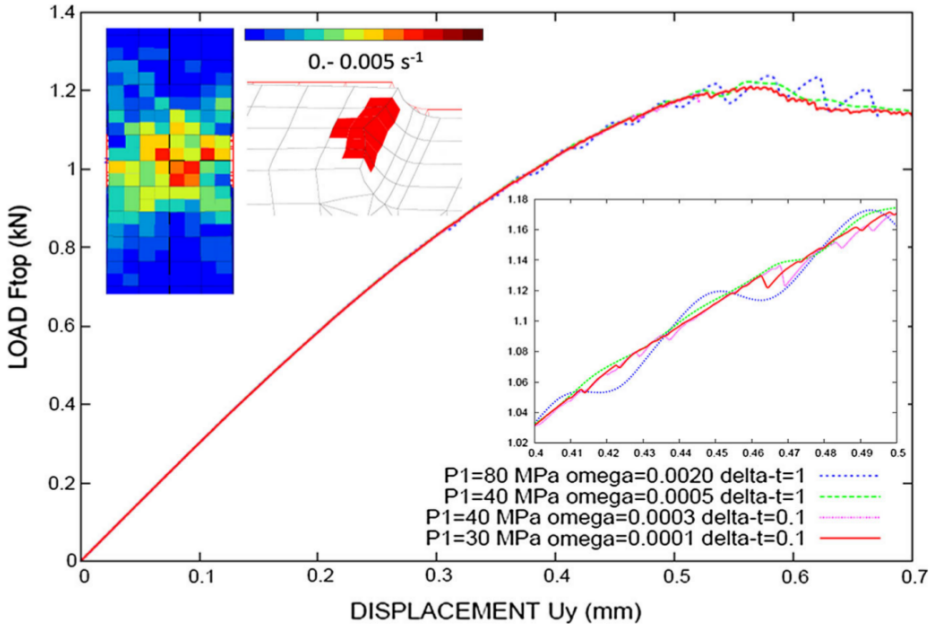

Figure 6.27 – Load (kN) versus displacement curves, effect of DSA parameters P_1 and ω, coarse mesh. The maximum time increment is Δt = 1 s for ω = 0.0020 and 0.0005, Δt = 0.1 s for ω = 0.0003 and 0.0001. Right insert zoom with U_y range 0.4-0.5 mm (time = 400-500 s). Left inserts for the red continuous curve (P_1 = 30 MPa and ω = 0.0001), (i) average equivalent strain rate for U_y range 0.4129 – 0.4139 mm (time = 412.9-413.9) in the L-section x = 37 mm (at Δx = 1 mm ahead of the notch, view from x+) and (ii) broken integration points (in red) for U_y = 0.4130 mm (time = 413), tilted mesh lower part $y < 0$, the notch is on the right, the initial meshes are in red.

Small load decreases are obtained for P_1 = 30 MPa and ω = 0.0001 (red curve in Fig. 6.27). For example, the load decreases from 1.0551 to 1.0531 kN for U_y = 0.4129 to U_y = 0.4139 mm. Four or five crossing incremental PLC bands can be guessed in the L-section x = 37 mm, from U_y = 0.4115 to U_y = 0.4145 mm, although they are smeared by the coarse mesh (left inset in Fig. 6.27). The band pattern and spacing are similar to the ones in Fig. 6.22. In these bands, the von Mises equivalent strain rate in the 0.4129-0.4139 interval is approximately 0.004 s^{-1} in a few integration points of the L-section; it is about

twice the average value in the full thickness. At $U_y = 0.4127$ and 0.4130 mm, two additional integration points are broken in the lower T-section $y < 0$ (left inset in Fig. 6.27), forming a small "triangular"crack with the prior six broken points at the notch tip. (The configuration is the same in the upper T-section $y > 0$.) There are no other "broken point events"in the large interval from $U_y = 0.3878$ to $U_y = 0.4544$ mm. It shows that the intermittent PLC bands and the broken point events are strongly related also for $P_1 = 30$ MPa and $\omega = 0.0001$. The load decreases because of simultaneous ductile damage (microvoids and/or microcracks, crack propagation) and DSA softening (dislocation unpinning) tentatively modelled by the porous plasticity, Coulomb fracture and KEMC models, respectively.

6.5 Appendix 2

In the J-Δa curve of Fig. 6.28, J is computed from the numerical load–displacement curve, according to ASTM1820 standard. Maximum crack growth length Δa_{max} is measured in the deformed geometry by taking the position of the farthest broken integration point in the fine mesh flat crack. The stepwise curve is due to the incremental crack propagation in FE simulations. The variation of J versus crack opening displacement (COD = 2 U_y = time/500) is also shown in Fig. 6.28. It can be noticed that the J-COD curve shows some oscillations after 0.6 mm. It corresponds to the oscillations in the load–displacement curve of Fig. 6.21. (These oscillations are not representative of the PLC effect because of the large maximum time step $\Delta t = 1$ s in the fine mesh simulations. Also, Δa_{max} is not representative of the complex crack growth shape that can be seen for example in Fig. 6.26(b). The present numerical $J - \Delta a$ curve is given for information purposes only.)

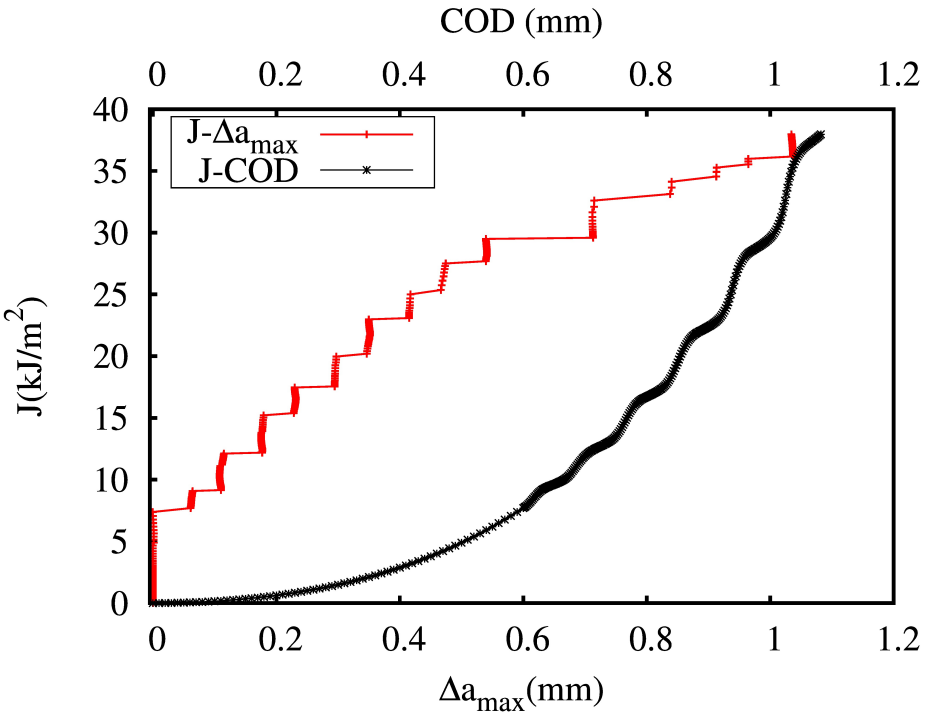

Figure 6.28 – Fine MESH 2 calculation, J versus Δa_{max} (red curve) and J versus COD (black curve).

Chapter 7

Conclusion and outlook

Conclusion

The objective of the thesis was to understand in more detail the influence of Portevin-Le Chatelier effect (PLC) on ductile fracture. In this context, studies were carried out along the following two lines:

1. Experimental characterisations and numerical simulations of PLC effect, especially plastic strain localization behaviour, in selected materials (see Chapters 3, 4 and 5).

2. Development of a damage model coupled with strain ageing term and numerical simulation of ductile fracture with the influence of PLC effect (see Chapters 5 and 6).

The main findings of this work are summarised below:

- **Correlation between dynamic strain ageing and slant fracture**

  Chapter 2 gives a global review about the Portevin-Le Chatelier effect from both experimental and numerical aspects. The PLC effects in Al-Cu and Al-Cu-Li alloys are particularly reviewed. The influence of loading path change (relaxation, strain rate change) on the PLC effect received little attention. The relation between slant fracture and dynamic strain ageing is discussed based on previous works. The slant fracture can be observed in the transverse plane (driven by plane stress state) or in the thickness plane (plane strain strain state) for plate tensile specimens. The manifestation of PLC effect does not cause slant fracture systematically. However, the PLC induced localization bands might be the precursor of slant fracture under certain test conditions such as that observed in round bar specimens [Wang et al., 2012; Clausen et al., 2004]. A direct observation of localization bands due to strain ageing by non-contact field measurement (e.g., DIC) before the onset of slant-fracture was still missing before the current work.

- **Introducing the influence of dynamic strain ageing on hardening rate in the strain ageing model**

  Chapter 3 presented a dislocation density based modified Kubin-Estrin-McCormick (KEMC) model in order to better describe the interaction between strain hardening and strain ageing phenomena based on previous experimental observations. The coupling between dynamic strain ageing and strain hardening is accounted for by

introducing a limitation of the dynamic recovery process due to DSA. This modification allows to increase the hardening rate in the temperature and strain rate domain where the pinning of dislocations by solute atoms is the most active i.e. for low strain rates or high temperatures. The new model formulation has been identified using material point simulations for a C-Mn steel over a large range of temperatures and strain rates. Results show a significant improvement on the description of hardening with respect to previous identifications. Serrations on the stress/strain curves as well as the associated plastic strain rate localization bands have been reproduced and illustrated using 2D and 3D finite element simulations.

- **Loading history dependent PLC effect**

  Chapter 4 is focused on the characterization of PLC effect in AA2139-T3, AA2198-T3R and AA2198-T8R alloys. PLC effect is not observed in constant strain rate tests at room temperature for AA2139-T3. The onset of PLC type serrations and localization is observed in relaxation and unloading ageing tests. Comparing the two strain rate jump tests, only the increasing one triggered PLC instabilities. In contrast to AA2139-T3 alloy, PLC effects were also observed for AA2198-T3R tensile specimens under constant strain rate loading condition. It is found that relaxation and a sudden strain rate change could trigger localization bands and significantly advance the onset of PLC effect in T3R material. PLC effect has not been observed for AA2198-T8R specimens. Only shallow localization bands could be seen after re-straining located in the region close to the shoulders of specimens. However, these bands failed to propagate.

  The premature triggering of PLC effects after re-straining has been reproduced by our FE simulations for the first time. It is worth noting that, with a properly chosen strain rate, the PLC free case under constant strain rate loading and triggering effect after relaxation could be reproduced. It seems that the propagation of the Lüders band following re-straining could be responsible for leaving behind a slightly heterogeneous mechanical state which allows for the early triggering of PLC bands. In addition, an important observation is that, according to our DIC measurements, localization bands can appear with very weak serrations on the stress-strain curve. This result could explain why some authors claimed that there is no PLC effect in the AA2198-T3R alloy.

- **Different strain localization behaviour and fracture modes in C-Mn steel SENT specimens at** 20 °C **and** 175 °C

  Chapter 5 presented experimental results about C-Mn steel SENT tests with DIC measurement. At 175 °C, the tested material is sensitive to PLC effect, whereas no PLC effect can be found at room temperature. Slant fracture is found in the thickness plane of the specimens tested at 175 °C, whereas flat fracture is observed in those tested at room temperature. For 175 °C tests, the PLC bands during crack propagation are confined to the crack tip area flipping up and down. In contrast, at room temperature there is no PLC band during crack propagation. The early non-symmetric development of plastic zone at 175 °C is the precursor of slant fracture. **We think that the strain bands due to PLC effect promote this loss of symmetry ans subsequent slant fracture.**

- **Simulations using Rousselier damage model coupled with strain ageing for modelling slant fracture**

Two kinds of coupled damage-DSA models have been studied in the current thesis. One is the macroscopic model as presented in Chapter 5 and Chapter 6.2. The model presented in Chapter 5 is the Rousselier model with void growth only. The model presented in Chapter 6.2 contains a modified nucleation term. The idea was to investigate if a rapid nucleation could promote damage development inside localization bands. 2D and 3D simulations of plate tensile specimen showed that this model is able to capture this damage procedure driven by PLC localization bands. However, simulations are not successful for modelling slant fracture in 3D round bars or in SENT specimens.

The final model is a fully coupled damage model built in the polycrystal framework involving strain ageing and Coulomb criterion in the slip system scale as presented in section 6.3. This model is applied for simulating the tearing of CT-like specimen in order to make a direct comparison with laminography-DVC results. Two major features observed by laminography-DVC, namely early stage multiple strain localization bands and flat-to-slant fracture have been reproduced. As presented in A.3, if DSA is not activated, multiple bands can not be obtained. Prior calculations using von Mises plasticity or the GTN model captured neither the localization bands nor the slant fracture (see e.g., A.3). Combining with the experimental results reported in Chapter 4, we can conclude that DSA is the physical origin of multiple localization bands observed in these aluminium alloys by laminography-DVC. In our simulations, stepwise propagation of crack is found which is due to the strain rate bursts related to PLC effect. However slant fracture can still be produced using the current model without DSA term.

Outlook

To verify the current conclusions about the influence of PLC effect on the non-symmetric development of plastic zone, additional experiments are proposed:

- High resolution DIC measurement for investigating the plastic activity around notch area of specimens might be interesting. The CT, SENT and Kahn specimens of 5xxx aluminium alloys are ideal candidates due to their strong PLC effect at room temperature which will make the experimental set-up much easier.

- The DIC measurement for the C-Mn round bar tensile test at high temperature will be useful for verifying if the slant fracture is following a slanted PLC band.

Concerning numerical simulations:

- Although the triggering effect is reproduced by current simulations using the KEMC model, the results are only in agreement with experimental observations under specific conditions such as a selected strain rate. The DSA model could be enhanced to account for these loading path change effect.

- The prediction of slant fracture in round tensile bar specimen is still a challenge. The PLC bands oscillate in the necked area in the current simulations with the macroscopic damage-DSA model with a modified nucleation term. In notched specimen, localization bands around notch tip are highly intermittent. A proper way to stabilize these bands might help damage to develop inside PLC bands. A possible way in the current model is to use a large value of k_c. However, large value

of k_c leads to early divergence due to the DSA model. The numerical integration of the DSA model could be improved to avoid early divergence. Further development to reduce the computation time is also necessary for applying such kind of models for industrial structures.

- As can be seen in 2D rectangular plate simulations, the band width produced by existing models is approximately that of one layer of elements. To get rid of mesh dependence, a regularization method has to be developed in simulating PLC bands and in the transition from flat to slant fracture. The procedure proposed by Mazière and Forest [2015] based on the introduction of strain gradient plasticity effects can be applied to regularise the current models.
- Reproducing flat-to-slant fracture in C-Mn steel is still a challenge. The strong measured localizations should be reproduced with more fidelity and also the unsymmetrical plastic zone, i.e. loss of symmetry.

Appendix A

Appendix

A.1 Prediction of fracture of notched round bar with the Rice-Tracey model

Different from the coupled damage models presented in Chapter 5 and 6, the prediction results using the uncoupled Rice-Tracey model [Rice and Tracey, 1969; Beremin, 1981] and the new strain ageing model presented in Chapter 3 are presented here. The Rice-Tracey model describes the void growth ratio of a spherical void with radius R in a rigid perfectly plastic material at high stress triaxiality:

$$\frac{\dot{R}}{R} = \dot{p}0.283 \exp\left(\frac{3}{2}\frac{\sigma_m}{\sigma_{eq}}\right), \quad R(0) = R_0 \tag{A.1}$$

where σ_m is the hydrostatic stress; σ_{eq} is the equivalent stress; R_0 is the initial void radius; $\dot{p}$ is the equivalent plastic strain rate. Fracture is assumed to occur when the void growth ratio $\frac{R}{R_0}$ at the centre point reaches a critical value $\left(\frac{R}{R_0}\right)_c$.

We tested our model proposed in Chapter 3. Simulations of AE4 specimen are performed at each temperature with the parameters identified in Chapter 3 with the strain ageing model. Following the assumption in Wang [2011], the criterion of fracture is temperature independent considering that the fractography shows little difference at 20 °C and at 200 °C. The drop of ductility at 200 °C could be related to material behaviours.

The fracture criterion $\left(\frac{R}{R_0}\right)_c$ is identified at 20 °C by taking the corresponding void growth ratio at fracture point on the experimental curve as shown in Fig. A.1. With this criterion, the predictions at each temperature are made as shown in Fig. A.1.

As can be seen, a decrease in ductility was observed in the DSA domain which is similar to the previous predictions. Nevertheless, the predicted magnitude of the ductility drop was still less than experimental observations.

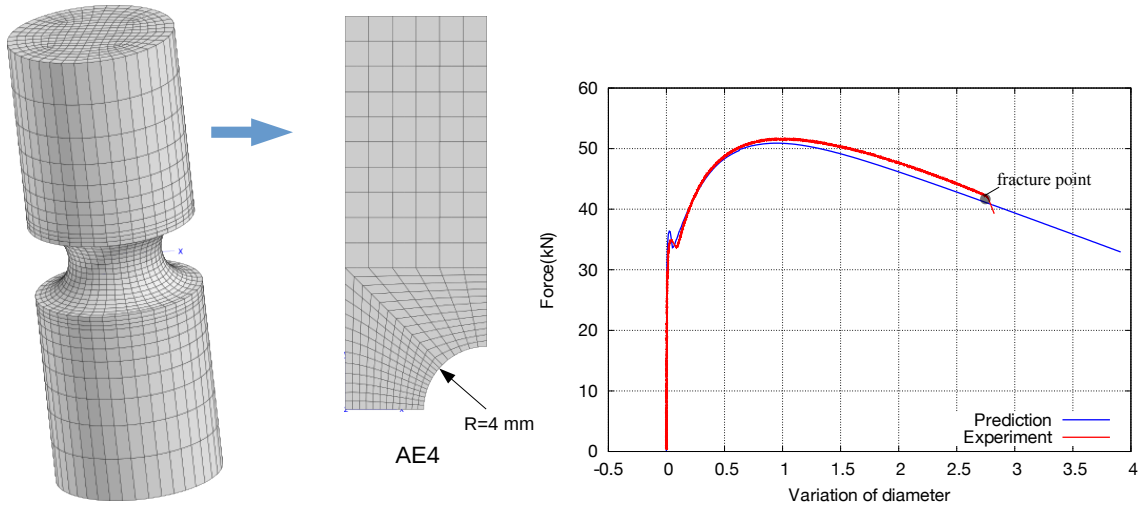

Figure A.1 – Mesh of AE4 specimen. Simulated curve and experimental curve at 20 °C.

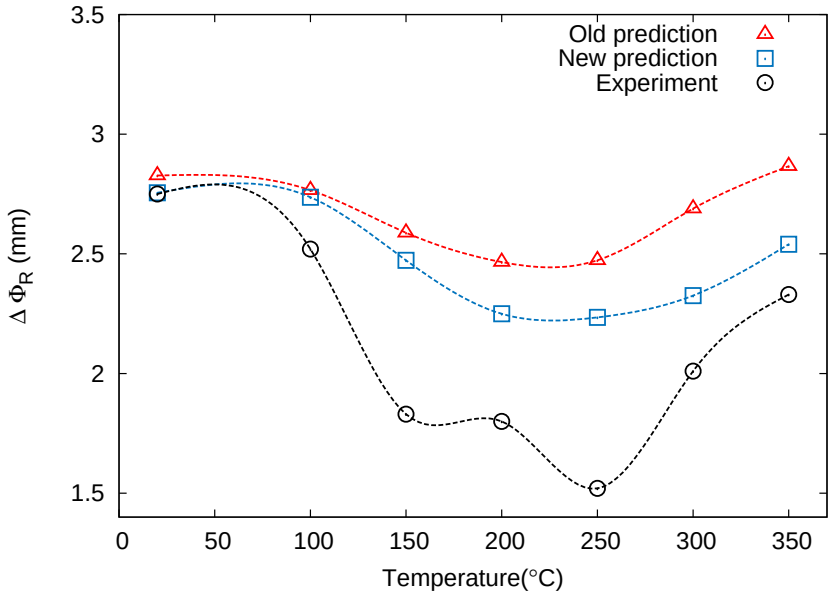

Figure A.2 – Prediction of fracture for AE4 in terms of diameter variation $\Delta\phi_R$: experimental measurement, old prediction by Wang [2011] and new prediction.

A.2 Experimental database of aluminium alloys

Table A.1 – Thickness of material sheet.

	AA2198-T3R	AA2198-T8R	AA6056	AA21939-T3	AA2024-T351
Thickness (mm)	2.0	2.0	1.4	4.7	1.8

Table A.2 – Constant strain rate tensile tests.

Tensile test conditions for aluminium alloys.					
	$2\times10^{-2}\,s^{-1}$	$10^{-2}\,s^{-1}$	$10^{-3}\,s^{-1}$	$10^{-4}\,s^{-1}$	$10^{-5}\,s^{-1}$
AA2198-T3R RT (Fig. 4.15, A.3)		••	•••	•	•
AA2198-T3R -50°C (Fig. A.5)			•		
AA2198-T8R RT (Fig. 4.16)		•	•	•	•
AA2198-T8R 0°C (Fig. A.5)			•		
AA2198-T8R -20°C (Fig. A.5)			•		
AA2198-T8R -50°C (Fig. A.5)			•		
AA2198-T8R 80°C (Fig. A.5)			•		
AA2139-T3 RT (Fig. 4.5)		••	••	•	•
AA6056 RT	•	•	•	•	•
AA2024-T351 RT		•	•	•	•
with relaxations at room temperature.					
	$2\times10^{-2}s^{-1}$	$10^{-2}s^{-1}$	$10^{-3}s^{-1}$	$10^{-4}s^{-1}$	$10^{-5}s^{-1}$
AA2198-T3R 4rl (Fig. 4.20)			•		
AA2198-T3R 1rl (Fig. 4.17, 4.18, 4.19)		•	•	•	
AA2198-T8R 4rl (Fig. 4.20)		•			
AA2139-T3 4rl (Fig. 4.6)		•			
AA6056		•	•		
with unloading.					
AA2139-T3 (Fig. 4.7)		•			
AA2198-T3R		•			

Note: 1. " • " marks the number of realised tests.
2. PLC sensitive tests are marked with green colour.
3."RT" stands for room temperature.
4. 1rl: with 1 relaxation; 4rl: with 4 relaxations.

Table A.3 – Tensile tests with strain rate jump.

	Increasing strain rate	Decreasing strain rate
AA2198-T3R (Fig. 4.21)	•	••
AA2198-T8R (Fig. 4.22)	•	•
AA2139-T3 (Fig. 4.8)	•	•
AA6056	•	
AA2024-T351	•	

A.2.1 Additional tests on AA2198 alloy

Fig. A.3 shows the repeated tensile tests for AA2198-T3R specimens at $\dot{E}$=10^{-2} s^{-1}. Fig. A.4 shows the repeated tensile tests for AA2198-T3R specimens at $\dot{E}$=10^{-3} s^{-1}. Fig. A.5 shows the tensile curves of AA2198-T8R specimens tested at different temperatures. There is no sign of PLC effect under these testing conditions. Fig. A.6 shows the spatio-temporal patterns for AA2198-T8R specimens tested different strain rates.

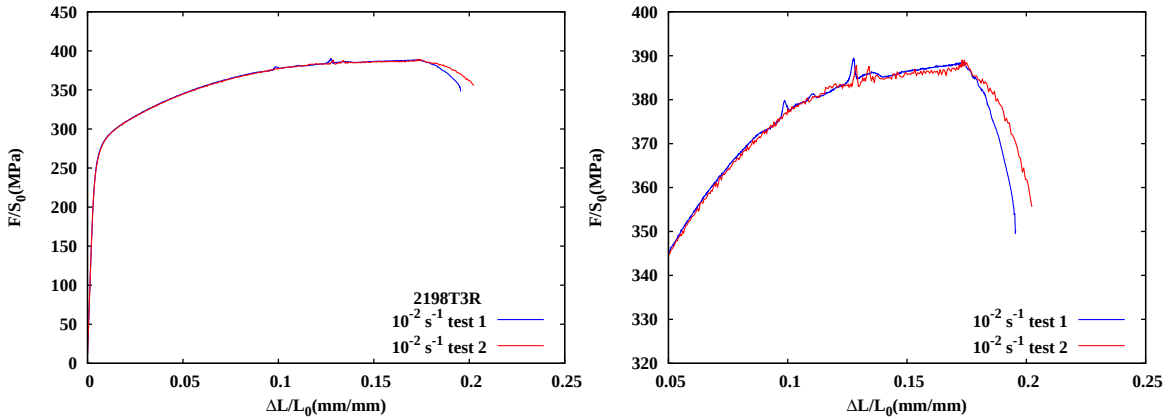

Figure A.3 – Repeated tests for AA2198-T3R specimens at room temperature and strain rate $\dot{E}$=10^{-2} s^{-1}.

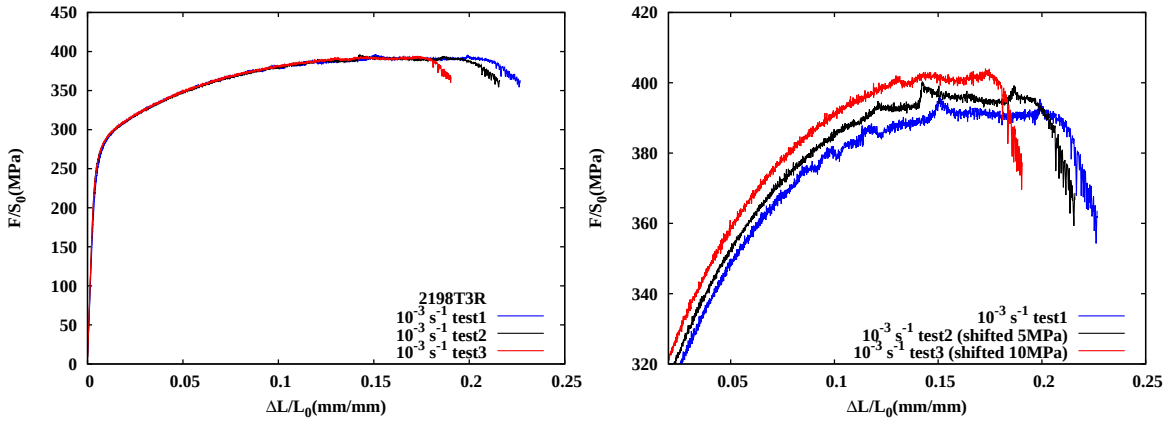

Figure A.4 – Repeated tests for AA2198-T3R specimens at room temperature and strain rate $\dot{E}$=10^{-3} s^{-1}. The curves in the zoom figure are shifted for a clear view.

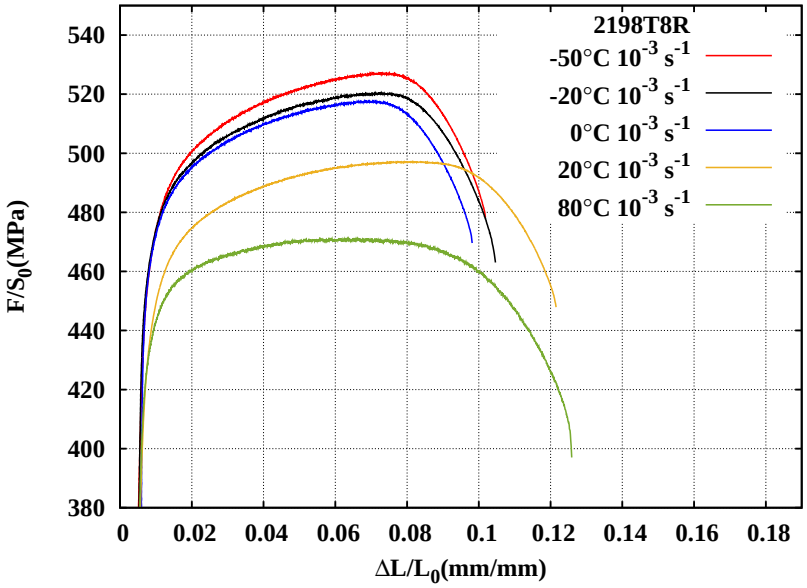

Figure A.5 – Tensile tests at different temperatures of AA2198-T8R specimens tested at $\dot{E}$=10^{-3} s^{-1}.

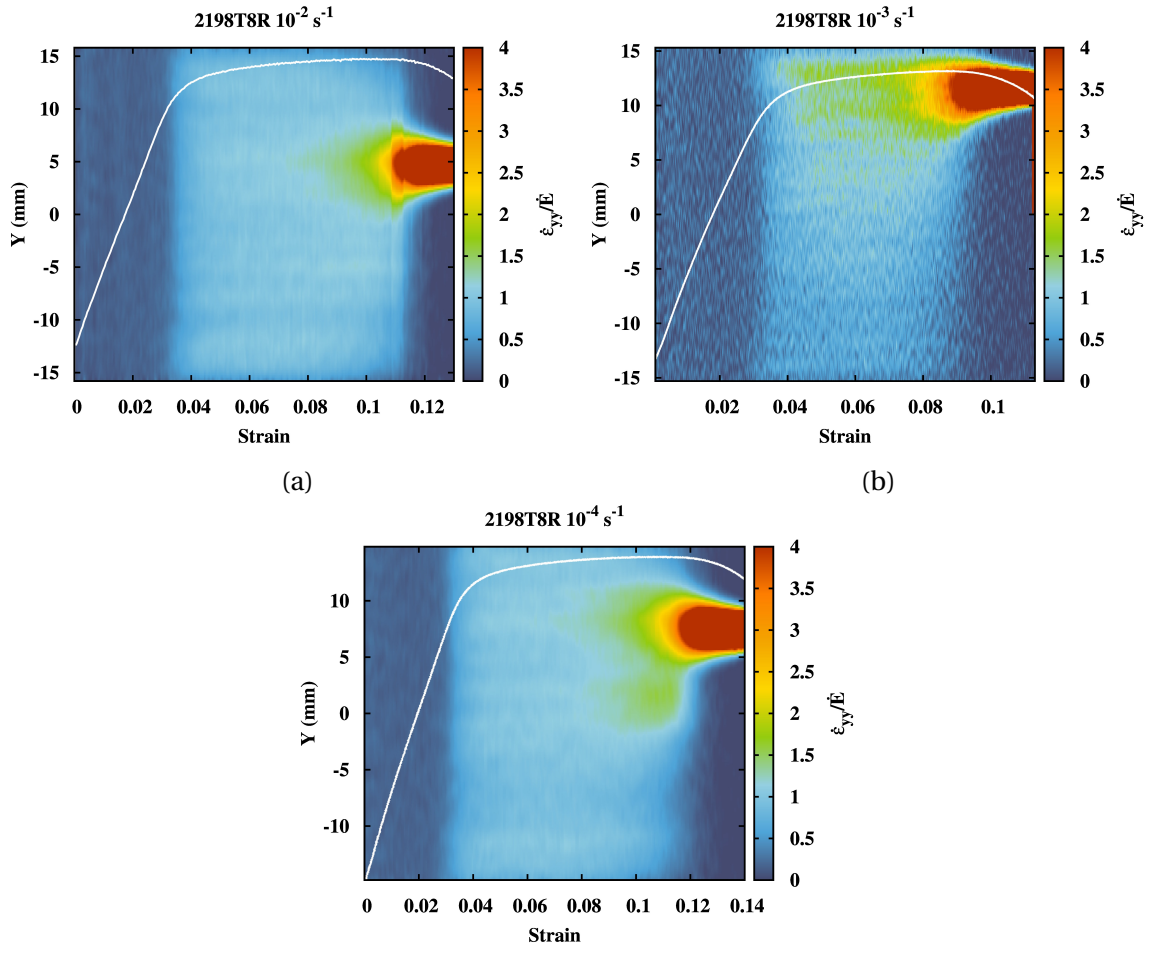

(a) (b) (c)

Figure A.6 – Spatio-temporal patterns of CSR tests at room temperature and different strain rates for AA2198-T8R.

A.3 Comparison of simulation results using different models of CT-like specimens

The result presented here is a supplement to section 6.3 which is reproduced from: Ren, S., Rousselier, G., Morgeneyer, T.F., Mazière, M. and Forest, S., 2016. Numerical investigation of dynamic strain ageing and slant ductile fracture in a notched specimen and comparison with synchrotron tomography 3D-DVC. Procedia Structural Integrity, 2, pp.3385-3392.

A.3.1 Equivalent strain fields

Fig. A.7 shows the incremental equivalent strain fields in the ROI 1 for four increments: step (0)-(1), step (1)-(2), step (2)-(3), step (3)-(4). These incremental equivalent strain fields were measured by the correlations between the current step and the previous one, i.e. the results of (1)-(2) is obtained by comparing the strain magnitude at step 2 with that at step 1. This strategy makes the localisation bands easier to be observed than the cumulated ones, that are always compared with the initial unloaded state. Fig. A.7(a) is the laminography-DVC measurement of the equivalent strain fields reported by Morgeneyer et al. [2014]. Multiple localisation bands were observed in front of the notch tip ($\sim 970\,\mu m$) at very early stage of loading steps.

Fig. A.7(b) presents the simulation results in the ROI 1 with the current full coupled model. At step (0)-(1), two orthogonal strain localisation bands are observed, which produced a highlighted area at band intersection. However, these two bands showed similar strain magnitude. In the experimental observation, a main slant band from the upper-right corner to the lower-left corner is more activated than the other (see Fig. A.7(a)). The material heterogeneity and real loading conditions in the experiment can obviously favour the appearance of a non-symmetric strain field. At step (1)-(2) and (2)-(3), the band activities became more active which are the same as the laminography observations. At step (1)-(2), a lot of smaller bands perpendicular or parallel to the two orthogonal bands are distributed over a large area in the ROI. At step (2)-(3), the bands began to lighten only in the area surrounding one of the two orthogonal bands (from upper-left to lower-right). Finally, a narrowing slanted localisation band was formed in this zone. The orientation of bands is approximately 45° to the loading direction both in the FE simulation and in experiments. The evolution of strain localisation band pattern is qualitatively in agreement with laminography observations, though the pattern is not strictly identical. We can not expect a completely deterministic prediction with PLC model who involves intrinsic instabilities.

To compare with the situation without PLC effect, the PLC term is eliminated by setting $P_1 = 0$ MPa and $R_s = 181$ MPa in lieu of $P_1 = 80$ MPa and $R_s = 101$ MPa. Fig. A.7(c) gives the equivalent strain field obtained by eliminating the PLC term, i.e. Rousselier damage model and Coulomb fracture criterion together in the polycrystalline framework. The multiple bands could not be observed any more. Strain began to concentrate along one slanted area at increment (2)-(3) and finally a slanted localisation band suddenly appeared at increment (3)-(4). As the stress level in this new trial without PLC is higher than that with PLC, the influence of Coulomb criterion is enhanced which advanced the crack propagation (initiated at increment (2)-(3)). Fig. A.7(d) shows the simulation with Tresca plasticity. It is clear that it is not enough to reproduce the experimental observations especially the slant fracture. Other simulations using GTN model and von Mises plasticity have been reported by Morgeneyer et al. [2014]. They did not reproduce the strain local-

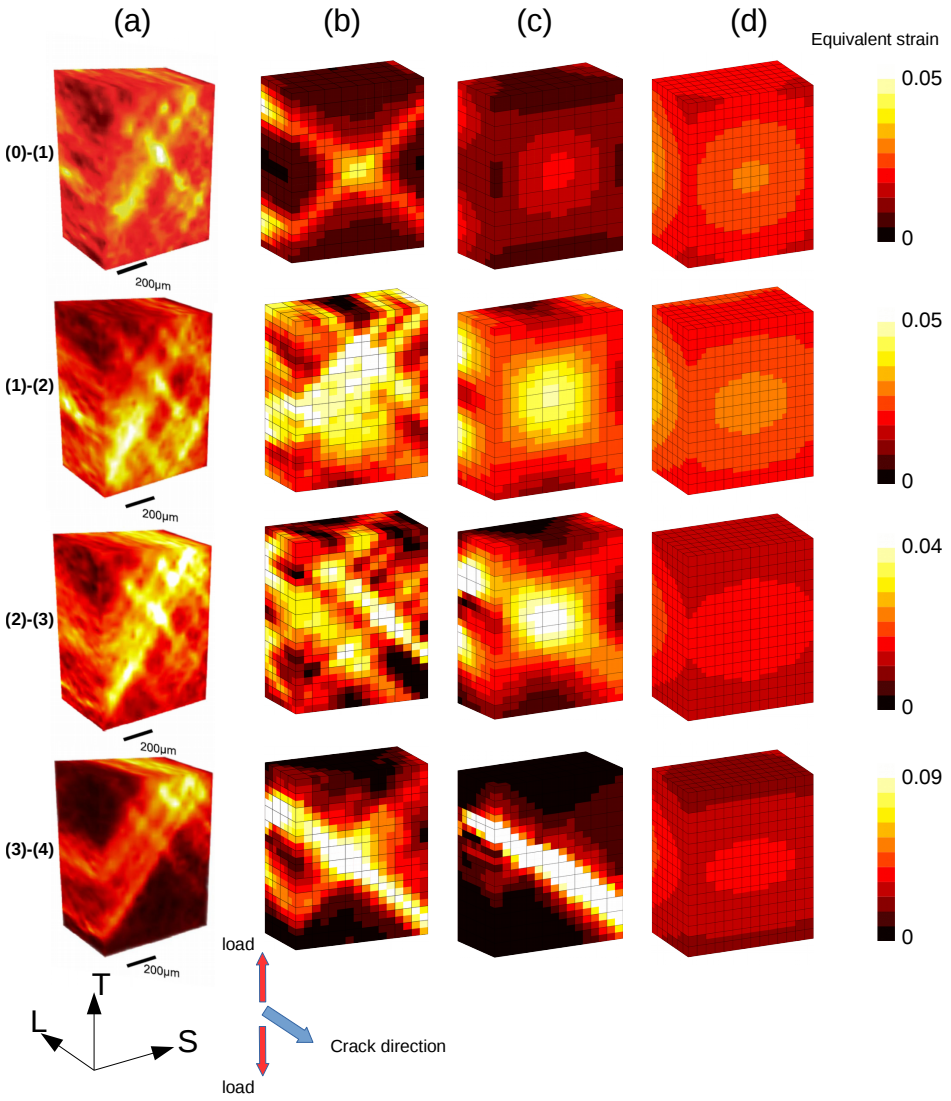

Figure A.7 – von Mises equivalent strain field in ROI 1 of increments (0)-(1), (1)-(2), (2)-(3) and (3)-(4). (a) Laminography-DVC analysis [Morgeneyer et al., 2014]; (b) Current full coupled model; (c) without PLC effect (polycrystalline+damage+Coulomb) (d) Tresca plasticity

.

isation bands nor the slant fracture. In Morgeneyer and Besson [2011], transition from flat to slant has been successfully reproduced numerically for a tear test of an aluminium sheet using void nucleation based on the Lode parameter for shear. This model is not supposed to reproduce the initial slant strain concentration band either.

The incremental equivalent strain fields in ROI 2 are shown in Fig. A.8(a). More than two bands were observed. At increment (2)-(3), a central band is activated. From increment (1)-(2) to (3)-(4), these bands are activated alternately. These activities are more evident on the specimen surfaces which will not be shown here due to space limitation. Those multiple bands and the alternating activity are not expected from Tresca plasticity (Fig. A.8(c)), von Mises plasticity or GTN model. The simulations results using von Mises plasticity and GTN are not presented here.

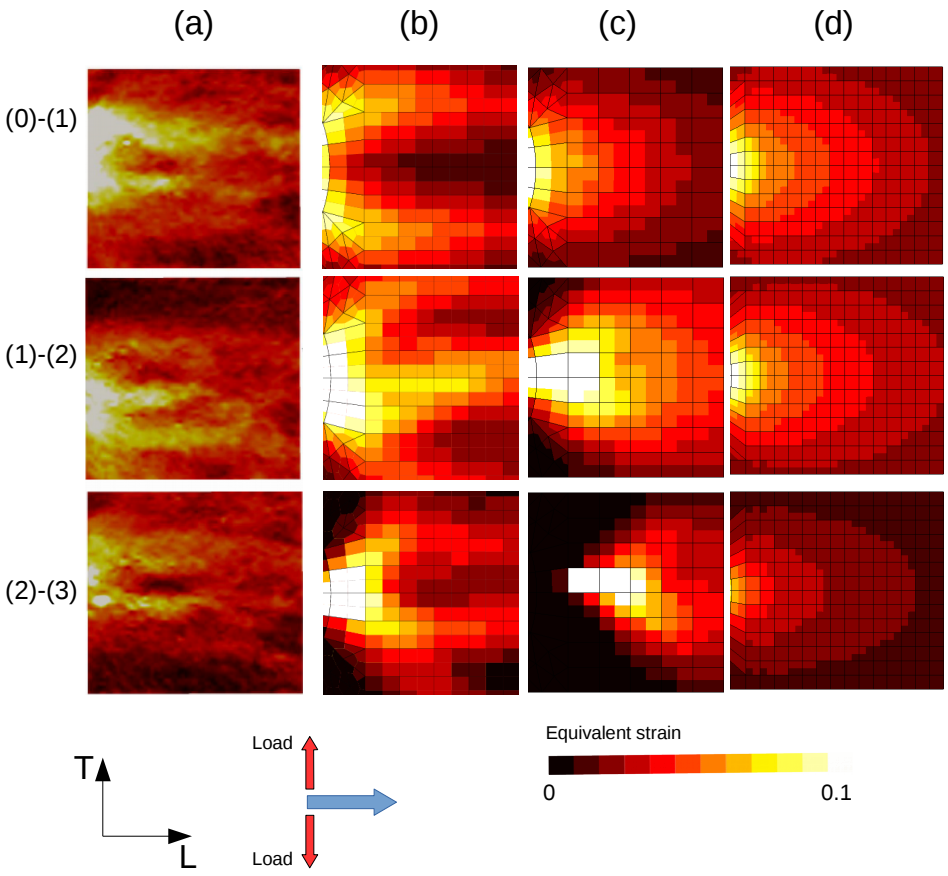

Figure A.8 – Incremental von Mises equivalent strain field in the T-L plane of ROI 2. (a) Laminography-DVC analysis at z = 0 mm [Buljac et al., 2016]; (b) Current full coupled model (z = -0.25 mm); (c) without PLC term at z = -0.125 mm (polycrystalline+damage+Coulomb); (d) Tresca (approximated using Bron) plasticity (z = 0 mm).

A.4 TU48C and A42

Reproduced experimental tensile curves of A42 steel [Marais, 2012] at room temperature and strain rate $10^{-2}\,s^{-1}$ is superposed with that of TU48C [Wang, 2011] in Fig. A.9. The curves of TU48C at 200 °C are also reproduced from [Wang, 2011].

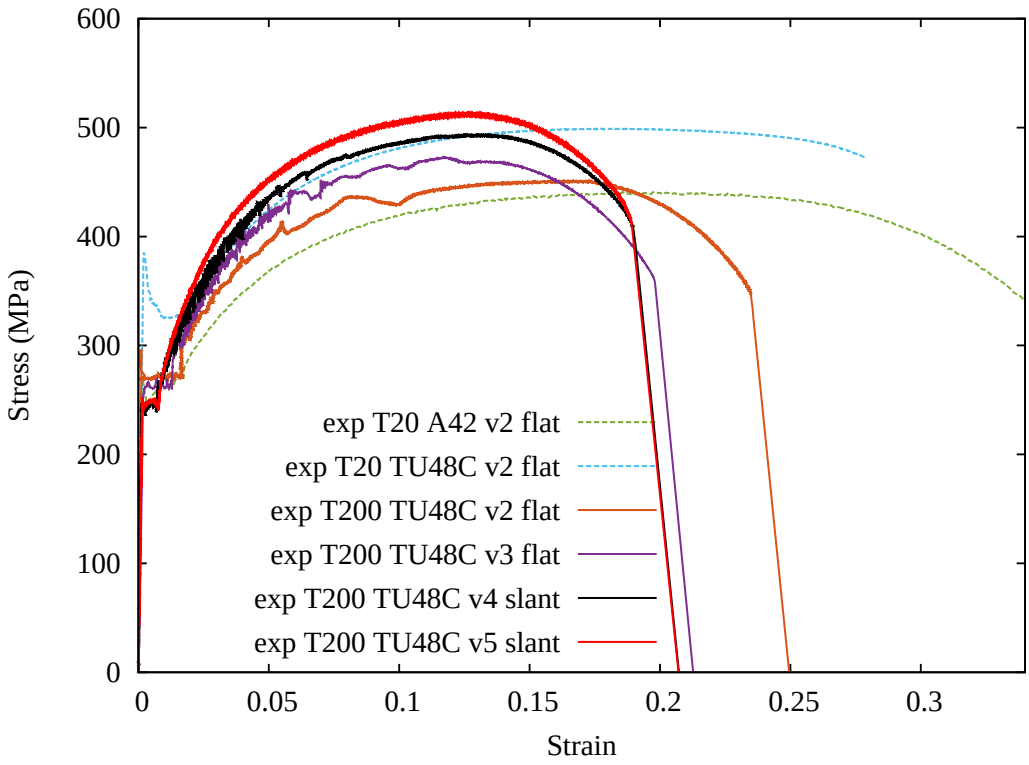

Figure A.9 – Tensile curves of round bar specimens of TU48C and A42 steels.

Bibliography

Aifantis, E. C. (1987). The physics of plastic deformation. *International Journal of Plasticity*, 3(3):211–247. (Cited page 194.)

Ait-Amokhtar, H., Vacher, P., and Boudrahem, S. (2006). Kinematics fields and spatial activity of Portevin–Le Chatelier bands using the digital image correlation method. *Acta Materialia*, 54(16):4365–4371. (Cited page 123.)

Alexopoulos, N. D., Migklis, E., Stylianos, A., and Myriounis, D. P. (2013). Fatigue behavior of the aeronautical Al–Li (2198) aluminum alloy under constant amplitude loading. *International Journal of Fatigue*, 56:95–105. (Cited pages 36 and 115.)

Allain, S., Bouaziz, O., Lebedkina, T., and Lebyodkin, M. (2011). Relationship between relaxation mechanisms and strain aging in an austenitic femnc steel. *Scripta Materialia*, 64(8):741–744. (Cited pages 17, 18, 82, 90, and 116.)

Amar, E. and Pineau, A. (1985). Interpretation of ductile fracture toughness temperature dependence of a low strength steel in terms of a local approach. *Engineering Fracture Mechanics*, 22(6):1061–1071. (Cited pages 13, 55, 92, and 123.)

Armstrong, P. and Frederick, C. (1966). A mathematical representation of the multiaxial bauschinger effect. *Report RD/B/N731*, Berkeley, UK. (Cited page 178.)

Asserin–Lebert, A., Besson, J., and Gourgues, A. (2005). Fracture of 6056 aluminum sheet materials: effect of specimen thickness and hardening behavior on strain localization and toughness. *Materials Science and Engineering: A*, 395(1–2):186 – 194. (Cited pages 38, 44, and 48.)

Balík, J., Lukáč, P., and Kubin, L. (2000). Inverse critical strains for jerky flow in Al-Mg alloys. *Scripta Materialia*, 42(5):465–471. (Cited pages 17, 82, and 90.)

Bargellini, R., Besson, J., Lorentz, E., and Michel-Ponnelle, S. (2009). A non-local finite element based on volumetric strain gradient: application to ductile fracture. *Computational Materials Science*, 45(3):762–767. (Cited page 186.)

Beardsmore, D., da Fonseca, J. Q., Romero, J., English, C., Ortner, S., Sharples, J., Sherry, A., and Wilkes, M. (2013). Study of Lüders phenomena in reactor pressure vessel steels. *Materials Science and Engineering: A*, 588:151–166. (Cited page 149.)

Behnood, N. and Evans, J. (1989). Plastic deformation and the flow stress of aluminium-lithium alloys. *Acta Metallurgica*, 37(2):687–695. (Cited page 34.)

Belotteau, J. (2009). *Comportement et rupture d'un acier au C-Mn en présence de vieillissement sous déformation*. PhD dissertation, Ecole Centrale Paris. (Cited pages 4, 13, 14, 15, 40, 41, 55, 61, and 125.)

Belotteau, J., Berdin, C., Forest, S., Parrot, A., and Prioul, C. (2009). Mechanical behavior and crack tip plasticity of a strain aging sensitive steel. *Materials Science and Engineering: A*, 526(1):156–165. (Cited pages 61, 76, 149, and 170.)

Benallal, A., Berstad, T., Børvik, T., Hopperstad, O., Koutiri, I., and De Codes, R. N. (2008). An experimental and numerical investigation of the behaviour of AA5083 aluminium alloy in presence of the Portevin–Le Chatelier effect. *International Journal of Plasticity*, 24(10):1916–1945. (Cited pages 56, 105, 135, 149, 170, and 183.)

Benallal, A., Berstad, T., Børvik, T., Clausen, A., and Hopperstad, O. (2006). Dynamic strain aging and related instabilities: experimental, theoretical and numerical aspects. *European Journal of Mechanics - A/Solids*, 25(3):397 – 424. (Cited pages 21, 22, 46, and 124.)

Benedyk, J. C. (2009). International temper designation systems for wrought aluminum alloys. *Light Metal Age*. (Cited page 29.)

Beremin, F. (1981). Cavity formation from inclusions in ductile fracture of A508 steel. *Metallurgical and Materials Transactions A*, 12(5):723–731. (Cited page 205.)

Bergheau, J.-M., Leblond, J.-B., and Perrin, G. (2014). A new numerical implementation of a second-gradient model for plastic porous solids, with an application to the simulation of ductile rupture tests. *Computer Methods in Applied Mechanics and Engineering*, 268:105–125. (Cited page 186.)

Bergström, Y. (1970). A dislocation model for the stress-strain behaviour of polycrystalline α-Fe with special emphasis on the variation of the densities of mobile and immobile dislocations. *Materials Science and Engineering*, 5(4):193–200. (Cited page 25.)

Besnard, G., Hild, F., and Roux, S. (2006). "finite-element" displacement fields analysis from digital images: application to portevin–le chatelier bands. *Experimental Mechanics*, 46(6):789–803. (Cited page 123.)

Besson, J. (2010). Continuum models of ductile fracture: a review. *International Journal of Damage Mechanics*, 19(1):3–52. (Cited pages 49 and 159.)

Besson, J., Brocks, W., Chabanet, O., and Steglich, D. (2001a). Ductile rupture of aluminum sheet materials. *Revue Européenne des Éléments Finis*, 10(2-4):401–415. (Cited pages 49 and 50.)

Besson, J., Cailletaud, G., Chaboche, J.-L., and Forest, S. (2009). *Non-linear mechanics of materials*, volume 167. Springer Science & Business Media. (Cited pages 57, 104, and 139.)

Besson, J., McCowan, C., and Drexler, E. (2013). Modeling flat to slant fracture transition using the computational cell methodology. *Engineering Fracture Mechanics*, 104:80–95. (Cited pages 50 and 159.)

Besson, J., Steglich, D., and Brocks, W. (2001b). Modeling of crack growth in round bars and plane strain specimens. *International Journal of Solids and Structures*, 38(46):8259–8284. (Cited pages 49, 50, and 159.)

Besson, J., Steglich, D., and Brocks, W. (2003). Modeling of plane strain ductile rupture. *International Journal of Plasticity*, 19(10):1517–1541. (Cited pages 38, 49, and 50.)

Böhlke, T., Bondár, G., Estrin, Y., and Lebyodkin, M. (2009). Geometrically non-linear modeling of the Portevin–Le Chatelier effect. *Computational Materials Science*, 44(4):1076–1088. (Cited pages 55, 56, 59, 82, 105, 123, 183, and 193.)

Brechet, Y. and Estrin, Y. (1994). On a pseudo-Portevin-Le Chatelier effect. *Scripta Matallurgica et Materialia*, 31:185–190. (Cited page 76.)

Brechet, Y. and Estrin, Y. (1995). On the influence of precipitation on the Portevin-Le Chatelier effect. *Acta Metallurgica et Materialia*, 43(3):955–963. (Cited page 34.)

Brechet, Y. and Estrin, Y. (1996). Pseudo-Portevin-Le Chatelier effect in ordered alloys. *Scripta Materialia*, 35(2):217–223. (Cited page 123.)

Brindley, B. (1970). The effect of dynamic strain-ageing on the ductile fracture process in mild steel. *Acta Metallurgica*, 18(3):325 – 329. (Cited page 42.)

Bron, F. and Besson, J. (2006). Simulation of the ductile tearing for two grades of 2024 aluminum alloy thin sheets. *Engineering Fracture Mechanics*, 73(11):1531–1552. (Cited pages 43 and 44.)

Buirette, C., Huez, J., Gey, N., Vassel, A., and Andrieu, E. (2014). Study of crack propagation mechanisms during charpy impact toughness tests on both equiaxed and lamellar microstructures of Ti–6Al–4V titanium alloy. *Materials Science and Engineering: A*, 618:546–557. (Cited page 126.)

Buljac, A. (2017). *Compréhension, observation et quantification des mécanismes de rupture ductile par imagerie 3D*. PhD dissertation, Paris Saclay. (Cited pages 45, 46, 47, and 110.)

Buljac, A., Morgeneyer, T., Helfen, L., and Hild, F. (2017). On deformation and damage micromechanisms in strong work hardening 2198 T3 aluminium alloy. *Acta Materialia*, submitted. (Cited page 83.)

Buljac, A., Taillandier-Thomas, T., Morgeneyer, T. F., Helfen, L., Roux, S., and Hild, F. (2016). Slant strained band development during flat to slant crack transition in AA 2198 T8 sheet: in situ 3D measurements. *International Journal of Fracture*, 200(1-2):49–62. (Cited pages 83, 124, 170, 172, 173, 174, 176, and 212.)

Böhlke, T., Bondár, G., Estrin, Y., and Lebyodkin, M. (2009). Geometrically non-linear modeling of the Portevin–Le Chatelier effect. *Computational Materials Science*, 44(4):1076–1088. (Cited pages 31 and 37.)

Cai, Y., Tian, C., Zhang, G., Han, G., Yang, S., Fu, S., Cui, C., and Zhang, Q. (2017). Influence of γ precipitates on the critical strain and localized deformation of serrated flow in ni-based superalloys. *Journal of Alloys and Compounds*, 690:707–715. (Cited page 123.)

Cai, Y., Yang, S., Wang, Y., Fu, S., and Zhang, Q. (2016a). Characterization of the deformation behaviors associated with the serrated flow of a 5456 Al-based alloy using two orthogonal digital image correlation systems. *Materials Science and Engineering: A*, 664:155–164. (Cited pages 88 and 123.)

Cai, Y., Zhang, Q., Yang, S., Fu, S., and Wang, Y. (2016b). Experimental study on three-dimensional deformation field of Portevin–Le Chatelier effect using digital image correlation. *Experimental Mechanics*, 56(7):1243–1255. (Cited page 84.)

Caillard, D. (2013). A TEM in situ study of alloying effects in iron. I—Solid solution softening caused by low concentrations of Ni, Si and Cr. *Acta Materialia*, 61(8):2793–2807. (Cited page 20.)

Caillard, D. (2016). Dynamic strain ageing in iron alloys: The shielding effect of carbon. *Acta Materialia*, 112:273–284. (Cited page 56.)

Cailletaud, G. (1992). A micromechanical approach to inelastic behaviour of metals. *International Journal of Plasticity*, 8(1):55–73. (Cited pages 106, 178, and 179.)

Calonne, V., Berdin, C., Saint-Germain, B., and Jayet-Gendrot, S. (2004). Damage and dynamic strain aging in a thermal aged cast duplex stainless steel. *Journal of Nuclear Materials*, 327(2–3):202 – 210. (Cited pages 13 and 40.)

Casarotto, L., Dierke, H., Tutsch, R., and Neuhäuser, H. (2009). On nucleation and propagation of PLC bands in an Al–3Mg alloy. *Materials Science and Engineering: A*, 527(1):132–140. (Cited page 123.)

Chaboche, J.-L. (1977). Viscoplastic constitutive equations for the description of cyclic and anisotropic behaviour of metals. *Bull. Acad. Polon. Sci., Ser. Sci. Tech.*, 25(1):33–42. (Cited page 178.)

Chaboche, J.-L., Gaubert, A., Kanouté, P., Longuet, A., Azzouz, F., and Mazière, M. (2013). Viscoplastic constitutive equations of combustion chamber materials including cyclic hardening and dynamic strain aging. *International Journal of Plasticity*, 46:1 – 22. (Cited page 56.)

Chakravartty, J., Wadekar, S., Sinha, T., and Asundi, M. (1983). Dynamic strain-ageing of A203D nuclear structural steel. *Journal of Nuclear Materials*, 119(1):51–58. (Cited pages 13, 55, and 123.)

Chen, J. (2011). *Ductile tearing of AA2198 aluminium-lithium sheets for aeronautic application*. PhD dissertation, Ecole des Mines de Paris. (Cited pages 29, 33, 34, 37, 38, 95, 96, 108, 174, 177, and 186.)

Cheng, T., Xu, X., Cai, Y., Fu, S., Gao, Y., Su, Y., Zhang, Y., and Zhang, Q. (2015). Investigation of portevin-le chatelier effect in 5456 Al-based alloy using digital image correlation. *Optics and Lasers in Engineering*, 65:89–92. (Cited page 123.)

Chihab, K., Estrin, Y., Kubin, L., and Vergnol, J. (1987). The kinetics of the portevin-le chatelier bands in an Al-5at% Mg alloy. *Scripta metallurgica*, 21(2):203–208. (Cited page 123.)

Chmelík, F., Pink, E., Król, J., Balík, J., Pešička, J., and Lukáč, P. (1998). Mechanisms of serrated flow in aluminium alloys with precipitates investigated by acoustic emission. *Acta Mater.*, 46(12):4435–4442. (Cited pages 33 and 123.)

Chmelík, F., Ziegenbein, A., Neuhäuser, H., and Lukáč, P. (2002). Investigating the Portevin-Le Chatelier effect by the acoustic emission and laser extensometry techniques. *Materials Science and Engineering: A*, 324(1):200–207. (Cited pages 84, 97, and 135.)

Cho, A. and Bes, B. (2006). Damage tolerance capability of an Al-Cu-Mg-Ag alloy (2139). In *Materials Science Forum*, volume 519, pages 603–608. Trans Tech Publ. (Cited page 30.)

Chu, C. and Needleman, A. (1980). Void nucleation effects in biaxially stretched sheets. *Journal of Engineering Materials and Technology(Transactions of the ASME)*, 102(3):249–256. (Cited pages 157, 160, 161, 180, and 196.)

Clausen, A. H., Børvik, T., Hopperstad, O. S., and Benallal, A. (2004). Flow and fracture characteristics of aluminium alloy AA5083–H116 as function of strain rate, temperature and triaxiality. *Materials Science and Engineering: A*, 364(1–2):260 – 272. (Cited pages 40, 42, 123, 170, and 201.)

Coër, J., Manach, P., Laurent, H., Oliveira, M., and Menezes, L. (2013). Piobert–Lüders plateau and portevin–le chatelier effect in an al–mg alloy in simple shear. *Mechanics Research Communications*, 48:1–7. (Cited page 124.)

Colas, D., Finot, E., Flouriot, S., Forest, S., Mazière, M., and Paris, T. (2014). Investigation and modeling of the anomalous yield point phenomenon in pure tantalum. *Materials Science and Engineering: A*, 615:283–295. (Cited page 26.)

Cottrell, A. H. and Bilby, B. (1949). Dislocation theory of yielding and strain ageing of iron. *Proceedings of the Physical Society. Section A*, 62(1):49. (Cited pages 19, 55, 64, and 123.)

Coulomb, C. (1773). Sur une application des règles de maximis et minimis à quelques problèmes relatifs à l'architecture. *Mémoire Académie Royale des Sciences*. (Cited page 171.)

Da Silva, J. R. G. and McLellan, R. B. (1976). Diffusion of carbon and nitrogen in BCC iron. *Materials Science and Engineering*, 26:83 – 87. (Cited page 65.)

Dablij, M. and Zeghloul, A. (1997). Portevin-Le Chatelier plastic instabilities: characteristics of deformation bands. *Materials Science and Engineering: A*, 237(1):1–5. (Cited page 31.)

Dalloz, A. (2007). *Étude de l'endommagement par la découpe des aciers dual phase pour application automobile*. PhD dissertation, Ecole des Mines de Paris. (Cited page 126.)

De Codes, R. N., Hopperstad, O., Engler, O., Lademo, O.-G., Embury, J., and Benallal, A. (2011). Spatial and temporal characteristics of propagating deformation bands in aa5182 alloy at room temperature. *Metallurgical and Materials Transactions A*, 42(11):3358–3369. (Cited page 123.)

Decreus, B., Deschamps, A., De Geuser, F., Donnadieu, P., Sigli, C., and Weyland, M. (2013). The influence of Cu/Li ratio on precipitation in Al–Cu–Li–x alloys. *Acta Materialia*, 61(6):2207–2218. (Cited pages 33 and 34.)

Delafosse, D., Lapasset, G., and Kubin, L. (1993). Dynamic strain ageing and crack propagation in the 2091 Al-Li alloy. *Scripta Metallurgica et Materialia*, 29(11):1379–1384. (Cited pages 37 and 170.)

Delaunois, F., Denil, E., Marchal, Y., and Vitry, V. (2017). Accelerated aging and portevin-le chatelier effect in aa 2024. In *Materials Science Forum*, volume 879, pages 524–529. Trans Tech Publ. (Cited page 37.)

Delpueyo, D., Balandraud, X., and Grédiac, M. (2016). Calorimetric signature of the Portevin–Le Chatelier effect in an aluminum alloy from infrared thermography measurements and heat source reconstruction. *Materials Science and Engineering: A*, 651:135–145. (Cited pages 188 and 193.)

Deschamps, A., Decreus, B., De Geuser, F., Dorin, T., and Weyland, M. (2013). The influence of precipitation on plastic deformation of Al–Cu–Li alloys. *Acta Materialia*, 61(11):4010–4021. (Cited pages 34, 35, 36, 37, 95, and 115.)

Dierke, H., Krawehl, F., Graff, S., Forest, S., Šachl, J., and Neuhäuser, H. (2007). Portevin–lechatelier effect in Al–Mg alloys: Influence of obstacles–experiments and modelling. *Computational Materials Science*, 39(1):106–112. (Cited pages 55, 66, and 82.)

Drozd, Z., Trojanová, Z., and Kúdela, S. (2004). Deformation behaviour of Mg-Li-Al alloys. *Journal of Alloys and Compounds*, 378(1):192–195. (Cited page 89.)

Dursun, T. and Soutis, C. (2014). Recent developments in advanced aircraft aluminium alloys. *Materials & Design*, 56:862–871. (Cited page 28.)

Dybiec, H. and Chaturvedi, M. (1991). Serrated yielding in inconel 718. *Archives of Metallurgy*, 36(3):341–352. (Cited page 123.)

El-Naaman, S. and Nielsen, K. (2013a). Observations on Mode I ductile tearing in sheet metals. *European Journal of Mechanics - A/Solids*, 42:54 – 62. (Cited pages 46 and 47.)

El-Naaman, S. A. and Nielsen, K. L. (2013b). Observations on mode i ductile tearing in sheet metals. *European Journal of Mechanics-A/Solids*, 42:54–62. (Cited page 159.)

Estrin, Y. and Kubin, L. (1989). Collective dislocation behaviour in dilute alloys and the Portevin-Le Chatelier effect. *Journal of the Mechanical Behavior of Materials*, 2(3-4):255–292. (Cited pages 21, 22, and 25.)

Estrin, Y. and McCormick, P. (1991). Modelling the transient flow behaviour of dynamic strain ageing materials. *Acta Metallurgica et Materialia*, 39(12):2977–2983. (Cited pages 24, 178, and 183.)

Feld-Payet, S., Besson, J., and Feyel, F. (2011). Finite element analysis of damage in ductile structures using a nonlocal model combined with a three-field formulation. *International Journal of Damage Mechanics*, 20(5):655–680. (Cited page 186.)

Felter, C. L. and Nielsen, K. L. (2017). Assisted crack tip flipping under mode I thin sheet tearing. *European Journal of Mechanics-A/Solids*, 64:58–68. (Cited pages 46 and 50.)

Forest, S., Lorentz, E., et al. (2004). Localization phenomena and regularization methods. *Local Approach to Fracture*, pages 311–371. (Cited page 186.)

Fournier, L., Delafosse, D., and Magnin, T. (2001). Oxidation induced intergranular cracking and Portevin-Le Chatelier effect in nickel base superalloy 718. *Materials Science and Engineering: A*, 316(1):166–173. (Cited pages 55 and 123.)

Fressengeas, C., Beaudoin, A., Lebyodkin, M., Kubin, L., and Estrin, Y. (2005). Dynamic strain aging: a coupled dislocation—solute dynamic model. *Materials Science and Engineering: A*, 400:226–230. (Cited pages 25, 27, 56, and 76.)

Fu, S., Cheng, T., Zhang, Q., Hu, Q., and Cao, P. (2012). Two mechanisms for the normal and inverse behaviors of the critical strain for the Portevin–Le Chatelier effect. *Acta Materialia*, 60(19):6650 – 6656. (Cited pages 66 and 82.)

Fu, S., Zhang, Q., Hu, Q., Gong, M., Cao, P., and Liu, H. (2011). The influence of temperature on the plc effect in Al-Mg alloy. *Science China Technological Sciences*, 54(6):1389–1393. (Cited page 10.)

Gomiero, P., et, Y., Louchet, F., Tourabi, A., and Wack, B. (1992). Microstructure and mechanical properties of a 2091 Al-Li alloy-III. Quantitative analysis of portevin le chatelier instabilities and relation to toughness in Al-Li, Al-Cu-Mg and Al-Li-Cu-Mg (2091) alloys. *Acta Metallurgica et Materialia*, 40(4):863–871. (Cited pages 37, 55, and 123.)

Graff, S. (2006). *Viscoplastic behavior of zirconium alloys in the temperatures range* 20 °C-400 °C*: characterization and modeling of strain ageing phenomena*. PhD dissertation, Ecole des Mines de Paris. (Cited pages 19, 23, and 24.)

Graff, S., Dierke, H., Forest, S., Neuhäuser, H., and Strudel, J.-L. (2008). Finite element simulations of the Portevin-Le Chatelier effect in metal-matrix composites. *Philosophical Magazine*, 88(28-29):3389–3414. (Cited pages 124, 129, and 139.)

Graff, S., Forest, S., Strudel, J.-L., Prioul, C., Pilvin, P., and Béchade, J.-L. (2004). Strain localization phenomena associated with static and dynamic strain ageing in notched specimens: experiments and finite element simulations. *Materials Science and Engineering: A*, 387:181–185. (Cited pages 55, 56, 124, 149, 170, and 183.)

Graff, S., Forest, S., Strudel, J.-L., Prioul, C., Pilvin, P., and Béchade, J.-L. (2005). Finite element simulations of dynamic strain ageing effects at V-notches and crack tips. *Scripta Materialia*, 52(11):1181–1186. (Cited pages 21 and 124.)

Gregson, P., McDarmaid, D., and Hunt, E. (1988). Post-yield deformation characteristics in Al–Li alloys. *Materials Science and Technology*, 4(8):713–718. (Cited page 33.)

Gruben, G., Hopperstad, O., and Børvik, T. (2013). Simulation of ductile crack propagation in dual-phase steel. *International Journal of Fracture*, 180(1):1–22. (Cited page 46.)

Gupta, C., Chakravartty, J., Wadekar, S., and Banerjee, S. (2006). Fracture behaviour in the dynamic strain ageing regime of a martensitic steel. *Scripta Materialia*, 55(12):1091–1094. (Cited pages 13 and 14.)

Gupta, S., Beaudoin, A. J., and Chevy, J. (2017). Strain rate jump induced negative strain rate sensitivity (NSRS) in aluminum alloy 2024: Experiments and constitutive modeling. *Materials Science and Engineering: A*, 683:143–152. (Cited pages 18, 56, 76, 82, and 105.)

Hähner, P. (1993). Modelling the spatiotemporal aspects of the Portevin-Le Chatelier effect. *Materials Science and Engineering: A*, 164(1-2):23–34. (Cited page 194.)

Halim, H., Wilkinson, D. S., and Niewczas, M. (2007). The Portevin–Le Chatelier (PLC) effect and shear band formation in an AA5754 alloy. *Acta Materialia*, 55(12):4151–4160. (Cited pages 15, 55, 76, and 123.)

Han, Z., Luo, H., and Wang, H. (2011). Effects of strain rate and notch on acoustic emission during the tensile deformation of a discontinuous yielding material. *Materials Science and Engineering: A*, 528(13):4372–4380. (Cited page 148.)

Helfen, L., Morgeneyer, T. F., Xu, F., Mavrogordato, M. N., Sinclair, I., Schillinger, B., and Baumbach, T. (2012). Synchrotron and neutron laminography for three-dimensional imaging of devices and flat material specimens. *International Journal of Materials Research*, 103(2):170–173. (Cited page 170.)

Hickey, W. F. and Ravi-Chandar, K. (2016). Transition from flat to slant fracture in ductile materials. In *Recent Trends in Fracture and Damage Mechanics*, pages 215–235. Springer. (Cited pages 39, 44, 45, and 124.)

Hild, F. and Roux, S. (2006). Digital image correlation: from displacement measurement to identification of elastic properties–a review. *Strain*, 42(2):69–80. (Cited page 79.)

Hild, F. and Roux, S. (2012). Comparison of local and global approaches to digital image correlation. *Experimental Mechanics*, 52(9):1503–1519. (Cited page 79.)

Hong, S. G. and Lee, S. B. (2005). Mechanism of dynamic strain aging and characterization of its effect on the low-cycle fatigue behavior in type 316L stainless steel. *J. Nucl. Mater.*, 340(2):307–314. (Cited page 56.)

Hopperstad, O., Børvik, T., Berstad, T., Lademo, O., and Benallal, A. (2007). A numerical study on the influence of the Portevin–Le Chatelier effect on necking in an aluminium alloy. *Modelling and Simulation in Materials Science and Engineering*, 15(7):747. (Cited page 16.)

Hornbuckle, B., Murdoch, H., Roberts, A., Kecskes, L., Tschopp, M., Doherty, K., Yu, J., and Darling, K. (2017). Property mapping of friction stir welded Al-2139 T8 plate using site specific shear punch testing. *Materials Science and Engineering: A*, 682:192–201. (Cited page 37.)

Huang, Z., Wagner, D., and Bathias, C. (2015). Some metallurgical aspects of dynamic strain aging effect on the low cycle fatigue behavior of C–Mn steels. *International Journal of Fatigue*, 80:113–120. (Cited page 124.)

Jiang, H., Zhang, Q., Chen, X., Chen, Z., Jiang, Z., Wu, X., and Fan, J. (2007). Three types of Portevin–Le Chatelier effects: Experiment and modelling. *Acta Materialia*, 55(7):2219–2228. (Cited page 37.)

Jiang, H., Zhang, Q., Wu, X., and Fan, J. (2006). Spatiotemporal aspects of the Portevin–Le Chatelier effect in annealed and solution-treated aluminum alloys. *Scripta Materialia*, 54(12):2041–2045. (Cited pages 30, 31, and 37.)

Jiang, Z. Y., Zhang, Q. C., Jiang, H. F., Chen, Z. J., and Wu, X. P. (2005). Spatial characteristics of the Portevin-Le Chatelier deformation bands in Al-4at% Cu polycrystals. *Materials Science and Engineering: A*, 403(1):154–164. (Cited pages 55 and 123.)

Jo, H. H. and Hirano, K.-I. (1987). Precipitation processes in Al-Cu-Li alloy studied by DSC. In *Materials Science Forum*, volume 13, pages 377–382. Trans Tech Publ. (Cited page 33.)

Kang, J., Wilkinson, D., Jain, M., Embury, J., Beaudoin, A., Kim, S., Mishira, R., and Sachdev, A. (2006). On the sequence of inhomogeneous deformation processes occurring during tensile deformation of strip cast AA5754. *Acta Materialia*, 54(1):209–218. (Cited pages 15 and 16.)

Karimi, A. (1981). *Etude sur machine molle de la déformation plastique hétérogène: cas d'un acier austenitique*. PhD dissertation, Ecole des Mines de Paris. (Cited page 10.)

Kim, J.-B. and Yoon, J. W. (2015). Necking behavior of AA6022-T4 based on the crystal plasticity and damage models. *International Journal of Plasticity*, 73:3–23. (Cited page 182.)

Kim, K.-C., Kim, J.-T., Suk, J.-I., Sung, U.-H., and Kwon, H.-K. (2004). Influences of the dynamic strain aging on the J–R fracture characteristics of the ferritic steels for reactor coolant piping system. *Nuclear Engineering and Design*, 228(1):151–159. (Cited pages 13, 55, and 123.)

Klusemann, B., Fischer, G., Böhlke, T., and Svendsen, B. (2015). Thermomechanical characterization of Portevin-Le Chatelier bands in AlMg3 (AA5754) and modeling based on a modified Estrin-McCormick approach. *International Journal of Plasticity*, 67:192–216. (Cited pages 56 and 123.)

Kocks, U. (1976). Laws for work-hardening and low-temperature creep. *Journal of Engineering Materials and Technology*, 98(1):76–85. (Cited pages 25 and 58.)

Kok, S., Beaudoin, A., Tortorelli, D., and Lebyodkin, M. (2002). A finite element model for the Portevin–Le Chatelier effect based on polycrystal plasticity. *Modelling and Simulation in Materials Science and Engineering*, 10(6):745. (Cited page 21.)

Kok, S., Bharathi, M., Beaudoin, A., Fressengeas, C., Ananthakrishna, G., Kubin, L., and Lebyodkin, M. (2003). Spatial coupling in jerky flow using polycrystal plasticity. *Acta Materialia*, 51(13):3651–3662. (Cited pages 104 and 181.)

Kröner, E. (1961). Zur plastischen verformung des vielkristalls. *Acta Metallurgica*, 9(2):155–161. (Cited page 179.)

Kubin, L. and Estrin, Y. (1984). Thermal effects in low-temperature deformation: The response to strain rate changes. *Crystal Research and Technology*, 19(6):853–862. (Cited page 129.)

Kubin, L. and Estrin, Y. (1990). Evolution of dislocation densities and the critical conditions for the Portevin-Le Chatelier effect. *Acta Metallurgica et Materialia*, 38(5):697–708. (Cited pages 55 and 178.)

Kubin, L. and Estrin, Y. (1991). Dynamic strain ageing and the mechanical response of alloys. *Journal de Physique III*, 1(6):929–943. (Cited page 12.)

Kubin, L., Styczynski, A., and Estrin, Y. (1992). Discontinuous yielding in an Al-Li-Zr alloy. *Scripta Metallurgica et Materialia*, 26(9):1423–1428. (Cited page 33.)

Kubin, L. P. (1994). Strain and strain rate softening instabilities: length scales and spatial couplings. In *Key Engineering Materials*, volume 97, pages 219–234. Trans Tech Publ. (Cited page 10.)

Kubin, L. P., Chihab, K., and Estrin, Y. (1988). The rate dependence of the Portevin-Le Chatelier effect. *Acta Metallurgica et Materialia*, 36(10):2707–2718. (Cited page 65.)

Kubin, L. P. and Estrin, Y. (1985). The Portevin-Le Chatelier effect in deformation with constant stress rate. *Acta Metallurgica et Materialia*, 33(3):397–407. (Cited pages 21, 24, 55, 124, and 178.)

Kumar, A. M. and Hirth, J. P. (1991). Mixed mode I/III fracture testing. *Scripta Metallurgica et Materialia*, 25(5):985–990. (Cited page 38.)

Kumar, S., Król, J., and Pink, E. (1996). Mechanism of serrated flow in binary Al-Li alloys. *Scripta Materialia*, 35(6):775–780. (Cited page 33.)

Kumar, S. and Pink, E. (1995). Effect of δ'precipitates on serrated flow. *Scripta Metallurgica et Materialia*, 32(5):749–753. (Cited page 34.)

Kuroda, M. and Tvergaard, V. (2007). Effects of texture on shear band formation in plane strain tension/compression and bending. *International Journal of Plasticity*, 23(2):244–272. (Cited page 45.)

Lacombe, P. (1985). L'effet Portevin-Le Chatelier: ses caractéristiques et ses conséquences sur les hétérogénéités de déformation plastique. *Matériaux et techniques*, 73(8-9):E5–E15. (Cited page 10.)

Lan, W., Deng, X., Sutton, M. A., and Cheng, C.-S. (2006). Study of slant fracture in ductile materials. *International Journal of Fracture*, 141(3-4):469–496. (Cited page 38.)

Le Cam, J.-B., Robin, E., Leotoing, L., and Guines, D. (2017). Calorimetric analysis of Portevin-Le Chatelier bands under equibiaxial loading conditions in Al–Mg alloys: Kinematics and mechanical dissipation. *Mechanics of Materials*, 105:80–88. (Cited page 124.)

Le Chatelier, A. (1909). Influence du temps et de la température sur les essais au choc. *Revue de métallurgie*, 6(8):914–917. (Cited pages 10 and 170.)

Le Jolu, T., Morgeneyer, T. F., Denquin, A., and Gourgues-Lorenzon, A.-F. (2015). Fatigue lifetime and tearing resistance of AA2198 Al–Cu–Li alloy friction stir welds: effect of defects. *International Journal of Fatigue*, 70:463–472. (Cited page 159.)

Le Jolu, T., Morgeneyer, T. F., Denquin, A., Sennour, M., Laurent, A., Besson, J., and Gourgues-Lorenzon, A.-F. (2014). Microstructural characterization of internal welding defects and their effect on the tensile behavior of FSW joints of AA2198 Al-Cu-Li alloy. *Metallurgical and Materials Transactions A*, 45(12):5531–5544. (Cited page 159.)

Leacock, A., McMurray, R., Brown, D., Poston, K., Cueto, E., and Chinesta, F. (2007). The influence of strain rate variations on the appearance of serrated yielding in 2024-T3 Al-clad aluminium alloy. In *AIP Conference Proceedings*, volume 907, pages 390–395. AIP. (Cited pages 18 and 82.)

Lebyodkin, M., Dunin-Barkowskii, L., Brechet, Y., Estrin, Y., and Kubin, L. (2000). Spatio-temporal dynamics of the Portevin–Le Chatelier effect: experiment and modelling. *Acta Materialia*, 48(10):2529–2541. (Cited pages 11 and 12.)

Lemaitre, J. and Chaboche, J.-L. (1994). *Mechanics of solid materials*. Cambridge University Press. (Cited page 25.)

Levenberg, K. (1944). A method for the solution of certain non-linear problems in least squares. *Quarterly of Applied Mathematics*, 2(2):164–168. (Cited page 183.)

Li, T. Q., Liu, Y. B., Cao, Z. Y., Jiang, D. M., and Cheng, L. R. (2010). The tensile properties and high cyclic fatigue characteristics of Mg-5Li-3Al-1.5Zn-2RE alloy. *Materials Science and Engineering: A*, 527:7808–7811. (Cited page 56.)

Lin, Y., Xia, Y.-C., Jiang, Y.-Q., Zhou, H.-M., and Li, L.-T. (2013). Precipitation hardening of 2024-T3 aluminum alloy during creep aging. *Materials Science and Engineering: A*, 565:420–429. (Cited page 30.)

Ling, C. and McCormick, P. (1990). Strain rate sensitivity and transient behaviour in an Al-Mg-Si alloy. *Acta Metallurgica et Materialia*, 38(12):2631–2635. (Cited page 88.)

Ling, C. and McCormick, P. (1993). The effect of temperature on strain rate sensitivity in an Al-Mg-Si alloy. *Acta Metallurgica et Materialia*, 41(11):3127–3131. (Cited page 88.)

Lipski, A. and Mroziński, S. (2012). The effects of temperature on the strength properties of aluminium alloy 2024-T3. *Acta Mechanica et Automatica*, 6(3):62–66. (Cited page 37.)

Louat, N. (1981). On the theory of the Portevin-Le Chatelier effect. *Scripta Metallurgica*, 15(11):1167–1170. (Cited pages 20 and 23.)

Louche, H., Vacher, P., and Arrieux, R. (2005). Thermal observations associated with the Portevin-Le Chatelier effect in an Al-Mg alloy. *Materials Science and Engineering: A*, 404(1):188–196. (Cited page 55.)

Lüders, W. (1860). Über die äusserung der elasticität an stahlartigen eisenstäben und stahlstäben, und über aine beim biegen solcher stäbe beobachtete molecularbewegung. *Dingler's Polytechnisches Journal, 4th series*, 5:18–22. (Cited page 9.)

Luo, M. and Rousselier, G. (2014). Modeling of large strain multi-axial deformation of anisotropic metal sheets with strength-differential effect using a Reduced Texture Methodology. *International Journal of Plasticity*, 53:66–89. (Cited pages 178, 179, 181, and 183.)

Lyons, J., Liu, J., and Sutton, M. (1996). High-temperature deformation measurements using digital image correlation. *Experimental Mechanics*, 36(1):64–70. (Cited page 129.)

Mahgoub, E., Deng, X., and Sutton, M. A. (2003). Three-dimensional stress and deformation fields around flat and slant cracks under remote Mode I loading conditions. *Engineering Fracture Mechanics*, 70(18):2527–2542. (Cited pages 43 and 159.)

Mahmoud, S. and Lease, K. (2003). The effect of specimen thickness on the experimental characterization of critical crack-tip-opening angle in 2024-T351 aluminum alloy. *Engineering Fracture Mechanics*, 70(3):443–456. (Cited pages 38 and 44.)

Maire, E. and Withers, P. J. (2014). Quantitative X-ray tomography. *International Materials Reviews*, 59(1):1–43. (Cited page 170.)

Maire, E., Zhou, S., Adrien, J., and Dimichiel, M. (2011). Damage quantification in aluminium alloys using in situ tensile tests in X-ray tomography. *Engineering Fracture Mechanics*, 78(15):2679–2690. (Cited page 170.)

Manual, V.-D. (2010). Vic-3d manual. correlated solutions. *Inc., Columbia, SC*. (Cited pages 81 and 129.)

Marais, A. (2012). *Influence du vieillissement statique sur la transition ductile-fragile des aciers au C-Mn*. PhD dissertation, Ecole des Mines de Paris. (Cited pages 25 and 213.)

Marais, A., Mazière, M., Forest, S., Parrot, A., and Le Delliou, P. (2012). Identification of a strain-aging model accounting for lüders behavior in a C-Mn steel. *Philosophical Magazine*, 92(28-30):3589–3617. (Cited pages 26, 56, 58, 61, 62, 66, 105, 124, 125, and 140.)

Marchenko, A., Mazière, M., Forest, S., and Strudel, J.-L. (2016). Crystal plasticity simulation of strain aging phenomena in α-titanium at room temperature. *International Journal of Plasticity*, 85:1–33. (Cited page 170.)

Max, B., Viguier, B., Andrieu, E., and Cloue, J.-M. (2014). A re-examination of the Portevin-Le Chatelier effect in alloy 718 in connection with oxidation-assisted intergranular cracking. *Metallurgical and Materials Transsactions: A*, 45A:5431–5441. (Cited page 76.)

Mazière, M. (2007). *Overspeed burst of turboengine disks*. PhD dissertation, Ecole des Mines de Paris. (Cited page 56.)

Mazière, M. (2017). Modelling the Portevin-Le Chatelier effect in metallic alloys. *HDR Université Pierre et Marie Curie*. (Cited page 26.)

Mazière, M., Besson, J., Forest, S., Tanguy, B., Chalons, H., and Vogel, F. (2010). Numerical aspects in the finite element simulation of the Portevin–Le Chatelier effect. *Computer Methods in Applied Mechanics and Engineering*, 199(9):734–754. (Cited pages 24, 55, 56, 65, 89, 104, 124, 139, and 170.)

Mazière, M. and Dierke, H. (2012). Investigations on the Portevin-Le Chatelier critical strain in an aluminum alloy. *Computational Materials Science*, 52(1):68–72. (Cited pages 10, 12, 66, 69, 71, 74, 116, 117, 118, and 123.)

Mazière, M. and Forest, S. (2015). Strain gradient plasticity modeling and finite element simulation of Lüders band formation and propagation. *Continuum Mechanics and Thermodynamics*, 27(1-2):83. (Cited pages 66, 194, and 204.)

Mazière, M., Luis, C., Marais, A., Forest, S., and Gaspérini, M. (2017). Experimental and numerical analysis of the Lüders phenomenon in simple shear. *International Journal of Solids and Structures*, 106:305–314. (Cited pages 26, 66, and 194.)

Mazière, M. and Pujol d'Andrebo, Q. (2015). Portevin-Le Chatelier effect under cyclic loading: experimental and numerical investigations. *Philosophical Magazine*, 95(28-30):3257–3277. (Cited page 123.)

McCormick, P. (1988). Theory of flow localisation due to dynamic strain ageing. *Acta Metallurgica*, 36(12):3061 – 3067. (Cited pages 21, 22, 23, 24, 55, 56, 58, 88, 89, 104, 124, and 178.)

McCormick, P. and Ling, C. (1995). Numerical modelling of the Portevin-Le Chatelier effect. *Acta Metallurgica et Materialia*, 43(5):1969–1977. (Cited pages 24 and 178.)

Méric, L., Poubanne, P., and Cailletaud, G. (1991). Single crystal modeling for structural calculations: part 1—model presentation. *Journal of Engineering Materials and Technology*, 113(1):162–170. (Cited page 107.)

Mesarovic, S. D. (1995). Dynamic strain aging and plastic instabilities. *Journal of the Mechanics and Physics of Solids*, 43(5):671–700. (Cited page 124.)

Miglin, M. T., Van Der Sluys, W. A., Futato, R. J., and Domian, H. A. (1985). Effects of strain aging in the unloading compliance J test. In *Elastic-Plastic Fracture Test Methods: The User's Experience*. ASTM International. (Cited pages 13 and 55.)

Moreno, J.-C. (1998). *Vieillissement dynamique dans les joints soudés d'acier au carbonne manganèse: Relation entre les paramètres métallurgiques et le comportement mécanique*. PhD dissertation, Châtenay-Malabry, Ecole Centrale Paris. (Cited page 14.)

Morgeneyer, T. F. (2008). *Micromechanical studies and modelling of toughness in high strength aluminium alloys*. PhD dissertation, University of Southampton. (Cited page 43.)

Morgeneyer, T. F. and Besson, J. (2011). Flat to slant ductile fracture transition: Tomography examination and simulations using shear-controlled void nucleation. *Scripta Materialia*, 65(11):1002–1005. (Cited pages 49, 50, 159, 186, and 211.)

Morgeneyer, T. F., Besson, J., Proudhon, H., Starink, M., and Sinclair, I. (2009). Experimental and numerical analysis of toughness anisotropy in AA2139 Al-alloy sheet. *Acta Materialia*, 57(13):3902–3915. (Cited pages 179 and 184.)

Morgeneyer, T. F., Helfen, L., Mubarak, H., and Hild, F. (2013). 3d digital volume correlation of synchrotron radiation laminography images of ductile crack initiation: an initial feasibility study. *Experimental Mechanics*, 53(4):543–556. (Cited page 170.)

Morgeneyer, T. F., Taillandier-Thomas, T., Buljac, A., Helfen, L., and Hild, F. (2016). On strain and damage interactions during tearing: 3D in situ measurements and simulations for a ductile alloy (AA2139-T3). *Journal of the Mechanics and Physics of Solids*. (Cited pages 82, 92, 93, 119, 124, 159, 161, 167, 170, 188, 189, 192, and 193.)

Morgeneyer, T. F., Taillandier-Thomas, T., Helfen, L., Baumbach, T., Sinclair, I., Roux, S., and Hild, F. (2014). In situ 3-D observation of early strain localization during failure of thin Al alloy (2198) sheet. *Acta Materialia*, 69:78–91. (Cited pages 4, 5, 38, 39, 44, 50, 51, 83, 110, 111, 119, 124, 150, 170, 171, 172, 173, 174, 175, 177, 178, 182, 190, 192, 195, 210, and 211.)

Mulford, R. and Kocks, U. (1979). New observations on the mechanisms of dynamic strain aging and of jerky flow. *Acta Metallurgica*, 27(7):1125–1134. (Cited page 20.)

Nahshon, K. and Hutchinson, J. (2008). Modification of the Gurson model for shear failure. *European Journal of Mechanics-A/Solids*, 27(1):1–17. (Cited page 159.)

Nasiri-Abarbekoh, H., Ekrami, A., and Ziaei-Moayyed, A. (2013). Effects of thickness and texture on mechanical properties anisotropy of commercially pure titanium thin sheets. *Materials & Design*, 44:528–534. (Cited page 39.)

Needleman, A. and Rice, J. (1978). Limits to ductility set by plastic flow localization. In *Mechanics of Sheet Metal Forming*, pages 237–267. Springer. (Cited pages 37 and 44.)

Needleman, A. and Tvergaard, V. (1992). Analyses of plastic flow localization in metals. *Applied Mechanics Reviews*, 45(3S):S3–S18. (Cited page 38.)

Nielsen, K. L. and Hutchinson, J. (2017). Steady-state, elastic-plastic growth of slanted cracks in symmetrically loaded plates. *International Journal of Impact Engineering*, 108:286–294. (Cited page 46.)

Nogueira de Codes, R. and Benallal, A. (2011). Influence of specimen geometry on the Portevin–Le Chatelier effect due to dynamic strain aging for the AA5083-H116 aluminum alloy. *Journal of Mechanics of Materials and Structures*, 6(7):951–968. (Cited pages 84, 87, 97, 149, and 150.)

Ovri, H., Jägle, E. A., Stark, A., and Lilleodden, E. T. (2015). Microstructural influences on strengthening in a naturally aged and overaged Al–Cu–Li–Mg based alloy. *Materials Science and Engineering: A*, 637:162–169. (Cited pages 34 and 35.)

Ovri, H. and Lilleodden, E. T. (2015). New insights into plastic instability in precipitation strengthened Al–Li alloys. *Acta Materialia*, 89(0):88–97. (Cited pages 34, 35, 36, 37, 95, and 115.)

Pan, B., Qian, K., Xie, H., and Asundi, A. (2009). Two-dimensional digital image correlation for in-plane displacement and strain measurement: a review. *Measurement Science and Technology*, 20(6):062001. (Cited pages 80 and 81.)

Papasidero, J., Doquet, V., and Mohr, D. (2014). Determination of the effect of stress state on the onset of ductile fracture through tension-torsion experiments. *Experimental Mechanics*, 54(2):137–151. (Cited page 159.)

Pardoen, T., Hachez, F., Marchioni, B., Blyth, P., and Atkins, A. (2004). Mode I fracture of sheet metal. *Journal of the Mechanics and Physics of Solids*, 52(2):423–452. (Cited page 43.)

Pardoen, T. and Hutchinson, J. (2003). Micromechanics-based model for trends in toughness of ductile metals. *Acta Materialia*, 51(1):133–148. (Cited page 159.)

Penning, P. (1972). Mathematics of the Portevin-Le chatelier effect. *Acta Metallurgica*, 20(10):1169–1175. (Cited pages 21, 22, 55, and 124.)

Picu, R., Vincze, G., Ozturk, F., Gracio, J., Barlat, F., and Maniatty, A. (2005). Strain rate sensitivity of the commercial aluminum alloy AA5182-O. *Materials Science and Engineering: A*, 390(1):334–343. (Cited pages 55, 84, and 88.)

Pineau, A., Benzerga, A. A., and Pardoen, T. (2016). Failure of metals I: Brittle and ductile fracture. *Acta Materialia*, 107:424–483. (Cited pages 43 and 44.)

Pink, E. and Król, J. (1995). Precipitation and serrated flow in AlZn10. *Acta Metallurgica et Materialia*, 43(6):2351–2357. (Cited page 31.)

Pink, E., Kumar, S., and Tian, B. (2000). Serrated flow of aluminium alloys influenced by precipitates. *Materials Science and Engineering: A*, 280(1):17–24. (Cited page 34.)

Piobert, G. (1842). Expérience sur la pénétration des projectiles dans le fer forgé. *Mémoire de l'Artillerie*, page 505. (Cited page 9.)

Polmear, I. (2005). *Light alloys: from traditional alloys to nanocrystals*. Butterworth-Heinemann. (Cited pages 28 and 32.)

Portevin, A. and Le Chatelier, F. (1923). Sur un phénomène observé lors de l'essai de traction d'alliages en cours de transformation. *Comptes Rendus de l'Académie des Sciences Paris*, 176:507–510. (Cited pages 10 and 170.)

Prasad, K. and Kamat, S. V. (2008). Transient flow behaviour in a near alpha titanium alloy Timetal 834 in the dynamic strain aging regime. *Materials Science and Engineering: A*, 490(1):477–480. (Cited page 55.)

Prasad, K. and Varma, V. K. (2008). Serrated flow behavior in a near alpha titanium alloy IMI 834. *Materials Science and Engineering: A*, 486(1):158–166. (Cited page 123.)

Prasad, N. E., Gokhale, A., and Wanhill, R. (2013). *Aluminum-lithium alloys: processing, properties, and applications*. Butterworth-Heinemann. (Cited pages 32 and 33.)

Ranc, N., Du, W., Ranc, I., and Wagner, D. (2016). Experimental studies of Portevin-Le Chatelier plastic instabilities in carbon-manganese steels by infrared pyrometry. *Materials Science and Engineering: A*, 663:166–173. (Cited page 123.)

Ranc, N. and Wagner, D. (2005). Some aspects of Portevin–Le Chatelier plastic instabilities investigated by infrared pyrometry. *Materials Science and Engineering: A*, 394(1–2):87–95. (Cited pages 31, 37, 55, and 123.)

Ranc, N. and Wagner, D. (2008). Experimental study by pyrometry of Portevin–Le Chatelier plastic instabilities—Type A to type B transition. *Materials Science and Engineering: A*, 474(1–2):188–196. (Cited pages 31 and 37.)

Rao, K. B. S., Kalluri, S., Halford, G. R., and McGaw, M. A. (1995). Serrated flow and deformation substructure at room temperature in inconel 718 superalloy during strain controlled fatigue. *Scripta Matallurgica et Materialia*, 32(4):493–498. (Cited pages 55 and 123.)

Ren, S.-C., Rousselier, G., Morgeneyer, T. F., Mazière, M., and Forest, S. (2016). Numerical investigation of dynamic strain ageing and slant ductile fracture in a notched specimen and comparison with synchrotron tomography 3D-DVC. *Procedia Structural Integrity*, 2:3385–3392. (Cited pages 178 and 195.)

Rice, J. R. and Tracey, D. M. (1969). On the ductile enlargement of voids in triaxial stress fields. *Journal of the Mechanics and Physics of Solids*, 17(3):201–217. (Cited page 205.)

Rioja, R. J. and Liu, J. (2012). The evolution of Al-Li base products for aerospace and space applications. *Metallurgical and Materials Transactions A*, 43(9):3325–3337. (Cited pages 30 and 33.)

Rivalin, F., Pineau, A., Di Fant, M., and Besson, J. (2001). Ductile tearing of pipeline-steel wide plates: I. dynamic and quasi-static experiments. *Engineering Fracture Mechanics*, 68(3):329–345. (Cited page 46.)

Rosen, A. and Bodner, S. (1969). Repeated discontinuous yielding of 2024 aluminum alloy. *Materials Science and Engineering*, 4(2–3):115–122. (Cited pages 30, 31, and 37.)

Rousselier, G. (1981). Finite deformation constitutive relations including ductile fracture damage. *Three-dimensional constitutive relations and ductile fracture.(A 83-18477 06-39) Amsterdam, North-Holland Publishing Co., 1981,*, pages 331–355. (Cited pages 160 and 178.)

Rousselier, G. (1987). Ductile fracture models and their potential in local approach of fracture. *Nuclear Engineering and Design*, 105(1):97–111. (Cited pages 139, 160, and 183.)

Rousselier, G. (2001). Dissipation in porous metal plasticity and ductile fracture. *Journal of the Mechanics and Physics of Solids*, 49(8):1727–1746. (Cited page 139.)

Rousselier, G., Barlat, F., and Yoon, J. (2009). A novel approach for anisotropic hardening modeling. Part I: Theory and its application to finite element analysis of deep drawing. *International Journal of Plasticity*, 25(12):2383–2409. (Cited pages 107 and 181.)

Rousselier, G., Barlat, F., and Yoon, J. (2010). A novel approach for anisotropic hardening modeling. Part II: Anisotropic hardening in proportional and non-proportional loadings, application to initially isotropic material. *International Journal of Plasticity*, 26(7):1029–1049. (Cited page 181.)

Rousselier, G. and Leclercq, S. (2006). A simplified "polycrystalline" model for viscoplastic and damage finite element analyses. *International Journal of Plasticity*, 22(4):685–712. (Cited page 179.)

Rousselier, G. and Luo, M. (2014). A fully coupled void damage and Mohr–Coulomb based ductile fracture model in the framework of a Reduced Texture Methodology. *International Journal of Plasticity*, 55:1–24. (Cited pages 50, 160, 161, 171, 178, 181, 182, 184, 186, and 194.)

Rousselier, G., Luo, M., and Mohr, D. (2012). Macroscopic plasticity modeling of anisotropic aluminum extrusions using a reduced texture methodology. *International Journal of Plasticity*, 30:144–165. (Cited pages 106 and 107.)

Rousselier, G., Morgeneyer, T. F., Ren, S., Mazière, M., and Forest, S. (2017). Interaction of the Portevin–Le Chatelier phenomenon with ductile fracture of a thin aluminum CT specimen: experiments and simulations. *International Journal of Fracture*, 206(1):95–122. (Cited pages 50, 104, 111, 139, and 149.)

Rousselier, G. and Quilici, S. (2015). Combining porous plasticity with Coulomb and Portevin-Le Chatelier models for ductile fracture analyses. *International Journal of Plasticity*, 69:118–133. (Cited pages 5, 50, 140, 170, 178, 179, 183, 186, 196, and 197.)

Sai, K., Cailletaud, G., and Forest, S. (2006). Micro-mechanical modeling of the inelastic behavior of directionally solidified materials. *Mechanics of Materials*, 38(3):203–217. (Cited pages 106 and 179.)

Scheider, I. and Brocks, W. (2003). Simulation of cup–cone fracture using the cohesive model. *Engineering Fracture Mechanics*, 70(14):1943–1961. (Cited page 49.)

Simonsen, B. C. and Törnqvist, R. (2004). Experimental and numerical modelling of ductile crack propagation in large-scale shell structures. *Marine Structures*, 17(1):1 – 27. (Cited pages 46, 48, 150, and 159.)

Sleeswyk, A. (1958). Slow strain-hardening of ingot iron. *Acta Metallurgica*, 6(9):598–603. (Cited page 20.)

Springer, F. and Schwink, C. (1991). Quantitative investigations on dynamic strain ageing in polycrystalline CuMn alloys. *Scripta Metallurgica et Materialia*, 25(12):2739–2744. (Cited pages 25 and 61.)

Strudel, J. (1979). Interactions des dislocations avec des impuretés mobiles. *Dislocation et Déformation Plastique, Ecole d'Eté Yravals, les Editions de Physique*, pages 199–222. (Cited page 10.)

Subramanian, K. and Duncan, A. (2000). Tensile properties for application to type I and type II waste tank flaw stability analysis (u). Technical report, WSRC-TR-2000-00232, Westinghouse Savannah River Company, Aiken, SC. (Cited page 9.)

Suh, C. H., Jung, Y.-C., and Kim, Y. S. (2010). Effects of thickness and surface roughness on mechanical properties of aluminum sheets. *Journal of mechanical science and technology*, 24(10):2091–2098. (Cited page 39.)

Sutton, M., Dawicke, D., and Newman, J. (1995). Orientation effects on the measurement and analysis of critical ctoa in an aluminum alloy sheet. In *Fracture Mechanics: 26th Volume*. ASTM International. (Cited page 44.)

Sutton, M., Turner, J., Bruck, H., and Chae, T. (1991). Full-field representation of discretely sampled surface deformation for displacement and strain analysis. *Experimental Mechanics*, 31(2):168–177. (Cited page 79.)

Sutton, M. A. (2008). Digital image correlation for shape and deformation measurements. In *Springer Handbook of Experimental Solid Mechanics*, pages 565–600. Springer. (Cited page 129.)

Sutton, M. A. (2013). Computer vision-based, noncontacting deformation measurements in mechanics: a generational transformation. *Applied Mechanics Reviews*, 65(5):050802. (Cited page 81.)

Swaminathan, B., Abuzaid, W., Sehitoglu, H., and Lambros, J. (2015). Investigation using digital image correlation of Portevin-Le Chatelier effect in hastelloy x under thermomechanical loading. *International Journal of Plasticity*, 64:177–192. (Cited page 123.)

Tabata, T., Fujtta, H., and Nakajima, Y. (1980). Behavior of dislocations in Al-Mg single crystals observed by high voltage electron microscopy. *Acta Metallurgica*, 28(6):795–805. (Cited page 20.)

Taupin, V., Chevy, J., and Fressengeas, C. (2016). Effects of grain-to-grain interactions on shear strain localization in al–cu–li rolled sheets. *International Journal of Solids and Structures*, 99:71–81. (Cited pages 119 and 193.)

Tekoğlu, C., Hutchinson, J., and Pardoen, T. (2015). On localization and void coalescence as a precursor to ductile fracture. *Philosophical Transactions of the Royal Society of London A: Mathematical, Physical and Engineering Sciences*, 373(2038):20140121. (Cited pages 38 and 39.)

Teng, X. (2008). Numerical prediction of slant fracture with continuum damage mechanics. *Engineering Fracture Mechanics*, 75(8):2020–2041. (Cited page 50.)

Thevenet, D., Mliha-Touati, M., and Zeghloul, A. (1999). The effect of precipitation on the Portevin-Le Chatelier effect in an Al–Zn–Mg–Cu alloy. *Materials Science and Engineering: A*, 266(1):175–182. (Cited page 31.)

Tong, W., Tao, H., Zhang, N., and Hector, L. G. (2005). Time-resolved strain mapping measurements of individual Portevin–Le Chatelier deformation bands. *Scripta Materialia*, 53(1):87–92. (Cited page 123.)

Trojanová, Z., Drozd, Z., Lukáč, P., and Chmelík, F. (2005). Deformation behaviour of Mg–Li alloys at elevated temperatures. *Materials Science and Engineering: A*, 410:148–151. (Cited page 89.)

Tvergaard, V. and Needleman, A. (1984). Analysis of the cup-cone fracture in a round tensile bar. *Acta Metallurgica*, 32(1):157–169. (Cited page 49.)

Van den Beukel, A. (1975). Theory of the effect of dynamic strain aging on mechanical properties. *Physica Status Solidi*, 30(1):197–206. (Cited pages 20, 23, and 55.)

Van den Brink, S., Van Den Beukel, A., and McCormick, P. (1975). Strain rate sensitivity and the Portevin-Le Chatelier effect in Au–Cu alloys. *Physica Status Solidi (a)*, 30(2):469–477. (Cited page 89.)

Van Den Brink, S. H., Van Den Beukel, A., and McCormick, P. G. (1977). The influence of specimen dimensions and machine stiffness on the Portevin-Le Chatelier effect in an Al–Cu alloy. *Physica Status Solidi (a)*, 41(2):513–521. (Cited page 37.)

Verma, P., Rao, G. S., Chellapandi, P., Mahobia, G., Chattopadhyay, K., Srinivas, N. S., and Singh, V. (2015). Dynamic strain ageing, deformation, and fracture behavior of modified 9Cr–1Mo steel. *Materials Science and Engineering: A*, 621:39 – 51. (Cited pages 41, 42, and 66.)

Wagner, D., Moreno, J., and Prioul, C. (1998). Dynamic strain aging sensitivity of heat affected zones in C–Mn steels. *Journal of Nuclear Materials*, 252(3):257–265. (Cited pages 13 and 55.)

Wagner, D., Moreno, J., Prioul, C., Frund, J., and Houssin, B. (2002). Influence of dynamic strain aging on the ductile tearing of C–Mn steels: modelling by a local approach method. *Journal of Nuclear Materials*, 300(2):178–191. (Cited page 13.)

Wagner, D., Roubier, N., and Prioul, C. (2006). Measurement of sensitivity to dynamic strain aging in C–Mn steels by internal friction experiments. *Materials Science and Technology*, 22(3):301–307. (Cited page 124.)

Wang, B. and Pan, B. (2016). Subset-based local vs. finite element-based global digital image correlation: A comparison study. *Theoretical and Applied Mechanics Letters*, 6(5):200–208. (Cited page 80.)

Wang, H. (2011). *Mechanical behavior and fracture of the C-Mn steels in the presence of dynamic strain aging*. PhD dissertation, Ecole Centrale Paris. (Cited pages 4, 12, 13, 24, 59, 60, 61, 62, 64, 140, 205, 206, and 213.)

Wang, H., Berdin, C., Mazière, M., Forest, S., Prioul, C., Parrot, A., and Le-Delliou, P. (2011). Portevin–le chatelier (plc) instabilities and slant fracture in C–Mn steel round tensile specimens. *Scripta Materialia*, 64(5):430 – 433. (Cited pages 4, 16, 38, 40, 64, and 170.)

Wang, H., Berdin, C., Mazière, M., Forest, S., Prioul, C., Parrot, A., and Le-Delliou, P. (2012). Experimental and numerical study of dynamic strain ageing and its relation to ductile fracture of a C–Mn steel. *Materials Science and Engineering: A*, 547:19 – 31. (Cited pages 55, 56, 58, 59, 61, 62, 63, 64, 76, 92, 123, 125, 148, 161, 165, and 201.)

Wang, S. and Starink, M. (2005). Precipitates and intermetallic phases in precipitation hardening Al–Cu–Mg–(Li) based alloys. *International Materials Reviews*, 50(4):193–215. (Cited page 30.)

Warner, T. (2006). Recently-developed aluminium solutions for aerospace applications. In *Aluminium Alloys 2006 - ICAA10*, volume 519 of *Materials Science Forum*, pages 1271–1278. Trans Tech Publications. (Cited pages 32 and 95.)

Wenman, M. and Chard-Tuckey, P. (2010). Modelling and experimental characterisation of the Lüders strain in complex loaded ferritic steel compact tension specimens. *International Journal of Plasticity*, 26(7):1013–1028. (Cited pages 124 and 149.)

Wijler, A. and Van Westrum, J. S. (1971). On the difference between lüders bands and Portevin-Le Chatelier bands. *Scripta Metallurgica*, 5(10):821–824. (Cited page 10.)

Wu, W., Wang, Y., Wang, J., and Wei, S. (2014). Effect of electrical pulse on the precipitates and material strength of 2024 aluminum alloy. *Materials Science and Engineering: A*, 608:190 – 198. (Cited page 37.)

Xiao, Y., Zeng, P., and Lei, L. (2016). Effect of double-edge semi-circular notches on the mechanical response of superelastic NiTi shape memory alloy: Experimental observations. *The Journal of Strain Analysis for Engineering Design*, 51(8):555–562. (Cited page 149.)

Xiong, S., Zhang, Q., Cao, P., and Xiao, R. (2009). Effect of precipitate on PLC effect in 2024 Al alloy. *Acta Metallurgica Sinica*, 45(7):892–896. (Cited page 30.)

Xu, X., Su, Y., Cai, Y., Cheng, T., and Zhang, Q. (2015). Effects of various shape functions and subset size in local deformation measurements using dic. *Experimental Mechanics*, 55(8):1575–1590. (Cited page 84.)

Xue, L. (2007). *Ductile fracture modeling-theory, experimental investigation and numerical verification*. PhD dissertation, Massachusetts Institute of Technology. (Cited pages 40 and 41.)

Xue, L. and Wierzbicki, T. (2008). Ductile fracture initiation and propagation modeling using damage plasticity theory. *Engineering Fracture Mechanics*, 75(11):3276–3293. (Cited page 50.)

Xue, L. and Wierzbicki, T. (2009). Numerical simulation of fracture mode transition in ductile plates. *International Journal of Solids and Structures*, 46(6):1423–1435. (Cited pages 43, 49, and 50.)

Yilmaz, A. (2016). The Portevin–Le Chatelier effect: a review of experimental findings. *Science and Technology of Advanced Materials*. (Cited page 11.)

Yoon, J., Lee, B., Oh, Y., and Hong, J. (1999). Effects of loading rate and temperature on J–R fracture resistance of an SA516-Gr. 70 steel for nuclear piping. *International Journal of Pressure Vessels and Piping*, 76(9):663–670. (Cited pages 13 and 14.)

Yuzbekova, D., Mogucheva, A., Zhemchuzhnikova, D., Lebedkina, T., Lebyodkin, M., and Kaibyshev, R. (2017). Effect of microstructure on continuous propagation of the Portevin–Le Chatelier deformation bands. *International Journal of Plasticity*, 96:210 – 226. (Cited pages 16, 17, and 123.)

Zaiser, M. and Hähner, P. (1997). Oscillatory modes of plastic deformation: theoretical concepts. *Physica Status Solidi B*, 199(2):267–330. (Cited page 70.)

Zambo, S. and Wert, J. (1993). Effects of Li concentration and a Mg addition on serrated flow in Al-Li alloys. *Scripta Metallurgica et Materialia*, 29(12):1523–1528. (Cited page 34.)

Zdunek, J., Brynk, T., Mizera, J., Pakieła, Z., and Kurzydłowski, K. J. (2008). Digital image correlation investigation of portevin–le chatelier effect in an aluminium alloy. *Materials Characterization*, 59(10):1429–1433. (Cited page 123.)

Zhang, F., Bower, A., and Curtin, W. (2012). The influence of serrated flow on necking in tensile specimens. *Acta Materialia*, 60(1):43–50. (Cited pages 16 and 55.)

Zhang, Q., Jiang, Z., Jiang, H., Chen, Z., and Wu, X. (2005). On the propagation and pulsation of Portevin-Le Chatelier deformation bands: An experimental study with digital speckle pattern metrology. *International Journal of Plasticity*, 21(11):2150–2173. (Cited page 123.)

Zhang, S., McCormick, P., and Estrin, Y. (2001). The morphology of Portevin–Le Chatelier bands: finite element simulation for Al–Mg–Si. *Acta Materialia*, 49(6):1087–1094. (Cited pages 21, 24, 56, 124, 170, and 178.)

Zhao, K. and Fan, R. (2016). The effect of pulse electric current on the mechanical properties and fracture behaviors of aluminum alloy AA5754. *Journal of Engineering Materials and Technology*, 138(4):041009. (Cited page 48.)

Résumé

Récemment, les observations in-situ par laminographie aux rayons X (au synchrotron) montrent que les multiples bandes de localisation sont les précurseurs de l'endommagement et éventuellement de la rupture en biseau. Ces bandes peuvent être liées aux phénomènes de vieillissement par la déformation (type effet de Lüders ou Portevin-Le Chatelier (PLC)) dont l'influence sur la rupture est encore mal compris. Ces effets sont pourtant observés dans de nombreux alliages industriels comme les aluminiums de la série 2000 ou 5000, ou par exemple, dans le cas des aciers C-Mn pour lesquels un creux de ductilité est observé dans la gamme de température oú ces effets sont les plus marqués. L'objectif de la thèse consiste à caractériser l'effet PLC et évaluer son influence sur le développement de l'endommagement et donc sur la rupture finale. D'abord, l'effet de vieillissement sur l'écrouissage a été introduit dans un modèle basé sur la densité de dislocations en utilisant les résultats dans la littérature. Ensuite, certains alliages d'aluminium de la série 2000 et un acier C-Mn ont été étudiés par essais mécaniques avec corrélation d'images. Le déclenchement prématuré de localisation a été observé pendant les essais de relaxation, de déchargement et de changement de vitesse pour certains alliages d'aluminium. Les bandes autour de l'entaille dans l'éprouvette d'acier C-Mn ont été observées à haute température. Deux modes de rupture différents ont été observés dans les deux températures. Ces résultats sont comparés avec ceux du modèle KEMC. Enfin, un modèle de comportement couplant les effets de vieillissement (type KEMC) et d'endommagement (type Rousselier) a été développé pour tenter d'expliquer les interactions observées expérimentalement entre ces deux phénomènes.

Mots Clés

Rupture ductile, laminography 3D in-situ, corrélation d'image, simulation par éléments finis, alliages industriels, effet Portevin-Le Chatelier

Abstract

Recently, in-situ observations by X-ray laminography (at synchrotron) show that the multiple localization bands are the precursors of damage and possibly the slant fracture. These bands can be related to the strain ageing effect (Lüders or Portevin-Le Chatelier (PLC)) whose influence on the fracture is still poorly understood. These effects are observed in many industrial alloys such as 2000 or 5000 series aluminium alloys, or, for example, in the C-Mn steels for which a ductility drop is observed in the temperature range where these effects are most pronounced. The aim of the thesis is to characterize the PLC effect and to evaluate its influence on the development of ductile damage and therefore on the final fracture. Firstly, the influence of strain ageing on strain hardening was introduced in a model based on the dislocation density using results from the literature. Secondly, several 2000 series aluminium alloys and a C-Mn steel were investigated by mechanical tests combined with Digital Image Correlation. The premature triggering of localization bands was observed in tensile tests involving relaxation, unloading and strain rate jump for certain aluminium alloys. The bands around the notch in the specimens of C-Mn steel were observed at high temperature. Two different modes of fracture were observed at the two temperatures. These results are compared with those produced with the KEMC model. Thirdly, a constitutive model combining the strain ageing (type KEMC) and damage (type Rousselier) was developed in order to explain the experimentally observed interactions between these two phenomena.

Keywords

Ductile fracture, 3D in-situ laminography, digital image correlation, finite element simulation, Industrial alloys, Portevin–Le Chatelier effect